THERMAL MATURATION-INDUCED EVOLUTION OF THE ELASTIC AND TRANSPORT PROPERTIES OF ORGANIC-RICH SHALES

A DISSERTATION

SUBMITTED TO THE DEPARTMENT OF GEOPHYSICS

AND THE COMMITTEE ON GRADUATE STUDIES

OF STANFORD UNIVERSITY

IN PARTIAL FULFILLMENT OF THE REQUIREMENTS

FOR THE DEGREE

OF DOCTOR OF PHILOSOPHY

Adam M. Allan

September 2015

This dissertation is online at: http://purl.stanford.edu/vj625gh3300

I certify that I have read this dissertation and that, in my opinion, it is fully adequate in scope and quality as a dissertation for the degree of Doctor of Philosophy.

Tiziana Vanorio, Primary Adviser

I certify that I have read this dissertation and that, in my opinion, it is fully adequate in scope and quality as a dissertation for the degree of Doctor of Philosophy.

Stephan Graham

I certify that I have read this dissertation and that, in my opinion, it is fully adequate in scope and quality as a dissertation for the degree of Doctor of Philosophy.

Gerald Mavko

Approved for the Stanford University Committee on Graduate Studies.

Patricia J. Gumport, Vice Provost for Graduate Education

This signature page was generated electronically upon submission of this dissertation in electronic format. An original signed hard copy of the signature page is on file in University Archives.

ABSTRACT

The primary focus of this dissertation is to improve the applicability of rock physics models for elastic anisotropy and fluid transport in organic-rich shale through the development and implementation of practical workflows and pioneering experimental methodologies. Shale accounts for the vast majority of rocks in sedimentary basins and, subsequently, the elastic anisotropy of shale must be comprehensively understood for proper processing and interpretation of surface seismic studies. Additionally, as unconventional reservoirs are increasingly targeted, the development of detailed physical relationships between geochemical indicators of hydrocarbon generation and retention with parameters quantifiable from remote sensing surveys, such as elastic anisotropy from seismic surveys, are key to improving unconventional exploration procedures and workflows. Further, the development of relationships between these geochemical indicators and transport properties, such as porosity and permeability, will be vital to the identification of sweet spots and the development of improved recovery efforts in unconventional reservoirs. However, previous attempts at developing these relationships by comparing shale samples from a vast range of formations are suspected to be contaminated by issues of heterogeneity in mineralogy, organic matter type, texture, and burial history between the samples.

In this dissertation, I provide further evidence that relationships developed by comparing samples from multiple formations are obfuscated, or indeed corrupted, by inter-sample heterogeneity. Subsequently, I develop a pioneering methodology for the characterization of a single sample before and after inducing hydrocarbon generation (also called thermal maturation) on individual core plugs. This process is implemented in two manners: firstly, an experimentally simple method in which samples are thermally matured without any applied confining pressure, and, secondly, an experimentally taxing method in which samples are matured in a purpose-built vessel under in situ confining pressures.

The first lesson learned in this dissertation is that confining pressure must be applied during thermal maturation to preserve the integrity of the sample for future experimental characterization. Without applied confining pressure, the pore pressure induced by hydrocarbon generation can fracture the rock. This fracturing overwhelms any maturation-dependent elastic signature developed in the intact rock matrix, and, as such, renders the sample of little use in developing the complex geochemical-rock physical relationships we desire.

By applying confining pressure during thermal maturation, fracturing is suppressed, and the induced evolution of microstructures and geophysical parameters can be experimentally constrained. Through these experiments, it is determined that the greatest control on organic-rich shale evolution during thermal maturation is the initial microstructure of the thermally immature rock. In organic-rich shales consisting of an aligned siliciclastic matrix and dispersed lenticular organic bodies, hydrocarbon generation and expulsion forms aligned sets of microcracks that, when filled with fluids, will be acoustically detectable as an increase in elastic anisotropy. Further, the development of these microcracks can result in significant increases in the permeability of these samples. Subsequently, thermal maturation of such a laminar shale may be both acoustically detectable and indicate improved production rates. Contrastingly, in organic-rich micritic rocks or siltstones consisting of a weakly aligned matrix and disordered, amorphous organic bodies, microcracks do not align. Subsequently, there is no anisotropic signature of thermal maturation. However, an initial microstructure in which the organic matter occurs as a pore-filling phase results in severe velocity decreases and permeability increases as that pore-filling material is expelled from the system. As a result, regions of thermal maturity may be identifiable in weakly aligned rocks too, albeit by targeting low velocity zones rather than increases in elastic anisotropy.

ACKNOWLEDGEMENTS

I would like to begin by expressing my immense gratitude to my advisers: Tiziana Vanorio for accepting me into her group, supporting me during my time here, challenging and aiding me along the way, and, most importantly, allowing me to repeatedly break equipment in her laboratory; and Gary Mavko for bringing me to Stanford in the first place and his remarkably entertaining conversations – for an ornithologist, that is. I would also like to thank Tapan Mukerji for teaching me the vast majority of my computer/programming knowledge and putting up with my early ineptitude in such projects. Finally, I would like to thank Stephan Graham for serving on my committee and correcting numerous issues of misused geologic terminology. Finally-finally, special thanks to all of the amazing staff in the Department of Geophysics – Tara, Nancy, Fuad, Jared, Michelle, Claudia, Susan, and Vanessa – for being completely awesome and preventing me from being kicked out by forgetting to submit many, many pieces of paperwork.

I am indebted to the William R. and Sara Hart Kimball Stanford Graduate Fellowship for funding the majority of my time at Stanford University and the Stanford Rock Physics and Borehole Geophysics Project for funding the remainder. Furthermore, I am most grateful to ENI S.p.A. and Chevron for providing the majority of the samples studied in this thesis. Perhaps most of all, I am thankful for Tony Clark and his willingness/ability to repair all of the aforementioned broken equipment and his tireless work in designing, building, and maintaining the HTHP. A special thank you is due to my present and former office mates – Randi, Arjun, Qiang Fu, Dario, Amrita, Ammar, Tony, and Humberto – and all the students and postdocs that I have met in SRB and SRPL over the past 5+ years – Kevin, Richa, Ramil, Ratna, Danica, Piyapa, Adam, Nishank, Fabian, Stephanie, Kenichi, Yu Xia, Chisato, Yuki, Jane, Priyanka, Sabrina, Iris, Natt, Uri, Abrar, Abdullah, Pinar, Salma, Dulcie, and Krongrath (this research group is too big). It was a pleasure to work with, learn from, and have my patience tried by all of you.

I have made many lifelong friends during my time in California: Denys, who survived living with me for 3 years while eating theoretically fatal amounts of Jack in the Box, Kevin, who isn't half bad for a Cardinals fan, Chris, who certainly isn't the worst Englishman I've ever met, Matt for only knocking me off my bike once, and Nick and Dave who were clearly completely at peace with being inferior golfers to me. I'd be remiss if I didn't thank Jason, Andreas, and Gader for contributing (likely minimally) to numerous trivia victories, and Ian, Nik, Suzanne, Rall, Sam, Brad, Ossian, Solomon, Jesse, Jens, and Alex for providing... let's go with levity... along the way. There are likely several hundred other people who deserve to be mentioned here for putting up with my shenanigans for this long, I can only hope this sentence suffices.

Finally, I'd like to mention my loved ones. My parents who not only resisted all temptation to put me up for adoption or otherwise sell me, but also supported me deeply with their time and love, but most importantly a roof, warm food, and tuition. My siblings, Kip and Madzi, who, no matter how far I go in life, will always remind me about *that one time*(!) I slurred onstage. And my dear Margot, who made up admirably for making me camp in the snows of Yosemite by listening to my (near) constant whining about lab work, shale, experimental science, numerical science, microscopes, lasers, geophysics in general, and a host of other minutiae.

Thank you all.

TABLE OF CONTENTS

LIST OF FIGURES

LIST OF TABLES

Chapter 1

INTRODUCTION

1.1 Motivation and Objectives

This thesis is concerned, broadly, with the relationship between experimentally obtained velocity and permeability values, microstructure, and thermal maturity for a suite of organic-rich shales. The experimental analyses that compose this thesis are separable into two main groups: the relation of microstructure and thermal maturity to elastic anisotropy and permeability, respectively. The combination of these investigations then enables a thorough and comprehensive analysis of the evolution of organic-rich shale as a result of thermal maturation. Or in other words, this thesis aims to address the question: how does the thermal decomposition of organic matter, and the resultant expulsion of produced hydrocarbons, affect the geophysical (e.g., elastic and transport) properties of the bulk rock?

The combination of greater awareness of, and concern with, anthropogenic global warming and the proven ability to recover hydrocarbons in great quantity from source rocks motivate the need for a more thorough understanding of the rock physics of organic-rich shale. Natural gas produces 43% fewer carbon dioxide emissions per unit of energy than coal (EIA, 1998); subsequently, natural gas is seen as a viable 'bridge fuel' for electricity generation between current heavily coal-driven practices and a future based on renewable energy resources. As a result, the Energy Information Administration (EIA) project that natural gas will exceed coal as the primary

source of electricity by 2035, with 43%-47% of electricity in the U.S. being generated from natural gas in 2040 (EIA, 2014). This increase in natural gas consumption is projected to be fueled by a 113% increase in domestic dry gas production from shale (EIA, 2013), which surpasses domestic demand and results in the U.S. becoming a net exporter of natural gas by 2020 (EIA, 2014). With time, however, the price of natural gas is projected to increase by 3.7% per year to 2040 due to increases in the cost of production (EIA, 2014). It is, subsequently, of the utmost importance that unconventional shale gas reserves be targeted and produced as efficiently and with as much regard for environmental safety as possible.

Traditionally, the exploration of conventional hydrocarbon reservoirs has relied heavily on the quantitative interpretation of geophysical attributes through the rock physics characterization of the inorganic rock frame and the fluid contained in it. In contrast, the characterization of unconventional shale reservoirs has relied strongly on geochemical data, which, by analyzing the organic phase from well-core samples, cuttings, and basin modeling techniques, addresses complex questions of hydrocarbon quantity, quality, and maturity. Clearly, the problem cannot be decoupled: any modification occurring within the organic phase resulting from its deposition, burial, maturation, and expulsion inherently affects the bulk rock properties, microstructure, and, in turn, the geophysical attributes. The investigation of the interplay of organic geochemistry, shale microstructure, and rock physical properties in this thesis is a first step towards resolving the interconnected nature of the evolving organic and inorganic phases and, subsequently, improve the characterization of unconventional reservoirs. By understanding the relationship between thermal maturity (the parameter that quantifies the degree to which the process of thermal maturation has occurred), the possible changes that thermal maturation brings to the rock, and, in turn, the elastic and transport properties of shale we may better remotely identify 'sweet spots' within unconventional reservoirs. In this thesis, I document an experimental approach to singling out possible factors/properties that are needed to inform next generation rock physics models for unconventional reservoirs. Through this work, we hope to enable the improved identification of locations that have generated economic quantities of hydrocarbons through elastic signatures and be better able to quantify the economic viability of the accumulation through characterization of the porosity and permeability of the shale.

The generation of fluid hydrocarbons from solid organic matter in the, typically, tight pore space of shale causes increases in the pore pressure within isolated pores in and adjacent to organic bodies. The relaxation of the accumulated pore pressure is dependent upon the migration of generated hydrocarbons along pressure-induced microcracks propagating through the mineral matrix of the rock. When open, these microcracks will, if sufficiently co-aligned, alter the elastic anisotropy of the shale and the connectivity of the pore network. There exists substantial experimental analysis of the elastic and transport properties of shale in the rock physics literature that attempts to discriminate the relative importance of microcracks from the intrinsic properties of the solid rock (e.g., Vernik, 1993; Johnston and Christensen, 1995; Dewhurst and Siggins, 2006; Wang and Reed, 2009; Vermylen, 2011). However, the extension of these analyses to the direct study of the thermal evolution of shale is almost absent. The primary contribution to the elastic evolution of shale with thermal maturation is the so-called Vernik dataset (Vernik and

Nur, 1992; Vernik and Landis, 1996; Vernik and Liu, 1997). This dataset documents the elastic anisotropy of organic-rich shales as a function of thermal maturity, but relies on a sample set of rocks with widely varying mineralogies and depositional and burial histories. Subsequently, the interpretation of thermal maturity-dependent trends from this dataset may be corrupted by the overprinting of mineralogical, depositional, or diagenetic effects which may have variable effects on the respective thermally maturing sample. Ideally, any thermal maturity-dependent trends would be fit to data detailing the evolution of samples from a common source, e.g., the same geologic formation. Similarly, any attempt to compare the published shale permeability data (e.g., Kwon et al., 2001, 2004; Bustin et al., 2008; Ghanizadeh et al., 2013; Wang and Reed, 2009; Heller et al., 2014; Bhandari et al., 2015) as a function of thermal maturity is affected by this same deficiency, as there exists no comprehensive study of the effect of thermal evolution on the transport properties of individual organic-rich shales.

The chapters of this thesis document the evolution of a comprehensive methodology for relating the thermal maturity of organic-rich shale to the shale microstructure and rock properties, and the application of this methodology to a broad suite of organic-rich shale samples. These relations are made through a combination of classical rock physics measurements, such as grain density, porosity, permeability, acoustic velocity, and elastic anisotropy, and emergent high-resolution imaging techniques, such as scanning electron microscopy (SEM), confocal laser scanning microscopy (CLSM), and X-ray microtomography (microCT). Furthermore, I apply this methodology iteratively to samples that are thermally matured in the laboratory through pyrolysis experiments, which, for the very first time, are conducted under pressures that are relevant to reservoir conditions. In so doing, I am able to identify the effect of thermal maturation on the microstructure and physical properties of the rock while minimizing mineralogical or diagenetic overprints. The applicability of iterative characterization pre- and post-pyrolysis is then addressed through comparison to organic-rich shale samples that have been matured naturally in situ.

Subsequently, through the progression of this thesis, I attempt to enhance the understanding of organic-rich shale by addressing the following primary questions:

1. Are we able to iteratively characterize whole core plugs pre- and post-pyrolysis (Chapter 2)?

2. What is/are the dominant source/sources of elastic anisotropy in naturally matured organic-rich shales (Chapter 4)?

3. How do the relative magnitude of anisotropic sources change as a function of applied stresses (Chapter 4)?

4. How do the elastic properties of organic-rich shale evolve as a function of pyrolysis-induced thermal maturation (Chapter 5)?

5. How do the transport properties of organic-rich shale evolve as a function of pyrolysis-induced thermal maturation? Does the scale of investigation have any effect on this evolution (Chapter 6)?

6. What control does shale microstructure/texture have on the thermally induced evolution of organic-rich shale (Chapters 5 and 6)?

1.2 Thesis Outline

The following is a brief summary of the contents and results of each chapter in this thesis.

Chapter 2 is a documentation of the proof of concept for the experimental application of iterative pyrolysis and sample characterization as a function of thermal maturity. This study was conducted on a pair of Kimmeridge Shale samples and a Woodford Shale sample. The pyrolysis experiments were conducted without applied confining pressure at Biomarker Technologies, Inc. I document a significant (up to 200%) increase in P-wave anisotropy at all confining pressures. This increase in anisotropy coincides with the development of severe hydrocarbon expulsion-induced cracks throughout the sample. The degree of anisotropy increase and sample cracking is attributed to the lack of confining pressure during unconfined pyrolysis. Most importantly, however, this pilot project proves the feasibility of iterative characterization pre- and post-pyrolysis, and raises a series of questions about the evolution of shale properties with induced thermal maturation, which define the remainder of the thesis. Namely, what role will applied confining pressure during pyrolysis play in the evolution of the sample? And why does the post-pyrolysis, high pressure elastic anisotropy diverge from the initial, mineral alignment-dependent values?

In Chapter 3, I present the novel experimental methodology that I implement in Chapters 5 and 6 to comprehensively characterize organic-rich shale in terms of acoustic velocity, elastic anisotropy, permeability, and microstructure of the organic-rich shale samples. I also discuss the pyrolysis experiments I conducted in the Stanford Rock Physics Laboratory and the nature of the pyrolysis reactor built in our laboratory (Clark and Vanorio, 2015). Also presented is a detailed characterization of the mineral composition, mineral alignment, and geochemistry of the samples studied in Chapters 4 through 6. Finally, I highlight the important effect of thermal maturity on the difference between total and effective porosity in organic-rich shale.

In advance of applying the novel experimental methodology to iterative characterization pre- and post-pyrolysis, I test the methodology on a suite of naturally matured shale samples. Chapter 4 details the variable acoustic velocity and elastic anisotropy of this suite of samples; particularly, in the context of the relative magnitude of sources of elastic anisotropy. This analysis demonstrates definitively that the intrinsic anisotropy of organic-rich shale (or any other rock exhibiting preferential crystallographic alignment) should be considered a function of the bulk crystallographic preferred alignment (CPO) of the shale, rather than as a function of clay content. For reference, bear in mind that CPO is a measure of the crystallographic alignment rather than the lattice alignment (LPO). This crystallographic alignment more completely describes the deformation of minerals than LPO, and, as such, is the preferred parameter of crystallographers (H.-R. Wenk, personal communication, 2015). I also explicitly document that the extrinsic contribution to anisotropy is a function of aligned compliant, crack-like, porosity. I then illustrate that, for the samples collected in this dataset, intrinsic anisotropy accounts for greater than 70%

of the total anisotropy. Finally, as with consideration of the Vernik dataset, the extraction of thermal maturity-dependent trends is obfuscated by the superimposed variability in mineralogy, microstructure, and sample preparation-induced cracking.

Chapter 5 presents the evolution of the acoustic velocity and elastic anisotropy of a pair of organic-rich Barnett Shale and Green River samples as a function of induced thermal maturity. The samples considered in this chapter are matured in the laboratory through confined, closed anhydrous pyrolysis experiments at reservoir pressures. As a result of this study, I determine that the microstructure of the sample is the primary factor in determining the elastic evolution of shale upon pyrolysis. The clay-rich, laminar Barnett Shale sample exhibits a clear increase in microcracking and sensitivity to pressure of vertically propagating P- and S-wave velocities. However, unlike for the Kimmeridge Shale in Chapter 2, the sample remains intact, and, at high confining pressure, the velocities return to the pre-pyrolysis value – indicating that the high confining pressure increase in anisotropy noted in Chapter 2 was a result of the extreme magnitude of fracturing observed. The largely randomly oriented, micritic Green River sample, however, exhibits a consistent, isotropic decrease in P- and S-wave velocities (up to 10%) post-pyrolysis. In this sample, I observe no microcracks nor any preferential alignment to any measure of physical evolution, e.g., porosity or velocity. Conceptual models are developed for each shale for comparison to permeability trends observed in Chapter 6.

In Chapter 6, I document the evolution of permeability as a function of thermal maturity in the same suite of organic-rich shales as discussed in Chapters 4 and 5. For purposes of comparison, I present results for both in situ and ex situ matured samples. I also use digital representations of micron-scale rock geometries, obtained through focused ion beam scanning electron microscopy (FIB-SEM), to numerically simulate the contribution to permeability of the sample matrix, in the absence of microcracks. Comparison of the whole-plug experimental values and micron-scale numerical values enables evaluation of the scale and location, e.g., in organics versus through cracks, of flow-paths in the shales. In all cases, the permeability increases post-pyrolysis, in some cases by as much as 6 orders of magnitude. The permeability increases post-pyrolysis reported in Chapter 6 correspond strongly with the conceptual models in Chapter 5, further identifying that shale microstructure is the dominant factor in determining organic-rich shale evolution upon thermal maturation. Finally, I address the issues of directly comparing experimental and numerical permeability values and directly comparing sample measurements (e.g., permeability) post-pyrolysis to measurements of naturally matured samples in the same window of thermal maturity.

Finally, in Chapter 7, I provide some final remarks on both the results of this thesis and future problems in the experimental study of the thermal maturity-dependent evolution of organic-rich shale.

1.3 List of Published Papers

The earlier contributions to this thesis, particularly Chapters 2 through 4, are published in Allan and Mavko (2013), Allan et al. (2014b), and Allan et al. (2015b), respectively. Subsets of these chapters have been published as 4 expanded abstracts: Allan and Mavko (2012), Allan et al. (2013a), Allan et al. (2014a), and Allan et al. (2015b). The contents of Chapters 5 and 6 are currently in preparation for publication. Additionally, this work has also been presented at numerous professional conferences including the International Workshop on Rock Physics (Allan et al., 2013b), the International Symposium on Energy Challenges and Mechanics (Allan and Vanorio, 2014), and the Engineering Mechanics Institute Conference (Allan et al., 2015a).

1.4 References

Allan, A. M. and G. Mavko, 2012, The effect of adsorption and diffusion on the gas permeability of kerogen: SEG Technical Program Expanded Abstracts 2012.

Allan, A. M. and G. Mavko, 2013, The effect of adsorption and Knudsen diffusion on the steady-state permeability of microporous rocks: Geophysics, 78:D75–D83.

Allan, A. M. and T. Vanorio, 2014, A multi-scale, multi-physics approach to organic-rich shale characterization: presented at the Second International Symposium on Energy Challenges and Mechanics.

Allan, A. M., T. Vanorio, and J. E. P. Dahl, 2013a, Thermal maturation-induced variation of P-wave anisotropy of organic-rich shale: SEG Technical Program Expanded Abstracts 2013.

Allan, A. M., T. Vanorio, and J. E. P. Dahl, 2013b, Thermal maturation-induced variation of P-wave anisotropy and dry resistivity of organic-rich shale: presented at the Second International Workshop on Rock Physics.

Allan, A. M., W. Kanitpanyacharoen, and T. Vanorio, 2014a, Velocity anisotropy variation in organic-rich shale as a function of confining pressure: SEG Technical Program Expanded Abstracts 2014.

Allan, A. M., T. Vanorio, and J. E. P. Dahl, 2014b, Pyrolysis-induced P-wave velocity anisotropy in organic-rich shales: Geophysics, 79:D41–D53.

Allan, A. M., C. Clark, and T. Vanorio, 2015a, Multi-phase macro- and micro-characterization of organic-rich shale upon pyrolysis-induced thermal maturation: presented at the Engineering Mechanics Institute Conference.

Allan, A. M., W. Kanitpanyacharoen, and T. Vanorio, 2015b, A multi-scale methodology for the analysis of velocity anisotropy in organic-rich shale: Geophysics, 80:C73–C88.

Bhandari, A. R., P. B. Flemings, P. J. Polito, M. B. Cronin, and S. L. Bryant, 2015, Anisotropy and stress dependence of permeability in the Barnett Shale: Transport in Porous Media.

Bustin, R. M., A. M. M. Bustin, X. Cui, J. K. Ross, and V. S. Murthy Pathi, 2008, Impact of shale properties on pore structure and storage characteristics: SPE Shale Gas Production Conference, SPE 119892.

Clark, A. C. and T. Vanorio, 2015, A niche system for inducing thermo-chemo-mechanical processes in rocks and materials: SRB Volume 142.

Dewhurst, D. N. and A. F. Siggins, 2006, Impact of fabric, microcracks and stress field on shale anisotropy: Geophysics Journal International, 165:135–148.

EIA, 1998: Natural gas 1998: Issues and Trends.

EIA, 2013: Annual energy outlook.

EIA, 2014: Annual energy outlook.

Ghanizadeh, A., M. Gasparik, A. Amann-Hildenbrand, Y. Gensterblum, and B. M. Krooss, 2013, Lithological controls on matric permeability of organic-rich shales: An experimental study: Energy Procedia, 40:127–136.

Heller, R., J. Vermylen, and M. Zoback, 2014, Experimental investigation of matrix permeability in gas shales: AAPG Bulletin, 98:975–995.

Johnston, J. E. and N. I. Christensen, 1995, Seismic anisotropy of shales: Journal of Geophysical Research, 100:5991–6003.

Kwon, O., A. K. Kronenberg, A. F. Gangi, and B. Johnson, 2001, Permeability of Wilcox shale and its effective pressure law: Journal of Geophysical Research, 106:19339–19353.

Kwon, O., A. K. Kronenberg, A. F. Gangi, B. Johnson, and B. E. Herbert, 2004, Permeability of illite-bearing shale: 1. Anisotropy and effects of clay content and loading: Journal of Geophysical Research, 109:B10205.

Vermylen, J. P., 2011, Geomechanical studies of the Barnett Shale, Texas, USA: PhD Dissertation, Stanford University.

Vernik, L., 1993, Microcrack-induced versus intrinsic elastic anisotropy in mature HC-source shales: Geophysics, 58:1703–1706.

Vernik, L. and C. Landis, 1996, Elastic anisotropy of source rocks: Implications for hydrocarbon generation and primary migration: AAPG Bulletin, 80:531–544.

Vernik, L. and X. Liu, 1997, Velocity anisotropy in shales: A petrophysical study: Geophysics, 62:521–532.

Vernik, L. and A. Nur, 1992, Ultrasonic velocity and anisotropy of hydrocarbon source rocks: Geophysics, 57:727–735.

Wang, F. P. and R. M. Reed, 2009, Pore networks and fluid flow in gas shales: SPE Annual Technical Conference and Exhibition: SPE 124253.

Chapter 2

THE EVOLUTION OF THE ELASTIC ANISOTROPY OF ORGANIC-RICH SHALE UPON THERMAL MATURATION – PART 1: UNCONFINED PYROLYSIS

Abstract

In this study, we address the feasibility of the repeated characterization of the effective porosity, microstructure, and ultrasonic velocity of organic-rich shale pre- and post-pyrolysis. This study serves as a first attempt at/pilot study for establishing cause-and-effect relationships between geochemical parameters and microstructure/rock physics as organic-rich shales thermally

mature. Such a set of relationships is necessary given the poor understanding of the sources of elastic anisotropy in organic-rich shale in the rock physics literature. Given the importance of organic-rich shales as both source rocks and unconventional reservoirs, it is imperative that a thorough understanding of shale rock physics is developed. In order to minimize auxiliary effects, e.g., mineralogical variations among samples, we study the induced evolution of three pairs of vertical and horizontal shale plugs through dry, unconfined pyrolysis experiments in lieu of traditional samples from a range of in situ thermal maturities. The directional dependence of the sensitivity of P-wave velocity to pressure shows a significant increase post-pyrolysis indicating the development of considerable aligned soft porosity, e.g., microcracks. Time-lapse, high-resolution BSE-SEM images complement this analysis through the identification of extensive microcracking within and proximally to kerogen bodies. As a result of the extensive microcracking, the P-wave velocity anisotropy, as defined by the Thomsen parameter epsilon, increases by up to 1.25 at low confining pressures. Additionally, the degree of microcracking is shown to increase as a function of the thermally producible hydrocarbons, or hydrocarbon generative potential, of each shale. At 50 MPa confining pressure, P-wave anisotropy values increase by up to 0.64 over those measured in the baseline, immature window. The increase in anisotropy at high confining pressure may indicate a source of anisotropy in addition to microcracking – potentially clay mineralogical transformations or the development of intrinsic anisotropy in the organic matter through aromatization. Most importantly, however, this study documents the potential for the successful characterization of samples post-pyrolysis that will compose much of the remainder of this thesis.

2.1 Introduction

The effect of the maturation of organic matter upon burial on the elastic anisotropy of shales remains poorly understood. This lack of understanding contributes to a central problem in rock physics: how to interpret the often-scattered elastic anisotropy trends observed in shale. Given that shales account for 75% of rocks in sedimentary basins (Jones and Wang, 1981), it is pivotal that the elastic anisotropy of shale and its evolution with burial and subsequent organic maturation be more fundamentally understood to facilitate proper processing of surface seismic studies. It has been documented (Banik, 1984; Sayers, 1999, 2005) that incorrect representations of anisotropy in seismic processing can propagate into significant errors in normal-moveout (NMO) and dip-moveout (DMO) corrections, migration, and amplitude-versus-offset (AVO) analysis. Furthermore, in order to provide more accurate constraints to rock physical models, it is necessary that the elastic anisotropy of shales and processes governing its evolution be more fully understood.

In organic-rich shale, the co-existence of both the organic and inorganic components makes the source of intrinsic elastic anisotropy inherently complex, varying due to changes that both components experience during thermal maturation. The strong alignment commonly observed in the texture of organic-rich shales results from the slow sedimentation of clay minerals from suspension, sufficiently slow organic deposition and little bioturbation to not disturb the clay alignment, and burial-induced compaction. This strong alignment results in significant intrinsic

elastic anisotropy in shale (Kaarsberg, 1959; Jones and Wang, 1981; Vernik and Nur, 1992; Hornby, 1998; Johnston and Christensen, 1995; Sayers, 1999, 2005; Wang, 2002; Valcke et al., 2006; Wenk et al., 2007; Lonardelli et al., 2007; Kanitpanyacharoen et al., 2011; Vasin et al., 2013; Allan et al., 2015). This intrinsic anisotropy is overprinted by sub-horizontal microcracks created by, amongst other causes, pressure release after coring and the expulsion of hydrocarbons generated from the kerogen of organic-rich shale (Vernik, 1993; Johnston and Christensen, 1995; Dewhurst and Siggins, 2006; Allan et al., 2014, 2015).

Understanding of the nature of the anisotropy of organic-rich shale in the rock physics literature is still severely lacking. One published database has comprehensively compiled anisotropic measurements (assuming a TI medium after Thomsen (1986)) with geochemical parameters, e.g., hydrogen index (HI) and total organic carbon (TOC) (Vernik and Nur, 1992; Vernik, 1993; Vernik and Landis, 1996; Vernik and Liu, 1997). Subsequent work by Vanorio et al. (2008) reinterpreted this dataset as a function of vitrinite reflectance (R_0). Vanorio et al. identified two maxima in the anisotropy of organic-rich shale as a function of thermal maturity (Figure 2.1); these maxima correspond to samples at peak maturity ($R_0 \sim 0.65$) and post-mature samples ($R_0 \sim 1.3$). Due to the negligible velocity-sensitivity to pressure of the data describing the early oil window peak, the maximum in anisotropy at peak maturity is hypothesized to correspond to the aromatization of complex hydrocarbons in maturing kerogen resulting in more planar carbon-rings in the organic content as described by Peters et al. (2004). The second anisotropy peak in post-mature samples is correlated to microcrack development due to the increase in the velocity-sensitivity to pressure in those samples. Study of the Vernik dataset is limited, however, by the use of samples at a range of naturally induced thermal maturities. To acquire the necessary range of maturity values, the samples are drawn from a wide range of shale formations resulting in considerable lithological, depositional, and mineralogical variability among samples which complicates the extraction of thermal maturation-dependent trends from rock physics measurements. Indeed we observe in Figure 2.1 that immature and post-mature samples are predominantly siliceous dolomites, siliceous shales, and opal-CT porcelanites, while the oil window samples are reported as shales and marls. This lithologic variability may obfuscate any truly vitrinite reflectance-dependent changes in the elastic anisotropy.

We remove the complicating factors arising from disparate provenance and diagenetic histories between samples by inducing thermal maturation in individual shale samples in the laboratory. The approach of this study stems from the objective difficulty of unraveling a posteriori the elastic anisotropy of a continuous maturation sequence. By studying single samples iteratively as maturation is induced, all rock physics trends identified are attributed to the thermally driven evolution of the porosity, crack density, clay evolution, and kerogen morphology and distribution. Most importantly, this work serves as a pilot study testing the feasibility of iterative rock physics measurements on whole core plugs pre- and post-pyrolysis – a first-of-its-kind experimental methodology. At each stage in the induced thermal maturity series, we measure effective porosity and acoustic velocity anisotropy and sensitivity to pressure of three thermally immature samples from the Vernik sample collection characterized by different levels of initial TOC. Additionally, we apply scanning electron microscopy (SEM) to identify changes in the

shale microstructure, development of microcracks, and changes in the kerogen microstructure. In coupling laboratory measurements with high-resolution imaging we attempt to extract the effect of kerogen evolution on the intrinsic anisotropy of the shale composite.

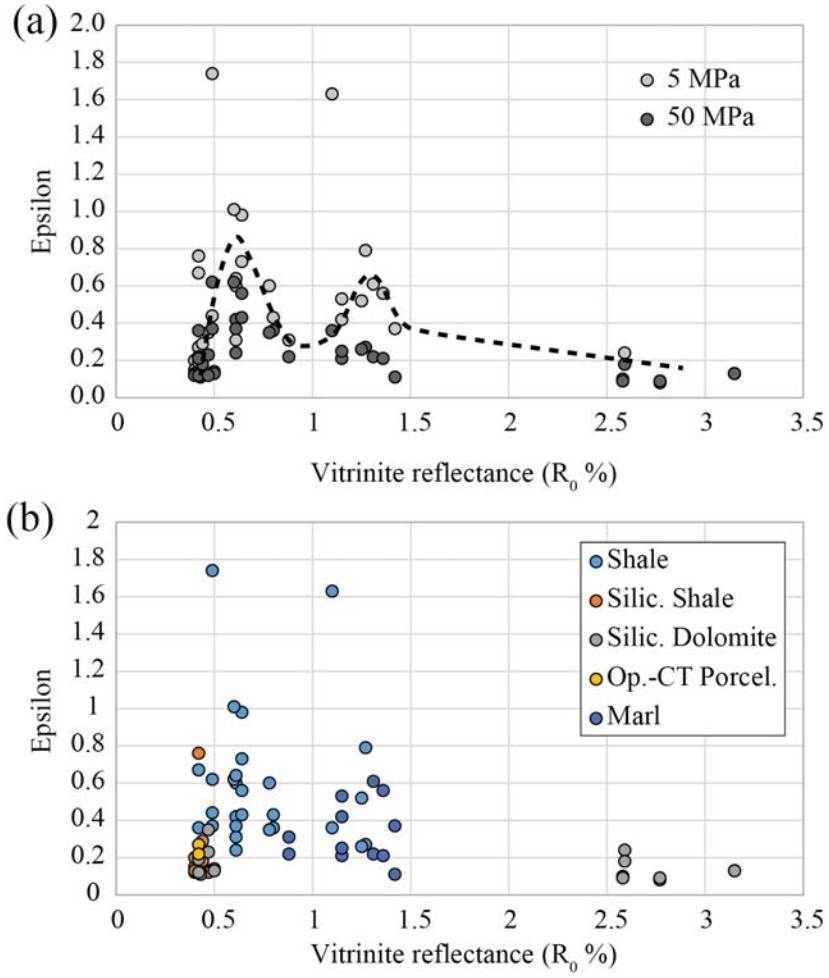

Figure 2.1: P-wave anisotropy, epsilon, as a function of vitrinite reflectance. (a) P-wave anisotropy measured at both low (light gray) and high (dark gray) confining pressures, adapted from Vanorio et al. (2008). A dashed black trend line is added to the low confining pressure values to demonstrate the two-peaked trend discussed in the text. (b) Epsilon as a function of vitrinite reflectance colored by reported lithology. Abbreviations are siliceous (silic.) and opal-CT porcelanite (Op.-CT Porcel.).

2.2 Sample Characterization

2.2.1 Sample Selection, Organic Content, and Mineralogy

The samples used in this study were selected from the remaining repository of samples used in the compilation of the Vernik dataset. The sample set consisted of one sample from the Woodford Shale and two samples from the Kimmeridge Shale (hereafter, labelled W6431, K2730, and

K2749, respectively), where each sample consists of two mutually orthogonal core plugs (see section 2.3). Note, while the original characterization of W6431 was previously reported in Vernik and Landis (1996) and Vernik and Liu (1997), samples K2730 and K2749 were previously unpublished (now published in Allan et al., 2014). All samples are cylindrical cores of approximately 1 inch diameter by 1 inch length. Of primary importance during selection is that all samples are immature with respect to oil generation so as to establish a baseline measurement for comparison to samples post-pyrolysis. In the absence of vitrinite reflectance data, thermal maturity was established through the temperature at which hydrocarbon generation attains a maximum (RockEval parameter T_{MAX}). The two Kimmeridge samples exhibit T_{MAX} values less than 435 °C, indicative of thermally immature samples (Peters and Cassa, 1994). Additionally, while the Kimmeridge samples (K2730 and K2749) lack vitrinite reflectance data, they were cored 1 m and 20 m shallower, respectively, than the immature ($R_0 = 0.47\%$) sample 2750 of Vernik and Landis (1996). Secondary consideration was given to sampling from a distribution of total organic carbon (TOC) values so as to vary the expected magnitude of the effect of thermal maturation on the average properties of the composite. In this manner, the three samples selected for full characterization include one relatively organic-poor sample from the Woodford Shale and two organic-rich Kimmeridge Shale samples (Table 2.1).

Table 2.1: Properties used to select samples for pyrolysis experiments, including total organic carbon (TOC), thermally producible hydrocarbons (S_2) measured in mg of hydrocarbons per gram of dry rock, hydrogen index (HI) measured in mg of hydrocarbons per gram of TOC, vitrinite reflectance (R_0), and the temperature of maximum hydrocarbon expulsion from RockEval (T_{MAX}). Additionally, reported porosity (ϕ) values from Vernik and Landis (1996) (denoted by subscript 0) are compared to effective porosity values measured in this study (subscript 1).

Sample	φ_0 (p.u.)	φ_1 (p.u.)	TOC (wt. %)	S_2 (mg/g)	HI (mg/g)	R_0 (%)	T_{MAX} (°C)
W6431	0.7	0.7	2.26	N/A	540	0.49	N/A
K2730	15.0	9.5	5.96	25.38	426	N/A	421
K2749	13.3	8.0	10.09	41.74	414	N/A	434

As previously stated, the samples used in this study were initially cored and characterized in the 1990s. In the intervening two decades, the samples were kept in an open atmosphere, which can be expected to have resulted in significant alteration of the plugs. The qualitative degree to which this expected alteration has affected the physical condition of the plugs in hand sample, however, is minimal. Both Woodford sample plugs, and three of the four Kimmeridge plugs exhibited no visible cracking in hand sample; only the vertically cored K2730 plug exhibited visible cracking. Additionally, none of the samples shows any dehydration-induced friability or loss of consolidation. Before performing any experiments, all samples were kept in an oven at 55 °C until mass loss stabilized prior to measurement to ensure the samples were dry while minimizing clay alteration/dehydration. Throughout this thesis I use the term *dry* to indicate that there is no residual *free* water in the pore space of the shale – there may still be considerable water bound to the surfaces of, or within, clay platelets and organic bodies. Given that this *bound* water cannot be removed without damaging/altering the shale, the sample is considered dry once all free water is removed.

The thermally immature samples were re-characterized to account for any alterations that had occurred over approximately two decades in storage and, hence, set a baseline for defining the evolution of the samples post-pyrolysis. The effective porosity was measured through helium porosimetry and compared to the porosity values presented in Vernik and Landis (1996) and unpublished internal documents (Table 2.1). Error in helium porosimetry measurements of the thermally immature samples was less than 1 porosity unit (p.u.). The error in porosimetry measurements is primarily driven by the error in assuming a right circular cylindrical form for the bulk sample volume. Sample W6431 can be considered to have negligible initial effective porosity. As can be seen in Table 2.1, the effective porosity values measured in this study are up to 40% less than the porosity values reported in the 1990s. Given that the porosity values reported by Vernik and Landis (1996) are total porosity values computed from densities not porosimetry-derived effective porosity values, this difference is likely a physical difference between the total and effective porosities of the samples. The available mineralogical data are presented in Table 2.2. All mineralogical data come from X-ray diffraction (XRD) measurements conducted by C. Landis then at Arco Oil and Gas. Similarly, C. Landis conducted all RockEval pyrolysis and vitrinite reflectance measurements (Table 2.1).

Table 2.2: Available mineralogical data and kerogen type for the samples used in this study. The $*$ notation indicates average values for two siliceous shale samples from the Woodford formation, while the symbol 'N/A' indicates that data is not reported in unpublished internal documents. Abbreviations are quartz (Qtz) and feldspar (Fsp).

Sample	Qtz+Fsp (Vol. %)	Clays (Vol. %)	Carbonate (Vol. %)	Pyrite (Vol. %)	Kerogen Type
W6431	60*	20*	12*	3*	II
K2730	23	39	N/A	8	II
K2749	25	25	N/A	11	II

t

2.2.2 Microstructure

The initial, thermally immature microstructure of each sample is documented in Figure 2.2. SEM images of the Kimmeridge Shale samples (Figure 2.2.a-c) document a clear preferential microstructural alignment. The strong alignment of the Kimmeridge samples is exhibited by the clay-rich mineral matrix, the preferential alignment of organic-rich bodies and pyritic accumulations in K2749, and the co-alignment of cracks subparallel to bedding in K2730. The crystallographic alignment of the clay-rich mineral matrix of the Kimmeridge Shale is supported through the analysis of X-ray diffraction images. The degree of maximum crystallographic preferred orientation (CPO) of the clay content in the bedding plane (personal communication, W. Kanitpanyacharoen, 2015) for the proximal sample 2750 is 4.15 m.r.d. (m.r.d.: multiples of a random distribution). This value indicates that it is over four times more likely that a given clay mineral is co-aligned with the bedding plane than in a randomly oriented sample. Further discussion of the X-ray diffraction image collection and CPO data analysis is provided in Chapter 3.

Contrastingly, the quartz-rich Woodford sample exhibits no visible bedding in hand sample nor at the scale of SEM images. Note the greater resolution required to identify microstructural features for W6431 – the pixel size in Figure 2.2.d is roughly a factor of six less than in Figure 2.2.c (41.3 nm and 261.1 nm, respectively). Subsequently, W6431 is more correctly identified as an organic siltstone, rather than a classic shale, and, as such, serves as a negligibly bedded, clay-poor point of comparison to the well-bedded, clay-rich Kimmeridge samples.

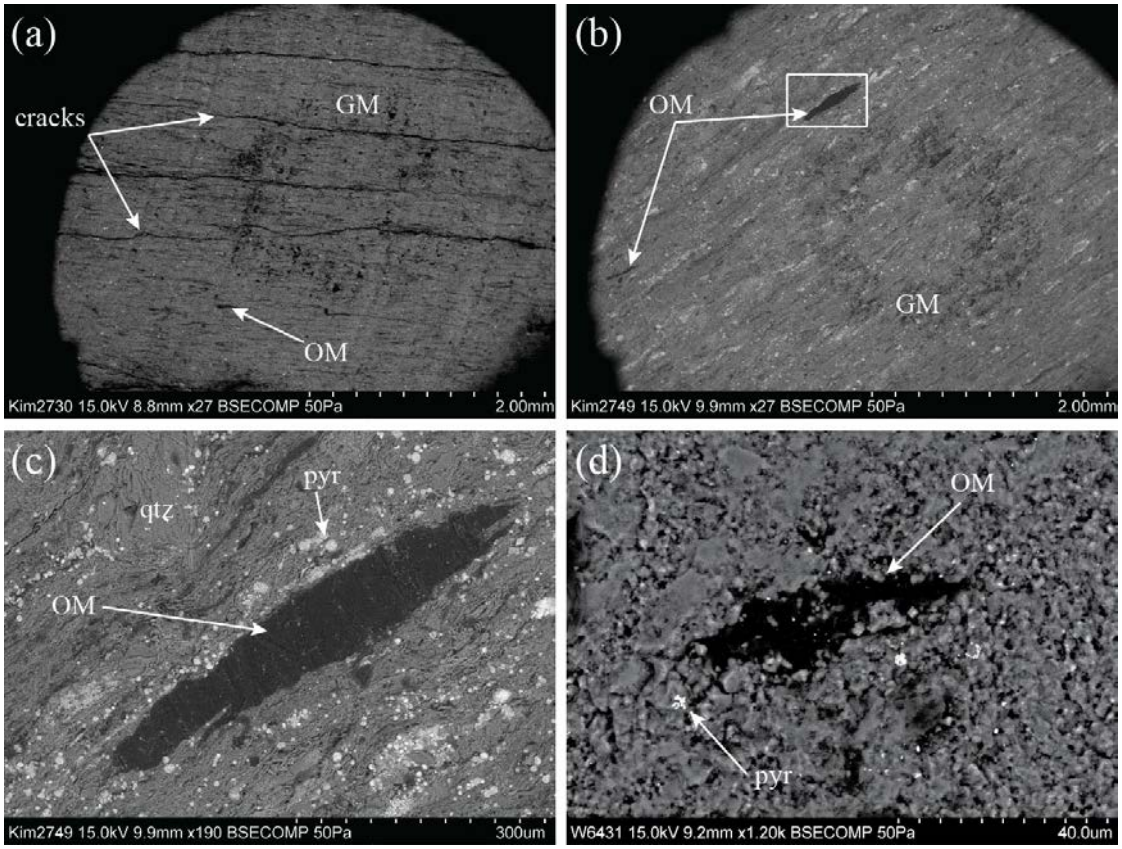

Figure 2.2: (a, b) Millimeter-scale SEM images of K2730 and K2749 microstructure. The faint, dark circle in both images (labeled GM) is a graphite marking used for time-lapse imaging. (c,d) Higher-resolution SEM images of representative kerogen morphology in K2749 and W6431. Image (c) is taken within the white box marked in image (b). Features identified by white arrows include cracks, pyrite (pyr), organic matter (OM), and quartz (qtz).

2.3 Experimental Methodology

P-wave velocity measurements were made on two plugs for each of the three samples – one plug cored parallel to bedding denoted as the 90°or horizontal sample, and the other plug cored perpendicular to bedding denoted as the 0°or vertical sample. By measuring the ultrasonic velocity of the two mutually orthogonal plugs and considering the sample as vertically transversely isotropic (VTI), we are able to characterize the elastic constants c_{11}, c_{33} and the anisotropic parameter epsilon (Thomsen, 1986) as in Equations 2.1 - 2.3, where ρ_B is the sample bulk

density, $V_P(90^\circ)$ is the P-wave velocity parallel to bedding, and $V_P(0^\circ)$ is the P-wave velocity perpendicular to bedding.

$$c_{11} = \rho_B \left(V_P\left(90^\circ\right)\right)^2 \tag{2.1}$$

$$c_{33} = \rho_B \left(V_P\left(0^\circ\right)\right)^2 \tag{2.2}$$

$$\varepsilon = \frac{c_{11} - c_{33}}{2c_{33}} \tag{2.3}$$

All velocity measurements were conducted at hydrostatic confining pressures ranging between 0.9 MPa to 50 MPa. The pressure loading and unloading cycles are shown in Figure 2.3. During velocity experiments, the samples were jacketed with rubber (Tygon ®) tubing to prevent intrusion of the confining fluid. Velocity measurements were made with the pulse transmission method using a 1 MHz pulse.

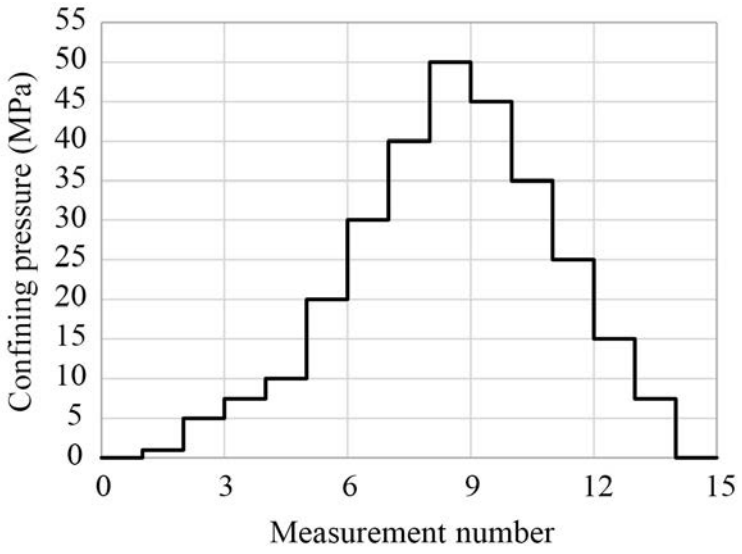

Figure 2.3: A schematic representation of the hydrostatic confining pressures at which waveform arrival times were measured.

Before picking the first arrival of the waveform the samples were allowed to stabilize to account for viscoelastic relaxation resulting from the change in confining load. The sample strain was measured as a function of time with three external linear potentiometers, and waveforms were picked once the cumulative relaxation over a 15 minute period was less than 1 micron. The changes in sample length were related to changes in porosity by assuming that pore contraction was the sole source of calculated strain, i.e., the mineral frame was incompressible. The error in P-wave velocity measurements was approximately 1% resulting in errors in the calculated P-wave anisotropy, epsilon, of between 3% and 5% for the Kimmeridge samples and 10% and 50% for the Woodford sample. The significantly higher error computed for the Woodford sample stems from the relative isotropy of the Woodford sample ($\varepsilon \sim 0.015$).

SEM images were captured using a Hitachi S-3400N VP-SEM at the Stanford Medical School Cell Sciences Imaging Facility (CSIF). To indicate changes in atomic number, as a proxy for mineralogy, all images were collected in backscattered electron (BSE) mode under a 50 Pa vacuum with a beam voltage of 15.0 kV. Additionally, all images were captured from the horizontal samples so as to sample the organic content within multiple bedding planes. In order to image the effect on microstructure of pyrolysis, BSE-SEM images were taken iteratively at the same area of the sample face after each pyrolysis experiment. Due to the thermal properties of graphite, graphite markings were used to mark areas of interest in a manner that would enable relocation post-pyrolysis.

Dry pyrolysis experiments were performed at Biomarker Technologies, Inc. in vessels at atmospheric confining pressure to induce maturation of the organic matter. Prior to heating, the samples were flushed with argon to ensure anoxic conditions in the pore space. The samples were re-characterized in two stages, in addition to the immature baseline: (a) the wet-gas window, and (b) the dry-gas window. The wet-gas window is defined by vitrinite reflectance values of between 1.3% (the onset of the gas window) and 2.0%. At vitrinite reflectance values greater than 2.0% and less than 4.0% (the onset of greenschist metamorphism), the organic matter is identified as being in the dry-gas window (Horsfield and Rullkötter, 1994). The wet-gas window was reached by heating at 380 °C for 72 hours, resulting in partial oil cracking (approximately 32% conversion of liquid to gas for both the Kimmeridge and Woodford samples) as determined by diamondoid analyses according to Dahl et al. (1999). Subsequent heating at 400 °C for 72 hours resulted in over 90% oil cracking for the Kimmeridge plugs (results were not obtained for the Woodford sample), suggesting dry-gas window levels of thermal maturity following this final pyrolysis stage. Furthermore, RockEval analysis was performed on the dry-gas window Kimmeridge samples – there was insufficient residual Woodford material for RockEval analysis. The RockEval results, documented in Table 2.3, exhibit a large reduction in the remaining thermally producible hydrocarbons (S_2) of the samples. The two order of magnitude drop in S_2 coupled with the values of T_{MAX} in excess of 470 °C confirm that the samples are extremely post-mature (Peters and Cassa, 1994). That the TOC of K2730 is greater post-pyrolysis than pre-pyrolysis is indicative of geochemical heterogeneity between the two subsamples used for RockEval analysis. Indeed, the low HI value post-pyrolysis confirms that the remaining TOC is largely inert carbon – only 2 mg of hydrocarbons per gram of TOC.

Table 2.3: Geochemical characterization of the Kimmeridge Shale samples, pre- and post-pyrolysis at 400 °C for 72 hours, derived from RockEval analysis. Abbreviations are as in Table 2.1, with the addition of free, retained hydrocarbons (S_1) measured in mg of hydrocarbons per gram of dry rock.

Sample	TOC (wt. %)	S_1 (mg/g)	S_2 (mg/g)	T_{MAX} (°C)	HI (mg/g)
K2730_pre	5.96	3.40	25.38	421	426
K2730_post	6.74	0.78	0.11	497	2
K2749_pre	10.09	4.07	41.74	434	414
K2749_post	7.09	0.69	0.12	>500	2

The application of this novel time-lapse experimental technique to the iterative characterization of shale samples results in a complex, multi-step experimental procedure. Subsequently, for clarity, the order of operations is illustrated in Figure 2.4.

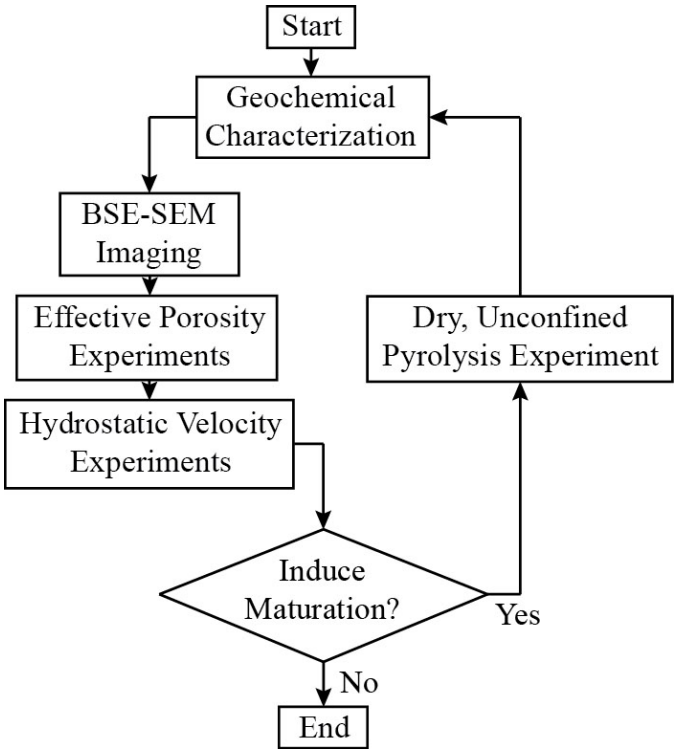

Figure 2.4: A schematic flowchart of the ordering of experimental procedures in the pilot iterative shale rock physics method.

2.4 Experimental Results

2.4.1 Baseline, Immature Window

The P-wave velocity as a function of confining pressure for each of the 6 plugs is shown in the Figure 2.5. As expected, the low effective porosity, low TOC Woodford sample is significantly acoustically faster than the more porous, more organic- and clay-rich Kimmeridge samples. The considerable pressure-sensitivity of the P-wave velocity of the vertical K2730 plug is attributed to the preexisting visible crack most likely created by coring-induced pressure release. The corresponding P-wave velocity anisotropy, as represented by the Thomsen parameter epsilon, is shown in Figure 2.6. The significant anisotropy at low confining pressure exhibited by sample K2730 is a result of the aforementioned preexisting crack. The remaining 5 plugs, however, exhibit considerably less pressure-sensitivity of P-wave velocity or epsilon, which is indicative of minimal preexisting cracking or compliance within the samples. This relative lack of pressure-sensitivity is further indicative of minimal alteration resulting from prolonged exposure to open atmospheric conditions in storage. Note the extreme values of epsilon (>0.5) for the Kimmeridge

samples result from the combination of unsaturated measurements and the strongly aligned, clay-rich nature of the mineral matrix. While the significantly lower anisotropy of the Woodford samples results from the clay-poor, quartzose frame of the rock which exhibits no alignment or bedding in SEM or hand sample.

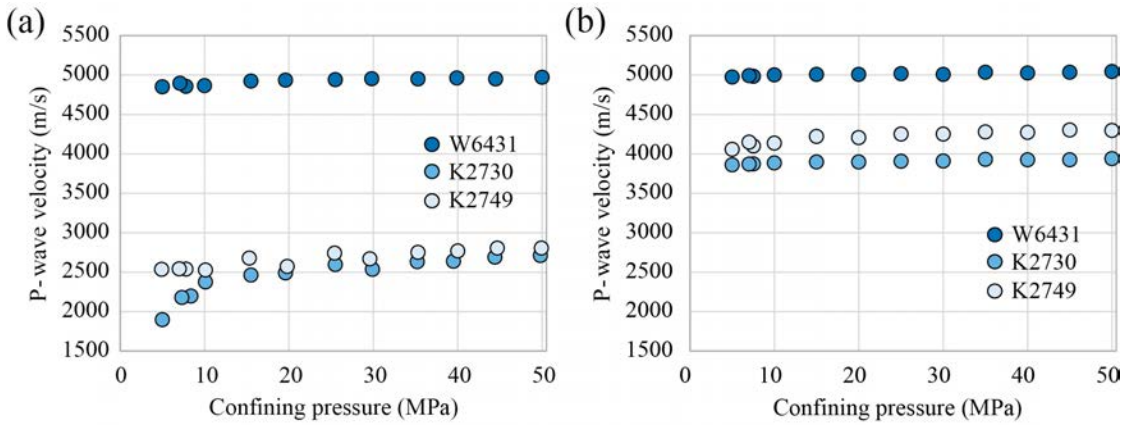

Figure 2.5: P-wave velocity of the immature samples as a function of confining pressure. (a) P-wave velocity perpendicular to bedding. (b) P-wave velocity parallel to bedding.

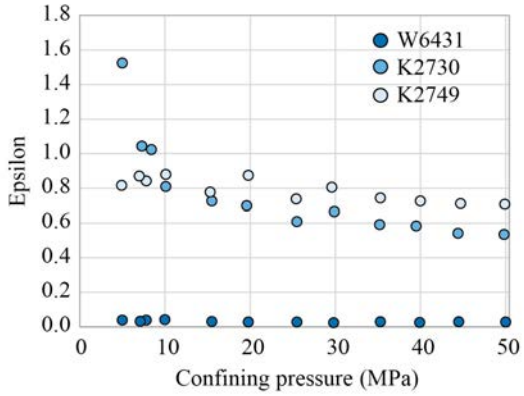

Figure 2.6: P-wave anisotropy parameter, epsilon, as a function of confining pressure for the immature samples.

2.4.2 Wet-Gas Window

After pyrolyzing the samples to the wet-gas window, all four of the Kimmeridge plugs exhibited severe cracking subparallel to bedding that split the samples into 2-3 intact fragments. The Kimmeridge plugs were secured with polytetrafluoroethylene (PTFE) tape to enable further characterization. During acoustic experiments, the reassembled plugs exhibited no sliding along the pyrolysis-induced cracks as exemplified by both the waveforms in Figure 2.7 and non-discontinuous measurements of axial strain. The lack of sliding indicates that, during acoustic experiments under confining pressure, the samples are stable and do not disrupt the coupling between the faces of the sample and the pressure transducers. Rather than exhibiting signal

degradation associated with the disruption of the sample-transducer coupling with increasing confining pressure, the waveforms (Figure 2.7) show a travel time and attenuation decrease and a frequency content increase that is indicative of the cracks closing rather than sliding. In addition to the development of visible cracks, all six plugs emitted a strong odor of hydrocarbons post-pyrolysis.

The change in effective porosity as a function of confining pressure is shown in Figure 2.8. Negative porosity values reflect the underestimation of the initial effective porosity of the thermally immature W6431 – this phenomenon is discussed thoroughly in Chapter 3. The P-wave velocity as a function of confining pressure in both the immature and wet-gas windows is documented in Figure 2.9. As expected from the observed effective porosity increase, the P-wave velocity of all plugs decreases significantly; furthermore, the pressure-sensitivity of the P-wave velocity also increases significantly for all plugs, except the pre-cracked vertically cored K2730 plug. The consistent, significant increase in the pressure-sensitivity of the samples coupled with the effective porosity increase is indicative of the development of significant soft porosity, e.g., microcracks.

The evolution of the P-wave velocity anisotropy, epsilon, is shown in Figure 2.10. Epsilon is seen to increase relative to the immature window values at both high (50 MPa) and low (7 MPa) confining pressure. Epsilon in the wet-gas window is also more pressure-sensitive indicating that microcracks are both more abundant at low confining pressure and predominantly subparallel to bedding (Figure 2.10).

2.4.3 Dry-Gas Window

Upon pyrolysis to the dry-gas window, the plugs we recovered in the same condition as was documented in the wet-gas window. The change in effective porosity as a function of confining pressure between the wet-gas and dry-gas windows is shown in Figure 2.8. The magnitude of change in effective porosity generated during the second step of pyrolysis (i.e., wet- to dry-gas window) is largely negligible with comparison to the first step (i.e., immature to wet-gas window).

The P-wave velocity as a function of confining pressure at all three stages of thermal maturity (immature, wet-gas, and dry-gas windows) is documented in Figure 2.9. As expected from the negligible porosity evolution, the variation in P-wave velocity associated with the second pyrolysis experiment is considerably less pronounced than in the wet-gas window. The exceptions to the trend of minimal variation are the vertically cored K2730 and K2749 plugs, which experienced a non-negligible velocity decrease. All velocity data reported in Figure 2.9 is also tabulated in Appendix A.

The softening of the vertical K2730 and K2749 plugs results in a further increase in P-wave anisotropy upon pyrolysis to the dry-gas window (Figure 2.10). Epsilon remains highly pressure sensitive for the Kimmeridge samples. For W6431, however, epsilon exhibits a decrease in both magnitude and pressure-sensitivity.

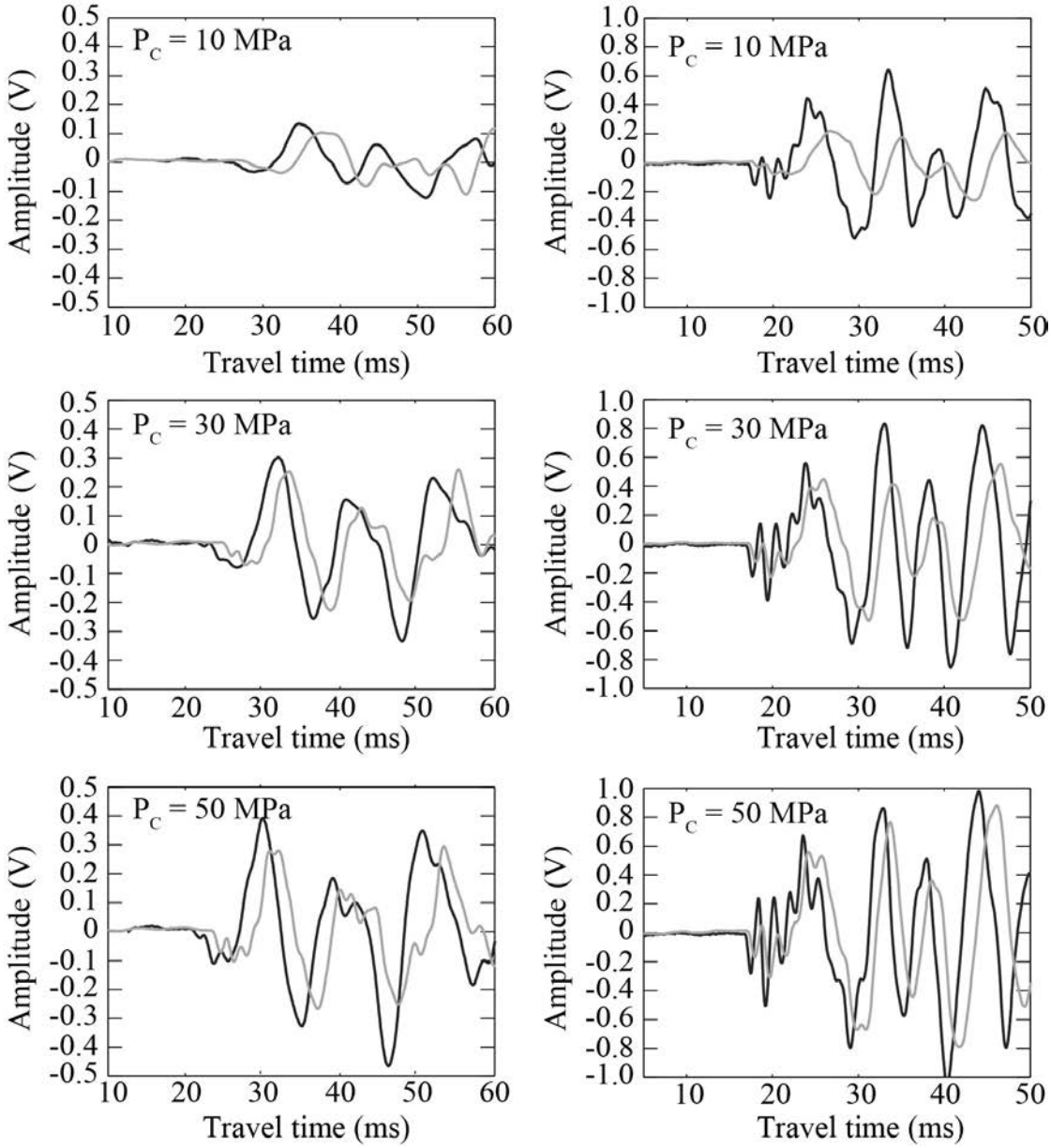

Figure 2.7: Waveforms recorded for sample K2749. Left column: vertically cored (0°) plugs. Right column: horizontally cored (90°) plugs. The top row shows waveforms at 10 MPa confining pressure, the middle shows waveforms at 30 MPa confining pressure, and the bottom row shows waveforms at 50 MPa, respectively. Black curves were collected in the immature window, while the grey curves were collected in the wet-gas window.

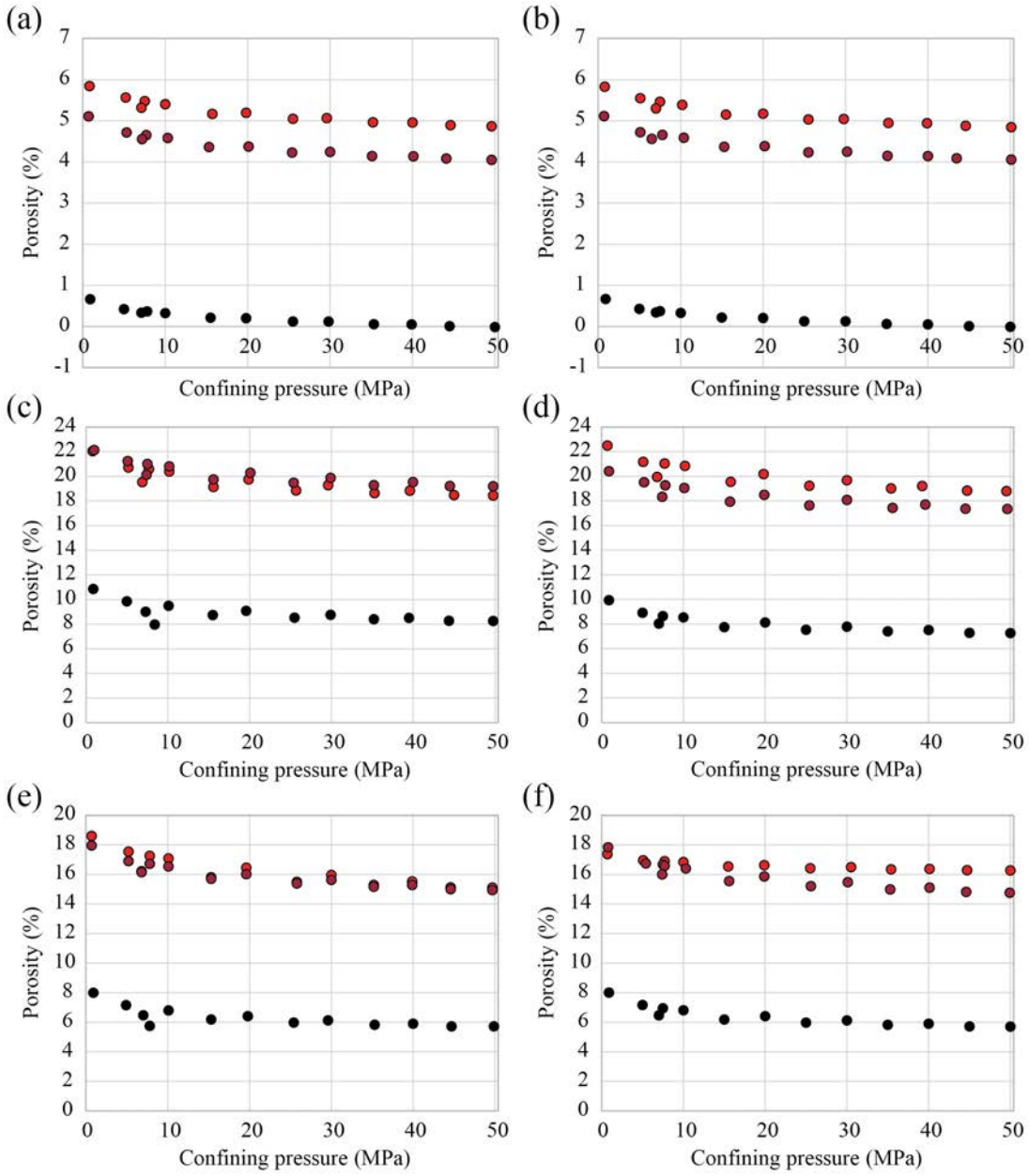

Figure 2.8: The effective porosity, as a function of confining pressure, of the samples in the immature (black), wet-gas (red), and dry-gas (dark red) windows. (a, c, e) Effective porosity of vertically cored (0°) plugs. (b, d, f) Effective porosity of horizontally cored (90°) plugs. (a, b) W6431. (c, d) K2730. (e, f) K2749.

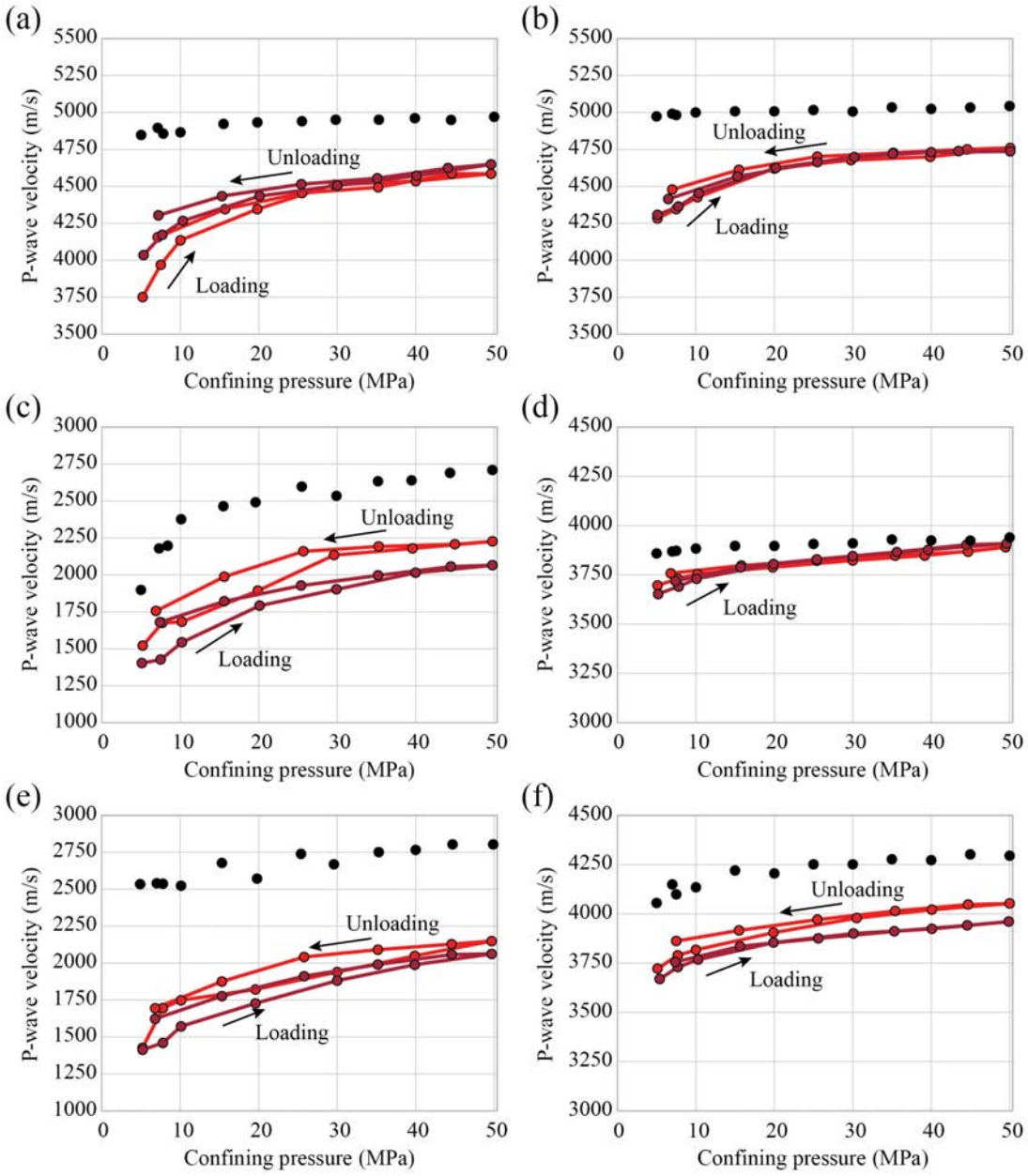

Figure 2.9: P-wave velocity of samples, as a function of confining pressure, in the immature (black), wet-gas (red), and dry-gas (dark red) windows. (a, c, e) P-wave velocity of the vertical (0°) plugs. (b, d, f) P-wave velocity of the horizontal (90°) plugs. (a, b) W6431. (c, d) K2730. (e, f) K2749. Solid lines and arrows are used to indicate hysteresis between the loading and unloading curves.

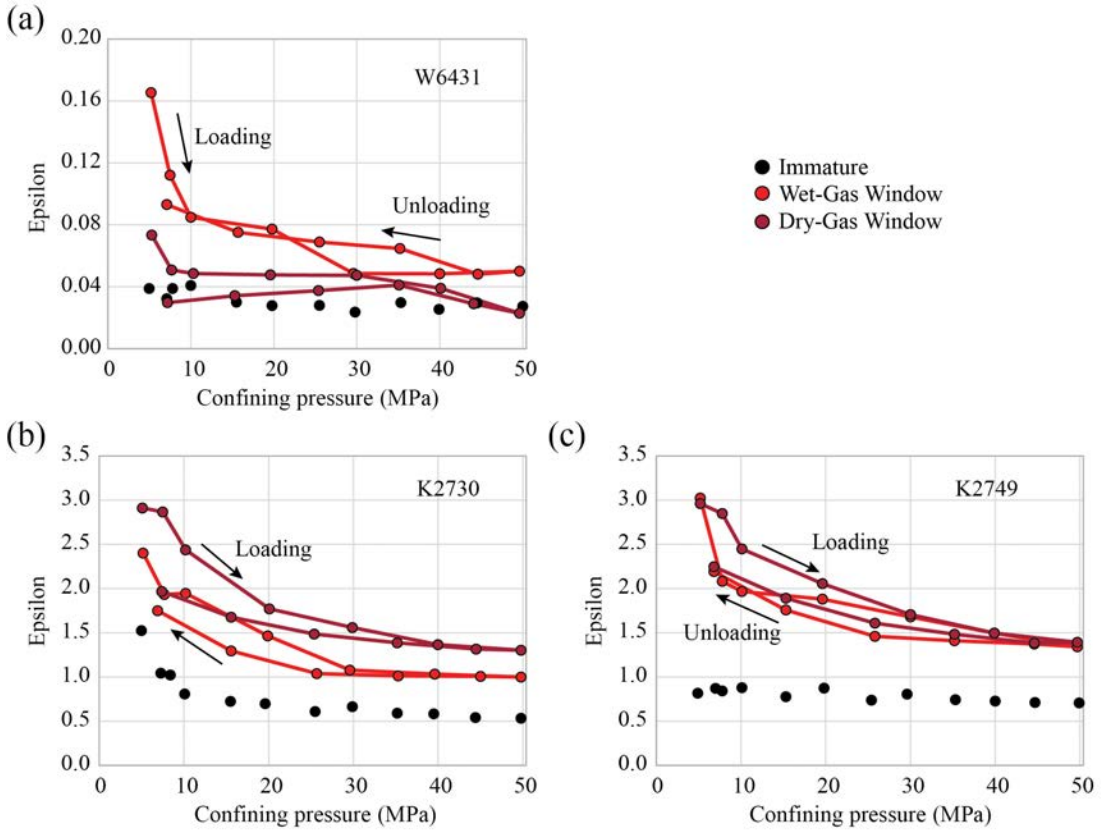

Figure 2.10: P-wave anisotropy parameter, epsilon, as a function of confining pressure, of samples in the immature (black), wet-gas (red), and dry-gas (dark red) windows. Solid lines and arrows are used to indicate hysteresis between the loading and unloading curves. (a) W6431. (b) K2730. (c) K2749.

2.5 Discussion

2.5.1 Experimental Procedure

It is important to note that due to the strong elastic anisotropy of the shale samples in this study, under the assumed VTI symmetry, the cylindrical plugs deform elliptically under hydrostatic confining pressure. To account for the anisotropic deformation, the total volume reduction (proxy for porosity loss) of a plug at a given confining pressure is represented as a function of the axial strain computed for both plug orientations from sample lengths during loading. The total volume as a function of confining pressure, P_c, for both vertically and horizontally cored cylindrical plugs is given in Equations 2.4 and 2.5, respectively: where V_T is the total sample volume, L is the sample length, d is the sample diameter, and ε is the computed axial strain – in all instances a subscript 0 or 90 indicates the plug orientation, while a superscript asterisk indicates the unconfined, benchtop measurement.

$$V_{T,0}(P_C) = \frac{\pi}{4} L_0(P_C) \left[d_0^* - d_0^* \varepsilon_{90}(P_C) \right]^2 \tag{2.4}$$

$$V_{T,90}(P_C) = \frac{\pi}{4} L_{90}(P_C) \left[d^*_{90} - d^*_{90}\varepsilon_{90}(P_C)\right] \left[d^*_{90} - d^*_{90}\varepsilon_0(P_C)\right] \tag{2.5}$$

The tendency for shale to deform elasto-visco-plastically has been well documented in laboratory studies (e.g., de Waal and Smits, 1988; Chang et al., 1997; Dudley et al., 1998; Hagin and Zoback, 2004; Chang and Zoback, 2009). Sone (2012) studied the effect of ductile creep behavior on ultrasonic velocities by combining static measurements of sample deformation as a function of time with dynamic measurements of ultrasonic velocities for a wide range of shale mineralogies. The experimental results of Sone indicate that allowing the sample to settle for 3 hours can result in an up to 2% increase in P-wave modulus. The calculated error in P-wave modulus for this study is up to 4%; subsequently, by waiting until cumulative axial variation in sample length is less than 1 micron over a 15 minute period before wavelets were picked, we assume that the samples have sufficiently settled and that the results presented here are not affected by artifacts of creep deformation.

2.5.2 Physical Evolution upon Pyrolysis

2.5.2.1 Effective Porosity and Grain Density

The evolution of the sample porosity and grain density, as quantified by helium porosimetry, as a function of thermal maturity is documented in Table 2.4. Furthermore, the values composing Figure 2.8 detailing the evolution of porosity as a function of confining pressure are tabulated in Appendix B.

As previously noted, upon pyrolysis to the wet-gas window all four of the Kimmeridge plugs exhibited severe cracking subparallel to bedding that split the samples into 2-3 intact fragments, while sample W6431 remained intact. The generation of plug-scale through-going cracks in strongly laminar organic-rich shale after heating above 350 °C was also identified via syn-pyrolysis X-ray tomography by Kobchenko et al. (2011). A discussion on the source of the generation of through-going fractures is documented in Section 2.5.4. The porosity of the Kimmeridge plugs doubles post-pyrolysis (Table 2.4) due to a combination of the conversion and expulsion of organic matter and the loss of shale fragments from open fracture faces during transportation. However, the order of magnitude increase in the porosity of the intact W6431 and significant increase in grain density (between 5% and 9% for Kimmeridge samples) indicates a primarily geochemical source of porosity generation for all samples. The generation and expulsion of hydrocarbons from kerogen necessitates a decrease in the solid material of the sample to satisfy the principle of the conservation of mass; additionally, hydrocarbon generation results in an increase in the porosity of the residual organic matter (e.g., Loucks et al., 2009; Curtis et al., 2012). Furthermore, the conversion and expulsion of low density, initially thermally immature kerogen ($\sim$1.2-1.3 g/cm^3; Okiongbo et al., 2005), results in an increase in the grain density of the remaining rock frame. Subsequently, the noted mass loss, grain density increase, and corresponding porosity increase upon pyrolysis to the wet-gas window is attributed, primarily, to the generation of organic porosity.

Table 2.4: Physical properties (mass, effective porosity, and grain density) at each stage of thermal maturity. Core plug orientations are indicated with a V for the vertically cored plug and an H for the horizontally cored plug.

Sample	Thermal Maturity	Mass (g)	Porosity (%)	Grain Density (g/cm^3)
W6431_V	Immature	31.54	0.52±0.86	2.489±0.003
	Wet-Gas	30.54	5.68±0.45	2.580±0.003
	Dry-Gas	30.48	5.11±0.53	2.574±0.002
W6431_H	Immature	32.72	0.67±0.46	2.566±0.004
	Wet-Gas	32.13	5.61±0.53	2.601±0.002
	Dry-Gas	32.00	5.11±0.69	2.591±0.006
K2730_V	Immature	30.30	10.23±0.95	2.440±0.003
	Wet-Gas	27.50	22.06±0.54	2.624±0.002
	Dry-Gas	27.53	22.13±0.67	2.636±0.015
K2730_H	Immature	30.21	9.50±0.58	2.370±0.003
	Wet-Gas	28.17	22.41±1.24	2.588±0.003
	Dry-Gas	28.04	20.41±3.63	2.595±0.013
K2749_V	Immature	30.25	7.94±0.47	2.430±0.004
	Wet-Gas	28.34	18.57±0.27	2.592±0.002
	Dry-Gas	28.31	17.97±0.51	2.595±0.014
K2749_H	Immature	27.94	8.02±0.76	2.501±0.004
	Wet-Gas	26.41	17.29±1.26	2.645±0.003
	Dry-Gas	26.08	17.84±1.60	2.660±0.011

Significantly less physical evolution of the samples was observed upon pyrolysis to the dry-gas window. The samples were returned from pyrolysis in much the same physical condition as pre-pyrolysis, i.e., 2-3 intact fragments split subparallel to bedding. Helium porosimetry experiments indicated a change in porosity of less than 1 p.u. for all samples except the horizontal K2730 plug; however, the experimental error for this cracked sample was 3 p.u. – due to the irregular geometry of the heavily cracked sample. Additionally, the grain density, which increased by 5%-9% in the TOC-rich Kimmeridge samples after the first pyrolysis experiment, changed by less than 0.5% for all samples after pyrolysis to the dry-gas window. Subsequently, compared to the changes invoked by pyrolysis to the wet-gas window, the physical evolution of the plugs post-pyrolysis to the dry-gas window is negligible.

2.5.2.2 Microstructural Alteration

The microstructural alteration of the organic-rich shale samples upon pyrolysis is documented through time-lapse SEM images at the same location on the surface of the horizontally cored plug. Time-lapse SEM imaging of the Woodford sample was corrupted by the intrusion of molasses (used as an acoustic couplant). As a consequence, no time-lapse images of W6431 are shown here.

The evolution of the microstructure of the Kimmeridge Shale upon pyrolysis to the wet-gas window is documented in Figure 2.11. The previously documented organic body in sample K2749 (Figure 2.2) exhibits significant microcracking both adjacent to and cross-cutting the organic body itself. Significant microcracking in the mineral matrix around the organic body is also identified, much of which correlates with smaller, lenticular bodies of organic matter in the immature window image. Subsequently, we determine that cracking occurs both at the scale of the hand sample, i.e., through-going cracks that split the plug, and at the scale of 10s to 100s of microns. Higher resolution imaging, e.g., focused-ion beam scanning electron microscopy (FIB-SEM), is not available to determine if cracking also exists below the micron-scale in and around the smaller, dispersed organic bodies nor to identify hydrocarbon generation-induced pores within the organic matter.

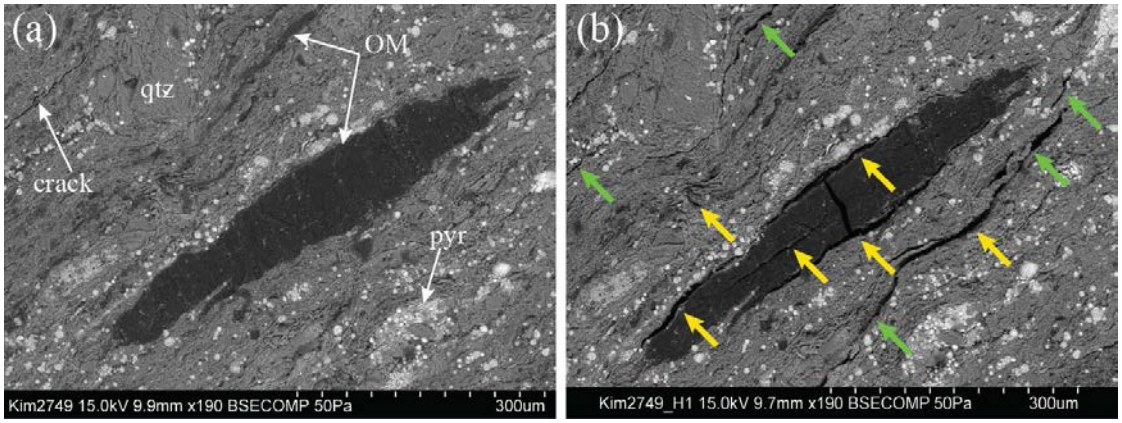

Figure 2.11: Time-lapse SEM images of the evolving kerogen morphology in K2749. (a) Immature window as in Figure2.2.c. (b) The same spot on the surface of K2749 in the wet-gas window showing significant cracking in and adjacent to the organic body. Regions of severe microcracking are identified with yellow arrows. The regions of microcracking that are co-located with smaller lenticular bodies of organic matter in (a) are identified with green arrows. Features identified by white arrows include cracks, pyrite (pyr), organic matter (OM), and quartz (qtz). Note the pixel size, p, is identical across the two images (p = 261.1 nm).

Figure 2.12 clearly shows significantly less microstructural alteration to the microstructure after pyrolysis to the dry-gas window. At the millimeter-scale (Figure 2.12.a-d), K2730 and K2749 exhibit some small development of new cracks and/or widening of pre-existing cracks; however, the bulk texture, by and large, remains the same. Similarly, there is little evidence of additional microcracking in and around the large organic body in K2749 (Figure 2.12.e-f). Additionally, there is some evidence for the healing/closure of microcracks (Figure 2.12.e-f). Subsequently, we can infer that the initial hydrocarbon generation and expulsion affected the majority of the microstructural alteration during pyrolysis to the wet-gas window. This initial alteration may then have created a sufficiently connected pore network such that future hydrocarbon products need not alter the microstructure further to be expelled from the sample. This microstructural observation correlates well with the negligible effective porosity and grain density evolution post-pyrolysis to the dry-gas window.

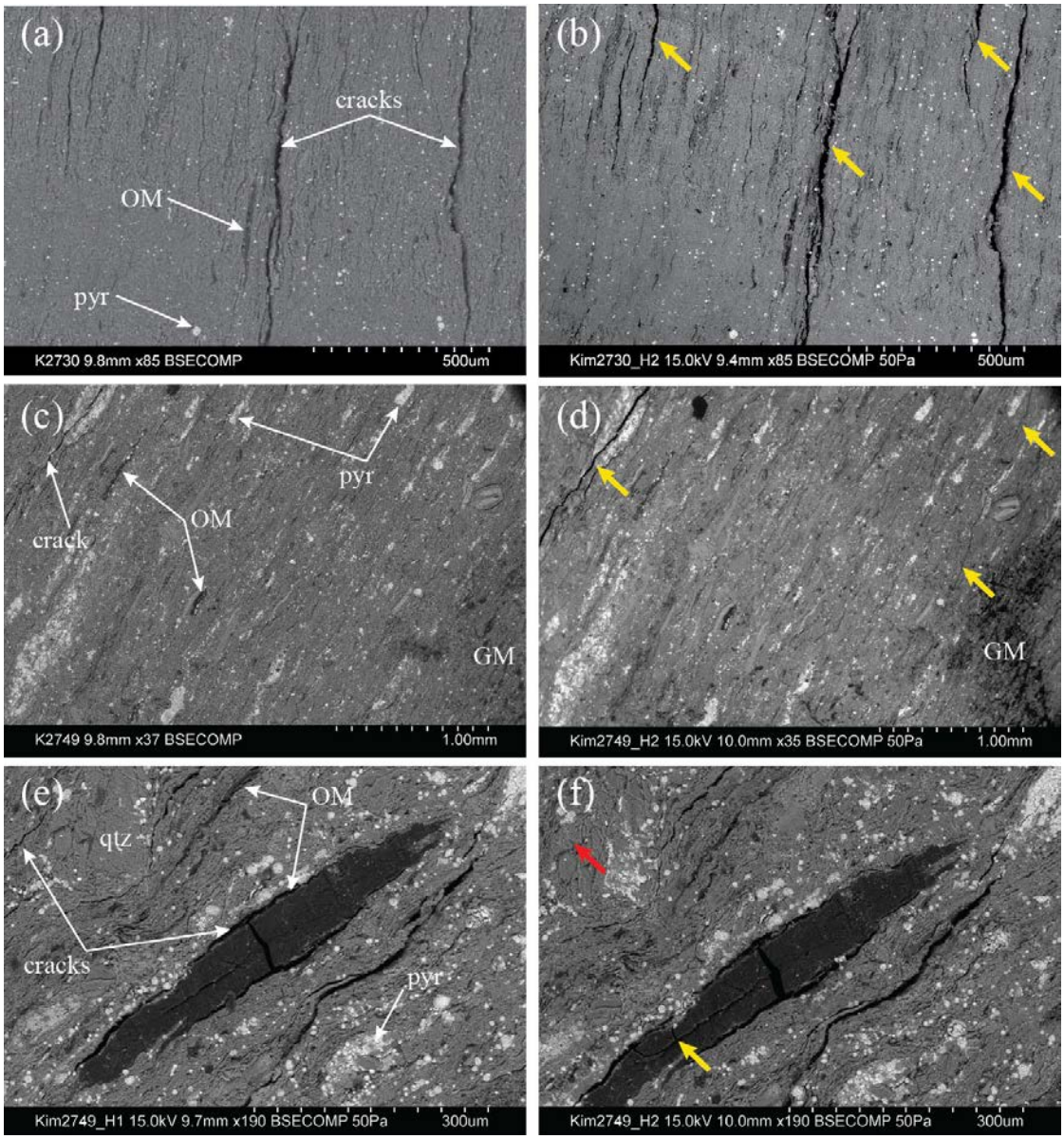

Figure 2.12: Time-lapse SEM images of the evolving microstructure of K2730 (a, b) and K2749 (c-f) in the wet-gas (left column) and dry-gas (right column) windows. Examples of additional microcracking or microcrack widening are identified with yellow arrows, while the red arrow indicates apparent microcrack healing or closure. Again, the dark circle in (c, d), labeled GM, is a graphite marking used for time-lapse imaging. Features identified by white arrows include cracks, pyrite (pyr), organic matter (OM), and quartz (qtz). The pixel size, p, in the time-lapse images are identical (a, b: p = 1.341 µm; e, f: p = 261.1 m) except in images (b: p = 1.341 µm) and (c: p = 1.417 µm).

2.5.3 Evolution of Elastic Properties upon Pyrolysis

2.5.3.1 Acoustic Velocity

Upon pyrolysis to the wet-gas window, both the Woodford and Kimmeridge samples exhibited a significant decrease in velocity magnitude. The change in velocity magnitude is sensible given the previously noted order of magnitude increase and doubling of the porosity of the Woodford and Kimmeridge samples, respectively. In addition to the magnitude decrease, there is a consistent increase in the pressure-sensitivity of velocity as reported in Table 2.5. The sensitivity to pressure of velocity is defined by

$$\frac{\Delta V_P}{\Delta P_C} = \frac{[V_P(P_C = 50) - V_P(P_C = 5)]}{(50 - 5)} \tag{2.6}$$

where $V_P(P_C)$ is the P-wave velocity at confining pressure P_C. At low confining pressure, e.g., 5 MPa, the noted cracks in the immature vertical K2730 plug severely suppress that change in pressure-sensitivity – a decrease in pressure-sensitivity of 2.3 m s^{-1} MPa^{-1} versus an increase of 10.1 m s^{-1} MPa^{-1} for K2749. The increase in pressure-sensitivity is greatest for W6431 ($\sim$16 m s^{-1} MPa^{-1}) as a result of the relative insensitivity of the baseline, thermally immature sample. It is important to note that the pressure-sensitivity of the vertical plug is consistently greater than that of the horizontal plug (Table 2.5). The increased compliance of the vertical plug indicates that the compliant porosity, or microcracks, imaged to be subparallel to bedding at small scales on the sample face (Figure 2.11), are consistently oriented subparallel to bedding at all scales.

Table 2.5: Pressure-sensitivity of P-wave velocity and velocity hysteresis in each window of thermal maturity as defined in Equations 2.6 and 2.7. Core plug orientations are indicated with a V for the vertically cored plug and an H for the horizontally cored plug.

Sample	Velocity-Sensitivity to Pressure, $\Delta V_p/\Delta P_c$ (m s^{-1} MPa^{-1})			Velocity Hysteresis (m s^{-1})		
	Imm	Wet-Gas	Dry-Gas	Imm	Wet-Gas	Dry-Gas
W6431_V	2.7±1.5	18.5±1.3	13.6±1.4	40±70	185±60	130±60
W6431_H	1.6±1.6	10.6±1.4	9.6±1.4	10±35	130±60	50±60
K2730_V	18.0±0.7	15.7±0.6	14.7±0.6	–20±30	80±25	250±20
K2730_H	1.8±1.2	4.3±1.2	5.7±1.2	–5±55	30±55	30±50
K2749_V	6.0±0.8	16.1±0.6	14.4±0.6	5±35	-5±25	165±20
K2749_H	5.3±1.3	7.4±1.2	6.5±1.2	50±60	75±55	25±55

As previously noted, after further pyrolysis to the dry-gas window, the velocity evolution of the plugs is largely negligible. Additionally, what meaningful changes do occur are interpreted not to be associated with additional microcracking of the samples due to the constancy of the pressure-sensitivity of velocity (Table 2.5). It is hypothesized that the lack of significant acoustic property evolution between the wet- and dry-gas windows is a result of the preservation of an extensive, percolating microcrack network created during pyrolysis to the wet-gas window. The

significant microcracking identified in the wet-gas window provides a network of conduits through which gas generated by oil cracking in the dry-gas window can be readily expelled without significant pore pressure build-up and additional microcracking. The interpreted lack of substantial microcracking after pyrolysis to the dry-gas window is complemented by the, previously discussed, limited visible alteration of the Kimmeridge Shale microstructure (Figure 2.12).

In addition to an increase in the pressure-sensitivity of velocity, Figure 2.9 documents an increase of velocity hysteresis upon unloading post-pyrolysis. Again, this effect is most pronounced in the vertical samples (Table 2.5). The hysteresis $H(\chi)$ of an experimental variable, χ, e.g., P-wave velocity, is defined as in Equation 2.7 where χ_U and χ_D are the values of χ at 7 MPa on the loading and unloading stress paths, respectively.

$$H(\chi) = \chi_D - \chi_U \tag{2.7}$$

The hysteresis between the loading and unloading stress paths indicates differing degrees of pore opening and closure during the experiment. Subsequently, velocity hysteresis is attributed to the inelastic closure of microcracks, induced by pyrolysis, upon loading. As a result of the inelastic nature of this deformation, upon unloading a fraction of the induced microcracks do not reopen and the composite rock remains stiffer, e.g., acoustically faster, at the same confining pressure.

2.5.3.2 Elastic Moduli

As is to be expected, the elastic moduli c_{11} and c_{33} (defined in Equations 2.1 and 2.2) mirror the trends observed in the velocity measurements (Figure 2.13). Indeed, from the velocity, bulk density, and elastic moduli values reported in the Appendices, it is observed that the increase in velocity with confining pressure is considerably greater than the increase in bulk density, and of a magnitude that better reflects the increase in the elastic moduli. This observation is consistent with the hypothesis of significant, co-aligned microcracking of the shale. As confining pressure is increased, the compliant porosity closes. However, the narrow aperture of the microcracks contributes only a small fraction of the effective porosity; subsequently, the bulk density increases little. The same degree of microcrack closure, however, causes a considerable increase in the contact area within the mineral matrix resulting in significant stiffening of the elastic moduli (and subsequently acoustic velocity) of the composite rock.

2.5.3.3 Elastic Anisotropy

The significant increase in P-wave velocity anisotropy (all values recorded in Appendix C) and development of anisotropy-sensitivity to pressure (Tables 2.6 and 2.7) in each sample is inferred to result from severe microcracking of the shale plugs after pyrolysis from the immature to the wet-gas window. The experimental observations and interpreted microcracking agree well with the proposed development and evolution of microcracking made in Vernik and Nur (1992), Vernik (1993), and Vernik and Liu (1997). In this study, however, the interpreted extensive

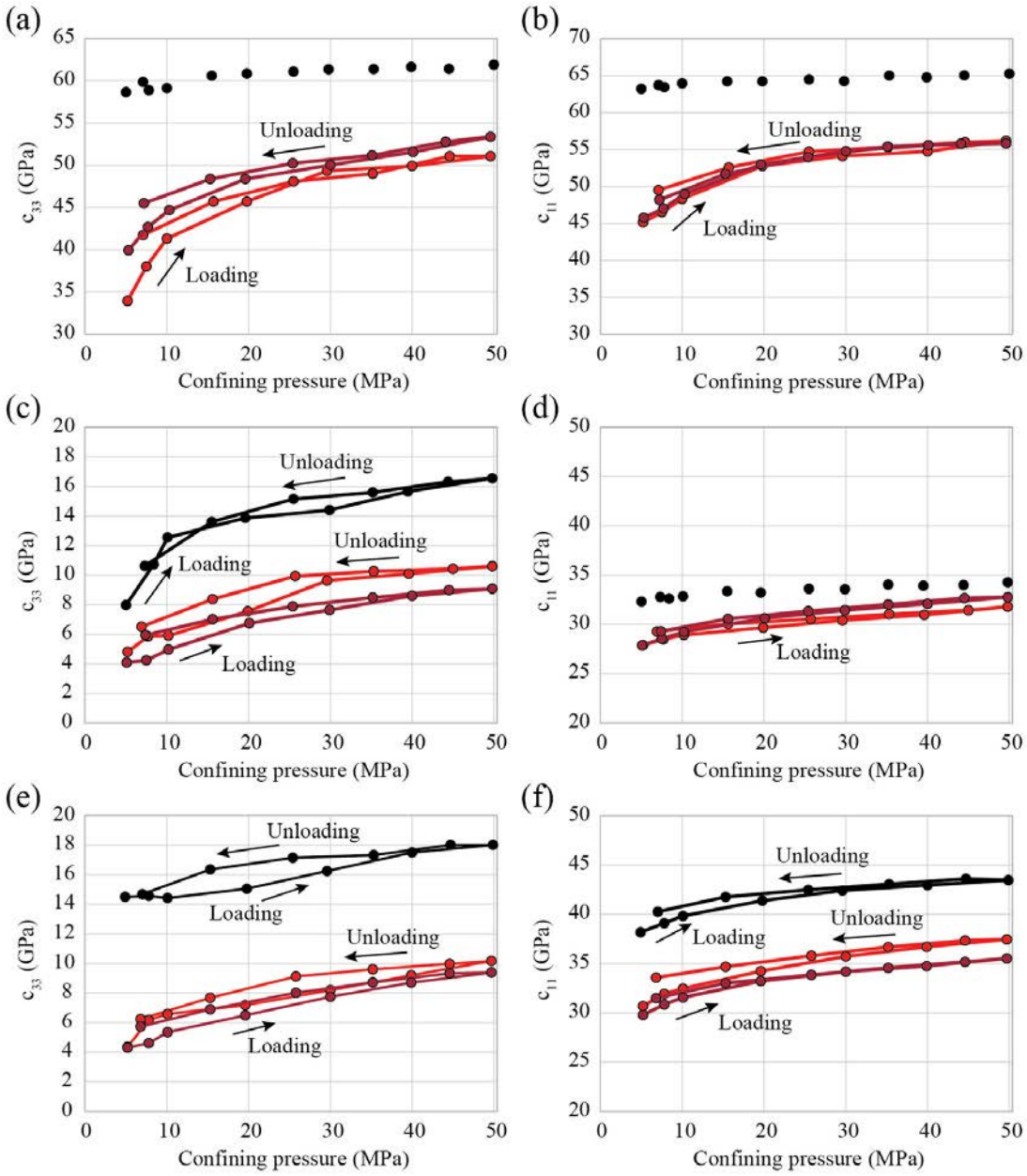

Figure 2.13: P-wave velocity-derived dynamic elastic stiffness of samples in the immature (black), wet-gas (red), and dry-gas (dark red) windows. (a, c, e) c_{33}. (b, d, f) c_{11}. (a, b) W6431. (c, d) K2730. (e, f) K2749. Solid lines and arrows are used to indicate hysteresis between the loading and unloading curves.

microcracking is visually confirmed by time-lapse BSE-SEM imaging. As previously noted, upon pyrolysis to the wet-gas window, severe microcracking is identified (Figure 2.11) within, adjacent to, and in the mineral matrix surrounding kerogen bodies; additionally, the induced microcracks are predominantly sub-parallel to bedding as proposed by Vernik (1993). Note, the values in Table 2.6 are computed by Equation 2.8, where the subscript one indicates pre-pyrolysis and the subscript two indicates post-pyrolysis.

$$\Delta\varepsilon = \varepsilon_2(P_C = 50) - \varepsilon_1(P_C = 50) \tag{2.8}$$

Table 2.6: Change in elastic anisotropy (epsilon) as defined in Equation 2.8.

Sample	Change in Elastic Anisotropy			
	Pyrolysis Experiment 1		Pyrolysis Experiment 2	
	P_c = 7 MPa	P_c = 50 MPa	P_c = 7 MPa	P_c = 50 MPa
W6431	0.07±0.02	0.02±0.02	-0.06±0.02	-0.03±0.02
K2730	0.91±0.06	0.46±0.04	0.93±0.14	0.30±0.08
K2749	1.24±0.06	0.64±0.05	0.77±0.10	0.05±0.06

Table 2.7: Anisotropy hysteresis at 7 MPa confining pressure in each window of thermal maturity as defined in Equation 2.7.

Sample	Anisotropy Hysteresis		
	Immature	Wet-Gas	Dry-Gas
W6431	-0.01±0.02	-0.02±0.02	-0.02±0.02
K2730	0.02±0.04	-0.18±0.07	-0.90±0.17
K2749	0.03±0.04	0.11±0.08	-0.60±0.10

The increase in the P-wave anisotropy of W6431 is minimized by the nature of the sample softening post-pyrolysis. While the Kimmeridge samples exhibit preferential softening of the vertically cored plugs due to the co-alignment of microcracks, the Woodford sample softens to a similar degree in both plugs (Figure 2.9; Table 2.5) indicating that induced microcracks in the weakly bedded siltstone are more randomly oriented. The effect of stress path dependence of the P-wave anisotropy at 7 MPa confining pressure, i.e., anisotropy hysteresis, is negligible for W6431 (Table 2.7). The hysteresis of the Kimmeridge samples, again, increases significantly and is attributed to the irreversible closure of a fraction of the induced, aligned microcracks.

The softening of the vertically cored K2730 and K2749 samples results in P-wave anisotropy increases of 0.91 and 1.24 at 7 MPa confining pressure, respectively (Table 2.6). In addition to exhibiting a significant increase in P-wave anisotropy at low confining pressure, at 50 MPa confining pressure, the samples exhibit an increase in epsilon of 0.46 and 0.64 in epsilon, respectively (Table 2.6). The strong velocity hysteresis developed in the vertically cored K2730 plug due to stiffening of the samples on the stress loading path results in a decrease in epsilon of 0.18 at 7 MPa confining pressure upon unloading (Table 2.7). Sample K2749 exhibits an increase in anisotropy upon unloading of 0.11, e.g., the sign of the hysteresis is reversed; however, this is primarily attributed to differences in the loading and unloading confining pressures at 7 MPa during the experiment – note the offset between data points in Figure 2.10.

Upon pyrolysis to the dry-gas window, the P-wave anisotropy of the shale samples at 50 MPa confining pressure is, again, up to 0.30 higher than the baseline immature window measurement (note, the offset was up to 0.64 in the wet-gas window). We hypothesize that at high confining pressure, when all induced cracks are closed, the intrinsic anisotropy of the mineral matrix should be recovered. Subsequently, the increase in epsilon at high confining pressure may indicate that a significant number of microcracks remain open at high confining pressure. Alternatively, under the assumption that the majority of soft porosity is closed at high confining pressures, an additional source of anisotropy develops upon thermal maturation. This additional anisotropy may be due to temperature-induced clay mineral transformations, e.g., smectite-illite transition or dehydration of clays, or an increase in the intrinsic anisotropy of the organic matter through aromatization (i.e., graphitization of the pyrobitumen). In this latter context, it is worth mentioning that pyrographite (or pyrolytic graphite) shows a hexagonal layered structure with the C-axis oriented perpendicular to layering. The high elastic anisotropy of graphite is reported in the literature to be caused by the different nature of atomic interaction between covalent bonds in the plane of a layer and van der Waals' forces between layers (Levin et al., 1992; Dutton and Dewhurst, 2007). Indeed, Papadakis and Bernstein (1963) report a P-wave anisotropy parameter of $\varepsilon = 0.51$ for pyrographite, comparable to computed values for illite ($0.48 < \varepsilon < 0.62$; Wenk et al., 2007). Furthermore, in-plane and through-plane electrical and thermal conductivity measurements performed by Tian et al. (2013) also show strongly anisotropic electron and photon transport in graphite nanoplatelet-based composites. Future studies must then attempt to discriminate the previously identified potential sources of high confining pressure anisotropy evolution by incorporating additional laboratory experiments, e.g., crystallographic-preferred orientation (CPO; Kanitpanyacharoen et al., 2012), permeability at high confining pressure, and shear-wave splitting measurements.

Subsequently, the evolution of acoustic properties after unconfined pyrolysis contains information on the degree of bedding in the sample. The large increase (up to 1.24; Table 2.6) in P-wave anisotropy coupled with the preferential softening of the vertically cored plugs (Figure 2.9; Table 2.4) for the well-bedded Kimmeridge Shale samples indicates the development of substantial bedding-parallel microcracking. The largely orientation-independent softening of the weakly bedded Woodford sample (Figure 2.9) is indicative of more randomly oriented microcracking. Subsequently, in the absence of in situ, potentially anisotropic, confining stresses, cleavage planes and structural weaknesses, e.g., bedding planes, drive the orientation of hydrocarbon expulsion-induced microcracking. In the absence of weakened bedding planes, microcracks propagate in a more poorly oriented, grain-contact driven geometry. Clearly, the post-pyrolysis P-wave anisotropy values for the Kimmeridge Shale samples (Figure 2.10) are overestimates of in situ values – epsilon values are greater than 1.0 at all monitored confining pressures. The elevated anisotropy values are attributed to exaggerated cracking during pyrolysis experiments. There are two potential sources for the exaggeration in the degree of microcracking: firstly, the pyrolysis protocol employed in this study, e.g., no confining pressure during pyrolysis experiments, and secondly, differential thermal expansion of minerals. By performing pyrolysis experiments at atmospheric confining pressure, very little pore pressure build-up is required to fracture the surrounding mineral matrix; subsequently, a given degree of microcracking is reached through the

conversion of a significantly lesser volume of reactive kerogen to fluid hydrocarbons, e.g., at a lower level of thermal maturity. At the same time, after previous study of the effect of temperature on the elastic properties of crustal rocks (e.g., Kern, 1978), it is possible that the strains induced by differential thermal expansion of minerals will cause additional microcracking within the composite above approximately 100-200 °C. However, the measurements of Kern (1978) were performed on igneous and metamorphic rocks under extremely different conditions to those in our pyrolysis experiments (temperatures up to 700 °C and confining pressures up to 0.6 GPa).

In order to address concerns of thermal expansion, we study a largely inorganic shale (TOC < 1 wt. %; discussed further in Chapters 3 and 4) pre- and post-pyrolysis. The acoustic evolution of the sample, however, was inconclusive with regard to thermal evolution, as the rock stiffened post-pyrolysis as a result of the precipitation or deposition of an iron sulfide across large swathes of the sample faces. Subsequently, further study of inorganic shale is required to conclusively exclude potential expansion-induced microcracking.

2.5.4 The Role of Hydrocarbon Expulsion

In order to corroborate the hypothesis of hydrocarbon expulsion-induced microcracking, I calculate the potential pore pressure generated by kerogen conversion to methane. Given the thermally producible hydrocarbons (S_2 in Table 2.1) for sample K2730 is 25.4 mg per gram of dry rock, we can calculate that, assuming 60% conversion of kerogen, K2730 will generate 420 mg of hydrocarbons during the first pyrolysis experiment. If we assume that methane is the sole hydrocarbon product of the kerogen decomposition reaction, then K2730 will generate 0.03 mols of methane. The pore pressure increase induced by the generation of 0.03 mols of methane at 380 °C in a 1.5 cm^3 volume (the measured pore volume of the thermally immature sample) can then be calculated by the ideal gas law to be 110 MPa (15,750 psi). In the same manner, the pore pressure increase induced by 60% conversion of kerogen to methane in K2749 is calculated to be 350 MPa (51,000 psi). The significant increase in the induced pore pressure for sample K2749 results from the increased value of S_2 (Table 2.1) of the kerogen and the smaller pore volume of sample K2749 (1.1 cm^3 versus 1.5 cm^3 for K2730). The accumulation of between 110 and 350 MPa of pore pressure within a low permeability, unconfined shale sample should be sufficient to induce microcracking as the generated pore fluid attempts to equilibrate. Further, similar imaging work by Kobchenko et al. (2011) and Yenugu (2014) document the same scale of fracturing as a result of hydrocarbon generation and expulsion in other organic-rich shales.

As previously discussed, we attribute the decrease in the P-wave velocity of all samples to the increase in the effective porosity of the plugs, which given the geometry (low aperture) of microcracks is attributed predominantly to porosity generated within the organic matter. However, the decrease of P-wave velocity is not proportional to the effective porosity gain; rather, the decrease in velocity is well correlated with the baseline TOC of the immature window samples (Figure 2.14). We plot changes as a function of baseline TOC as RockEval data indicating hydrocarbon generative potential is not available for all samples. Note, however, that for the Kimmeridge Shale samples, TOC and HGP are positively correlated (Table 2.1). Thus, we can say that the change in velocity for Kimmeridge samples is correlated with HGP. Additionally, the

change in P-wave anisotropy values at 50 MPa confining pressure between the immature and wet-gas windows also exhibits a correlation with baseline TOC (Figure 2.14). The correlation between baseline TOC/HGP and both velocity decrease and magnitude change in P-wave anisotropy suggests that HGP governs the degree of generated effective porosity. This is intuitive, in that, greater hydrocarbon generation results in greater mass/volume loss from the kerogen during pyrolysis experiments. The increased mass/volume loss would then result in a greater degree of void space/porosity generated in and around the organic matter of two otherwise similar samples. The velocity-TOC trend is suppressed in Figure 2.14 for horizontally cored samples, and, most likely, indicates a contribution from TOC-dependent microcrack density given the lower sensitivity of compressional waves to microcracks that are sub-parallel to propagation in this orientation.

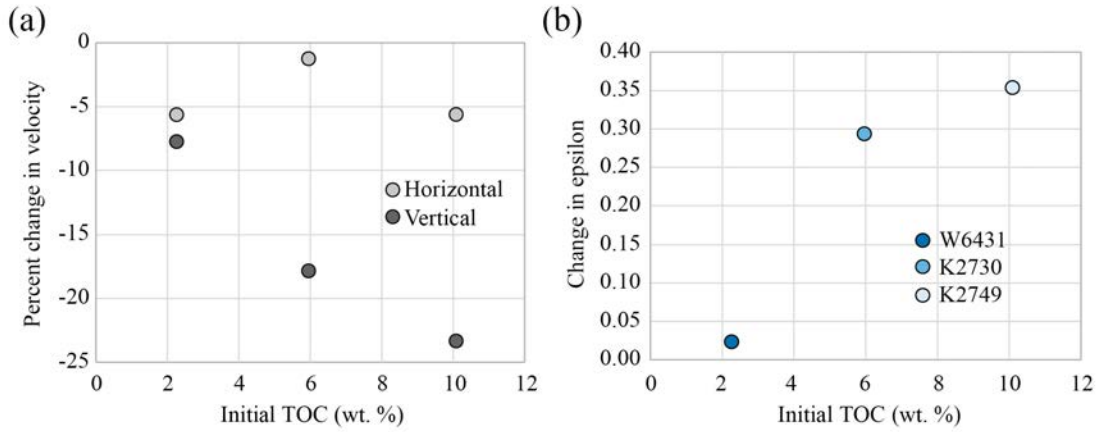

Figure 2.14: Acoustic and elastic evolution upon pyrolysis from the immature to the wet-gas window as a function of baseline TOC at 50 MPa confining pressure. (a) Percent change in P-wave velocity magnitude. (b) Anisotropy magnitude evolution.

Finally, it is observed that the large kerogen body in Figure 2.11 has narrowed by 25% in the bedding-normal direction and 2% in the bedding-parallel direction after pyrolysis to the wet-gas window. This areal reduction of the kerogen body is attributable to either mass loss from kerogen conversion to hydrocarbons or an increase in the density of kerogen due to the volatilization of the organic macromolecules – in either case, a result of the generation and expulsion of hydrocarbons. The areal reduction of the kerogen is, subsequently, evidence that the evolution of anisotropy in these samples is not entirely attributable to the thermally induced microcracking. Additionally, the lack of anisotropy evolution between the wet- and dry-gas windows after a 72 hour exposure to 400 °C may indicate that thermal microcracking is a secondary effect to hydrocarbon generation and expulsion. However, in an attempt to slow the generation and expulsion of fluid hydrocarbons to appropriate in situ rates, minimize the effect of thermal microcracking, and more closely model the orientation and density of microcracking induced in situ, this pilot study indicates that future work should induce thermal maturation via pyrolysis experiments at representative reservoir confining pressures. By increasing the confining pressure and monitoring pore pressure build-up during pyrolysis experiments, the development of through-going, sample-splitting cracks may be suppressed, enabling deeper analysis of rock physics trends induced by thermal maturation.

2.6 Conclusions

In this pilot study, we have presented a unique dataset detailing the evolution of P-wave anisotropy and velocity sensitivity to pressure of organic-rich shale as a function of induced thermal maturation. This study is, indeed, a first attempt at iteratively characterizing the evolution of whole core plugs upon induced thermal maturation in the rock physics literature. The acoustic results obtained indicate significant microcrack development after pyrolysis to the wet-gas window through a significant increase in velocity sensitivity to pressure as hypothesized in Vernik (1993). However, through the implementation of time-lapse BSE-SEM imaging in this study, the development of microcracks is corroborated visually. Further analysis indicates that the degree of microcracking between the immature and wet-gas windows is positively correlated with the thermally producible hydrocarbons or hydrocarbon generative potential of the organic content of the shale.

Additionally, an increase of up to 0.64 in P-wave anisotropy values at 50 MPa confining pressure post-pyrolysis suggests that microcracks may not be closing at high confining pressures or that the intrinsic anisotropy of the organic matter increases upon pyrolysis due to graphitization of the residual organic carbon. The increase in anisotropy at all confining pressures may potentially be attributed to an additional contribution to microcracking generated by thermal strains induced by differential expansion of the constitutive minerals; however, the negligible evolution of both acoustic properties and microstructure between the wet- and dry-gas windows (after further pyrolysis at 400 °C for 72 hours) indicates that thermal microcracking is less significant than hydrocarbon expulsion as a source of anisotropy and microstructural evolution in these experiments. The negligible evolution between the wet- and dry-gas window measurements is, therefore, attributed to a preserved, preexisting microcrack network created during the first pyrolysis experiment facilitating the expulsion of hydrocarbons generated during future pyrolysis experiments with minimal pore pressure build-up. The anomalously high values of epsilon, e.g., >0.5, recorded at all pressures and stages of thermal maturity for the Kimmeridge Shale samples are attributed to both the strong crystallographic alignment of the clay-rich matrix and the unsaturated nature of co-aligned, subparallel to bedding compliant porosity.

Most importantly, this pilot study proves the feasibility of the iterative characterization of the porosity, velocity, and microstructure pre- and post-pyrolysis-induced thermal maturation. It is clear, however, through the development of through-going, sample-splitting cracks that future pyrolysis experiments must be conducted under reservoir confining pressure conditions. Increasing the effective pressure during pyrolysis measurements will serve to minimize the development of both microcracks and sample-scale cracks in the rock by requiring that maturation proceed further before the pore pressure exceeds the pressure confining that pore. In order to more thoroughly characterize the sample evolution and, in particular, identify the source of the anisotropy increase at high confining pressure, additional measurements must be implemented in any updated methodology. These additional measurements include monitoring the shear wave velocity and permeability and imaging nano-scale microstructures and microcrack orientations. Finally, future studies must incorporate a more gradual sampling of the thermal maturation sequence.

That is, given that little evolution is observed beyond the wet-gas window, future studies must target pyrolysis from the immature state to the oil window, and then to the gas window. Our updated methodology is discussed in Chapter 3 before being implemented in Chapters 4 through 6.

2.7 Appendix

2.7.1 Appendix A: Acoustic Velocity Dataset

Table 2A.1: Acoustic velocity (m/s) perpendicular to bedding as a function of confining pressure (P_C). Windows of thermal maturity are abbreviated as Imm (immature), Wgw (wet-gas window), and Dgw (dry-gas window).

Pc	W6431			K2730			K2749		
(MPa)	Imm	Wgw	Dgw	Imm	Wgw	Dgw	Imm	Wgw	Dgw
5	4848	3751	4035	1898	1520	1403	2535	1427	1414
7.5	4857	3969	4172	2196	1675	1427	2538	1697	1460
10	4866	4136	4266	2376	1682	1544	2524	1750	1573
20	4933	4346	4434	2490	1893	1791	2573	1822	1728
30	4952	4512	4506	2534	2133	1902	2669	1940	1883
40	4961	4536	4572	2638	2178	2013	2767	2050	1990
50	4970	4585	4649	2709	2226	2065	2804	2150	2063
45	4950	4586	4623	2690	2207	2055	2804	2129	2058
35	4951	4494	4555	2633	2192	1996	2751	2091	1991
25	4941	4454	4514	2596	2159	1928	2740	2042	1912
15	4923	4345	4434	2464	1987	1821	2678	1876	1777
7	4896	4156	4303	2179	1756	1680	2542	1695	1624

Table 2A.2: Acoustic velocity (m/s) parallel to bedding as a function of confining pressure (P_C). Windows of thermal maturity are abbreviated as Imm (immature), Wgw (wet-gas window), and Dgw (dry-gas window).

Pc	W6431			K2730			K2749		
(MPa)	Imm	Wgw	Dgw	Imm	Wgw	Dgw	Imm	Wgw	Dgw
5	4973	4283	4307	3859	3696	3653	4055	3722	3670
7.5	4982	4346	4364	3873	3730	3691	4099	3789	3730
10	5000	4427	4453	3884	3754	3730	4135	3818	3769
20	5008	4621	4625	3897	3788	3805	4206	3905	3854
30	5007	4677	4698	3910	3823	3846	4252	3979	3901
40	5025	4701	4731	3925	3848	3877	4273	4022	3924
50	5043	4759	4738	3939	3890	3908	4295	4053	3961
45	5034	4751	4739	3924	3868	3903	4302	4047	3942
35	5035	4727	4722	3929	3847	3865	4277	4015	3911
25	5017	4702	4664	3907	3822	3829	4251	3971	3876
15	5008	4612	4567	3897	3799	3788	4220	3916	3835
7	4991	4479	4415	3869	3758	3719	4149	3863	3756

2.7.2 Appendix B: Porosity Evolution with Confining Pressure Dataset

Table 2B.1: Sample porosity (ϕ) as a function of confining pressure (P_C) for sample W6431. Windows of thermal maturity are abbreviated as imm (immature), wgw (wet-gas window), and dgw (dry-gas window). The plug orientations are denoted as vertical (0°) and horizontal (90°), respectively.

P_C (MPa)	W6431imm		W6431wgw		W6431dgw	
	φ(0°) (%)	φ(90°) (%)	φ(0°) (%)	φ(90°) (%)	φ(0°) (%)	φ(90°) (%)
1	0.52	0.66	5.68	5.61	5.11	5.11
5	0.27	0.42	5.39	5.33	4.72	4.72
7.5	0.22	0.37	5.31	5.24	4.65	4.66
10	0.18	0.33	5.23	5.17	4.58	4.59
20	0.05	0.21	5.02	4.96	4.37	4.38
30	-0.03	0.12	4.89	4.83	4.24	4.25
40	-0.10	0.05	4.79	4.72	4.14	4.15
50	-0.16	-0.01	4.69	4.63	4.05	4.06
45	-0.14	0.01	4.72	4.66	4.08	4.09
35	-0.09	0.06	4.79	4.73	4.14	4.15
25	-0.03	0.12	4.88	4.82	4.23	4.24
15	0.06	0.22	5.00	4.93	4.35	4.37
7	0.19	0.34	5.15	5.08	4.55	4.56

Table 2B.2: Sample porosity (ϕ) as a function of confining pressure (P_C) for sample K2730. Windows of thermal maturity are abbreviated as imm (immature), wgw (wet-gas window), and dgw (dry-gas window). The plug orientations are denoted as vertical (0°) and horizontal (90°), respectively.

P_C (MPa)	K2730imm		K2730wgw		K2730dgw	
	φ(0°) (%)	φ(90°) (%)	φ(0°) (%)	φ(90°) (%)	φ(0°) (%)	φ(90°) (%)
1	10.23	9.50	22.06	22.41	22.13	20.41
5	9.21	8.53	20.74	21.10	21.24	19.51
7.5	8.95	8.27	20.61	20.97	21.01	19.26
10	8.86	8.17	20.41	20.77	20.81	19.05
20	8.44	7.75	19.78	20.14	20.28	18.49
30	8.12	7.43	19.30	19.66	19.88	18.07
40	7.86	7.17	18.85	19.22	19.54	17.71
50	7.61	6.91	18.47	18.83	19.19	17.34
45	7.64	6.94	18.50	18.86	19.22	17.36
35	7.75	7.06	18.66	19.03	19.28	17.43
25	7.88	7.19	18.87	19.24	19.47	17.64
15	8.09	7.40	19.18	19.53	19.76	17.94
7	8.36	7.67	19.55	19.91	20.12	18.32

Table 2B.3: Sample porosity (ϕ) as a function of confining pressure (P_C) for sample K2749. Windows of thermal maturity are abbreviated as imm (immature), wgw (wet-gas window), and dgw (dry-gas window). The plug orientations are denoted as vertical (0°) and horizontal (90°), respectively.

P_C (MPa)	K2749imm		K2749wgw		K27491dgw	
	φ(0°) (%)	φ(90°) (%)	φ(0°) (%)	φ(90°) (%)	φ(0°) (%)	φ(90°) (%)
1	7.94	8.02	18.57	17.29	17.97	17.84
5	7.10	7.18	17.51	16.21	16.90	16.77
7.5	6.89	6.96	17.23	15.93	16.72	16.59
10	6.74	6.82	17.04	15.74	16.55	16.42
20	6.35	6.43	16.42	105.11	16.02	15.89
30	6.07	6.15	15.92	14.60	15.64	15.51
40	5.85	5.93	15.49	14.16	15.29	15.16
50	5.66	5.74	15.07	13.74	14.95	14.82
45	5.67	5.75	15.09	13.75	15.01	14.88
35	5.78	5.86	15.25	13.91	15.17	15.04
25	5.92	6.00	15.46	14.13	15.39	15.26
15	6.13	6.21	15.77	14.45	15.71	15.59
7	6.41	6.49	16.18	14.87	16.15	16.02

2.7.3 Appendix C: Velocity-Derived Elastic Dataset

Table 2C.1: Computed elastic moduli and Thomsen's elastic anisotropy parameter epsilon as a function of confining pressure (P_C) for sample W6431. Windows of thermal maturity are abbreviated as imm (immature), wgw (wet-gas window), and dgw (dry-gas window).

P_C (MPa)	W6431imm			W6431wgw			W6431dgw		
	C_{11} (GPa)	C_{33} (GPa)	ε (-)	C_{11} (GPa)	C_{33} (GPa)	ε (-)	C_{11} (GPa)	C_{33} (GPa)	ε (-)
5	63.19	58.65	0.039	45.15	33.93	0.165	45.79	39.93	0.073
7.5	63.45	58.89	0.039	46.54	38.02	0.112	47.05	42.71	0.051
10	63.95	59.13	0.041	48.32	41.31	0.085	49.02	44.69	0.048
20	64.23	60.84	0.028	52.76	45.71	0.077	53.00	48.38	0.048
30	64.24	61.35	0.024	54.13	49.34	0.048	54.76	50.03	0.047
40	64.76	61.63	0.025	54.74	49.91	0.048	55.59	51.56	0.039
50	65.27	61.90	0.027	56.17	51.07	0.050	55.81	53.37	0.023
45	65.02	61.39	0.030	55.96	51.06	0.048	55.80	52.76	0.029
35	65.01	61.36	0.030	55.34	49.00	0.064	55.38	51.18	0.041
25	64.50	34.09	0.028	54.72	48.09	0.069	53.98	50.22	0.037
15	64.23	60.59	0.030	52.58	45.71	0.075	51.69	48.38	0.034
7	63.70	59.84	0.032	49.51	47.74	0.093	48.19	45.49	0.030

Table 2C.2: Computed elastic moduli and Thomsen's elastic anisotropy parameter epsilon as a function of confining pressure (P_C) for sample K2730. Windows of thermal maturity are abbreviated as imm (immature), wgw (wet-gas window), and dgw (dry-gas window).

P_C (MPa)	K2730imm			K2730wgw			K2730dgw		
	C_{11} (GPa)	C_{33} (GPa)	ε (-)	C_{11} (GPa)	C_{33} (GPa)	ε (-)	C_{11} (GPa)	C_{33} (GPa)	ε (-)
5	32.31	7.98	1.525	27.90	4.81	2.402	27.87	4.08	2.912
7.5	32.63	10.71	1.023	28.46	5.85	1.934	28.54	4.24	2.867
10	32.86	12.55	0.809	28.91	5.91	1.945	29.23	4.97	2.438
20	32.22	13.85	0.699	29.67	7.55	1.466	30.62	6.74	1.771
30	33.57	14.39	0.666	30.40	9.64	1.077	31.44	7.64	1.558
40	33.91	15.65	0.584	30.97	10.10	1.033	32.09	8.60	1.367
50	34.26	16.55	0.535	31.79	10.60	0.999	32.76	9.08	1.304
45	33.98	16.31	0.542	31.43	10.42	1.008	32.66	8.99	1.316
35	34.03	15.60	0.591	31.03	10.25	1.013	32.01	8.48	1.388
25	33.60	15.15	0.609	30.54	9.92	1.039	31.33	7.89	1.487
15	33.36	13.61	0.725	30.04	8.37	1.294	30.56	7.02	1.678
7	32.78	10.62	1.044	29.28	6.51	1.750	29.31	5.94	1.967

Table 2C.3: Computed elastic moduli and Thomsen's elastic anisotropy parameter epsilon as a function of confining pressure (P_C) for sample K2749. Windows of thermal maturity are abbreviated as imm (immature), wgw (wet-gas window), and dgw (dry-gas window).

P_C (MPa)	K2749imm			K2749wgw			K2749dgw		
	C_{11} (GPa)	C_{33} (GPa)	ε (-)	C_{11} (GPa)	C_{33} (GPa)	ε (-)	C_{11} (GPa)	C_{33} (GPa)	ε (-)
5	38.18	14.50	0.816	30.69	4.36	3.023	29.81	4.31	2.960
7.5	39.10	14.58	0.841	31.92	6.18	2.083	30.86	4.61	2.849
10	39.84	14.44	0.880	32.48	6.58	1.967	31.57	5.35	2.448
20	41.40	15.06	0.874	34.23	7.19	1.881	33.23	6.50	2.055
30	42.43	16.26	0.805	35.74	8.20	1.678	34.19	7.76	1.704
40	42.96	17.51	0.727	36.72	9.20	1.495	34.75	8.70	1.497
50	43.48	18.02	0.707	37.48	10.17	1.342	35.54	9.39	1.392
45	43.62	18.01	0.711	37.35	9.98	1.372	35.17	9.34	1.383
35	43.07	17.33	0.743	36.69	9.61	1.410	34.57	8.72	1.482
25	42.49	17.16	0.738	35.80	9.13	1.460	33.85	8.02	1.609
15	41.78	16.36	0.777	34.69	7.68	1.758	33.02	6.90	1.891
7	40.26	14.69	0.870	33.59	6.24	2.191	31.50	5.73	2.247

2.8 References

Allan, A. M., T. Vanorio, and J. E. P. Dahl, 2014, Pyrolysis-induced P-wave velocity anisotropy in organic-rich shales: Geophysics, 79:D41–D53.

Allan, A. M., W. Kanitpanyacharoen, and T. Vanorio, 2015, A multi-scale methodology for the analysis of velocity anisotropy in organic-rich shale: Geophysics, 80:C73–C88.

Banik, N. C., 1984, Velocity anisotropy in shales and depth estimation in the North Sea basin: Geophysics, 49:1411–1419.

Chang, C. and M. D. Zoback, 2009, Viscous creep in room-dried unconsolidated Gulf of Mexico shale (I): Experimental results: Journal of Petroleum Science and Engineering, 69:239–246.

Chang, C., D. Moos, and M. D. Zoback, 1997, Anelasticity and dispersion in dry unconsolidated sand: International Journal of Rock Mechanics and Mining Science, 34:402.

Curtis, M. E., B. J. Cardott, C. H. Sondergeld, and C. S. Rai, 2012, Development of organic porosity in the Woodford Shale with increasing thermal maturity: International Journal of Coal Geology, 103:26–31.

Dahl, J. E., J. M. Moldowan, K. E. Peters, G. E. Claypool, M. A. Rooney, G. E. Michael, M. R. Mello, and M. L. Kohnen, 1999, Diamondoid hydrocarbons as indicators of natural oil cracking: Nature, 399:54–57.

de Waal, J. A. and R. M. M. Smits, 1988, Prediction of reservoir compaction and surface subsidence: Field application of a new model: SPE Formation Evaluation, 3:347–356.

Dewhurst, D. N. and A. F. Siggins, 2006, Impact of fabric, microcracks and stress field on shale anisotropy: Geophysics Journal International, 165:135–148.

Dudley, J. W., M. T. Myers, R. D. Shew, and M. M. Arasteh, 1998, Measuring compaction and compressibilities in unconsolidates reservoir materials by time-scaline creep: SPE Reservoir Evaluation and Engineering, 5:51324.

Dutton, B. and R. J. Dewhurst, 2007, Graphite anisotropy measurements using laser-generated ultrasound: Journal of Optics A, Pure and Applied Optics, 9:S7–S11.

Hagin, P. N. and M. D. Zoback, 2004, Viscous deformation of unconsolidated sands - Part 1: Time-dependent deformation, frequency dispersion, and attenuation: Geophysics, 69:731–741.

Hornby, B. E., 1998, Experimental laboratory determination of the dynamic elastic properties of wet, drained shales: Journal of Geophysical Research, 103:29945–29964.

Horsfield, B. and J. Rullkötter, 1994, Diagenesis, catagenesis, and metagenesis of organic matter, in L. B. Magoon, and W. G. Dow, eds., The petroleum system - From source to trap: AAPG, AAPG Memoir, 60:189–199.

Johnston, J. E. and N. I. Christensen, 1995, Seismic anisotropy of shales: Journal of Geophysical Research, 100:5991–6003.

Jones, L. E. A. and H. F. Wang, 1981, Ultrasonic velocities in Cretaceous shales from the Williston basin: Geophysics, 46(3):288–297.

Kaarsberg, E. A., 1959, Introductory studies of natural and artificial argillaceous aggregates by sound-propagation and X-ray diffraction methods: Journal of Geology, 67:447–472.

Kanitpanyacharoen, W., H.-R. Wenk, F. B. Kets, C. Lehr, and R. Wirth, 2011, Texture and anisotropy of Qusaiba shales: Geophysical Prospecting, 59:536–556.

Kanitpanyacharoen, W., F. B. Kets, H.-R. Wenk, and R. Wirth, 2012, Mineral preferred orientation and microstructure in the Posidonia shale in relation to different degrees of thermal maturity: Clay and Clay Minerals, 60:315–329.

Kern, H., 1978, The effect of high temperatire and high confining pressure on compressional wave velocities in quartz-bearing and quartz-free igneous and metamorphic rocks: Tectonophysics, 44:185–203.

Kobchenko, M., H. Panahi, F. Renard, D. K. Dysthe, A. Malthe-Sørenssen, A. Mazzini, J. Scheibert, B. Jamtveit, and P. N. Meakin, 2011, 4D imaging of fracturing in organic-rich shales during heating: Journal of Geophysical Research, 116:B12201.

Levin, V. M., R. G. Maev, K. I. Maslov, T. A. Senjushkina, I. G. Grigorieva, and I. Baranchikova, 1992, Study of structure and properties of highly anisotropic materials by acoustomicroscopial methods: In Ermert, H. and H. P. Harjes, editors, 19th International Symposium on Acoustical Imaging, pages 651–655: Springer.

Lonardelli, I., H.-R. Wenk, and Y. Ren, 2007, Preferred orientation and elastic anisotropy in shales: Geophysics, 72(2):D33–D40.

Loucks, R. G., R. M. Reed, S. C. Ruppel, and D. M. Jarvie, 2009, Morphology, genesis, and distribution of nanometer-scale pores in siliceous mudstones of the Mississippian Barnett shale: Journal of Sedimentary Research, 79:848–861.

Okiongbo, K. S., A. C. Aplin, and S. R. Larter, 2005, Changes in type II kerogen density as a function of maturity: Evidence from the Kimmeridge Clay Formation: Energy and Fuels, 19: 2495–2499.

Papadakis, E. P. and H. Bernstein, 1963, Elastic moduli of pyrolitic graphite: Journal of the Acoustical Society of America, 35:521–524.

Peters, K. E. and M. R. Cassa, 1994, Applied source rock geochemistry, in L. B. Magoon, and W. G. Dow, eds., The petroleum system - From source to trap: AAPG, AAPG Memoir, 60: 93–120.

Peters, K. E., C. C. Walters, and J. M. Moldowan, 2004, The biomarker guide: Volume 2, Biomarkers and isotopes in petroleum systems and earth history: Cambridge University Press.

Sayers, C. M., 1999, Stress-dependent seismic anisotropy of shales: Geophysics, 64:93–98.

Sayers, C. M., 2005, Seismic anisotropy of shales: Geophysical Prospecting, 53:667–676.

Sone, H., 2012, Mechanical properties of shale gas reservoir rocks and its relation to the in-situ variation observed in shale gas reservoirs: PhD Dissertation, Stanford University.

Thomsen, L., 1986, Weak elastic anisotropy: Geophysics, 51:1954–1966.

Tian, X., M. E. Itkis, E. B. Bekyarova, and R. C. Haddon, 2013, Anisotropic thermal and electrical properties of thin thermal interface layers of graphite nanoplatelet-based composits: Scientific Reports, 3:1710.

Valcke, S. L. A., M. Casey, G. E. Lloyd, J. M. Kendall, and Q. J. Fisher, 2006, Lattice preferred orientation and seismic anisotropy in sedimentary rocks: Geophysics Journal International, 166:652–660.

Vanorio, T., T. Mukerji, and G. Mavko, 2008, Emerging methodologies to characterize the rock physics properties of organic-rich shales: The Leading Edge, 27:780–787.

Vasin, R., H.-R. Wenk, W. Kanitpanyacharoen, S. Matthies, and R. Wirth, 2013, Anisotropy of Kimmeridge sgake: Journal of Geophysical Research, 118:1–26.

Vernik, L., 1993, Microcrack-induced versus intrinsic elastic anisotropy in mature HC-source shales: Geophysics, 58:1703–1706.

Vernik, L. and C. Landis, 1996, Elastic anisotropy of source rocks: Implications for hydrocarbon generation and primary migration: AAPG Bulletin, 80:531–544.

Vernik, L. and X. Liu, 1997, Velocity anisotropy in shales: A petrophysical study: Geophysics, 62:521–532.

Vernik, L. and A. Nur, 1992, Ultrasonic velocity and anisotropy of hydrocarbon source rocks: Geophysics, 57:727–735.

Wang, Z., 2002, Seismic anisotropy in sedimentary rocks, part 2: Laboratory data: Geophysics, 62:521–532.

Wenk, H.-R., I. Lonardelli, H. Franz, K. Nihei, and S. Nakagawa, 2007, Preferred orientation and elastic anisotropy of illite-rich shale: Geophysics, 72(2):E69–E75.

Yenugu, M. R., 2014, Elastic, microstructural and geochemical characterization of kerogen maturity for shales: PhD Dissertation, University of Houston.

Chapter 3

A COMPREHENSIVE MULTI-SCALE, MULTI-PHYSICS METHODOLOGY FOR SHALE ELASTIC ANISOTROPY CHARACTERIZATION AND ORGANIC-RICH SHALE SAMPLE SET

Abstract

As identified in the previous chapter, it is pivotal to the interpretation of maturity-dependent trends in organic-rich shale datasets that a thorough understanding of the elastic behavior of shale is developed. In this chapter, we lay out the framework for experiments that single out the rock properties responsible for anisotropy and link them to geophysical observables. We thus present

a comprehensive, multi-scale, multi-physics experimental methodology for the characterization of the elastic anisotropy of organic-rich shale. Given the observations of Chapter 2, we define here two main contributions to anisotropy: an intrinsic shale anisotropy arising from the co-alignment of minerals and organic material in the rock frame and an extrinsic shale anisotropy arising from the co-alignment of compliant porosity and microcracks. The implementation of the methodology documented in this chapter enables the discrimination and comparison of the intrinsic and extrinsic factors contributing to elastic anisotropy both as a function of confining pressure and thermal maturity. In this experimental methodology, we explore the connections between classical rock physics experiments, e.g., acoustic velocity experiments, and emergent high-resolution imaging techniques, such as electron microscopy, fluorescence microscopy, and microtomography, to better characterize the heterogeneous and microstructurally complex shale at a range of length scales. Furthermore, we introduce the sample set that will be studied in the remaining chapters of this thesis. The mineralogy, microstructure, and geochemistry of these samples are discussed to demonstrate the breadth of samples included in this study. The samples in this set range from clay-rich, strongly laminated shales to randomly oriented, micritic samples, with a strong sampling of intermediate mineralogies and textures. By utilizing such a broad sample set, we enable a more comprehensive investigation of the elastic and transport properties of organic-rich shale in the following chapters.

3.1 Introduction

The completion of the pilot study (detailed in Chapter 2) raises additional questions that require the development of a comprehensive experimental methodology to more completely analyze the anisotropy of organic-rich shale. In particular, in order to address the post-pyrolysis increase in elastic anisotropy at high confining pressure observed in Chapter 2, it is necessary that we are first able to discriminate the individual sources of elastic anisotropy in shale so as to correctly identify all pyrolysis-induced phenomena that alter the elastic anisotropy. Additionally, further analysis of datasets composed of samples matured in situ, such as that compiled by Vernik (Vernik and Nur, 1992; Vernik and Landis, 1996; Vernik and Liu, 1997), will benefit greatly from the discrimination and comparison of the relative contribution to total anisotropy of each individual source. Furthermore, comprehensive characterization of the rock frame is of the utmost importance in applying fluid substitution models to shales (e.g., Gassmann, 1951).

As introduced in Chapter 2, the elastic anisotropy of organic-rich shale is attributed to the combination of an intrinsic mineral alignment-induced component and a compliant porosity-driven component which we term hereafter as the extrinsic contribution. The intrinsic anisotropy of shale results from depositional and burial effects including: the slow deposition from suspension of clay minerals, a low rate of organic deposition and a lack of bioturbation perturbing the developing mineral texture, and burial-induced compaction of clay platelets (Kaarsberg, 1959; Jones and Wang, 1981; Vernik and Nur, 1992; Hornby, 1998; Johnston and Christensen, 1995; Sayers, 1999, 2005; Wang, 2002; Valcke et al., 2006; Wenk et al., 2007; Lonardelli et al., 2007; Kanitpanyacharoen et al., 2011; Vasin et al., 2013; Allan et al., 2015). While the extrinsic component results from microcracking induced by effective stress decreases associated with, amongst

other sources, fluid generation (clay dehydration, hydrocarbon generation) and tectonic uplift (Vernik, 1993; Johnston and Christensen, 1995; Dewhurst and Siggins, 2006; Allan et al., 2014, 2015).

However, in addition to these two sources of anisotropy, the thermal alteration of organic matter is hypothesized to add to the intrinsic anisotropy of the rock. The thermal evolution of organic matter results in the development of structurally coplanar, carbon-rich rings in the residual pyrographite, which is highly anisotropic (Taylor et al., 1998; Peters et al., 2004). This will further contribute to the intrinsic anisotropy of the shale frame. Additionally, high-resolution microscopy showed that the porosity and topology of pores associated with kerogen evolve with increasing thermal maturity (Loucks et al., 2009; Walls and Sinclair, 2011; Curtis et al., 2012). It has also been shown that specific kerogen macerals (resinite and exsudatinite) may mobilize upon maturation and fill preexisting or developing microcracks in the mineral matrix of the shale (Tissot et al., 1974; Teerman et al., 1987; Prasad et al., 2011). The development of intrinsic anisotropy in residual kerogen and the propensity of organic matter to fill aligned microcracks will contribute to the intrinsic anisotropy of the shale composite upon burial-induced thermal alteration.

The elastic anisotropy of organic-rich shale is, then, a linear combination of these three individual sources. The relative contribution of each source to the total elastic anisotropy should vary from sample to sample and as a function of thermal maturity. Thus, the relative contributions must be discriminated experimentally to fully characterize the evolution of shale anisotropy as a function of thermal maturity. Subsequently, in this chapter, I present both the workflow that enables the experimental discrimination of the sources of anisotropy and a detailed description of the setup and parameters involved in each experimental method. Finally, given the well-noted heterogeneity of shale, in order to comprehensively characterize the evolution of the elastic and transport properties of shale, we have compiled an extensive set of organic-rich shale samples. The sample set covers both organic-rich and organic-poor samples, samples of a range of mineralogies (including argillaceous, quartzose, and calcareous samples), and a broad continuum of mineral alignments. The mineralogical, microstructural, and geochemical characterization of these samples is also discussed in this chapter to better illustrate the breadth of the sample set and limit redundancy in future chapters.

3.2 Structure of the Multi-Scale, Multi-Physics Methodology for Shale Characterization

As illustrated in Figure 3.1, our methodology combines classical rock-physics measurements with a suite of emergent high-resolution imaging techniques to discriminate the magnitude of each source of anisotropy in shale. The sources of elastic anisotropy are divided into three groups (rows two and three of Figure 3.1): anisotropy arising from the aligned mineral frame (intrinsic inorganic), anisotropy arising from thermal alteration of the residual organic matter (pyrographitization; intrinsic organic), and anisotropy arising from the co-alignment of compliant porosity/microcracks (extrinsic).

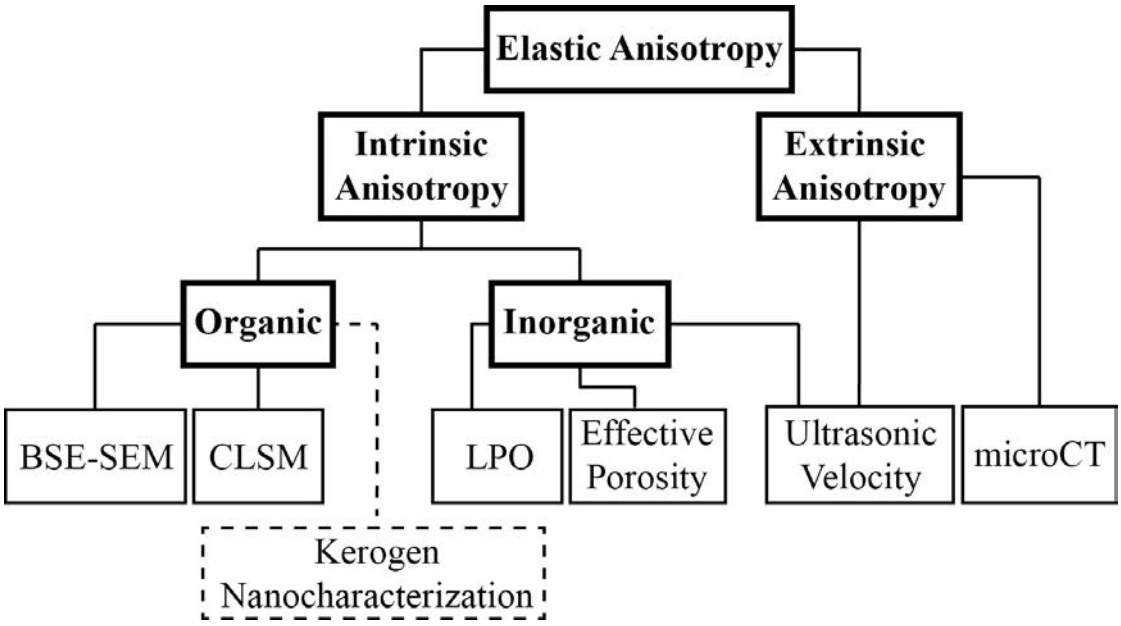

Figure 3.1: A flowchart of the techniques (standard text/boxes) used to characterize shale elastic anisotropy and its constitutive sources (bold text/boxes). The abbreviated techniques are discussed individually in Section 3.3. Kerogen nanocharacterization (dashed) is not included in this study, but is a component of ongoing work in our lab (S. Alsinan, personal communication, 2014).

The intrinsic anisotropy of the solid frame is quantified through ultrasonic velocity measurements at high confining pressure under the assumption that all effective compliant porosity is closed. The intrinsic inorganic component is singled out by combining high confining pressure anisotropy values with the X-ray diffraction (XRD)-derived crystallographic preferred orientation (CPO) of the mineral matrix. The pyrographitization-induced intrinsic organic component can then be identified through deviations from the anisotropy-CPO trend. To be attributed as organically sourced, however, any deviation must be supported by high-resolution images from backscattered electron scanning electron microscopy (BSE-SEM) and/or confocal laser scanning microscopy (CLSM) to visually identify the evolution of the distribution, alignment, and interrelation with the inorganic matrix of the organic matter, respectively.

The degree of extrinsic anisotropy is quantified through the combination of axial strain and acoustic velocity measurements during sample unloading and X-ray microtomographic (microCT) imaging. Acoustic and mechanical analysis allows the correlation of the opening of microcracks to an increase in anisotropy and a decrease in axial strain with decreasing confining pressure. The acoustic and mechanical evolution with confining pressure is then compared to digitally quantified crack volume density values from microCT volumes.

The magnitude of each source can then be compared to identify variations in the dominant source of elastic anisotropy both across samples and as a function of pressure and thermal maturity for an individual sample. The next section is devoted to a discussion of the individual experimental methods applied in the shale elastic anisotropy characterization methodology (row four of Figure 3.1).

3.3 Experimental Implementation of the Shale Characterization Methodology

3.3.1 Subsampling

As a result of sample size requirements for the different experimental techniques and destructive nature of some techniques, e.g., focused ion beam scanning electron microscopy (FIB-SEM; discussed in Chapter 6), it is necessary that each core plug is subsampled prior to characterization. As in Chapter 2, each sample is composed of two mutually orthogonal plugs – one cored parallel to bedding (horizontal) and one cored perpendicular to bedding (vertical). Each of the initially 3-4 cm long plugs comprising each sample are subsampled as illustrated in Figure 3.2. The subsampling procedure results in ∼2 cm long plugs for velocity analysis (both vertical and horizontal), a ∼0.2 cm long horizontal coin for XRD-based microstructural and mineralogical characterization, and an approximately 0.7-1.5 cm sample for permeability analysis (both vertical and horizontal – discussed in Chapter 6). The excess sample material and any irregularly shaped fragments are used for geochemical analysis. Fundamental to the use of multiple subsamples is the assumption that the microstructural, mineralogical, and geochemical properties are homogenous, within some tolerance, throughout the original plug. The validity of this assumption is discussed in the Discussion section and Appendix C.

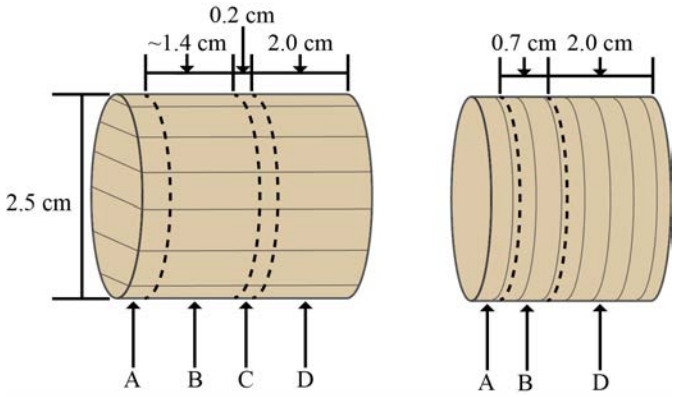

Figure 3.2: A schematic representation of the subsampling of the (left) horizontally and (right) vertically cored plugs. The labeled subsamples are: excess material used for geochemical analysis (A), a plug for permeability analysis (B; the permeability methodology is discussed in Chapter 6), a thin coin used for XRD experiments (C), and a plug for acoustic experiments (D). The approximate length of each subsample is labeled above the plugs.

3.3.2 Rock Physics Experiments

3.3.2.1 Helium Porosimetry

The effective porosity and grain density of the samples are determined, as in Chapter 2, through helium porosimetry. Porosimetry makes use of Boyle's law (Equation 3.1) and the

expansion of a known pressure of gas (in this study, helium) into a void space of known volume in which the rock has been placed. The pressure drop upon expansion can then be related to the solid/grain volume of the rock sample. Given the mass and bulk volume of the sample (from caliper-derived length and diameter measurements, assuming a right circular cylindrical form), the porosity and grain density can be trivially computed from the grain volume. The intrinsic experimental error in grain volume calculations is quite small (<0.05 cm^3); however, error associated with irregularly shaped or chipped samples can result in errors in derived effective porosity values of up to a couple of porosity units. Prior to helium porosimetry experiments (and all subsequent techniques), samples are kept in an oven at 40 °C until mass loss stabilizes to ensure that samples are dry with minimal alteration of the hydrated clay platelets and zeolites. As in the previous chapter, *dry* is taken to mean there is no remaining free water within the pore space. There may, however, be significant *bound* water in/around clay platelets and zeolite crystals. Given that the bound water cannot be removed without damaging/altering the shale, the bound water is not considered to affect the 'dryness' of the sample.

$$P_1V_1 = P_2V_2 \tag{3.1}$$

3.3.2.2 Acoustic Velocity Experiments

As in Chapter 2, all acoustic experiments are performed using the pulse transmission method. A schematic of the acoustic system is given in Figure 3.3. The sample is jacketed within a Tygon® tube sealed by two Viton® O-rings, which prevents the confining fluid from intruding the sample while allowing the transfer of stress to it. The sample is held between two pistons containing piezoelectric crystals, which convert the generated electrical pulse into an acoustic pulse and vice versa. Radial and axial chambers enable hydrostatic confining pressures to be attained through the filling of the chambers and either direct contact with the jacketed sample (radial) or the displacement of a piston (axial). The confining pressure is provided via hydraulic oil and a pneumatic pump. During experiments, the axial sample strain is computed from sample length changes continuously monitored (with a resolution of ∼8 seconds) by three external linear potentiometers (not shown in Figure 3.3). The radial strain is not directly monitored but assumed to be equal to that measured along the axial direction of the orthogonally oriented plug (see Chapter 2). All calculated axial strain is assumed to arise from pore compaction, i.e., the mineral frame is incompressible. For this system, the errors in P- and S-wave velocity measurements are approximately 1% and 2%, respectively.

During acoustic velocity experiments, we do not saturate the samples with any pore fluid. Further, the pore lines are kept open during the experiment. Thus, given that the samples have previously been dried with respect to free water, the acoustic experiments can be considered as drained experiments in which any compaction-induced pore pressure is free to dissipate. Note, however, that the assumption of a drained experiment will break down for samples with significant isolated, i.e., disconnected, porosity. Any compaction-induced pore pressure accumulation will not be able to relax within these pores; however, this complication is inescapable in experimental analysis of confined shales.

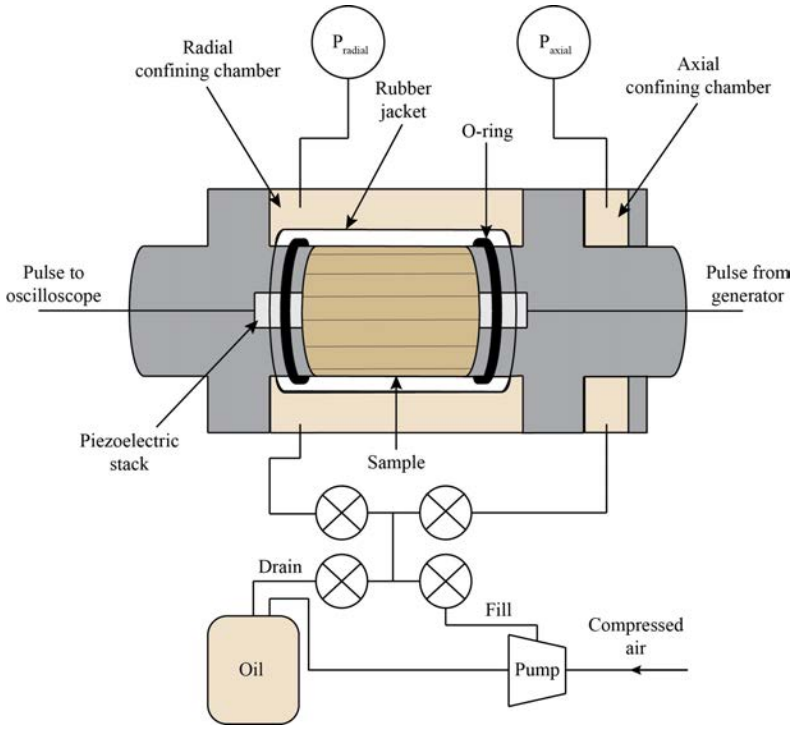

Figure 3.3: A schematic representation of the acoustic velocity setup.

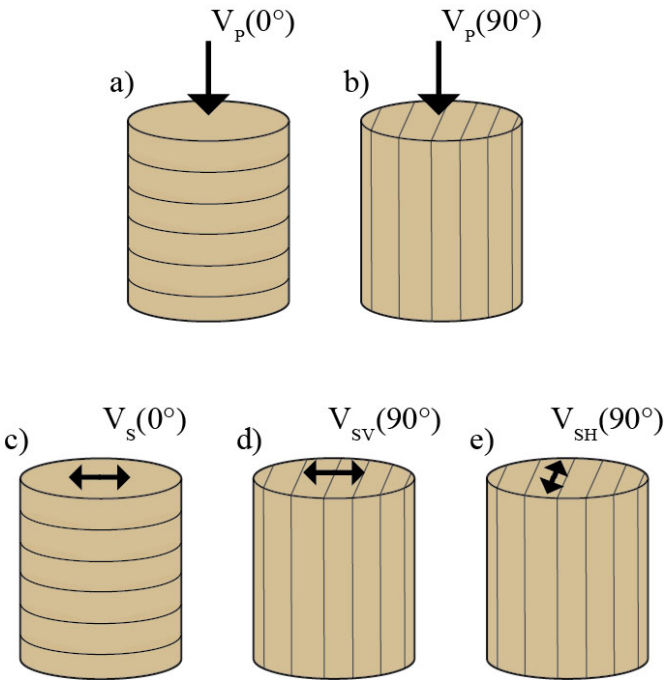

Figure 3.4: A schematic representation of the P- and S-wave phases recorded during acoustic velocity experiments: (a, c) vertically propagating P- and S-waves, (b) horizontally propagating P-wave, and two horizontally propagating S-waves – one polarized perpendicular to bedding (d) and the other polarized parallel to bedding (e).

All experiments discussed in this thesis are conducted with a 1 MHz compressional pulse and a 0.8 MHz shear pulse. The use of horizontal and vertical plugs combined with the geometry of the piezoelectric crystals in this system enables the characterization of 5 distinct phases: $V_P(0°)$, $V_P(90°)$, $V_S(0°)$, $V_{SH}(90°)$, $V_{SV}(90°)$ (Figure 3.4). The combination of acoustic velocity and bulk density measurements, ρ_B, enable the calculation of elastic moduli and Thomsen anisotropy parameters (Thomsen, 1986) as defined in Equations 3.2 - 3.7. Note that the bulk density as a function of confining pressure accounts for anisotropic mechanical compaction as discussed in Section 2.5.1. The error in calculated elastic anisotropy values is between 3% and 6%.

$$c_{11} = \rho_B \left(V_P(90°)\right)^2 \tag{3.2}$$

$$c_{33} = \rho_B \left(V_P(0°)\right)^2 \tag{3.3}$$

$$c_{66} = \rho_B \left(V_{SH}(90°)\right)^2 \tag{3.4}$$

$$c_{44} = \rho_B \left(V_S(0°)\right)^2 \tag{3.5}$$

$$\varepsilon = \frac{c_{11} - c_{33}}{2c_{33}} \tag{3.6}$$

$$\gamma = \frac{c_{66} - c_{44}}{2c_{44}} \tag{3.7}$$

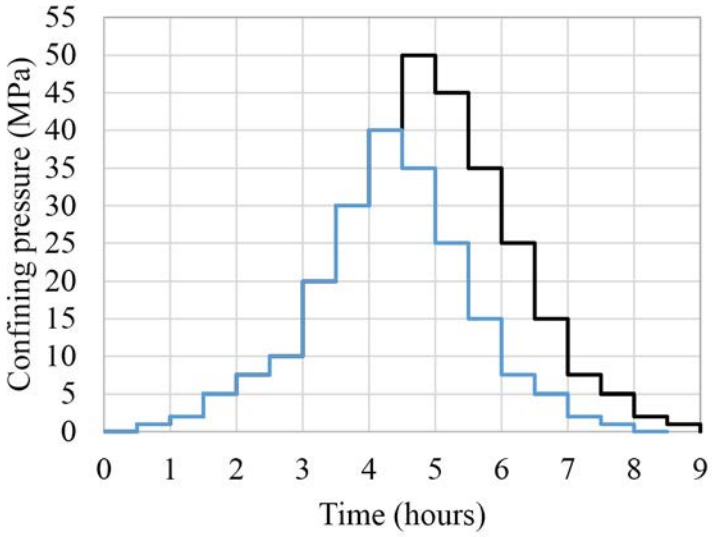

Figure 3.5: A schematic representation of the confining pressures at which waveform arrival times are measured as a function of experimental time. The blue curve identifies the pressure cycle for samples ENI1 and ENI2, whereas the black curve identifies the pressure cycle for all other samples

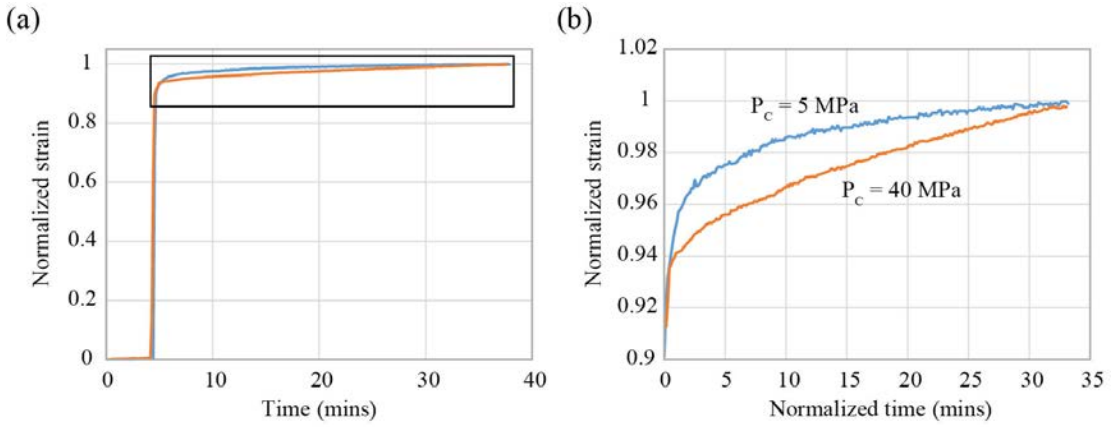

Figure 3.6: A representative example of the evolution of axial strain as a function of time after increasing the hydrostatic confining pressure from 2 MPa to 5 MPa (blue) and from 30 MPa to 40 MPa (orange). The axial strain is normalized to a maximum value of one. The entire change in axial strain is shown in (a), while (b) illustrates the change in the narrow region identified by the black box in (a). Additionally, the time axis in (b) has been normalized such that the hydrostatic confining pressure is increased at time zero.

The hydrostatic confining pressure loading and unloading protocol for each sample is documented as a function of experimental time in Figure 3.5. In our updated methodology, upon changing the confining pressure, the sample is left for 30 minutes to accommodate visco-elastic deformation. Figure 3.6 illustrates representative strain versus time curves for pressure steps from 2 MPa to 5 MPa and from 30 MPa to 40 MPa. It is clear that approximately 90% of the cumulative strain is purely elastic, and that within 5 minutes 95% of the total strain has been attained. Concurrently, we have noted that while the sample continues to strain for some time after the change in pressure (and will continue to strain beyond the 30 minute period), the acoustic velocity values for a hydrostatically confined sample change very little. P-wave velocities increase by no more than 60 m/s ($\leq$2%) over the first 10 minutes of visco-elastic compaction; however, further compaction has no resolvable effect on the velocity of the sample. Subsequently, we infer that allowing for visco-elastic compaction for 30 minutes results in sufficiently settled samples for high fidelity hydrostatically pressured acoustic velocity measurements.

3.3.2.3 Crystallographic Preferred Orientation (CPO) Analysis

High-energy synchrotron XRD experiments were conducted at beam-line 11-ID-C of the Advanced Photon Source (APS) at Argonne National Laboratory. The XRD measurements and processing of specific mineral alignment values were conducted for all samples by W. Kanitpanyacharoen (then, Stanford University), except the Barnett Shale samples which were measured and interpreted by Prof. H.-R. Wenk (University of California Berkeley) at the same facility.

A schematic of the experimental setup used at APS is provided in Figure 3.7. As discussed in Kanitpanyacharoen et al. (2015), an incident monochromatic X-ray beam with a wavelength and energy of 10.789 pm and 115 keV, respectively, is diffracted from a $\sim$10 mm^3 volume of sample while the sample is both translated and rotated about the horizontal axis. Translation

and rotation enable sufficient spatial and orientation sampling for statistical texture analysis. Diffraction patterns are recorded by a charged-couple device (CCD) detector a couple of meters from the sample. The diffraction patterns are then analyzed using the Rietveld method (Rietveld, 1969) via least-squares fitting of the experimental diffraction data to a calculated model. Rietveld refinement yields both volumetric fractions of the mineral phases and their respective crystallographic preferred orientation distribution functions (ODFs). The degree of CPO for each mineral parallel and perpendicular to the bedding plane can then be extracted from the ODF. A more comprehensive detailing of the analysis of diffraction patterns for crystallographic alignment can be found in Wenk et al. (1998, 2014).

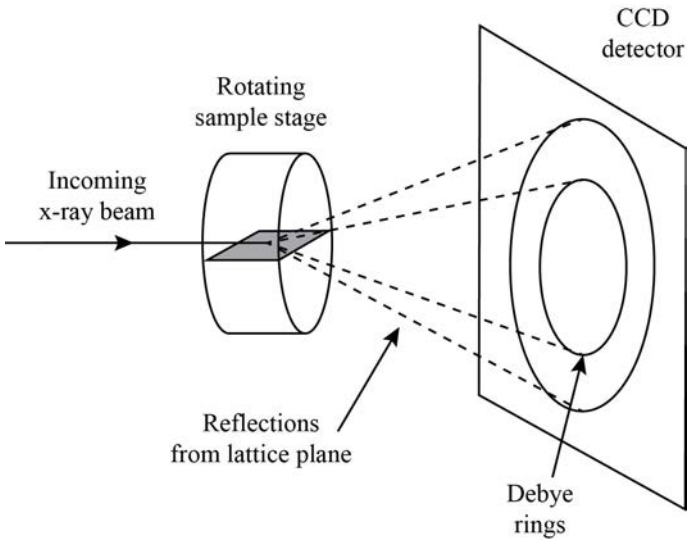

Figure 3.7: A schematic representation of the setup of the synchrotron diffraction experiment after Kanitpanyacharoen et al. (2011).

The degree of crystallographic alignment is reported in units of multiples of a random distribution (m.r.d.): this unit represents the likelihood of a crystal of a given mineral species being co-aligned with a given plane relative to the likelihood of that same alignment existing in a randomly oriented sample (Kocks et al., 2000). In addition to reporting the maximum and minimum CPO (the degree of alignment parallel and perpendicular to the bedding plane, respectively), I compute a sample average maximum CPO, CPO_{Avg}. This average value describes the degree of co-alignment with the bedding plane in the composite mineral frame and is defined in Equation 3.8 where χ is the set of mineral volume fractions and CPO is the set of maximum mineral alignments.

$$CPO_{Avg} = \chi \cdot CPO \tag{3.8}$$

In the computation of the average CPO, all unreported mineral phases, i.e., those that contribute less than 1-2 vol. % or exhibit too little alignment to be considered for texture analysis, are assumed to be randomly oriented ($CPO = 1$).

3.3.3 High-Resolution Imaging

3.3.3.1 Backscattered Electron Scanning Electron Microscopy (BSE-SEM)

The resolution of microscope techniques increases with increasing frequency of the radiation used to image the sample. In order to resolve the pertinent structures in microcrystalline shale samples, high-resolution imaging is required. SEM uses a beam of electrons to acquire information about the topology and elemental composition of a surface at a very high resolution (Egerton, 2005). Scanning electron microscopes generate an electron beam through the heating of a metallic filament, commonly tungsten. The beam is attracted toward the sample by an anode, focused by a magnetic lens, and mapped over the field of view by scanning coils. Electrons interacting with the sample, whether elastically backscattered or ejected from atomic orbitals in the sample surface (secondary electrons), are then recorded at detectors. A schematic of an SEM is documented in Figure 3.8, the entirety of this setup is kept under high vacuum during imaging.

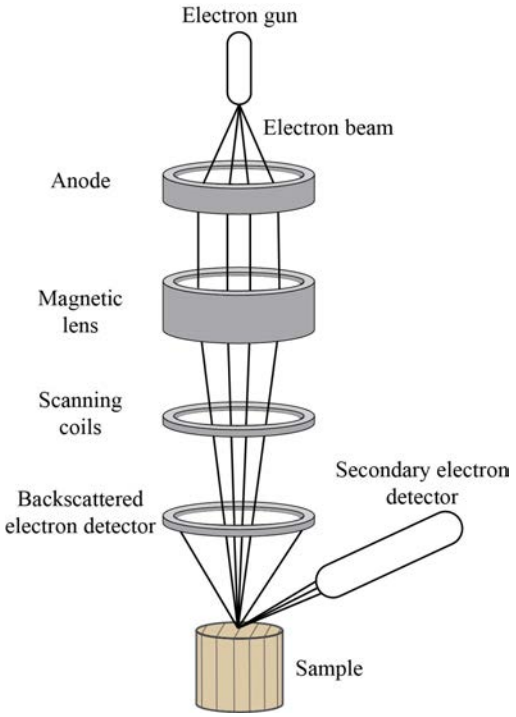

Figure 3.8: A schematic representation of the SEM setup after Ahmadov (2011).

The SEM images presented in this thesis were all collected at the Stanford Medical School Cell Science Imaging Facility (CSIF), using a Hitachi S-3400N variable pressure (VP)-SEM. All images were collected in backscattered electron mode (to document changes in mineral density across the image) under a 50-60 Pa vacuum with a beam voltage of 15.0 kV.

3.3.3.2 Confocal Laser Scanning Microscopy (CLSM)

Fluorescence microscopy techniques have long been used in the visualization and identification of organic macerals in coal and their degree of thermal alteration (e.g., Schochardt, 1943; Jacob, 1964; van Gizjel, 1967; Staplin, 1969). Recent studies have shown the utility of fluorescence microscopy, and in particular CLSM, to visualizing the three-dimensional distribution of organic matter (Nix and Feist-Burkhardt, 2003; Vanorio et al., 2008; Ahmadov et al., 2009), visualizing the morphology of individual organic macerals (Stasiuk, 1999), and quantifying the degree of thermal alteration (Teichmüller and Ottenjann, 1977; Teichmüller and Durand, 1983) in organic-rich shale. Given that fluorescence microscopy is non-destructive, the three-dimensional distribution of organic matter, and its evolution with thermal maturity, can be studied on samples being used for other rock physics or imaging methods, unlike, for instance, in FIB-SEM. This method is limited, however, by the thermal maturity of the samples. Above the oil death line (vitrinite reflectance ∼1.3%), the autofluorescence of organic matter is extinguished due to devolatilization of the residual organic matter (Han et al., 1993).

The advantage of CLSM over other fluorescence microscopy techniques lies in the principle of confocality, which is illustrated by a schematic CLSM system in Figure 3.9. A point source (laser) of light is focused on a diffraction-limited spot of a sample by a pinhole aperture, mirror, and objective lens (green rays in Figure 3.9). Within this spot, delocalized electrons in conjugate pi-bonds in the organic matter are excited and emit photons in all directions as the electrons return to a lower energy orbital. However, not only does the dichromatic mirror allow the transmission of only a set range of wavelengths of emitted light (red rays in Figure 3.9), but a second, conjugate/confocal pinhole aperture blocks emitted light from all but a specified focal plane in the sample (Robinson, 2001). Subsequently, the use of confocal pinholes blocks all out-of-focus background light that is typically present in traditionally acquired fluorescence images. Subsequently, crisp, high-resolution images of organic matter can be obtained in three-dimensions by stepping the focal plane into the sample.

The CLSM images documented in this thesis were all collected at the Stanford Medical School Cell Science Imaging Facility (CSIF), using a Zeiss LSM 510 microscope. Organic matter autofluorescence was detected in the blue, green, yellow/orange, and red domains, respectively. The excitation and detection parameters are given in Table 3.1. Volumes were sampled with a depth of up to 38 µm into the surface at two magnifications: (a) with a Plan Neo-fluar 10x air objective lens yielding a field of view of 0.9 x 0.9 mm and (b) with a Fluar 20x air objective lens yielding a field of view of 0.45 x 0.45 mm. All images were collected on horizontally cored plugs, so as to sample the organic content within multiple laminations.

3.3.3.3 X-Ray Microtomography (microCT) Imaging

X-ray microtomographic imaging uses much the same setup as the X-ray diffraction technique. In microCT a conic X-ray beam penetrates the sample and the transmitted X-rays are recorded on a detector as a two-dimensional representation of the sample. The sample is then

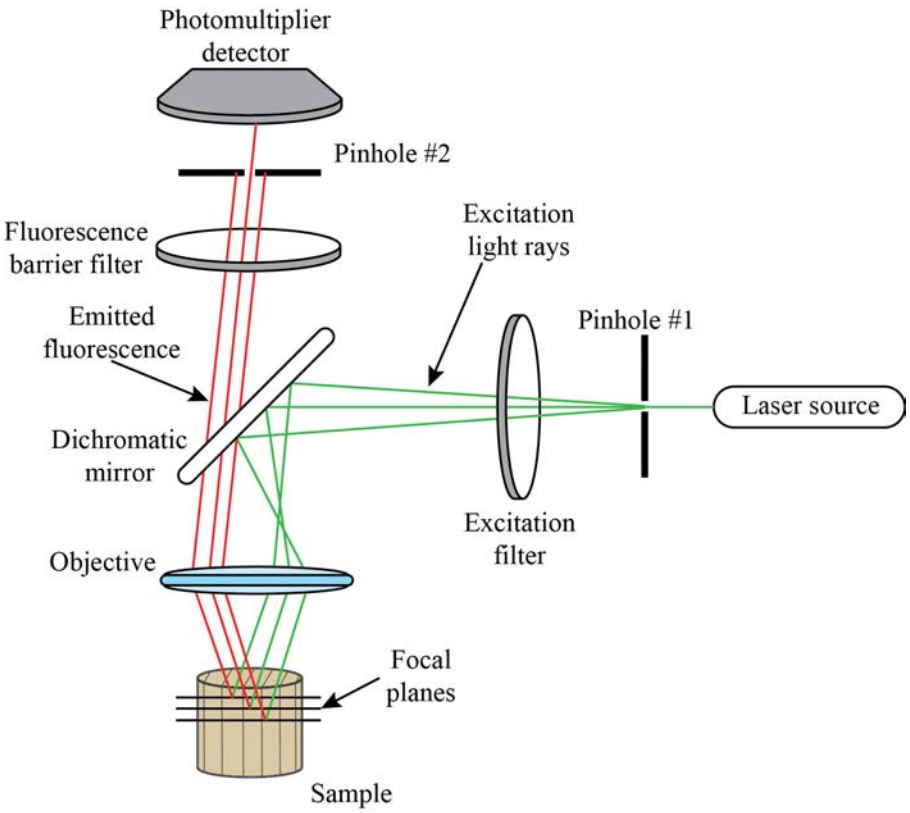

Figure 3.9: A schematic representation of the CLSM setup after Claxton et al. (2006).

rotated in steps such that a set of two-dimensional images or radiographs covering the entire sample is acquired. The two-dimensional slices are then digitally reconstructed as the three-dimensional sample where each voxel represents the attenuation coefficient of the material at that point. Subsequently, in grayscale, the brightest regions correspond to high-density minerals, e.g., pyrite, while the darkest regions are voids, and intermediate values correspond to the siliciclastic and/or calcareous mineral matrix. The resolution of the microCT volume is on the order of a few tens of microns. All microCT volumes in this thesis were imaged at Ingrain.

Table 3.1: The laser emission and photon detection parameters used in the acquisition of autofluorescence images by CLSM in the blue, green, yellow/orange, and red domains.

Color	Emission Wavelength (nm)	Detection Wavelengths (nm)	Laser
Blue	488	435-485	25 mW Ar
Green		500-550	
Yellow/Orange		565-615	
Red	543	>650	1 mW He-Ne

3.3.4 Confined, Closed Anhydrous Pyrolysis Experiments

The thermal maturation of organic matter is typically represented as a first-order reaction as a function of temperature and time (e.g., Pepper and Corvi, 1995). Given the extreme lengths of time required to thermally mature organic matter and produce hydrocarbons at representative in situ temperatures, it is necessary that laboratory methods of inducing thermal maturation be conducted at elevated temperatures. Pyrolysis, which involves the thermochemical decomposition of organic material in the absence of oxygen, is a common experimental method for imitating in situ thermal maturation. Pyrolysis experiments in the geochemical literature fall into three main groups: (a) hydrous pyrolysis, (b) open anhydrous pyrolysis, and (c) closed anhydrous pyrolysis (Lewan, 1994). Hydrous pyrolysis involves heating the rock sample in subcritical, liquid water, while in anhydrous pyrolysis no water is added to the reaction chamber. In open pyrolysis, the reaction products are swept (with an inert carrier gas or by thermal gradients) out of the thermally active regime, while in closed pyrolysis the products are trapped within the thermally active regime. Given the need in this work to pyrolyze whole core plugs and the difficulty associated with properly saturating those plugs, we perform anhydrous pyrolysis. Note, however, that these experiments are not truly anhydrous as there can be significant water bound in organic- and clay-rich shale that will be released into the pore space at high temperatures. The presence of this free water may be important to the oil-to-gas ratio generated during pyrolysis experiments (Lewan, 1994). In order to more physically mimic in situ thermal maturation, we both retain the products within the pore space (and a small volume of pore lines around the sample) and apply reservoir-scale, external confining pressure to the sample during pyrolysis. In this manner, we perform confined, closed anhydrous pyrolysis. To our knowledge, this methodology constitutes the first published attempt at pyrolyzing whole core plugs under applied confining pressure.

3.3.4.1 High Temperature-High Pressure (HTHP) Reactor Setup

Confined, closed anhydrous pyrolysis experiments are conducted in our laboratory using a purpose-built, high temperature-high pressure reactor (HTHP) designed and built in our laboratory (Clark and Vanorio, 2015). The HTHP system is an internally heated pressure vessel (autoclave) with a maximum pressure rating of 34.5 MPa (5,000 psi) at 510 °C (950 °F). The system consists of a 1 L volume, bolted closure reactor and is heated by a 200 W ceramic refractory heater. Due to the extreme temperatures used, in lieu of rubber tubing (melting point ∼180 °C), the sample is jacketed by annealed copper tubing to prevent the intrusion of confining fluid or loss of produced hydrocarbons. The rock sample is thermally isolated by cylindrical alumina spacers within the 26 mm inner diameter, 0.3 mm thick copper tube. The copper is flared and sealed around conical stainless steel end caps, which are connected to incoming and outgoing pore pressure lines. During experiments, the temperature is measured at a series of locations near the rock by a set of type-K thermocouples, one of which acts as the feedback sensor in a proportional-integral-derivative (PID) control loop. Further thermocouples are used to monitor the temperature throughout the vessel and pore lines. The HTHP is illustrated both schematically and photographically in Figures 3.10 and 3.11.

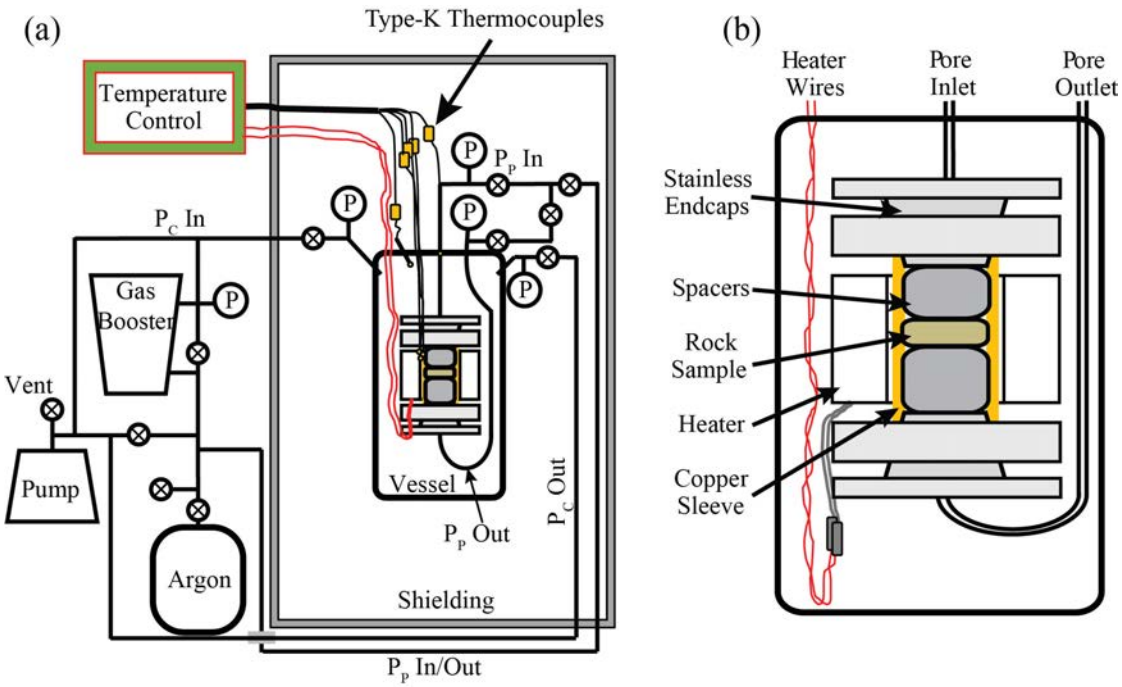

Figure 3.10: A schematic representation of HTHP system. (a) Entire system, including core holder, plumbing, and thermal wiring. (b) Enlarged schematic of the composition of the coreholder.

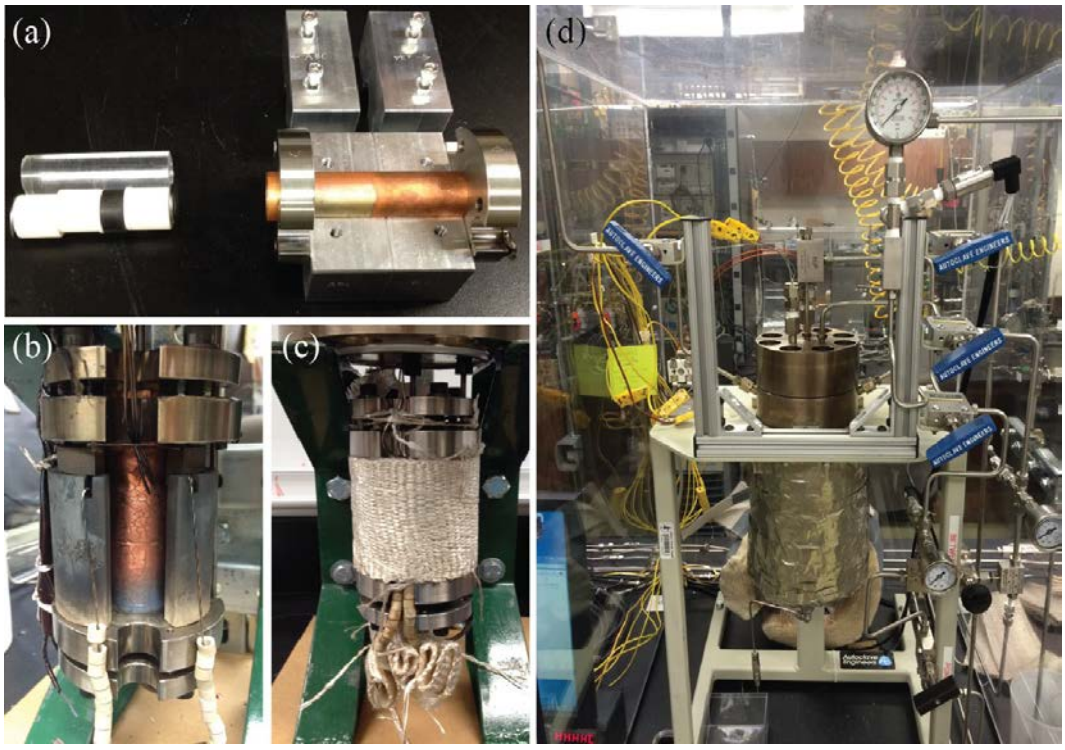

Figure 3.11: Photographic documentation of the HTHP system. (a) Coreholder assembly illustrating the copper jacket, steel flanges, sample, and alumina spacers (white cylinders). (b) Coreholder attached to top flange with heater surrounding copper jacket. (c) Coreholder fully assembled and insulated with silica tape. (d) Complete system within shielding.

3.3.4.2 Confined, Closed Anhydrous Pyrolysis Experimental Protocol

Before each experiment, the sample pore space, sealed in the coreholder, is placed under vacuum and flushed with argon gas to provide the anoxic environment required for kerogen pyrolysis rather than combustion. The confining space (which has also been vacuumed to remove oxygen) is then filled to an initial pressure ($P_1 \sim 10.6$ MPa) at room temperature with a gas booster. Once the desired confining pressure is attained, the pore space is charged with a small amount (∼0.5 MPa) of inert argon. Due to the high temperatures of the pyrolysis experiments, argon is used both to flush the sample and to apply the confining pressure within the vessel. The refractory heater is then switched on and increases the temperature at the feedback sensor by 2 °C/min to a specified intermediate temperature. This intermediate temperature is maintained for 6-10 minutes. The temperature is then ramped to the final pyrolysis temperature at 0.5 °C/min. The system is held at constant temperature for 72 hours. Due to thermal expansion of the confining argon, the confining pressure attains a greater value ($P_2 \sim 24$ MPa) upon heating. After 72 hours, the temperature is ramped down at 2 °C/min to 100 °C and then allowed to cool to room temperature over approximately 16 hours.

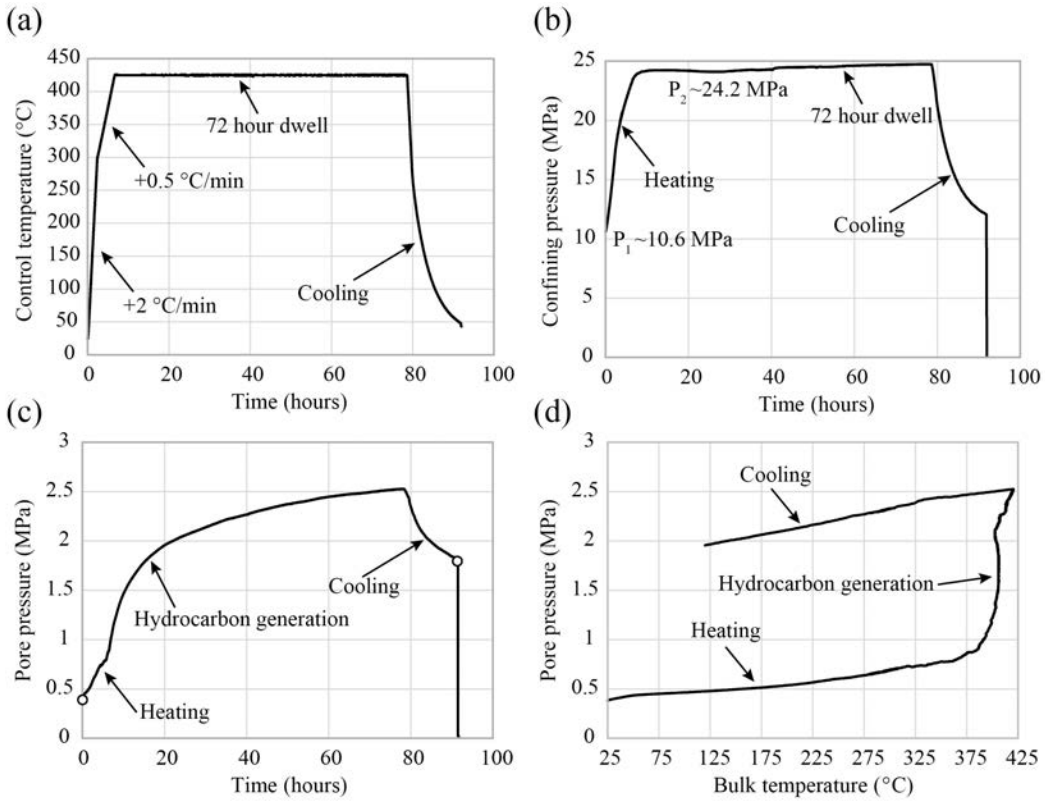

Figure 3.12: Temperature and pressure monitoring from an example confined pyrolysis experiment in the HTHP system. (a) Temperature of the PID control thermocouple as a function of time. (b) Confining pressure as a function of time. (c) Pore pressure as a function of time. (d) Pore pressure as a function of bulk temperature in the reactor (computed from the confining pressure using the ideal gas law). Regions of interest, e.g., heating, hydrocarbon generation, and cooling, are labeled. The white circles in (c) illustrate the non-thermal expansion-induced pore pressure accumulated during pyrolysis.

The pressure and temperature behavior as a function of time during a typical gas window pyrolysis experiment is shown in Figure 3.12. Thermal expansion of the argon in the pore space causes a clear increase in pore pressure during the labeled heating phase – at this time, the liberation and evaporation of bound water, if present, will also increase the pore pressure. During the 72 hour pyrolysis period, the pore pressure increases with time at a rate that decays as the experiment proceeds – this signal is attributed to the generation of hydrocarbons in the pore space. After cooling to room temperature, in this example, there is a 1.41 MPa increase in pore pressure attributable to generated reaction products, i.e., hydrocarbons. The ideal gas law indicates that this pressure increase corresponds to an increase by a factor of 4.8 in the moles of gas in the pore space, confirming hydrocarbon generation during pyrolysis.

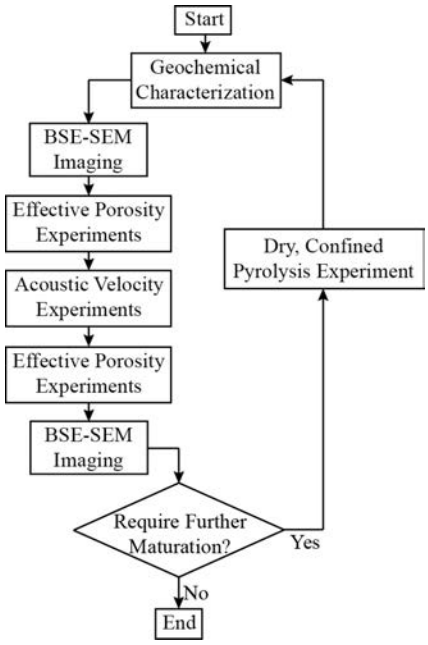

Figure 3.13: A schematic flowchart of the ordering of experimental methods and pyrolysis in the novel iterative shale rock physics methodology.

3.3.5 Iterative Implementation of the Shale Characterization Methodology

Organic-rich shale samples are matured to the oil window via pyrolysis at 360 °C-380 °C for 72 hours, while the gas window is reached via pyrolysis at 425 °C over the same period of time. The integration of pyrolysis experiments into the full workflow for velocity subsamples is documented in Figure 3.13. The baseline geochemistry, microstructure (via high-resolution imaging), porosity, and velocity of the samples are all characterized for samples *as received*. The porosity and microstructure are then re-characterized to account for any deformation that has occurred through loading/unloading during velocity experiments. The sample is then pyrolyzed and the characterization is repeated exactly as before. This process can be repeated as many times as necessary to sample the desired range of thermal maturities. Note, however, that the

mineralogy and degree of CPO are quantified only in the immature window of thermal maturity. A brief discussion of the omission of iterative mineralogy and CPO measurements is presented in Section 3.4.

3.4 Organic-Rich Shale Sample Set Characterization

In this section, I detail the (*as received*) physical condition, mineralogy, effective porosity, microstructure, and geochemistry of the large set of organic-rich shale samples studied in the next three chapters of this thesis. The sample labels, geographic provenance, depositional setting, and age are summarized in Table 3.2.

Table 3.2: Pertinent information relating to the provenance, age, and delivery of the samples studied in this thesis. Sample ENI1/ENI2 are cored approximately 1 meter apart in the same well. Samples ENI5/ENI6 are cored approximately 2 meters apart in the same well. Samples BW1/BW2 are cored approximately 40 meters apart in the same well. Hereafter, the samples labeled ENI will be commonly grouped as one set, the ENI Phase 1 samples.

Sample Label	Provenance	Depositional Setting	Age	Provided By
ENI1	Unreported	Marine	Devonian (Frasnian stage)	ENI S.p.A.
ENI2				
ENI4			Silurian	
ENI5			Devonian (Frasnian stage)	
ENI6				
Inorganic	Offshore Angola	Marine	Tertiary	Chevron
Green River	Green River Fm., outcrop	Lacustrine	Eocene	
BO	Barnett Fm., outcrop	Marine	Mississippian	ENI S.p.A.
BW1	Barnett Fm., well			
BW2				

3.4.1 Sample Preservation

All samples used in this study were provided pre-cored into horizontal and vertical plugs, and were then subsampled (as discussed in Section 3.3.1) and polished at Stanford. The preservation of the samples during transport to Stanford University varied by source. The samples provided by ENI S.p.A. were sealed in plastic wrap and aluminum foil and were largely dry upon arrival, while the samples provided by Chevron were preserved in plastic wrap and submerged in n-decane to prevent drying.

The coring and transportation of the samples had a varied effect on the physical condition of the samples as characterized in Figures 3.14 and 3.15. Note, that similar samples, e.g., samples from the same Barnett well have been binned with one representative plug shown, in Figures 3.14 and 3.15. The condition of the horizontal plugs is variable between samples and is not a simple function of preservation method. As can be seen in Figure 3.14, samples ENI1, ENI2, ENI4, BW1, and BW2 exhibit through-going fracturing subparallel to bedding, while the remaining samples show no visible fracturing or damage. The faces of the vertical plugs, in general, exhibit

less damage. The vertical Green River core has a perpendicular to bedding calcitic vein that traverses the sample. This vein is prone to fracturing as can be seen in Figure 3.15.d. The Barnett well image (Figure 3.15.f) is of a trim piece, thus the damage shown had no effect on any subsequent measurements. Due to the orientation of the vertical plugs, while not visible in Figure 3.15, there exists through-going, subparallel to bedding fractures in the vertical plugs of samples ENI4, ENI6, and BW1. The sample preparation-induced fractures are expected to have little effect on porosity, due to their low aspect ratio/volume; however, they may have a significant effect on the elastic properties of the samples and are, thus, intrinsically included in all interpretations.

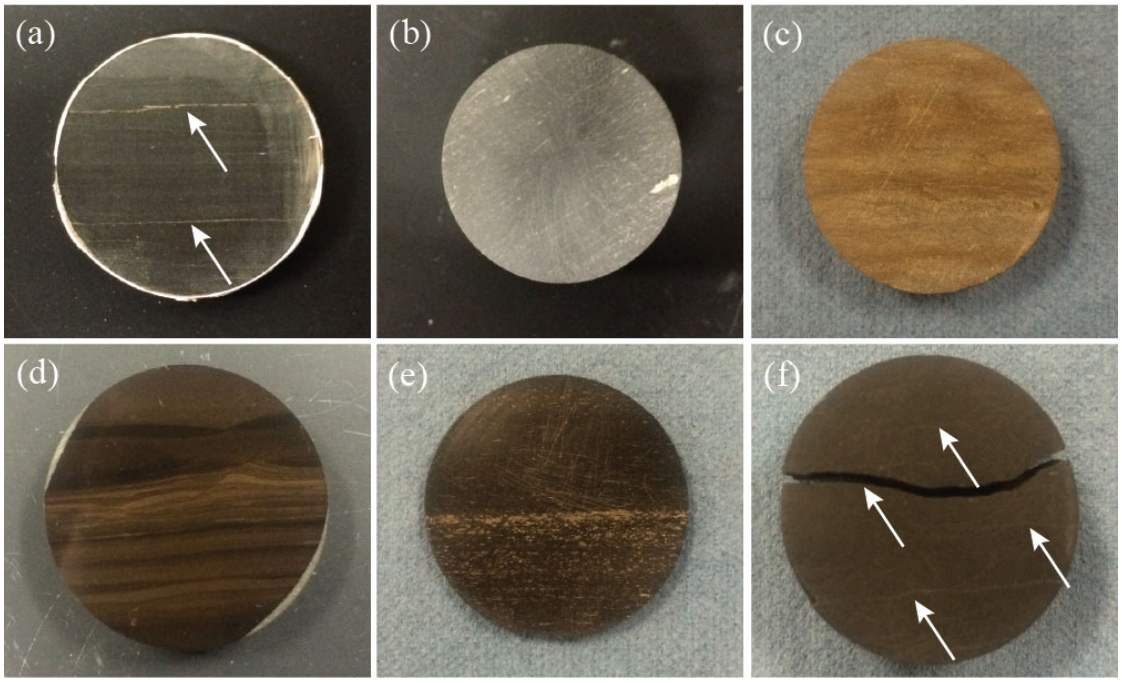

Figure 3.14: Photographic documentation of the condition of a representative face parallel to bedding for each sample – note that similar samples have been binned such that one image is shown as representative, e.g., Barnett samples from the same well. (a) ENI1. (b) ENI5. (c) Inorganic sample. (d) Green River sample (polished by S. Alsinan). (e) BO. (f) BW2. Through-going sample fractures are indicated by white arrows. Each plug is approximately one inch in diameter.

3.4.2 Mineralogy and Effective Porosity

The mineralogy, as derived from XRD experiments, is reported in Figure 3.16. The weight percent values in Figure 3.16 are divided into the relative fraction of quartz, clays, and major carbonates (calcite + dolomite), with all auxiliary phases listed as 'Other'. This is done in order to more clearly represent variability in the primary mineralogy of each sample. The complete mineralogy for each sample is listed in Appendix A. Furthermore, the samples have been binned as in Figures 3.14 and 3.15 and the standard deviation within a bin is noted on the pie chart. The greater range of values reported for the Barnett well samples is a result of one plug (vertical BW2) being 20% more quartz-rich (at the expense of carbonates) than the other three plugs.

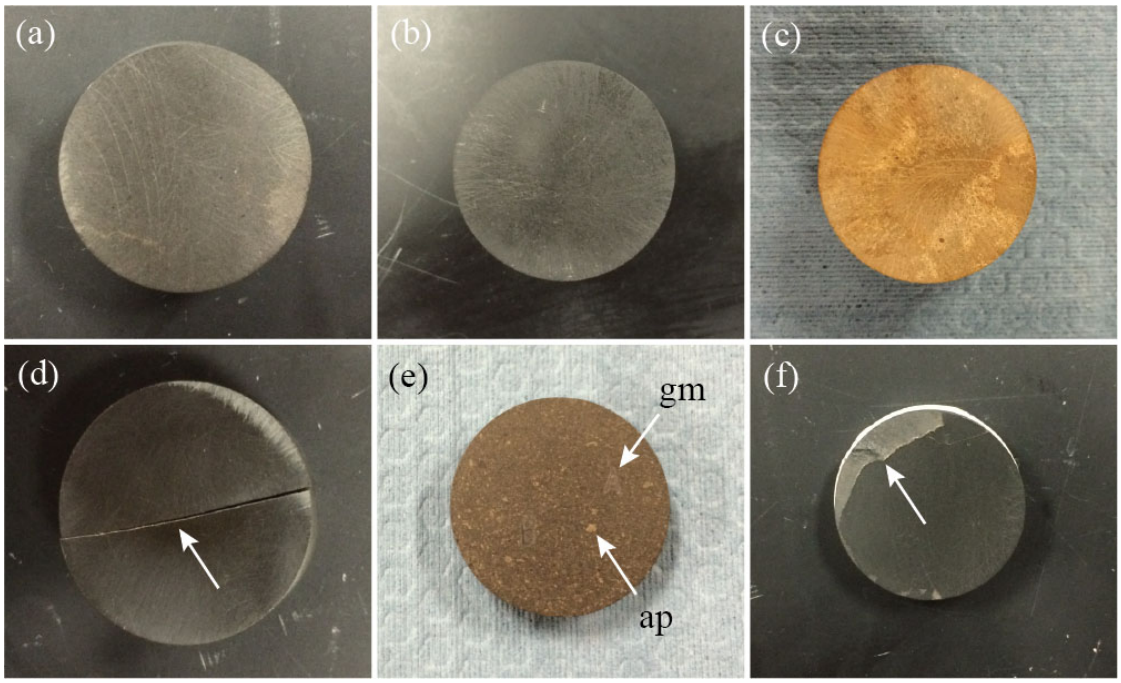

Figure 3.15: Photographic documentation of the condition of a representative face perpendicular to bedding for each sample – note that similar samples have been binned such that one image is shown as representative, e.g., Barnett samples from the same well. (a) ENI2. (b) ENI5. (c) Inorganic sample. (d) Green River sample. (e) BO. (f) BW2. Through-going sample fractures are indicated by white arrows. The through-going fracture coinciding with a calcitic vein in (d), graphite marking (gm) and visible apatite grains (ap) in (e), and roughness in core trimming (f) are all indicated by white arrows. Each plug is approximately one inch in diameter.

As can be seen in Figure 3.16, there is a wide range of mineralogies represented in this dataset. The ENI Phase 1 and Inorganic samples are more clay-rich (>50% clay). The Green River sample is a more complex mixture, primarily composed of carbonates with quartz, albite, and analcime but relatively little clay content. While the Barnett samples are predominantly siliciclastic mixtures of quartz and clay, although with a more considerable carbonate content in the well-derived samples at the expense of clay.

The bulk density and helium porosimetry-derived effective porosity and grain density values are reported for each velocity subsample in Table 3.3. There is a wide range in effective porosity values across the sample set, from less than 1% to almost 18%. The largest porosity values (>10%) are exhibited by outcrop Barnett Shale samples and the Inorganic sample. Meanwhile ENI1, ENI2, ENI4, and the Green River samples exhibit the lowest porosity – less than 5% for all, but only ∼1% for the Green River. The grain density values exhibit a bimodal behavior throughout the sample set. One group of plugs (ENI5,6, BW1,2, and Inorganic) have grain density values between 2.65 g/cc and 2.79 g/cc, which may be considered appropriate given the densities of the constitutive minerals. The second group is characterized by grain density values as low as 2.25 g/cc to 2.40 g/cc. The apparently anomalous nature of these grain density values is discussed in Section 3.5.2.

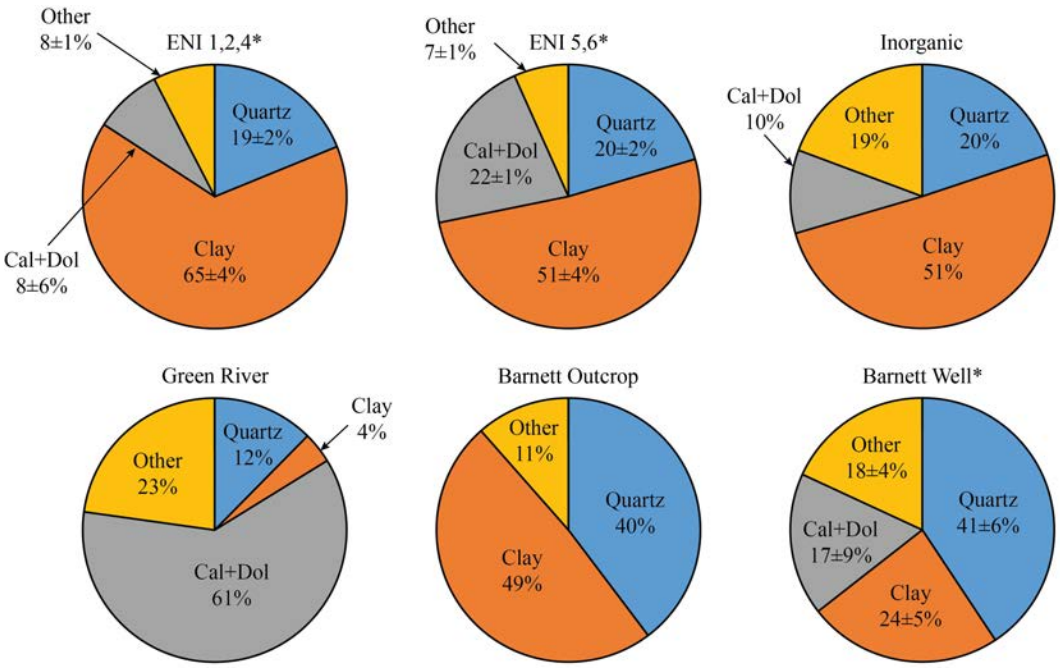

Figure 3.16: The mineralogical composition by weight of each sample. Note, auxiliary mineralogies, e.g., feldspar and pyrite, are binned as 'Other'. An asterisk (∗) indicates that samples have been averaged within a bin of like samples, e.g., Barnett samples from the same well.

Table 3.4 documents the standard deviation in effective porosity and grain density measurements across all four subsamples (velocity and permeability) derived from each sample. Additionally, the range of grain density values is given as a percentage of the mean value to more clearly represent the significance of the variability between subsamples. Vernik and Landis (1996) report a tolerance of 2% variability in grain density when considering multiple plugs as one sample. Applying this criterion to our samples, we note that the variability in grain density across the subsamples is appropriate for their consideration as a single sample.

3.4.3 Microstructure

In addition to a wide range of mineralogies, the microstructure of the samples shows a high degree of variability (Figure 3.17). The clay-rich matrix present in all but the Green River sample is generally too microcrystalline to resolve at a platelet or booklet-scale in these images. The alignment of organic bodies and microcracks, however, gives a strong indication both of bedding and of the predominant clay matrix alignment. Samples ENI2, Inorganic, and BO exhibit significant quantities of auxiliary minerals (calcite, quartz, and apatite, respectively) as a dispersed granular phase, while many of the calcite grains in ENI5 and BW2 are deformed into co-alignment with the bedding plane. In each of these samples (all but Green River), the organic matter, where visible, is present as a lenticular phase that is co-aligned with bedding. In all instances, pyrite is dispersed throughout the sample relatively uniformly, although with larger accumulations in BW2 and a clear framboid in BO.

Table 3.3: The helium porosimetry-derived porosity and grain density and the calculated bulk density for the velocity subsamples of each sample. The plug orientations are indicated by a V (vertically cored) and an H (horizontally cored).

Sample	Orientation	Effective Porosity (%)	Grain Density (g/cc)	Bulk Density (g/cc)
ENI1	V	2.40±0.50	2.380±0.012	2.322±0.004
	H	2.02±0.44	2.373±0.004	2.325±0.007
ENI2	V	1.96±0.47	2.407±0.011	2.359±0.004
	H	1.72±0.48	2.406±0.004	2.366±0.009
ENI4	V	3.74±0.43	2.559±0.011	2.463±0.002
	H	4.92±3.40	2.525±0.004	2.402±0.064
ENI5	V	7.64±0.28	2.656±0.005	2.454±0.004
	H	7.62±0.45	2.649±0.004	2.447±0.008
ENI6	V	10.70±0.50	2.750±0.015	2.456±0.003
	H	5.60±0.49	2.709±0.004	2.558±0.009
Inorganic	V	17.47±0.31	2.794±0.006	2.305±0.005
	H	17.55±0.44	2.787±0.005	2.298±0.008
Green River	V	0.53±0.48	2.259±0.007	2.246±0.003
	H	1.28±0.32	2.291±0.005	2.262±0.006
BO	V	13.23±0.36	2.317±0.008	2.012±0.004
	H	12.72±0.49	2.304±0.008	2.011±0.007
BW1	V	6.34±0.94	2.678±0.009	2.509±0.023
	H	5.29±0.68	2.649±0.007	2.509±0.016
BW2	V	7.10±0.91	2.630±0.013	2.443±0.018
	H	5.39±0.76	2.718±0.012	2.571±0.016

Table 3.4: The standard deviation in effective porosity and grain density measurements, derived from helium porosimetry experiments, for the two velocity and two permeability subsamples that compose each sample. The second grain density column gives the magnitude of the standard deviation relative to the mean in percent.

Sample	Standard Deviation in Measurements		
	Effective Porosity (p.u.)	Grain Density (g/cc)	Grain Density (%)
ENI1	0.88	0.006	0.24
ENI2	1.51	0.009	0.38
ENI4	0.87	0.022	0.86
ENI5	0.41	0.018	0.68
ENI6	2.21	0.023	0.83
Inorganic	0.40	0.018	0.66
Green River	0.57	0.016	0.68
BO	0.46	0.039	1.72
BW1	0.75	0.012	0.47
BW2	1.33	0.048	1.81

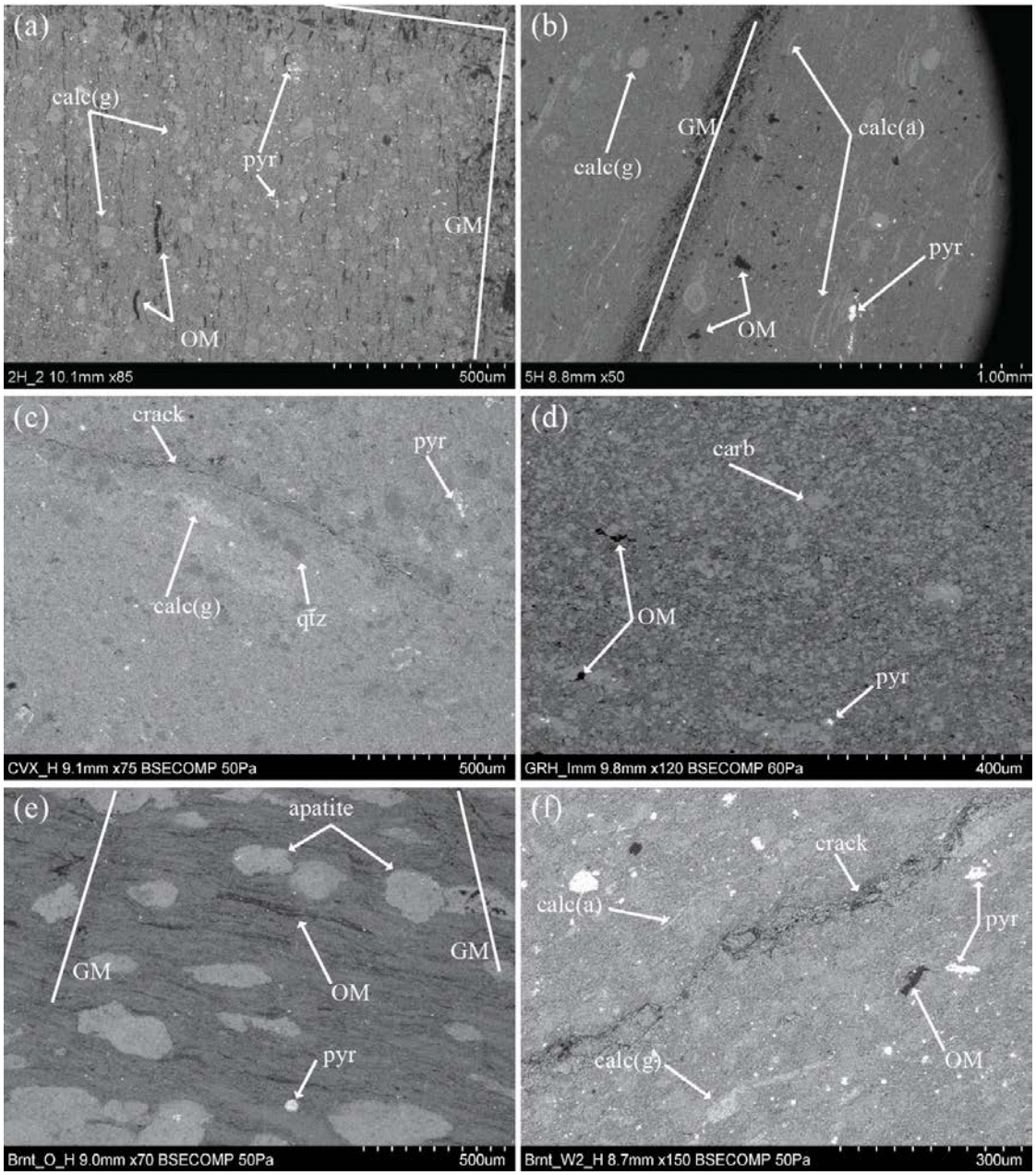

Figure 3.17: Representative SEM images of the microstructure of the samples within each bin used in Figure 3.14. (a) ENI2. (b) ENI5. (c) Inorganic. (d) Green River. (e) BO. (f) BW2. Identified features include cracks, organic matter (OM), aligned and granular calcite (calc(a) and calc(g), respectively), carbonate (carb), quartz (qtz) pyrite (pyr), and graphite markings used to recover image locations post-pyrolysis (GM).

The Green River sample is thoroughly anomalous microstructurally. The provided Green River sample is not a shale, but is more properly identified as an argillaceous dolomicrite, and, as such, the microstructure is reminiscent of classic granular media, albeit microcrystalline with little to no visible porosity. The organic matter in the Green River sample shows no preferential alignment. Rather the organic matter occurs as a pore-filling phase reminiscent of a heavy oil sand.

Microstructural observations of bulk mineral alignment are reinforced by CPO values of crystallographic co-alignment with the bedding plane (Table 3.5). The clay content in each sample exhibits preferential alignment with bedding – being 2 to 14 times more likely to be aligned with bedding than in a randomly oriented sample. The quartzose and calcitic components, however, generally exhibit a random texture. Exceptions to this are ENI1 and ENI2 which exhibit a weak alignment of quartz (80% less aligned than the average clay alignment), and ENI5 and ENI6 in which the greatest degree of alignment is shown by calcite and the alignment of quartz is of a similar magnitude to the illite-smectite phase. Minimum CPO values (available for all but the ENI Phase 1 samples) range from 0.2 to 0.7. These values indicate that, despite the strong maximum degree of CPO, a significant portion of the microcrystalline clay matrix is randomly oriented.

Table 3.5: CPO data as calculated from X-ray diffraction experiments. Values of maximum and minimum (where available), reported as max/min, (001) concentrations are given in units of multiples of a random distribution (m.r.d.). Dashes indicate the quantity or alignment of a mineral is too small to be considered for texture analysis. Reported minerals are abbreviated as illite-mica (Ill-mca), illite-smectite (Ill-sme), chlorite (Chl), kaolinite (Kln), quartz (Qtz), and calcite (Cal). The average maximum CPO for each sample is denoted as (Avg).

Sample	Ill-mca	Ill-sme	Chl	Kln	Qtz	Cal	Avg
ENI1	14.3	6.8	4.7	10.4	1.8	-	7.45
ENI2	11.1	6.5	4.8	7.1	1.7	-	5.33
ENI4	10.5	4.6	4.8	5.5	-	-	4.46
ENI5	4.3	2.7	3.4	3.4	2.4	4.9	3.35
ENI6	6.6	2.6	4.6	5.0	2.2	8.7	4.37
Inorganic	2.6/0.6	1.7/0.7	-	2.1/0.6	-	-	1.58
Green River	2.9/0.7	-	-	-	-	-	1.07
BO	6.6/0.3	-	6.0/0.2	-	-	-	3.98
BW1	6.8/0.2	3.3/0.3	-	-	-	-	2.69
BW2	3.8/0.3	-	-	-	-	-	1.59

The volume averaged CPO value for each sample documents a wide range of textures across the samples. The Green River sample, which is only 4% by volume clay, is effectively a randomly oriented sample (CPO = 1.07). While the Inorganic and well-derived Barnett samples are the most weakly aligned samples with greater than 20% clay by volume, with average CPO values less than 2.70. By comparison, the outcrop-derived Barnett sample is almost a factor of two more strongly aligned with the bedding plane (CPO $\sim$ 4). The ENI Phase 1 samples, particularly the >60% clay ENI1, ENI2, and ENI4, are the most strongly aligned samples. For instance, any given mineral crystal in ENI1 is 7.5 times more likely to be aligned with bedding than in a randomly textured sample. Subsequently, the samples collected range from randomly oriented, dolomicritic to poorly-to-intermediately textured, clay and quartz-rich to strongly textured, clay-rich samples.

3.4.4 Geochemistry

The geochemical properties of each sample (before any induced maturation) were quantified by RockEval analysis at an external service laboratory and are reported in Table 3.6. Note that in some samples, RockEval analysis can struggle to identify an appropriate value for T_{MAX} (taken as the thermal maturity indicator) resulting in values less than 400 °C. These anomalous values result from the emission of negligible quantities of hydrocarbons from extremely post-mature samples. Instances of this failure are identified in Table 3.6 by a double asterisk (**) and the anomalous value reported by the analysis can be considered as ∼500 °C (the maximum value in the test) for plotting purposes. Furthermore, extremely low hydrogen index (HI) and hydrocarbon potential (HP) values (<2 mg of hydrocarbons per gram of dry rock) confirm the post-maturity of those samples. Due to the destructive nature of RockEval analysis, the geochemistry of each subsample cannot be characterized while preserving the sample for further, e.g., acoustic or permeability, analysis. Subsequently, the geochemical properties are assumed to be homogeneous throughout the original plug – the validity of this assumption is addressed in Appendix C.

Table 3.6: Geochemical properties of each sample as characterized by RockEval analysis. The geochemical properties reported include total organic carbon (TOC), temperature of maximum hydrocarbon expulsion (T_{MAX}), free, retained hydrocarbons (S_1) and thermally producible hydrocarbons (S_2) measured in mg of hydrocarbons per gram of dry rock, hydrogen index (HI) and oxygen index (OI) measured in mg of hydrocarbons per gram of TOC, and hydrocarbon potential (HP) measured in mg of hydrocarbons per gram of dry rock. Double asterisks (**) in the T_{MAX} column indicate unreliable values due to low S_2 values.

Sample	TOC (wt. %)	T_{MAX} (°C)	S_1 (mg/g)	S_2 (mg/g)	HI (mg/g)	OI (mg/g)	HP (mg/g)
ENI1	7.49	427	4.96	39.80	532	16	44.76
ENI2	7.14	436	4.97	42.59	596	10	47.56
ENI4	4.34	441	2.93	14.61	337	10	17.54
ENI5	4.13	365**	0.63	0.86	21	13	1.49
ENI6	4.78	353**	0.54	0.23	5	9	0.77
Inorganic	0.58	426	0.06	0.61	105	448	0.67
Green River	9.14	419	4.8	71.23	780	10	76.03
BO	11.67	418	2.32	55.98	480	9	58.30
BW1	2.72	392**	0.63	0.47	17	17	1.10
BW2	2.63	496	0.38	0.32	12	16	0.70

As can be seen in Table 3.6, the sample set primarily separates into two groups based on T_{MAX} values: immature samples ($T_{MAX} < 435$ °C) and post-mature, gas window samples ($T_{MAX} > 470$ °C; Peters and Cassa, 1994). A third group, consisting of samples ENI2 and ENI4, exhibit early oil window levels of thermal maturity. As is expected, the thermal maturity as indicated by T_{MAX} shows a strong correlation with the hydrocarbon potential of the samples (Figure 3.18), where the hydrocarbon potential (defined as in Equation 3.9) is the quantity of ultimately producible hydrocarbons given exposure to high temperature for a sufficient period of time. Simply, the correlation in Figure 3.18 indicates that at lower levels of thermal maturity there remain greater quantities of producible hydrocarbons, while post-mature samples contain very little remaining hydrocarbons.

$$HP = S_1 + S_2 \tag{3.9}$$

One clear exception to the HP-T_{MAX} trend in Figure 3.18 is the Inorganic sample. While the Inorganic sample is technically organic-poor (containing 0.58 wt. % TOC), that organic matter contains very little hydrocarbon potential (0.67 mg of hydrocarbons per gram of dry rock) and, even when accounting for the very low TOC, has approximately 20% the hydrocarbons per gram of TOC (HI) as compared to the other immature samples. Coupling this dearth of hydrocarbon potential with the extreme oxygen index value (OI = 448) indicates that the Inorganic sample is either a very low potential Type III, gas-prone source rock or a largely inert, Type IV shale.

One final important point is to draw attention to the outcrop Barnett and Green River samples that will be pyrolyzed and iteratively studied in Chapters 5 and 6. Both samples contain approximately 10% organic carbon by weight and excellent petroleum potential ($S_2 > 20$ mg/g; Peters and Cassa, 1994). They differ in that the marine Barnett Shale contains predominantly Type II kerogen ($300 < HI < 600$), while the lacustrine Green River sample contains Type I kerogen ($HI > 600$). As a result of this difference, the Green River sample has significantly greater hydrocarbon potential than the Barnett Shale (76 mg/g and 58 mg/g, respectively).

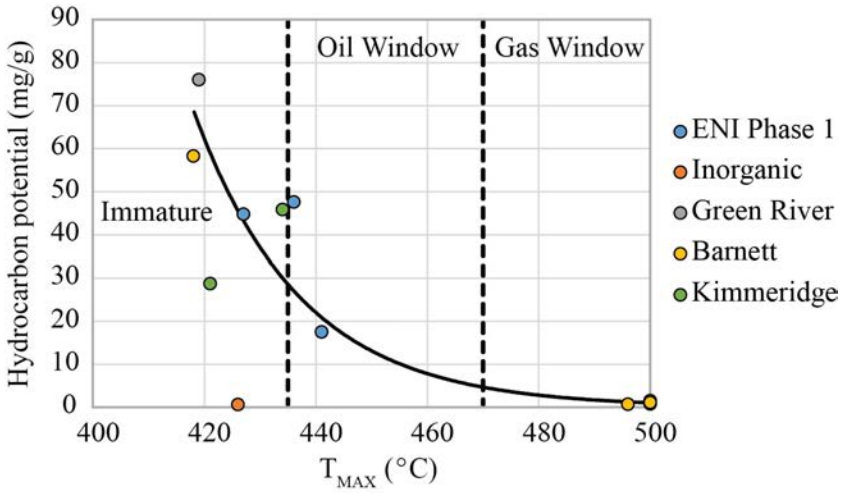

Figure 3.18: The hydrocarbon potential (HP) of each sample as a function of the RockEval parameter, T_{MAX}. The windows of thermal maturity are added to aid interpretation. The Kimmeridge samples from Chapter 2 have been added to complete the discussion, and an exponential trend ($R^2 = 0.96$) has been fit (omitting the Inorganic sample) to better demonstrate the relationship between HP and T_{MAX}.

3.5 Discussion

We have assembled an extensive set of samples that spans a broad range of mineralogies, degrees of mineral alignment, microstructures, and thermal maturities. Furthermore, we have developed a comprehensive methodology for the characterization of elastic anisotropy in organic-rich shale at a range of scales from microns to centimeters. In this section, I discuss three

issues highlighted during characterization of the sample set. These issues are: the implications of using helium porosimetry to determine porosity in organic-rich shale, a common misconception regarding the correlation of the intrinsic anisotropy of shale with clay content, and the effect of pyrolysis on mineralogy and CPO.

3.5.1 The Systematic Underestimation of Porosity in Organic-Rich Shale

It is important to consider that during porosimetry experiments the probe gas can only penetrate the porosity connected to the exterior of the sample (the effective porosity). Subsequently, disconnected porosity (the remainder of the total porosity) is considered a solid/grain component, which results in the overestimation of the grain volume and underestimation of the porosity and grain density. This is a problem both from the perspective of accurate sample characterization and for attempting to monitor porosity as a function of confining pressure during acoustic experiments. Recall that the immature Woodford Shale plugs in Chapter 2 had negative calculated porosities at confining pressures greater than approximately 40 MPa. Under the assumption that all compaction is accommodated by pore closure, rather than mineral compaction, the (even partial) compaction of unaccounted for porosity will result in an overestimation of the decrease in measured porosity with pressure. If the compaction of unaccounted for porosity is great enough or the effective porosity is low enough (as in Chapter 2), this effect can result in negative apparent porosities.

There is, however, a complicating factor in the assumption that all compaction is accommodated by pore closure. Organic matter, whether as solid kerogen or as semi-solid bitumen, has a bulk modulus of between 2.5 GPa (room temperature bitumen; Wolf, 2010) and 2.9-10 GPa (kerogen; Carmichael, 1989; Ahmadov et al., 2009), potentially quite close to the bulk modulus of water (2.25 GPa; Batzle and Wang, 1992). Given the compressibility of organic matter relative to both fluid and mineral values (e.g., quartz = 36.6 GPa; Simmons, 1965), the organic matter may accommodate some of the measured sample compaction. Attributing organic compaction to a deforming pore space would again serve to overestimate the porosity change with pressure. However, assuming an average bulk modulus, K_{OM}, for organic matter of 5 GPa, the *volumetric* strain, $\varepsilon_{\alpha\alpha}$, of that organic matter under a confining hydrostatic load, σ_0, of 50 MPa is 1% as calculated by Equation 3.10 (Mavko et al., 2009):

$$\varepsilon_{\alpha\alpha} = \frac{\sigma_0}{K_{OM}} \times 100. \tag{3.10}$$

Assuming that immature organic matter, a largely randomly oriented complex biopolymer (Vandenbroucke, 2003), deforms approximately isotropically, the axial strain would then be approximately 0.3%. The average axial strain calculated during acoustic experiments is 2.4±0.6%. Subsequently, kerogen compaction would appear to be a secondary factor.

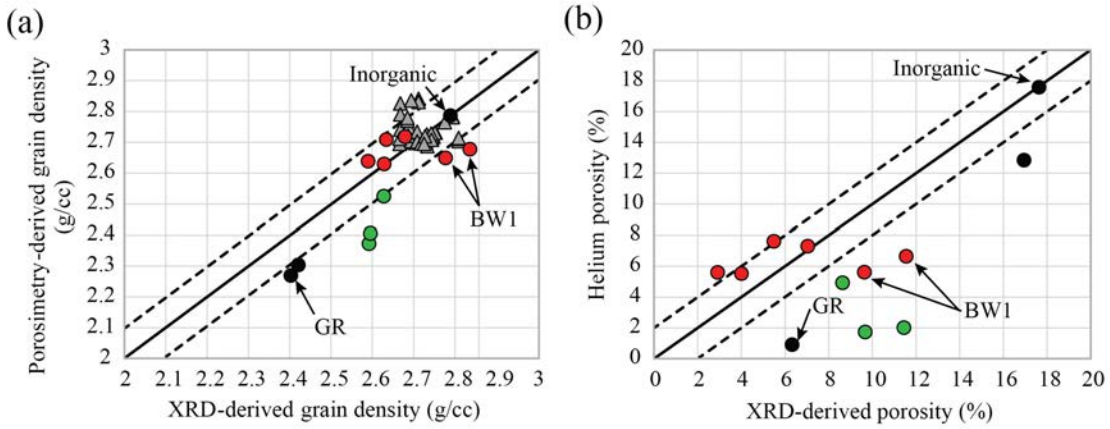

Figure 3.19: A comparison of helium porosimetry and X-ray diffraction-derived physical rock properties, colored by thermal maturity: immature (black), oil window (green), and gas window (red). (a) Grain density. (b) Porosity. All grey triangles are carbonate data provided from Clark et al. (in review). In each panel, the solid black line indicates agreement between the two measurements, while the dashed line indicates error in excess of ±0.1 g/cc and ±2%, respectively.

In Figure 3.19, the helium porosimetry-derived grain density and porosity are plotted as a function of the XRD-derived grain density and porosity, respectively. The calculation of grain density and porosity from the XRD-derived mineralogy is provided in Appendix B. Comparing the expected sample grain volume derived from the constitutive mineralogy to the known sample bulk volume enables the extraction of the total porosity, assuming mineralogy is homogeneous between subsamples (calculated values are listed in Table 3.7). As can be seen in Figure 3.19, the deviation between grain density and, in particular, porosity values from porosimetry and mineralogical calculation is greatest in immature to oil window maturity organic-rich shale samples. Subsequently, we attribute this deviation to the presence of low maturity, low porosity organic matter and retained, produced liquid hydrocarbons. Indeed, TOC and retained hydrocarbon values, averaged for each window of thermal maturity (Table 3.8), indicate that TOC is greatest in immature samples and that considerably more hydrocarbons are retained in the pore space of the immature and oil window samples. Furthermore, we know from high-resolution imaging studies that the greater organic content of the immature and oil window samples tends to be less porous than that in the gas window (e.g., Loucks et al., 2009; Walls and Sinclair, 2011; Curtis et al., 2012). Exceptions to this behavior are the immature inorganic sample (in which the agreement is strong) and the post-mature BW1 sample (in which porosimetry underestimates grain density and porosity). The strong agreement for the inorganic sample is quite sensible as there is very little organic matter (TOC = 0.58%) or retained hydrocarbons (S_1 = 0.06 mg/g) to block pore throats. The poor estimation of BW1 is attributable to the high XRD-derived grain density value (0.1 g/cc greater than nearby BW2), which, in turn, results from anomalously high pyrite and calcite contents (7% and 19%, respectively). Sample BW1 raises an important point, while porosimetry may underestimate porosity, XRD-derived values suffer from mineralogical heterogeneity between the subsample used for XRD analysis and the subsample being characterized for use in, e.g., acoustic experiments. Subsequently, both values, when available, should be considered in characterization of a given sample.

Table 3.7: The XRD-derived porosity and grain density values for comparison to experimental values in Table 3.3. The calculation of porosity and grain density from XRD-derived mineralogies is discussed in Appendix B.

Sample	XRD-Derived	
	Porosity (%)	Grain Density (g/cc)
ENI1	11.44	2.592
ENI2	9.67	2.595
ENI4	8.63	2.628
ENI5	5.48	2.590
ENI6	2.91	2.634
Inorganic	17.63	2.789
Green River	6.32	2.403
BO	16.94	2.421
BW1	9.63	2.777
BW2	4.00	2.679

Table 3.8: The average total organic carbon (TOC) and retained hydrocarbons (S_1) by window of thermal maturity. The anomalous, inorganic sample is omitted from the immature window average.

Window of Maturity	TOC (wt. %)	S_1 (mg/g)
Immature	8.58	4.09
Oil Window	7.56	10.42
Gas Window	4.32	2.92

The attribution of the deviation between the two methods to pore throat blockage by organics, hydrocarbons, or other fluids is reinforced by the inclusion of non-shale mineralogies in Figure 3.19. The set of carbonate samples (grey triangles; Clark and Vanorio, 2015, in review), which are inorganic and are not saturated with hydrocarbons, exhibit more consistent agreement between the two methodologies. Any deviation from this agreement may be attributed to (a) micrite or cement blockage of pores or (b) the aforementioned mineralogical heterogeneity between subsamples.

It is important to note that this effect will be magnified for probe gases other than helium. The pore throats in organic-rich shale, potentially on the order of nanometers (e.g., Loucks et al., 2009), may act as a molecular sieve (Bustin et al., 2008), allowing easier passage of helium (kinetic diameter 0.26 nm) while retarding or blocking the flow of nitrogen or methane (kinetic diameters of 0.36 nm and 0.38 nm, respectively). Furthermore, gases that adsorb to organic and clay surfaces such as methane and carbon dioxide may block narrow pore throats, preventing the penetration of porosity beyond that pore throat. In both cases, the grain density and porosity measured by porosimetry will be still greater underestimations of the true values.

3.5.2 Mineralogy and Crystallographic Alignment

3.5.2.1 The Correlation of Mineralogy and Crystallographic Alignment

It is common that shale properties are plotted and interpreted as a function of clay content or the sum of clay and organic content (e.g., Vernik and Landis, 1996; Vernik and Liu, 1997; Prasad et al., 2011; Zargari et al., 2011). Although these interpretations, particularly of elastic anisotropy, are sensible because the anisotropy of the mineral frame is dominated by the highly anisotropic nature of sheet silicates (Cholach and Schmitt, 2006; Wenk et al., 2007), there is, however, considerable scatter in the data. Clearly, it is the alignment, rather than existence, of clay crystals that leads to anisotropy in the composite shale – a randomly oriented clay aggregate is, in bulk, isotropic. We demonstrate in Figure 3.20 that, for the samples studied in this dissertation, an elevated clay content does not necessitate a strong alignment of clay crystals, while a general correlation exists, there is considerable scatter present. Furthermore, we have shown that non-clay minerals exhibit preferential co-alignment with bedding and, indeed, can be the most aligned phase (e.g., ENI5 and ENI6; Table 3.5). This observation has also been previously made in the literature through numerical simulation (Valcke et al., 2006). As a result, in future analysis we consider the CPO of the composite shale, not clay content nor clay alignment, as the pivotal variable for elastic anisotropy interpretation/modeling. The effect of the consideration of CPO on elastic anisotropy prediction and interpretation is documented in the following chapter.

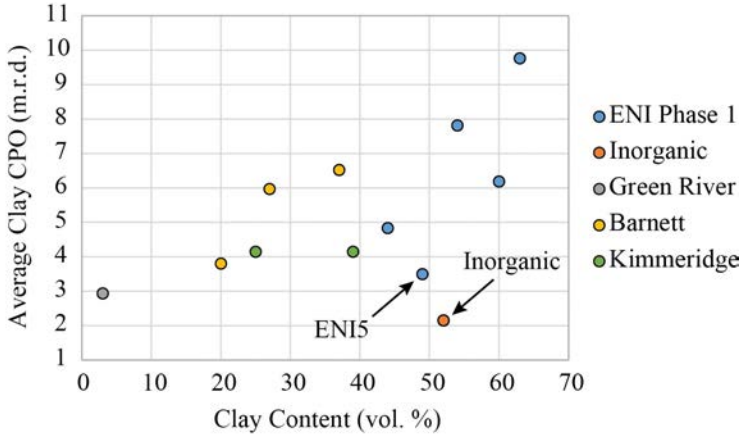

Figure 3.20: The average degree of crystallographic co-alignment of the clay species in each sample as a function of the volumetric clay content.

3.5.2.2 Mineralogy and CPO Re-Characterization Post-Pyrolysis

As noted in the presentation of our novel organic-rich shale characterization methodology, we do not quantify mineralogy or CPO post-pyrolysis. We do, however, have a set of measurements taken by W. Kanitpanyacharoen on two subsamples of the Inorganic and Green River samples – one *as received* subsample and the other post-pyrolysis at 400 °C for 72 hours. Note that these

measurements predate our in-house HTHP pyrolysis system, and, subsequently, were performed without applied confining pressure.

The mineralogy of the Inorganic and Green River samples pre- and post-pyrolysis is reported in weight fraction in Table 3.9. Given the weight fraction of each mineral species and the weight fraction of each element in that mineral, we can stoichiometrically evaluate the plausibility that the changes noted are attributable to chemico-thermally induced mineralogical evolutions within the sample. In the Inorganic subsamples, there is a 4.6% increase in the illite-smectite content where it is expected that exposure to elevated temperature should result in the dewatering of smectite and conversion to another phase. Furthermore, while the decomposition of pyrite to pyrrhotite is energetically favorable at these temperatures, the system loses too much iron (considering also the decomposition of siderite) and gains too much sulfur (especially considering that the relatively inert organic content will be a poor source of sulfuric compounds). Meanwhile, in the Green River subsamples there is an inexplicable 6 wt. % increase in calcium post-pyrolysis. In both cases, there is a sizeable (8.8-10.9 wt. %) development of previously nonexistent fluorite. This is particularly problematic as there is no mineral-bound nor gaseous source of fluorine during pyrolysis to account for the ∼5 wt. % fluorine of the entire sample post-pyrolysis. Indeed, the development of fluorite would require the presence of significant fluorapatite content that was not detected in the pre-pyrolysis sample. As a result of these issues, we determine that the mineralogical heterogeneity between plugs is too great to meaningfully determine a thermally dependent evolution.

Table 3.9: The relative mienralogy by weight of the Inorganic (Inorg.) and Green River samples *as received* (first row for each sample) and post-pyrolysis at 400 °C (second row). The minerals are abbreviated as follows illite-mica (Ill-mca), illite-smectite (Ill-sme), kaolinite (Kln), feldspar (Fsp), siderite (Sd), calcite (Cal), dolomite (Dol), analcime (Anl), pyrite (Py), pyrrhotite (Po), and fluorite (Fl). Due to the lack of change post-pyrolysis, quartz values are omitted from the table – hence the weight fractions do not sum to 100%. Dashes indicate the absence of that mineral species in the given sample.

Sample	Ill-mca	Ill-sme	Kln	Fsp	Sd	Cal	Dol	Anl	Py	Po	Fl
Inorg.	18.4	15.4	14.2	4.5	17.8	9.7	-	-	1.9	-	-
	19.2	20.0	12.9	8.6	2.5	1.3	-	-	-	8.5	10.9
Green River	3.8	-	-	11.2	-	18.2	42.8	11.6	-	-	-
	4.0	-	-	9.2	-	26.9	29.4	6.1	-	-	8.8

The pre-pyrolysis Inorganic and Green River subsamples are characterized by average CPO values of 1.58 and 1.07, indicative of a weak texture and an effectively random texture, respectively. The post-pyrolysis subsamples show a slight increase to 1.87 and 1.08, respectively. However, given the significant observed mineralogical heterogeneity, there is no basis to attribute such slight changes in CPO to meaningful reorientation of crystals rather than to a further indicator of heterogeneity. At this time, we have been unable to conduct iterative CPO quantification on a single subsample pre- and post-pyrolysis due to the fragility of the extremely small (2 mm thick) subsamples. It is important to note, however, that the heterogeneity exhibited between the separate subsamples is not great, and that average values (Inorganic: 1.73 ± 0.15, Green River: 1.08 ± 0.01) have no effect on the interpretation of textural strength.

3.6 Conclusions

In this chapter, we have presented a comprehensive experimental methodology for the laboratory characterization of the sources of elastic anisotropy in organic-rich shale. In this novel methodology, we incorporate conventional rock physics techniques, such as acoustic velocity experiments, with integrated high-resolution imaging techniques, such as SEM and CLSM, to discriminate intrinsic and extrinsic contributions to elastic anisotropy. Furthermore, this methodology is readily applicable to both the characterization of naturally matured samples and the iterative characterization of samples pre- and post-pyrolysis. In this manner, we enable both the identification of anisotropic trends in naturally matured shales (Chapter 4) and phenomenological observations of shale evolution upon induced thermal maturation (Chapters 5 and 6).

Additionally, we have detailed the mineralogy, microstructure, and geochemistry of a set of organic-rich shale samples to be studied in the remaining chapters of this thesis. This sample set encompasses a broad range of shales: including clay contents ranging from 4% to 71%, a continuum of crystallographic textures from effectively randomly oriented to strongly laminar, and from thermally immature to extremely post-mature samples. The breadth of the sample set enables a more thorough characterization of the variability and the source of that variability in the elastic and transport properties of organic-rich shale.

Finally, we emphasize the issues associated with characterizing porosity in tight rocks, particularly lower maturity organic-rich shale. Differences between the physically quantifiable effective porosity and total porosity are predominantly a function of microstructure – e.g., blocked pore throats, cementation, and organic distribution. Any disagreement between the effective and total porosity cannot be identified a priori and requires the quantification and comparison of porosity values from multiple sources, such as porosimetry/mercury intrusion and XRD-derived density-based analyses.

3.7 Appendix

3.7.1 Appendix A: Complete Sample Mineralogy Dataset

Table 3A.1: The complete mineralogical composition of each sample, in weight percent, from XRD analysis. The minerals are abbreviated as follows illite-mica (Ill-mca), illite-smectite (Ill-sme), chlorite (Chl), kaolinite (Kln), feldspar (Fsp), quartz (Qtz), calcite (Cal), dolomite (Dol), siderite (Sd), ankerite (Ank), apatite (Ap), analcime (Anl), and pyrite (Py). Dashes indicate the absence of that mineral species in the given sample.

Sample	Ill-mca	Ill-sme	Chl	Kln	Fsp	Qtz	Cal	Dol	Sd	Ank	Ap	Anl	Py
ENI1	17.4	23.5	4.1	25.5	2.0	18.5	1.0	3.0	-	-	-	-	5.0
ENI2	16.8	17.8	3.3	22.4	1.8	16.8	5.7	10.8	-	-	-	-	4.6
ENI4	14.1	23.0	4.4	23.8	4.2	21.2	1.0	3.2	-	-	-	-	5.1
ENI5	25.3	22.5	5.2	2.1	4.1	18.5	17.9	3.2	-	-	-	-	1.2
ENI6	23.3	16.8	5.1	2.6	6.6	22.4	16.5	5.3	-	-	-	-	1.4
Inorganic	18.4	15.4	-	14.2	4.5	18.1	9.7	-	17.8	-	-	-	1.9
Green River	3.8	-	-	-	11.2	12.4	18.2	42.8	-	-	-	11.6	-
BO	45.3		2.5	1.0	-	39.7	-	-	3.4	-	4.5	-	3.6
BW1	27.6		-	-	1.6	38.2	18.7	3.7	0.2	2.8	-	-	7.2
BW2	20.5		-	-	9.0	44.0	2.4	10.0	0.3	5.0	4.4	-	4.4

3.7.2 Appendix B: The Computation of Porosity from XRD-Derived Mineralogy and TOC

The following discussion documents how the grain density and total porosity of a sample can be estimated from the XRD-derived mineralogy, TOC, and mass and volume of the sample. Given that XRD-derived mineralogy information generally excludes organic carbon, i.e., the sum of the inorganic mineral phases is 100%, the organic mass must first be removed from the sample mass. The inorganic sample mass, m_{inorg}, is the total sample mass, m_{samp}, less the mass of kerogen, m_{ker} (Equation 3B.1). The mass of kerogen is computed from TOC under the assumption that kerogen is purely a compound of a fixed carbon-to-hydrogen ratio as in Equation 3B.2, where M_H, M_C, and HC are the molar masses of hydrogen and carbon and the molecular hydrogen-to-carbon ratio, respectively. The value of HC is a function of thermal maturity and kerogen type and is based on ranges of values reported in Peters and Cassa (1994).

$$m_{inorg} = m_{samp} - m_{ker} \tag{3B.1}$$

$$m_{ker} = (TOC \times m_{samp}) \left[\left(\frac{M_H}{M_C} \times HC \right) + 1 \right] \tag{3B.2}$$

The mass of each mineral phase can then be computed as in Equation 3B.3, where m_i and χ_i are the mass and weight percent of the i^{th} mineral phase.

$$m_i = m_{inorg} \times \chi_i \tag{3B.3}$$

The volume of each phase (both organic and inorganic), V_i, is then the quotient of the respective mass and density, ρ_i (Equation 3B.4). The densities used and references for those values are recorded in Table 3B.1.

$$V_i = \frac{m_i}{\rho_i} \tag{3B.4}$$

The grain volume is then the sample mass divided by the sum of the volume of each phase (both organic and inorganic; Equation 3B.5).

$$\rho_g = \frac{m_{samp}}{\Sigma_j V_j} \tag{3B.5}$$

The total porosity can then be estimated in the conventional manner from the grain and bulk volumes, as in Equation 3B.6 assuming a right circular cylindrical sample of diameter, d, and length, L.

$$\phi_T = \frac{V_B - V_G}{V_B} = 1 - \left(\frac{V_G}{V_B} \right) = 1 - \left(\frac{\Sigma_j V_j}{\left(\frac{\pi}{4} d^2 L \right)} \right) \tag{3B.6}$$

Table 3B.1: The mineral density values used in calculation of mineral volumes within a sample. Mineral phases are abbreviated as in Table 3A.1.

Mineral	Density (g/cc)	Reference
Ill-mca	2.682	Militzer et al. (2011)
Ill-sme	2.8247	
Chl	2.668	Joswig et al. (1980)
Kln	2.599	Militzer et al. (2011)
Fsp	2.623	Brown et al. (2006)
Qtz	2.6466	Heylinger et al. (2003)
Cal	2.71	Graf (1961)
Dol	2.838	Steinfink and Sans(1959)
Sd	3.87	Nesse (2013)
Ank	3.00	
Ap	3.19	
Anl	2.26	
Py	5.0109	Le Page and Rodgers (2005)
Kerogen	1.2-1.5	Okiongbo et al. (2005)

3.7.3 Appendix C: On the Assumption of Geochemical Homogeneity

In order to address the validity of the assumed homogeneity of geochemical properties throughout each sample, we report the geochemical properties of all samples for which we have RockEval analysis provided by two separate geochemical labs labeled as Labs A and B, respectively (Table 3C.1). As can be seen in Table 3C.1, the degree of agreement between measurements taken at the two labs varies between properties. The most pertinent of these properties (TOC, hydrocarbon potential, free hydrocarbons, and thermally producible hydrocarbons) are cross-plotted for facilitated comparison in Figure 3C.1.

Table 3C.1: The geochemical properties of each sample as characterized by RockEval analysis (as in Table 3.6). Data corresponding to samples labeled with an asterisk (∗) were provided by Lab A, all other data was collected at Lab B. Again, double asterisks (∗∗) in the T_{MAX} column indicate unreliable values due to low S_2 values.

Sample	TOC (wt. %)	T_{MAX} (°C)	S_1 (mg/g)	S_2 (mg/g)	HI (mg/g)	OI (mg/g)	HP (mg/g)
ENI1	7.49	427	4.96	39.80	532	16	44.76
ENI2	7.14	436	4.97	42.59	596	10	47.56
ENI1,2*	4.94	440	3.63	25.75	521	-	29.38
ENI4	4.34	441	2.93	14.61	337	10	17.54
ENI4*	3.12	447	0.07	17.33	303	-	17.40
ENI5	4.13	365**	0.63	0.86	21	13	1.49
ENI6	4.78	353**	0.54	0.23	5	9	0.77
ENI5,6*	6.9	>500	0.04	0.27	4	-	0.31
BO	11.67	418	2.32	55.98	480	9	58.30
BO*	12.66	419	1.21	53.62	424	-	54.83
BW1	2.72	392**	0.63	0.47	17	17	1.10
BW2	2.63	496	0.38	0.32	12	16	0.70
BW*	2.84	>500	0.01	0.56	11	-	0.57

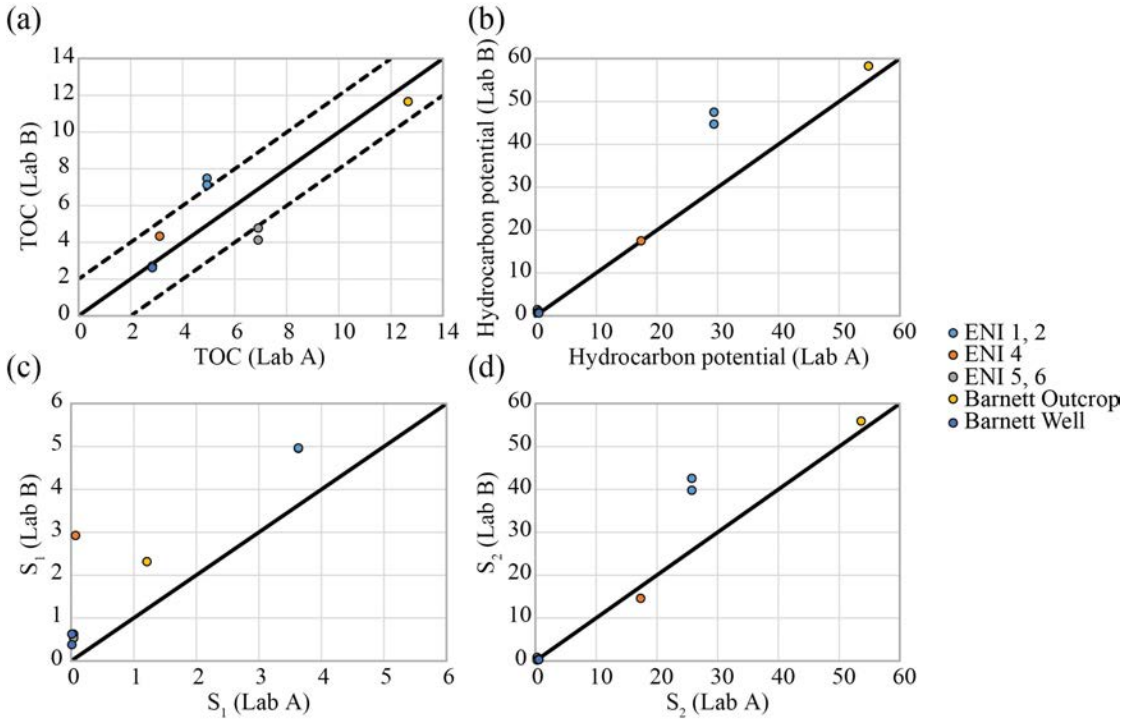

Figure 3C.1: A graphical representation of the variability between geochemical analyses conducted at Lab A and Lab B as listed in Table 3C.1. (a) Total organic carbon. (b) Hydrocarbon potential. (c) Free hydrocarbons. (d) Thermally producible hydrocarbons. In each panel, the solid black line indicates agreement between the values of the two labs. The dashed black lines in (a) indicates an error of ±2 weight percent.

The total organic carbon measurements between the two labs show some degree of heterogeneity; however, this heterogeneity is largely within ±2 weight percent (approximately ±0.04 g of organic carbon). That is to say, there is mischaracterization of organic-rich and organic-poor subsamples observed in this dataset. The hydrocarbon potential of the samples (Equation 3.9), in general, show strong agreement between the two labs, with the exception of samples ENI1 and ENI2. The majority of the disagreement for samples ENI1 and ENI2 stems from the underestimation of the thermally producible hydrocarbons (S_2) for these samples at Lab A. However, the stronger agreement in hydrogen index – which is measured in milligrams of hydrocarbons per gram of TOC – between the two labs indicates that the underestimation of total organic carbon at Lab A is the true source of the discrepancy between the two labs. Simply, there is less TOC in sample A to produce hydrocarbons, even though the TOC is very similar geochemically.

Furthermore, we observe that there is systematic underestimation of the free hydrocarbons (S_1) at Lab A. Given the noted geochemical similarity of the TOC within one sample between the two labs, this discrepancy is most likely attributable to differences in sample handling and preparation protocols at the two labs. Finally, given proximity, the need for consistency, and the greater preservation of retained hydrocarbons, all geochemical characterization post-pyrolysis discussed in future chapters is conducted at Lab B.

3.8 References

Ahmadov, R., 2011, Microtextural, elastic, and transport properties of source rocks: PhD Dissertation, Stanford University.

Ahmadov, R., T. Vanorio, and G. Mavko, 2009, Confocal laser scanning and atomic-force microscopy in estimation of elastic properties of the organic-rich Bazhenov formation: The Leading Edge, 28:18–23.

Allan, A. M., T. Vanorio, and J. E. P. Dahl, 2014, Pyrolysis-induced P-wave velocity anisotropy in organic-rich shales: Geophysics, 79:D41–D53.

Allan, A. M., W. Kanitpanyacharoen, and T. Vanorio, 2015, A multi-scale methodology for the analysis of velocity anisotropy in organic-rich shale: Geophysics, 80:C73–C88.

Batzle, M. and Z. Wang, 1992, Seismic properties of pore fluids: Geophysics, 57:1396–1408.

Brown, J. M., E. H. Abramson, and R. J. Angel, 2006, Triclinic elastic constants for low albite: Physics and Chemistry of Minerals.

Bustin, R. M., A. M. M. Bustin, X. Cui, J. K. Ross, and V. S. Murthy Pathi, 2008, Impact of shale properties on pore structure and storage characteristics: SPE Shale Gas Production Conference, SPE 119892.

Carmichael, R. S., 1989, Practical handbook of physical properties of rocks and minerals: CRC Press.

Cholach, P. Y. and D. R. Schmitt, 2006, Intrinsic elasticity of a textured transversely isotropic muscovite aggregate: Comparisons to the seismic anisotropy of schists and shales: Journal of Geophysical Research, 111:B09410.

Clark, A. C. and T. Vanorio, 2015, A niche system for inducing thermo-chemo-mechanical processes in rocks and materials: SRB Volume 142.

Claxton, N. S., T. J. Fellers, and M. W. Davidson, 2006, Microscopy, confocal, in J. G. Webster, ed.,: Encyclopedia of Medical Device and Instrumentation, 2nd ed., pages 449–477.

Curtis, M. E., B. J. Cardott, C. H. Sondergeld, and C. S. Rai, 2012, Development of organic porosity in the Woodford Shale with increasing thermal maturity: International Journal of Coal Geology, 103:26–31.

Dewhurst, D. N. and A. F. Siggins, 2006, Impact of fabric, microcracks and stress field on shale anisotropy: Geophysics Journal International, 165:135–148.

Egerton, R. F., 2005, Physical principles of electron microscopy: an introduction to TEM, SEM, and AEM: Springer.

Gassmann, F., 1951, Über die Elastizität poröser Medien: Vierteljahrsschrift der Naturforschenden Gesellschaft in Zürich, 96:1–23.

Graf, D. L., 1961, Crystallographic tables for the rhombohedral carbonates: American Mineralogist, 46:1283–1316.

Han, Z., J. C. Crelling, and Y. Zhou, 1993, Fluorescence intensity and alteration of coal macerals and their relation to coalification: Organic Geochemistry, 20:677–685.

Heylinger, P., H. Ledbetter, and S. Kim, 2003, Elastic constants of natural quartz: Journal of the Acoustical Society of America, 114:644–650.

Hornby, B. E., 1998, Experimental laboratory determination of the dynamic elastic properties of wet, drained shales: Journal of Geophysical Research, 103:29945–29964.

Jacob, H., 1964, Neue Erkenntisse auf dem gebiet der Luminenzmikroskopie fossiler Brennstoffe: Fortschr: Geologische Rheinld Westfalen, 12:569–588.

Johnston, J. E. and N. I. Christensen, 1995, Seismic anisotropy of shales: Journal of Geophysical Research, 100:5991–6003.

Jones, L. E. A. and H. F. Wang, 1981, Ultrasonic velocities in Cretaceous shales from the Williston basin: Geophysics, 46(3):288–297.

Joswig, W., H. Fuess, R. Rothbauer, Y. Takéuchi, and S. A. Mason, 1980, A neutron diffraction study of a one-layer triclinic chlorite (penninite): American Mineralogist, 65:349–352.

Kaarsberg, E. A., 1959, Introductory studies of natural and artificial argillaceous aggregates by sound-propagation and X-ray diffraction methods: Journal of Geology, 67:447–472.

Kanitpanyacharoen, W., H.-R. Wenk, F. B. Kets, C. Lehr, and R. Wirth, 2011, Texture and anisotropy of Qusaiba shales: Geophysical Prospecting, 59:536–556.

Kanitpanyacharoen, W., R. Vasin, H.-R. Wenk, and D. N. Dewhurst, 2015, Linking preferred orientations to elastic anisotropy in Muderong shale, Australia: Geophysics, 80:C9–C19.

Kocks, U. F., C. Tomé, and H.-R. Wenk, 2000, Texture and anisotropy: preferred orientations in polycrystals and their effect of materials properties: Cambridge University Press.

LePage, Y. and J. R. Rodgers, 2005, Ab initio elasticity of FeS_2 pyrite from 0 to 135 GPa: Physics and Chemistry of Minerals, 32:564–567.

Lewan, M. D., 1994, Assessing natural oil expulsion from source rocks by laboratory pyrolysis, in L. B. Magoon, and W. G. Dow, eds., The petroleum system - From source to trap: AAPG, AAPG Memoir, 60:201–210.

Lonardelli, I., H.-R. Wenk, and Y. Ren, 2007, Preferred orientation and elastic anisotropy in shales: Geophysics, 72(2):D33–D40.

Loucks, R. G., R. M. Reed, S. C. Ruppel, and D. M. Jarvie, 2009, Morphology, genesis, and distribution of nanometer-scale pores in siliceous mudstones of the Mississippian Barnett shale: Journal of Sedimentary Research, 79:848–861.

Mavko, G., T. Mukerji, and J. Dvorkin, 2009, The rock physics handbook, 2nd ed.: Cambridge University Press.

Militzer, B., H.-R. Wenk, S. Stackhouse, and L. Stixrude, 2011, First-principles calculation of the elastic moduli of sheet silicates and their application to shale anisotropy: American Mineralogist, 96:125–137.

Nesse, W. D., 2014, Introduction to optical mineralogy: Oxford University Press.

Nix, T. and S. Feist-Burkhardt, 2003, New methods applied to the microstructure of Messel oil shale: Confocal laser scanning microscopy (CLSM) and environmental scanning electron microscopy (ESEM): Geological Magazine, 140:469–478.

Okiongbo, K. S., A. C. Aplin, and S. R. Larter, 2005, Changes in type II kerogen density as a function of maturity: Evidence from the Kimmeridge Clay Formation: Energy and Fuels, 19: 2495–2499.

Pepper, A. S. and P. J. Corvi, 1995, Simple kinetic models of petroleum formation. Part I: Oil and gas generation from kerogen: Marine and Petroleum Geology, 12(3):291–319.

Peters, K. E. and M. R. Cassa, 1994, Applied source rock geochemistry, in L. B. Magoon, and W. G. Dow, eds., The petroleum system - From source to trap: AAPG, AAPG Memoir, 60: 93–120.

Peters, K. E., C. C. Walters, and J. M. Moldowan, 2004, The biomarker guide: Volume 2, Biomarkers and isotopes in petroleum systems and earth history: Cambridge University Press.

Prasad, M., K. C. Mba, T. E. McEvoy, and M. L. Batzle, 2011, Maturity and impedance analysis of organic-rich shales: SPE Reservoir Evaluation and Engineering, 14:533–543.

Rietveld, H. M., 1969, A profile refinement method for nuclear and magnetic structures: Journal of Applied Crystallography, 2:65–71.

Robinson, J. P., 2001, Principles of confocal microscopy, in Z. Darynkiewicz, H. A. Crissman, and J. P. Robinson, eds., Methods in cell biology, Volume 63: Academic Press.

Sayers, C. M., 1999, Stress-dependent seismic anisotropy of shales: Geophysics, 64:93–98.

Sayers, C. M., 2005, Seismic anisotropy of shales: Geophysical Prospecting, 53:667–676.

Schochardt, M., 1943, Grundlagen und neuere Erkenntnisse der angewandten Braunkohlenpetrographie: .

Simmons, G., 1965, Single crystal elastic constants and calculated aggregate properties: Journal of the Graduate Research Center of Southern Methodist University, 34:1–269.

Staplin, F. L., 1969, Sedimentary organic matter, organic metamorphism, and oil and gas occurences: Bulletin of Canadian Petroleum Geology, 17:47–66.

Stasiuk, J. D., 1999, Confocal laser scanning fluorescence microscopy of Botryococcus alginite from boghead oil shale, Boltysk, Ukraine: Selective preservation of various micro-algal components: Organic Geochemistry, 30:1021–1026.

Steinfink, H. and F. J. Sans, 1959, Refinement of the crystal structure of dolomite: American Mineralogist, 44:679–682.

Taylor, G. H., M. Teichmüller, A. Davis, C. F. K. Diessel, R. Littke, and P. Robert, 1998, Organic petrology: Gerbrüder Borntreger.

Teerman, S. C., J. C. Crelling, and G. B. Glass, 1987, Fluorescence spectral analysis of resinite macerals from coals of the Hanna Formation, Wyoming, U.S.A.: International Journal of Coal Geology, 7:315–334.

Teichmüller, M. and B. Durand, 1983, Fluouescence microscopical rank studies on liptinites and vitrinites in peat and coals and comparison with the results of Rock-Eval pyrolysis: International Journal of Coal Geology, 2:197–230.

Teichmüller, M. and K. Ottenjann, 1977, Art und diagenese von liptinitem unf lipoiden stoffen in einem erdolmuttergestein aufgrund fluoreszen mikroskopishen untersuchengen: Erdöl Kohle, 30:387–398.

Thomsen, L., 1986, Weak elastic anisotropy: Geophysics, 51:1954–1966.

Tissot, B., B. Durand, J. Espitalié, and A. Combaz, 1974, Influence of nature and diagenesis of organic matter in formation of petroleum: AAPG Bulletin, 58:499–506.

Valcke, S. L. A., M. Casey, G. E. Lloyd, J. M. Kendall, and Q. J. Fisher, 2006, Lattice preferred orientation and seismic anisotropy in sedimentary rocks: Geophysics Journal International, 166:652–660.

van Gizjel, P., 1967, Autofluorescence of fossil pollen and spores with special reference to age determination and coalification: Ledse Geol. Meded., 40:263–317.

Vandenbroucke, M., 2003, Kerogen: from types to model of chemical structure: Oil and Gas Science and Technology, 58:243–269.

Vanorio, T., T. Mukerji, and G. Mavko, 2008, Emerging methodologies to characterize the rock physics properties of organic-rich shales: The Leading Edge, 27:780–787.

Vasin, R., H.-R. Wenk, W. Kanitpanyacharoen, S. Matthies, and R. Wirth, 2013, Anisotropy of Kimmeridge sgake: Journal of Geophysical Research, 118:1–26.

Vernik, L., 1993, Microcrack-induced versus intrinsic elastic anisotropy in mature HC-source shales: Geophysics, 58:1703–1706.

Vernik, L. and C. Landis, 1996, Elastic anisotropy of source rocks: Implications for hydrocarbon generation and primary migration: AAPG Bulletin, 80:531–544.

Vernik, L. and X. Liu, 1997, Velocity anisotropy in shales: A petrophysical study: Geophysics, 62:521–532.

Vernik, L. and A. Nur, 1992, Ultrasonic velocity and anisotropy of hydrocarbon source rocks: Geophysics, 57:727–735.

Walls, J. D. and S. W. Sinclair, 2011, Eagle Ford Shale reservoir properties from digital rock physics: First Break, 29:97–101.

Wang, Z., 2002, Seismic anisotropy in sedimentary rocks, part 2: Laboratory data: Geophysics, 62:521–532.

Wenk, H.-R., S. Matthies, J. Donovan, and D. Chateigner, 1998, BEARTEX: A Windows-based program system for quantitative texture analysis: Journal of Applied Crystallography, 31: 262–269.

Wenk, H.-R., I. Lonardelli, H. Franz, K. Nihei, and S. Nakagawa, 2007, Preferred orientation and elastic anisotropy of illite-rich shale: Geophysics, 72(2):E69–E75.

Wenk, H.-R., L. Lutterotti, P. Kaercher, W. Kanitpanyacharoen, L. Miyago, and R. N. Vasin, 2014, Rietveld texture analysis from synchrotron diffraction images. II. Complex multiphase materials and diamond anvil cell experiments: Powder Diffraction, 29:220–232.

Wolf, K., 2010, Laboratory measurements and reservoir monitoring of bitumen sand reservoirs: PhD Dissertation, Stanford University.

Zargari, S., M. Prasad, K. C. Mba, and E. D. Mattson, 2011, Organic maturity, hydrous pyrolysis and elastic property in shales: Presented at Canadian Unconvential Resources Conference.

Chapter 4

ON THE SOURCES OF ELASTIC ANISOTROPY IN NATURALLY MATURED ORGANIC-RICH SHALE

Abstract

In this chapter, I apply the novel experimental methodology for the characterization of elastic anisotropy in shale, orginally presented in Chapter 3, to a wide set of naturally matured organic-rich shale samples. In this manner, I separate the relative contribution of the intrinsic and extrinsic sources of elastic anisotropy and characterize the shale frame for fluid substitution

modeling. The application of this methodology to naturally matured samples indicates that the elastic anisotropic response of organic-rich shale is dominated by the intrinsic, mineral alignment-driven, anisotropy of the rock frame. For the unsaturated samples characterized in this study, intrinsic anisotropy accounts for greater than 70% of the total values of both epsilon and gamma. Furthermore, the extrinsic anisotropy developed by the opening of compliant, crack-like, porosity upon unloading is found to be negligible at confining pressures greater than 25 MPa. For fluid-saturated measurements, i.e., non-zero pore pressure, the compliant pores will remain open at greater pore pressures. Subsequently, applying these results to saturated rocks at depth indicates that the extrinsic, crack-based source of anisotropy will continue to contribute at effective pressures greater than 25 MPa. However, for these shales, this study indicates that the extrinsic source of anisotropy will not exceed 30% of the total shale elastic anisotropy in situ.

4.1 Introduction

As previously identified, the current state of understanding of shale anisotropy is incomplete. At the simplest level, a thorough understanding of shale anisotropy is necessary for the proper processing of seismic studies (Banik, 1984; Sayers, 1999, 2005). However, at a higher level, the identification of thermal maturity-dependent trends in petrophysical properties such as porosity (e.g., Loucks et al., 2009), permeability (Chapter 6), and elastic anisotropy (e.g., Vernik and Nur, 1992; Vernik and Landis, 1996; Vernik and Liu, 1997; Allan et al., 2014) may prove pivotal to improvements in both unconventional reservoir characterization and production. Furthermore, the systematic discrimination of anisotropic sources (both intrinsic, frame-derived sources and extrinsic, compliant porosity-derived sources) and their relative magnitudes provides a wealth of petrophysical inputs that can better inform effective medium (e.g., self-consistent modeling (Berryman, 1980)) and fluid substitution (e.g., Gassmann, 1951) modeling of shales.

In order to begin to address the deficiencies in the understanding of elastic anisotropy in organic-rich shale, I implement a novel experimental characterization methodology to a broad set of naturally matured organic-rich shale samples, both introduced in Chapter 3. Specifically, in this chapter I develop correlations between high confining pressure elastic anisotropy measurements and mineral crystal alignment measurements and the pressure-sensitivity of anisotropy to mechanical compaction and image-based crack parameters. Furthermore, I attempt to isolate the contribution to intrinsic shale anisotropy of an increasingly anisotropic residual organic carbon phase through the incorporation of novel imaging techniques. Finally, these intrinsic and extrinsic sources are resolved to determine the primary controls of elastic anisotropy in naturally matured organic-rich shale samples.

4.2 Experimental Methodology and Sample Characterization

4.2.1 Experimental Methodology for Non-Pyrolyzed Samples

As the samples in this study are being investigated in their naturally matured state, e.g., with no pyrolysis-induced thermal maturation, there is no iterative characterization as laid out in the experimental flowchart of Figure 3.13. Rather all rock physics and high-resolution imaging experiments detailed in Section 3.3 are conducted one time on the *as received* samples. Subsequently, subsamples (Section 3.3.1) are used for helium porosimetry, acoustic velocity, X-ray diffraction (XRD), scanning electron microscopy (SEM), and confocal laser scanning microscopy (CLSM), and X-ray microtomography experiments as detailed schematically in Figure 4.1. All parameters of these experimental methods are as laid out in Chapter 3.

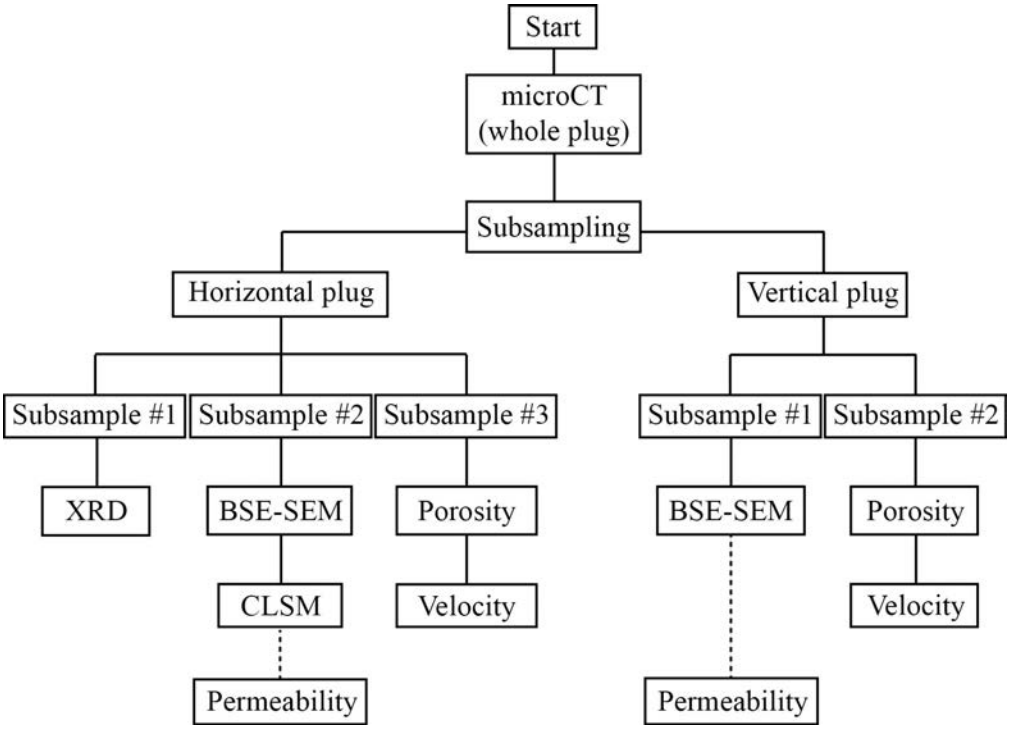

Figure 4.1: A schematic flowchart of the experimental workflow in the absence of iterative characterization pre- and post-pyrolysis. The permeability methodology and measurements will be discussed in Chapter 6.

4.2.2 Naturally Matured Sample Set

The set of samples studied in this chapter are previously reported in Section 3.4. For convenience, a summary of pertinent sample properties is given in Table 4.1 and Figure 4.2. The sample set includes 5 marine shale samples denoted as the ENI Phase 1 samples (or ENI 1 through ENI6 – the ENI3 sample is not reported), a largely inorganic sample, a lacustrine, outcrop

dolomicritic Green River sample, and three marine Barnett Shale samples – one from outcrop (BO) and two from a well (BW1 and BW2). The ENI Phase 1 samples are clay-rich, strongly textured, and span a range of thermal maturities from immature to the dry gas window, while the largely inorganic sample is also clay-rich but exhibits a lower degree of crystallographic alignment. The Green River sample is predominantly composed of carbonates, effectively randomly textured, and both thermally immature and with a 30% greater hydrocarbon potential than any other sample. The Barnett samples are predominantly siliciclastic (with greater carbonate content in the well-derived samples) samples of intermediate to strong alignment. The outcrop Barnett sample is thermally immature, while the well-derived samples are thermally post-mature.

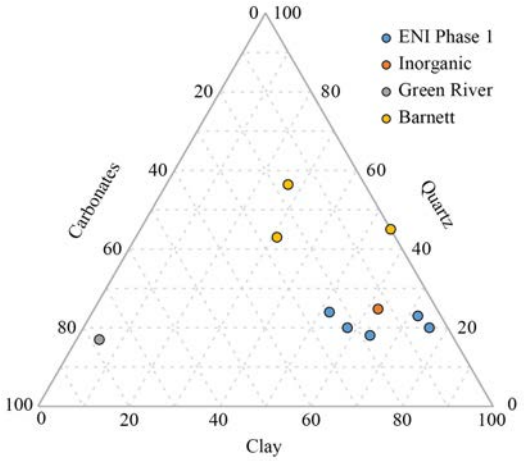

Figure 4.2: A ternary diagram representation of the primary mineralogy of each sample by weight. Each value has been normalized such that the total mineralogy excludes auxiliary mineral phases – i.e., clay + carbonates + quartz = 100%. The full mineralogy is documented in Appendix 3.7.1

Table 4.1: A recap of the pertinent properties (effective porosity, averaged crystallographic preferred orientation (CPO), window of thermal maturity, and hydrocarbon potential) characterizing the samples as presented in Chapter 3. The effective porosity is averaged across the two velocity subsamples. The hydrocarbon potential is given in milligrams of hydrocarbons per gram of dry rock and indicates the hydrocarbons ultimately recoverable from each sample.

Sample	Effective Porosity (%)	CPO	Thermal Maturity	Hydrocarbon Potential (mg/g)
ENI1	2.21±0.67	7.45	Immature	44.76
ENI2	1.84±0.67	5.33	Early Oil	47.56
ENI4	4.33±3.43	4.46		17.54
ENI5	7.63±0.53	3.35	Gas	1.49
ENI6	8.15±0.70	4.37		0.77
Inorganic	17.51±0.54	1.58	Immature	0.66
Green River	0.91±0.58	1.07		76.03
BO	12.98±0.61	3.98		58.30
BW1	5.82±1.16	2.69	Gas	1.10
BW2	6.25±1.19	1.59		0.70

4.3 Experimental Results

4.3.1 Acoustic Velocity Experiments

The measured P- and S-wave acoustic velocities for each sample are shown in Figures 4.3, 4.4, and 4.5. In all cases, the vertically propagating P-wave is slower and more pressure sensitive than the horizontally propagating phase – likely due to bedding and subparallel to bedding oriented microcracking. The greatest pressure-sensitivity of vertically propagating P-waves is shown by samples ENI4-6, BW1, and BW2, which were previously documented (with the exception of ENI5 and BW2) to exhibit through-going pressure release-induced fractures (Chapter 3). Although, the horizontal P-wave propagating through samples ENI6 and BW1 also exhibit significant sensitivity to pressure indicating a greater fraction of misaligned, with regard to bedding, compliant porosity. Furthermore, the directional dependence of P-wave velocity is severely suppressed for the Green River sample (Figure 4.3.d) due to the interlocking, non-laminar nature of the micritic mineral frame. The magnitudes of both the vertically and horizontally propagating compressional phases show good correlation with porosity (Figure 4.6).

The S-wave acoustic velocities are generally less pressure-sensitive (Figures 4.4 and 4.5). As expected for a VTI medium (Thomsen, 1986) the $V_S(0°)$ and $V_{SV}(90°)$ phases are, generally, quite similar in magnitude. Additionally, the $V_{SV}(90°)$ phase is considerably slower and more sensitive to confining pressure than the $V_{SH}(90°)$ phase. However, again the pressure-sensitivity and directional dependence of shear phases is minimized for the Green River sample (Figure 4.5.b). Contrastingly, the most pressure sensitive shear phase, by a considerable margin, is the $V_S(0°)$ phase of the fractured vertical BW1 plug (Figure 4.5.d). As with the P-wave velocities, the S-wave velocities show some correlation with porosity. This velocity-porosity correlation is greatest for the $V_{SH}(90)$, potentially indicating some crack-based heterogeneity in the more compliant $V_S(0°)$ and $V_{SV}(90°)$ phases (see Section 4.4.1 for a discussion of sample velocity heterogeneity).

The substantial hysteresis evident between the loading and unloading curves in the most pressure-sensitive samples and phases, e.g., $V_P(0°)$ and $V_S(0°)$, is attributed to the permanent, inelastic closure of microcracks with increasing confining pressure, which results in significantly greater velocities upon unloading. We assume that at the maximum confining pressure (40-50 MPa), all effective microcracks, i.e., those connected to plug surface, are closed; thereafter, upon unloading, the rock is assumed to behave elastically.

As in previous chapters, the elastic anisotropy of the samples is represented by the Thomsen anisotropic parameters epsilon and gamma (Equations 3.6 and 3.7). The calculated elastic anisotropy values are documented in Figures 4.7 and 4.8. The magnitude and pressure-sensitivity of epsilon is greatest for the clay-rich ($\sim$70%) ENI Phase 1 and Barnett samples, largely due to the previously noted elevated pressure-sensitivity of $V_P(0°)$ for these samples. Conversely, the Green River sample, which shows lower clay content ($<$5%), an interlocking dolomicritic texture, exhibits little to no pressure-sensitivity and a significantly lower magnitude of anisotropy, representative of the anomalous P-wave response to confining pressure noted in Figure 4.7.

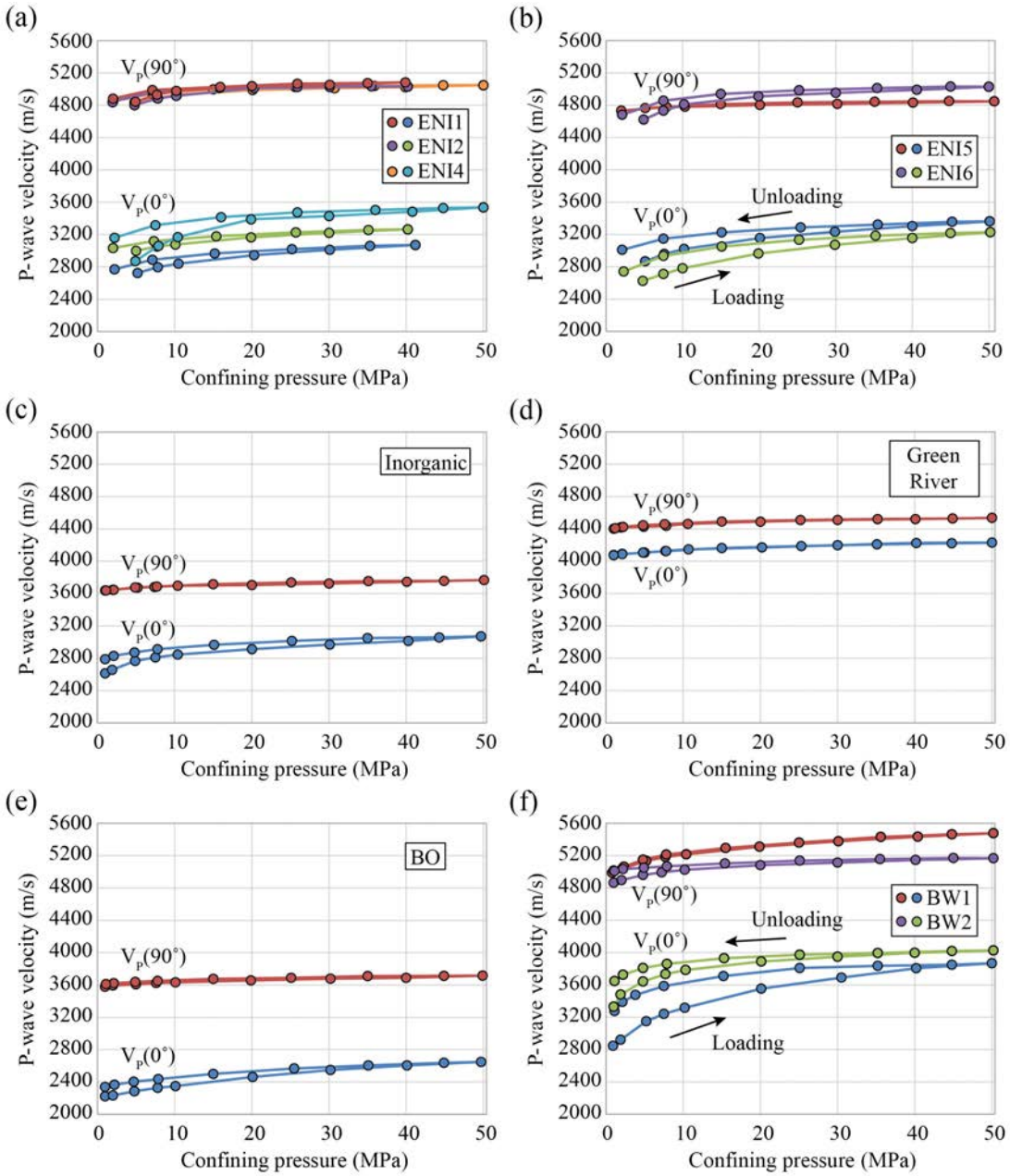

Figure 4.3: The P-wave acoustic velocity as a function of confining pressure both parallel and perpendicular to bedding. The samples have been binned where similarity permitted: (a) ENI Phase 1 immature to low maturity samples (ENI1, 2 and 4), (b) ENI Phase 1 post-mature samples (ENI5 and 6), (c) Inorganic, (d) Green River, (e) Barnett outcrop, and (f) Barnett well samples. Solid lines and arrows are used to indicate hysteresis between the loading and unloading curves.

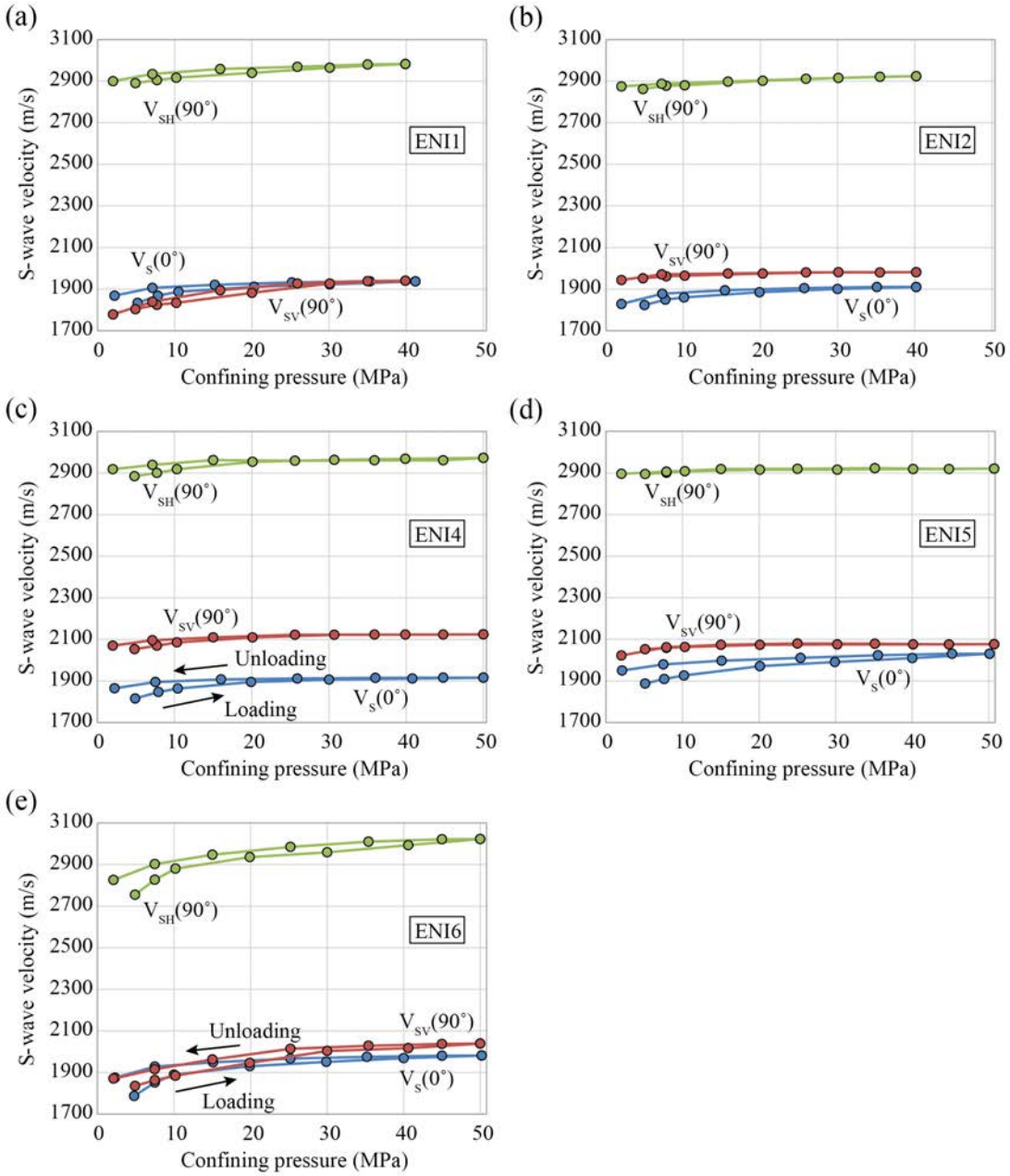

Figure 4.4: The S-wave acoustic velocity as a function of confining pressure both parallel and perpendicular to bedding for the ENI Phase 1 samples. (a) ENI1, (b) ENI2, (c) ENI4, (d) ENI5, (e) ENI6. Solid lines and arrows are used to indicate hysteresis between the loading and unloading curves.

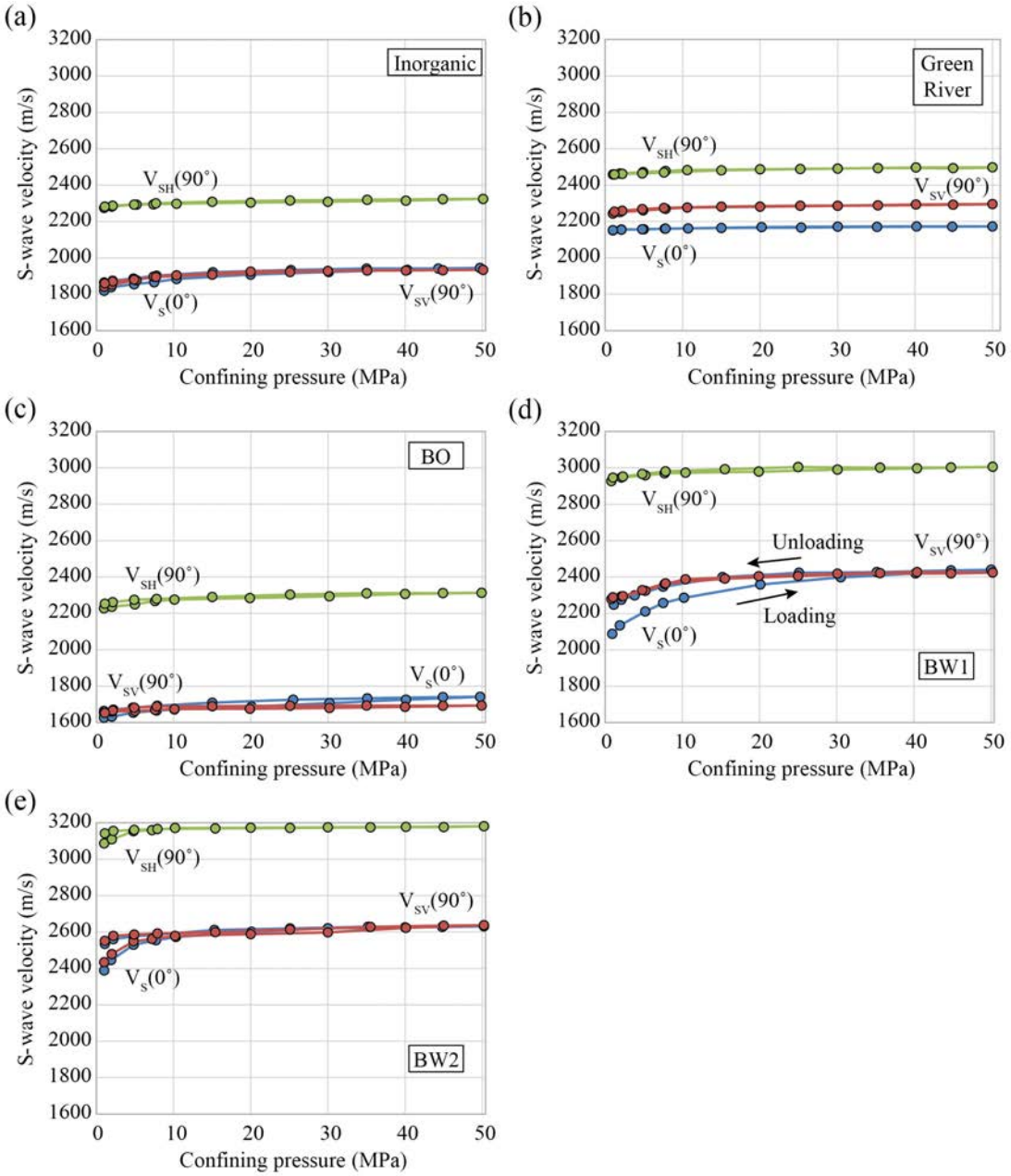

Figure 4.5: The S-wave acoustic velocity as a function of confining pressure both parallel and perpendicular to bedding for the Inorganic (a), Green River (b), BO (c), BW1 (d), and BW2 (e) samples. Solid lines and arrows are used to indicate hysteresis between the loading and unloading curves.

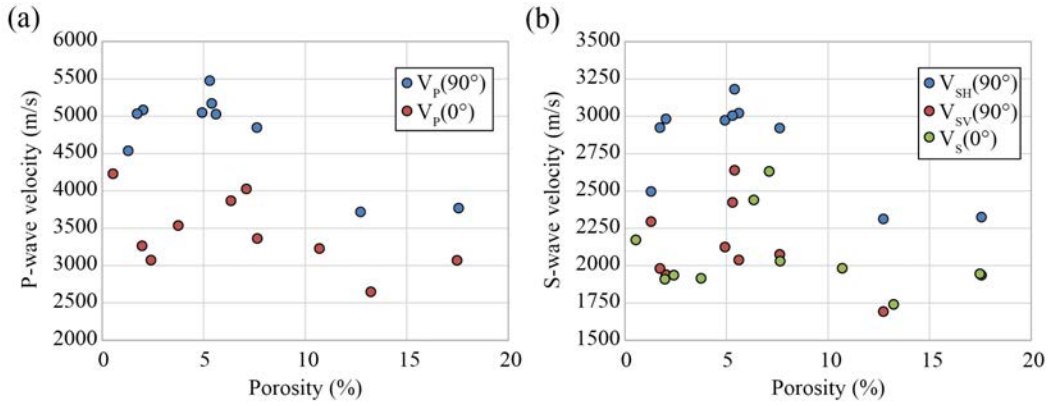

Figure 4.6: The P- (a) and S-wave (b) acoustic velocities as a function of porosity both parallel and perpendicular to bedding.

As with the shear wave velocities, gamma is significantly less sensitive to confining pressure than epsilon (Figure 4.8). As with epsilon, however, the greatest magnitude and pressure-sensitivity of gamma is exhibited by the ENI Phase 1 and Barnett samples. The significantly greater pressure-sensitivity of ENI1 and BW1 than that of the other samples is attributed to greater pressure release-induced cracking, as previously identified from hand sample (Figures 3.14 and 3.15). Again the magnitude and pressure-sensitivity of gamma exhibited by the Green River sample is anomalously low in comparison with the rest of the dataset. The relationship between epsilon and gamma, both for this dataset and across the broader literature, is discussed in Appendix A. While, all velocity, porosity, elastic moduli, and anisotropy values are reported, as a function of confining pressure, in Appendices C and D.

It merits comment that the dry anisotropy values reported in Figures 4.7 and 4.8 are extremely high, particularly for the clay-rich, laminar shales. As documented in Figures 4.3, 4.4, and 4.5, the co-alignment of compliant features, including microcracks, with the bedding plane results in lower acoustic velocities and elastic constants along the vertical axis, while the acoustic velocities and elastic constants in the horizontal plane are largely insensitive to the bedding-aligned cracks. Due to this relative sensitivity to co-aligned microcracks, substitution of a fluid into this dry frame will have a much greater effect on the vertically propagating phases than the horizontally propagating phases. Subsequently, it is expected that in situ fluid saturation will result in lower anisotropy values.

4.3.2 High-Resolution Imaging

Example slices from microCT volumes are shown in Figure 4.9 – note that microCT volumes were collected for only the ENI Phase 1 samples. Cracking, due to either early hydrocarbon maturation or pressure release during sample coring, is clear, strongly co-oriented, and volumetrically extensive in the immature to oil window samples (ENI1-4). Cracking is less visible, however, in the post-mature samples (ENI5, 6), although the pyrite content does exhibit co-alignment throughout the post-mature samples.

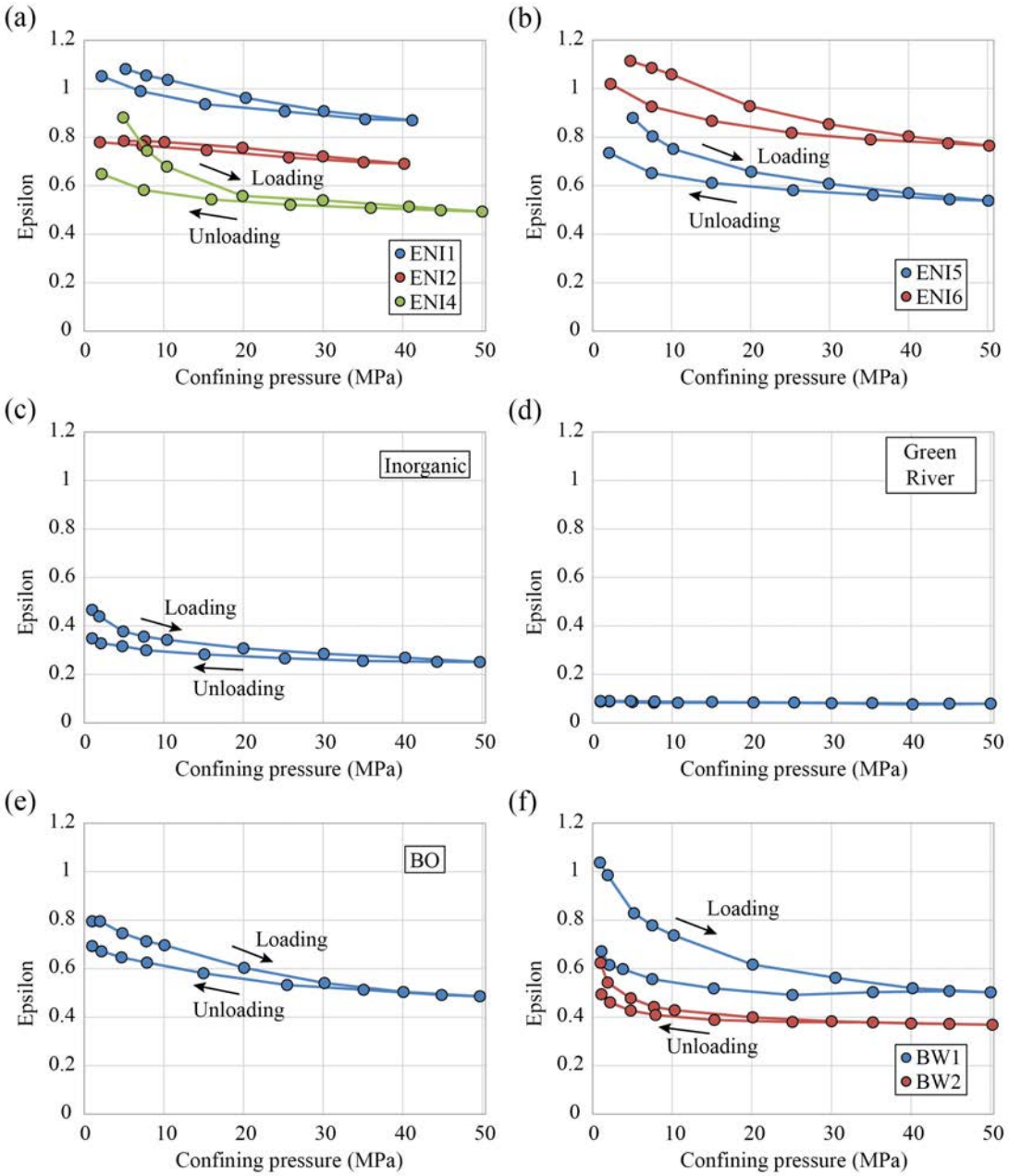

Figure 4.7: The Thomsen anisotropic parameter epsilon as a function of confining pressure. As in Figure 4.3, the samples have been binned where similarity permitted: (a) ENI Phase 1 immature to low maturity samples (ENI1, 2 and 4), (b) ENI Phase 1 post-mature samples (ENI5 and 6), (c) Inorganic, (d) Green River, (e) Barnett outcrop, and (f) Barnett well samples. Solid lines and arrows are used to indicate hysteresis between the loading and unloading curves.

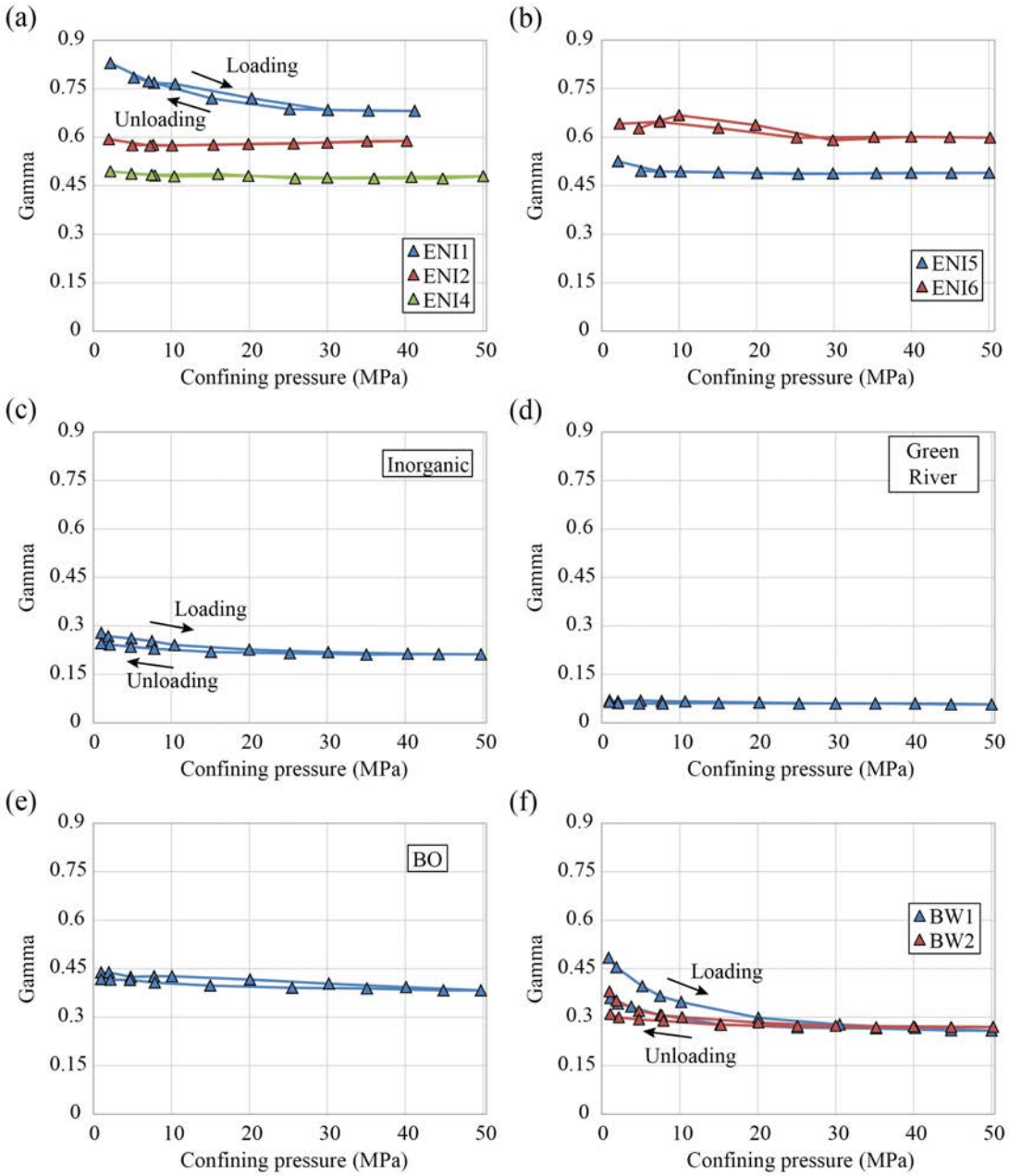

Figure 4.8: The Thomsen anisotropic parameter gamma as a function of confining pressure. As in Figure 4.3, the samples have been binned where similarity permitted: (a) ENI Phase 1 immature to low maturity samples (ENI1, 2 and 4), (b) ENI Phase 1 post-mature samples (ENI5 and 6), (c) Inorganic, (d) Green River, (e) Barnett outcrop, and (f) Barnett well samples. Solid lines and arrows are used to indicate hysteresis between the loading and unloading curves.

We obtain a higher resolution visual characterization of the samples by collocating backscattered electron scanning electron microscopy (BSE-SEM) and CLSM images. In this manner, we are able to combine the visualization of the microstructure of the shale, including mineral texture and mineral-organic interspacing, from SEM and the visualization of the distribution of organic matter by CLSM. Three examples of collocated BSE-SEM and CLSM images are given in Figures 4.10 and 4.11, relating to ENI1, ENI2, and BO, respectively. The BSE-SEM images in Figures 4.10 and 4.11 indicate a sample texture characterized by an extremely microcrystalline siliciclastic matrix (mid-gray colored) with dispersed, strongly aligned lenticular organic bodies (dark gray) and dispersed carbonates (Figure 4.10) and apatite (Figure 4.11) grains that often deform the organic lenses. At the same time, the CLSM images in Figure 4.10 allow immediate identification of organic bodies as the domains that fluoresce predominantly in the range of green to yellow wavelengths. Organic matter fluorescence at these wavelengths is expected due to the low level of thermal alteration in the immature to early oil window samples (Teerman et al., 1987; Michelsen and Khorasani, 1990). The fluorescence at blue wavelengths, particularly apparent in ENI2 (Figure 4.10.b), results from excitation of calcite grains in the focal plane. To better demonstrate the fluorescence of calcite, an inset from Figure 4.10.b is expanded with the blue spectrum enhanced in Figure 4.10.c.

Contrastingly, the organic matter documented in the BSE-SEM image of the Barnett outcrop sample does not exhibit fluorescence in the CLSM image (Figure 4.11). In order to better demonstrate this, the CLSM image is high-pass filtered and smoothed with a 3x3 median filter to minimize the low intensity, fine-scale noise (Figure 4.11.c). By incorporating white outlines of four collocated organic bodies (labeled as k1-k4), it is clear that the organic bodies in the outcrop Barnett sample are not fluorescing. Potential sources for this anomalous behavior are discussed in Section 4.4.2.2.

4.4 Discussion

4.4.1 Heterogeneity Arising from Using Multiple Plugs

Because this methodology uses two plugs (horizontally and vertically cored) to define each sample, it is important to address the potential for heterogeneity between the two plugs. In Figure 4.12, we illustrate the effective porosity and grain densities (both determined by helium porosimetry) of the horizontal plug as a function of the corresponding vertical plug values. The minimal deviation from the black line in Figure 4.12 indicates that compositional and microstructural heterogeneity between the plugs in each sample is low. Exceptions to this strong agreement are samples ENI6, for which the effective porosity values vary significantly while the grain density is quite uniform, and BW2, for which both the effective porosity and grain density values show significant disagreement. Both ENI6 and BW2 are characterized by significant coring-induced fracturing. Any surface roughness, asperities, or other defects preventing the effective closure of the fracture may have a significant effect on the porosity on the otherwise low porosity shale samples. The relative dissimilarity in the grain density measurements for BW2 is attributed to

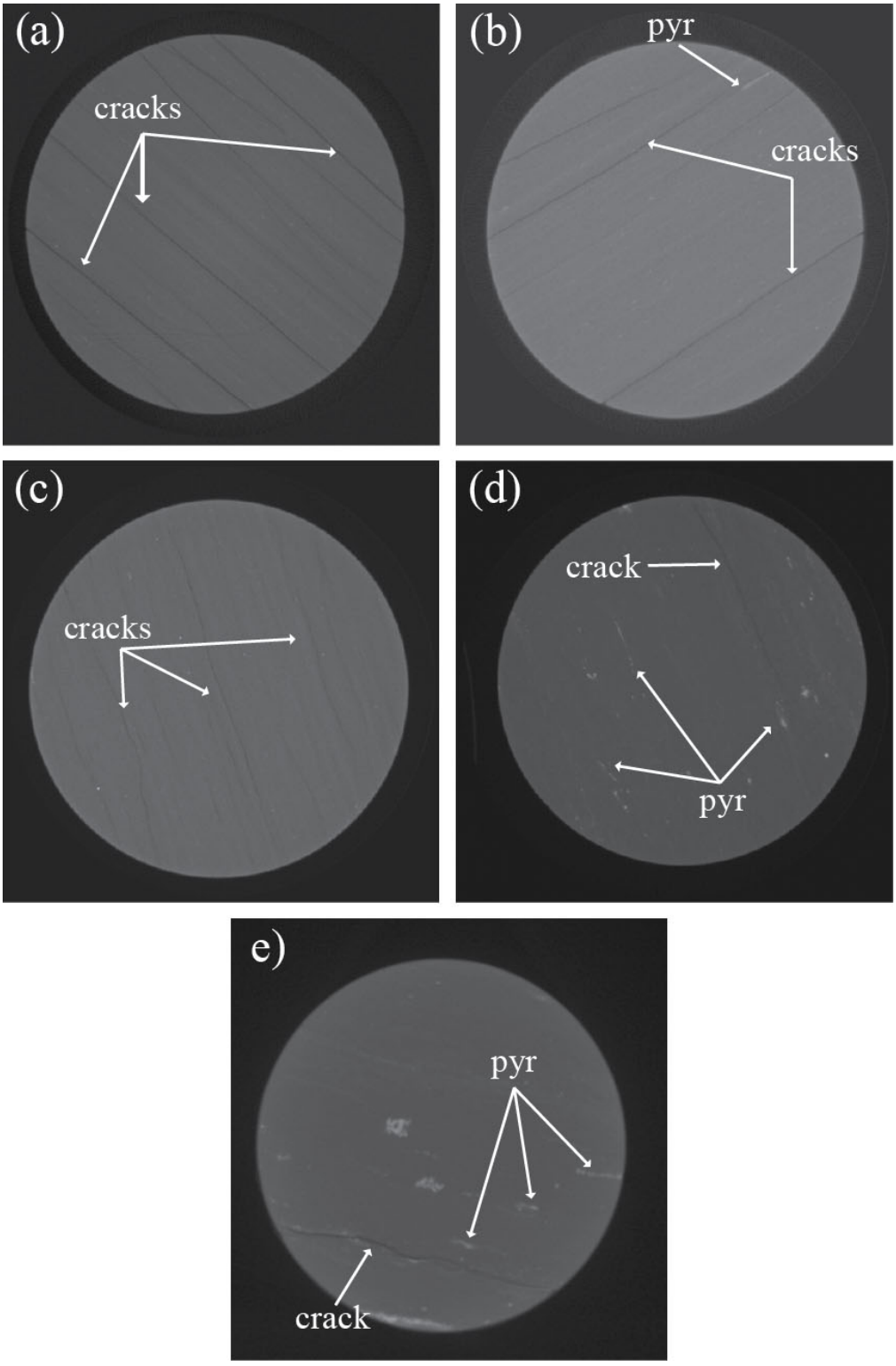

Figure 4.9: Example microCT slices from each of the ENI Phase 1 samples. (a) ENI1H, (b) ENI2H, (c) ENI4H, (d) ENI5H, and (e) ENI6H. Identified features include cracks and pyrite accumulations (pyr). Each sample is approximately 2.54 cm (1 inch) in diameter.

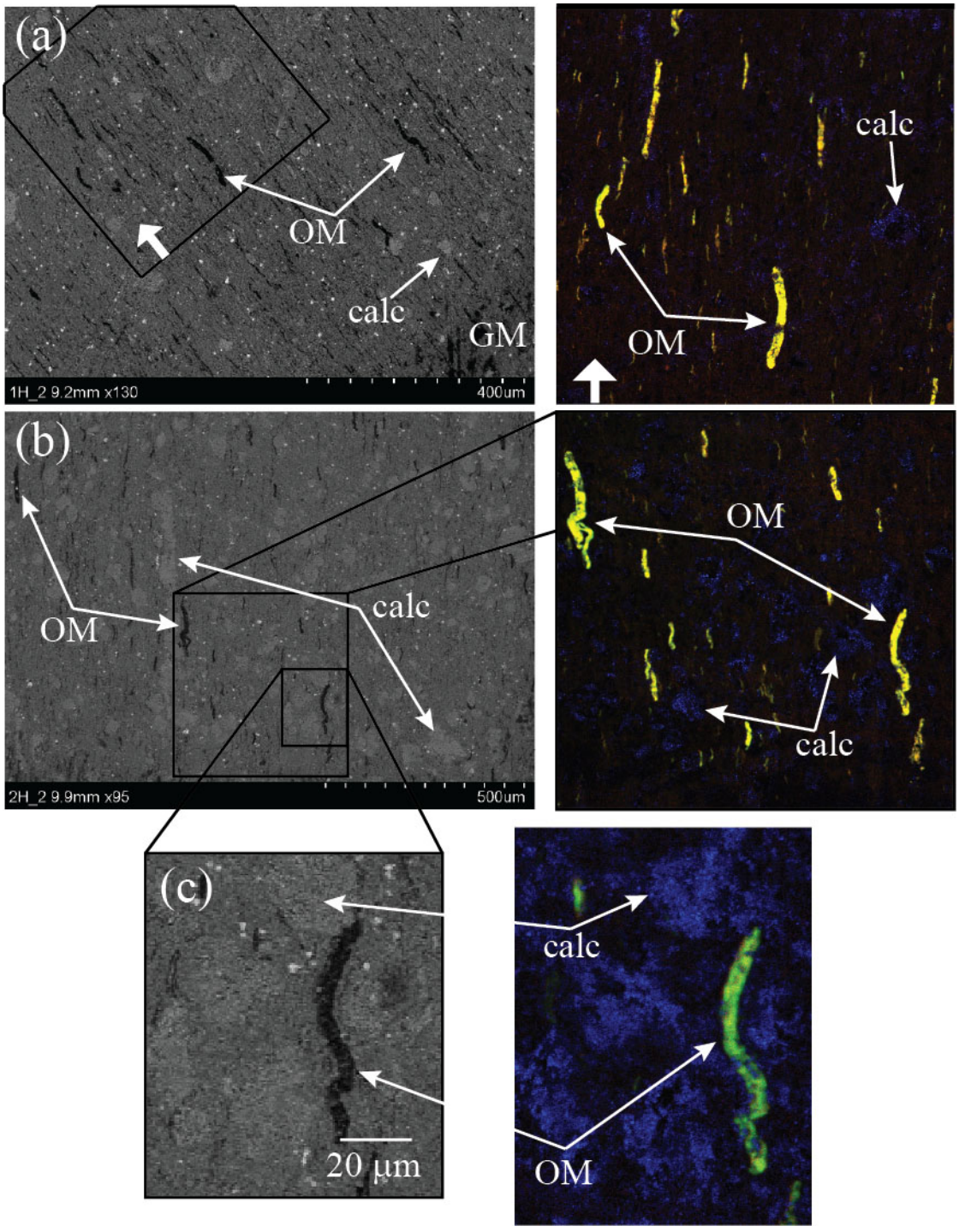

Figure 4.10: Example BSE-SEM images (left) and collocated 2D slices from CLSM volumes (right). Fluorescence in the range of green to red spectra corresponds with organic matter (OM), whereas fluorescence at blue wavelengths identifies calcite (calc). (a) ENI1H, (b) ENI2H, (c) comparison of SEM inset from (b) to a collocated blue spectrum-enhanced CLSM slice. A graphite marking used for relocating imaged areas is denoted by GM. The thick white arrow in the two images of (a) are in corresponding locations and orientations to represent the relative rotation of the two images. The CLSM images in (a) and (b) are 450 450 µm in dimension.

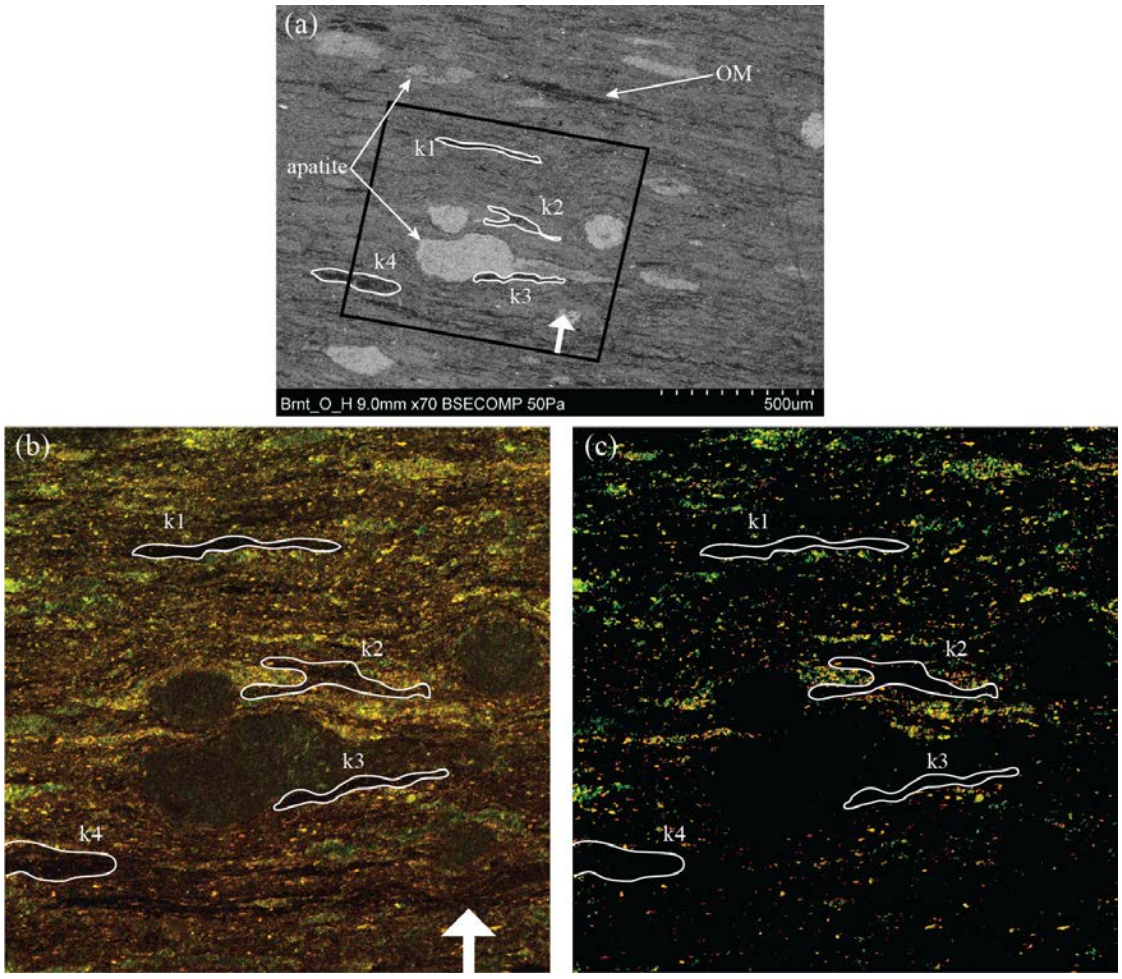

Figure 4.11: Example BSE-SEM image (a) with 2D CLSM slices pre- (b) and post-processing (c) collocated with the inset marked in (a) captured from the outcrop Barnett Shale sample. The organic matter in (a) clearly does not coincide with fluorescence in (b) and (c). To better illustrate this point, four organic bodies (labeled as k1-k4) have been bound in white in each image. The thick white arrows in (a) and (b) are in corresponding locations and orientations to represent the relative rotation of the two images. The CLSM images in (b) and (c) are 890 890 µm in dimension. Identified features include apatite and organic matter (OM).

mineralogical heterogeneity between the two plugs. The horizontal plug is 22% richer in carbonates (+3% calcite, +16% dolomite, and +3% ankerite), 14% poorer in quartz, and 7% poorer in illite-mica than the vertical plug, resulting in a 0.088 g/cc greater horizontal grain density. However, outside of these two exceptions, the physical heterogeneity between plugs is low across the sample set; furthermore, discussion in Chapter 3 indicated that the grain density variability within each sample is less than the 2% tolerance specified by Vernik and Landis (1996). Subsequently, we are confident that the individual plugs are sufficiently similar in physical properties to be considered as composite samples. Note that effective porosity and grain density measurements were not made for the horizontal plug subsamples used for XRD experiments due to the order of magnitude difference in sample scale. Subsequently, we assume that the bulk mineralogy and mineral orientation are homogeneous across the original, pre-subsampling horizontal plug.

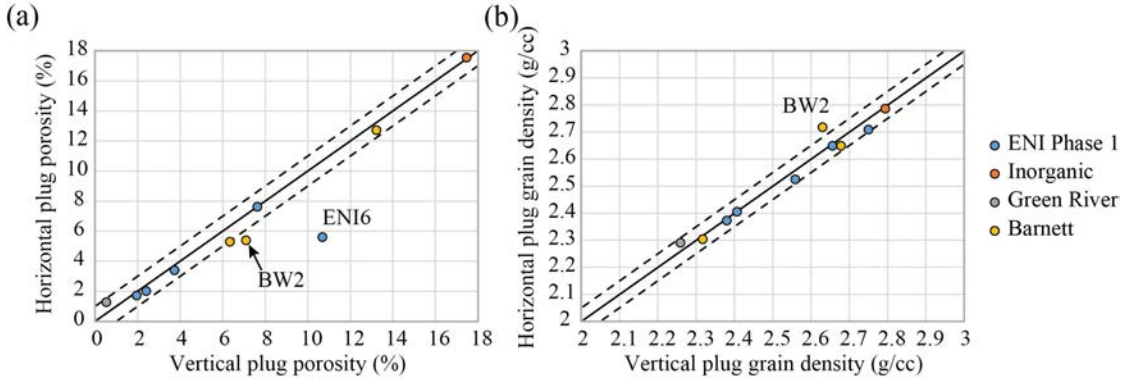

Figure 4.12: A comparison of the effective porosity (a) and grain density (b) of the horizontal plugs to those of the vertical plugs. The solid black lines indicate equal values, i.e., a pair of homogeneous plugs, while the dashed black lines indicate an error of ±1 p.u. and ±0.050 g/cc, respectively.

The effect of using two plugs per sample on S-wave velocity heterogeneity can also be quantified under the assumption that these samples are vertically transversely isotropic (VTI). In Figure 4.13, we crossplot the $V_{SV}(90°)$ and $V_S(0°)$ phases, which are equal, and will plot on the solid black line, for a perfectly VTI medium. Significant deviation from the solid black line in Figure 4.13.a indicates that, at low confining pressure, there is significant S-wave heterogeneity between the vertical and horizontal plugs – particularly those of the ENI Phase 1 samples and BW1. However, upon pressurizing the plugs to the maximum confining pressure (Figure 4.13.b), a near-total decrease in the heterogeneity between the plugs is observed. Upon unloading (Figure 4.13.c), the degree of heterogeneity increases, while remaining lower than the pre-stressed values. The improvement in agreement between Figures 4.13.a and 4.13.c is most apparent for ENI5 and BW1. The pressure-sensitivity of S-wave velocity heterogeneity indicates a crack-based origin. For example, differing degrees of cracking between plugs causes significant velocity heterogeneity at low confining pressure (when the cracks are open); however, at high confining pressure (when the cracks are closed) the intrinsic compositional and microstructural homogeneity between the plugs results in strong agreement in S-wave velocities. The noted hysteresis in heterogeneity upon unloading indicates that a fraction of the microcracks that close upon loading are deforming anelastically, i.e., they do not reopen elastically upon unloading. Variability in the increase of heterogeneity upon unloading between samples may then be related to variability in the fraction of anelastic crack closure between samples.

The exceptions to the trend of diminishing heterogeneity with increasing confining pressure are ENI4 and the Green River sample. The ENI4 sample is characterized by fractures through both the horizontal and vertical plugs; subsequently, $V_{SV}(90°)$ and $V_S(0°)$ are near equally pressure-sensitive and, thus, the degree of heterogeneity is maintained as a function of confining pressure. The lack of improvement in the Green River sample, however, is attributed to the randomly oriented, non-VTI, micritic microstructure observed in the plugs (Figure 3.17).

Further corroboration of the attribution of velocity heterogeneity in laminar shales to cracking is given by the microCT imaging of the whole plugs (Figure 4.9). Numerous cracks on the orders of 100s of microns are highlighted in the microCT slices. Variable densities of open cracks

of this aperture are hypothesized to be sufficient to generate the heterogeneity between plugs seen in our megahertz frequency (millimeter-scale wavelength), ultrasonic velocity measurements. Through this analysis, we determine that there is the potential for significant heterogeneity between plugs representing the same sample; however, for the laminar shale samples in this study, heterogeneity is minimized at high confining pressures upon the closure of cracks. We assume, given that we cannot quantify P-wave heterogeneity in the same manner, that crack closure at high confining pressure will have the same effect in minimizing potential heterogeneity in P-wave anisotropy values. Subsequently, sample selection, coring, and preservation practices are of the utmost importance in maintaining intrinsic homogeneity between plugs used in studies of shales.

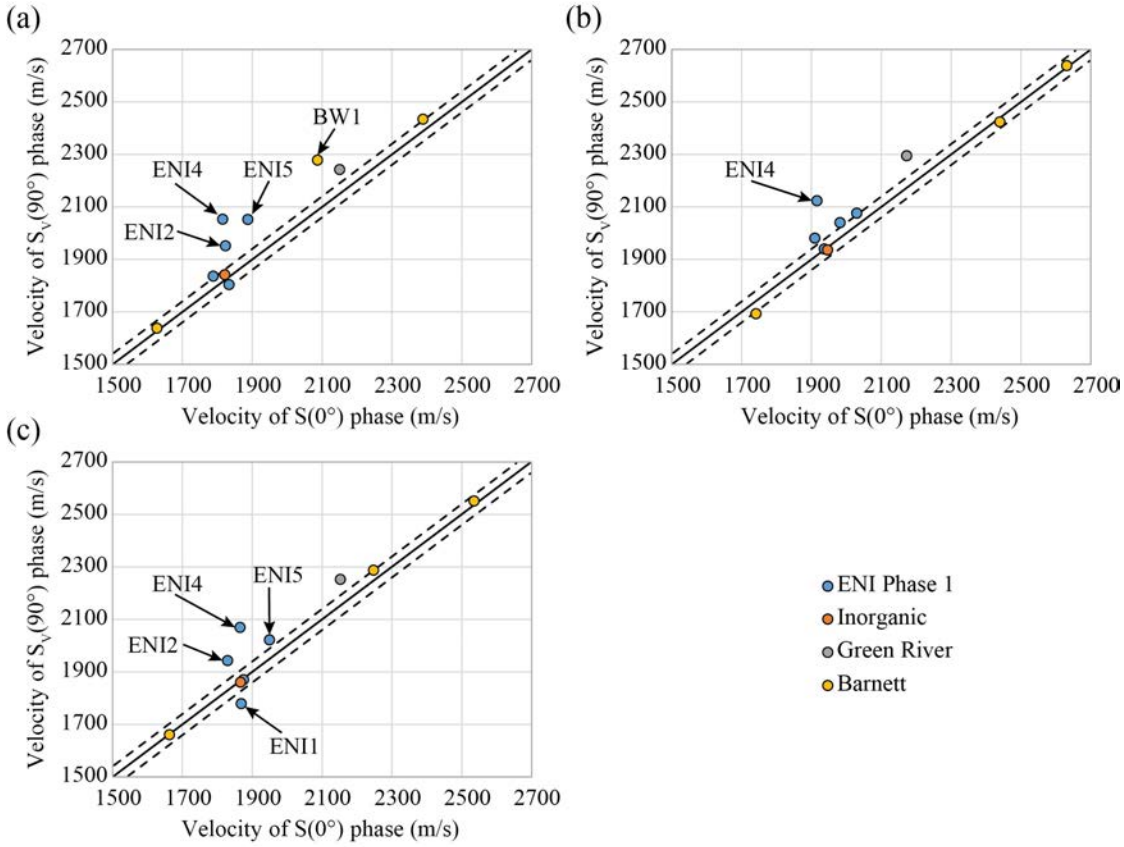

Figure 4.13: Crossplots of the $V_{SV}(90°)$ and $V_S(0°)$ phases at (a) the first confining pressure step (P_C = 1-5 MPa), (b) maximum confining pressure (P_C = 40-50 MPa), and (c) upon unloading (P_C = 1-2 MPa). For a set of homogeneous, perfectly VTI plugs, the points should fall on the solid black line. The dashed black lines mark a deviation of ±40 m/s from homogeneity, approximately the experimental error.

4.4.2 Discriminating Sources of Anisotropy

In the framework of the methodology presented in Chapter 3, we characterize the elastic anisotropy of organic-rich shale by two primary sources: (a) intrinsic, alignment-based anisotropy and (b) extrinsic, crack-dependent anisotropy. On one hand, the intrinsic anisotropy is itself a superposition of the alignment of mineral species and the alignment of the organic content. This

intrinsic component is best represented by the elastic anisotropy measured at high confining pressure, assuming that all effective microcracks are closed under the applied stress. On the other hand, the extrinsic anisotropy can be quantified by the increase in anisotropy as a function of decreasing confining pressure (Equation 4.1, where ψ is any measure of anisotropy, e.g., epsilon, and P_C is confining pressure) arising from the opening of compliant porosity, e.g., microcracks.

$$\Delta\psi = \psi\left(P_{C,max}\right) - \psi\left(P_{C,min}\right) \tag{4.1}$$

4.4.2.1 Intrinsic Inorganic Elastic Anisotropy

The intrinsic anisotropy at high confining pressure has been shown to correlate positively with the degree of alignment of a bulk clay assemblage (Johnston and Christensen, 1995). Further, the effect of the alignment of all mineral species on the ultrasonic velocity of shale has been numerically simulated (Valcke et al., 2006). In combining and furthering the methodologies of Johnston and Christensen (1995) and Valcke et al. (2006), we study the correlation of epsilon and gamma to a series of clay and crystal orientation-based parameters. Figures 4.14.a and 4.14.c show the often-used (e.g., Vernik and Landis, 1996; Vernik and Liu, 1997; Prasad et al., 2011; Zargari et al., 2011) general case of increasing anisotropy with clay content. Although this correlation is sensible as the anisotropy of the mineral frame is dominated by the highly anisotropic nature of sheet silicates (Cholach and Schmitt, 2006; Wenk et al., 2007), there is, however, considerable scatter in the data. We hypothesize that this scatter arises from differing microstructural packing/layering of clay minerals between samples: for instance, *reductio ad absurdum*, a clay-rich sample exhibiting no preferred orientation, e.g., a uniform orientation distribution function, will exhibit no bulk anisotropy.

After Johnston and Christensen (1995) and Valcke et al. (2006) combined with our observation of non-negligible crystallographic alignment in non-clay mineral species (Table 3.5), we assume that the alignment of the bulk mineral matrix is the predominant source of intrinsic anisotropy. Subsequently, we plot the high pressure anisotropy values as a function of the sample average crystallographic preferred orientation (Equation 3.8; Figure 4.14.b and 4.14.d). At first glance, it is clear that the scatter is considerably reduced when compared to the same data plotted as a function of the volumetric clay content. This improvement indicates that the elastic anisotropy is, as expected, better represented by the bulk alignment of the mineral frame rather than the volume of, albeit highly anisotropic, clay. Furthermore, the shape of the logarithmic best-fit lines for elastic anisotropy as a function of CPO (Figure 4.14) are sensible given that, as the fraction of aligned minerals approaches 100%, the corresponding change in elastic anisotropy will be less significant as compared to the impact of the initial development of an aligned texture.

The improvement in the scatter of high pressure epsilon and gamma values as a function of CPO relative to the same data as a function of clay content can be quantified through cross-validation. In doing so, we test the ability of both clay content and CPO-based models to predict the anisotropy of blind data. Cross-validation is implemented by iteratively removing each measurement from the dataset, updating the best-fit function, and predicting epsilon and

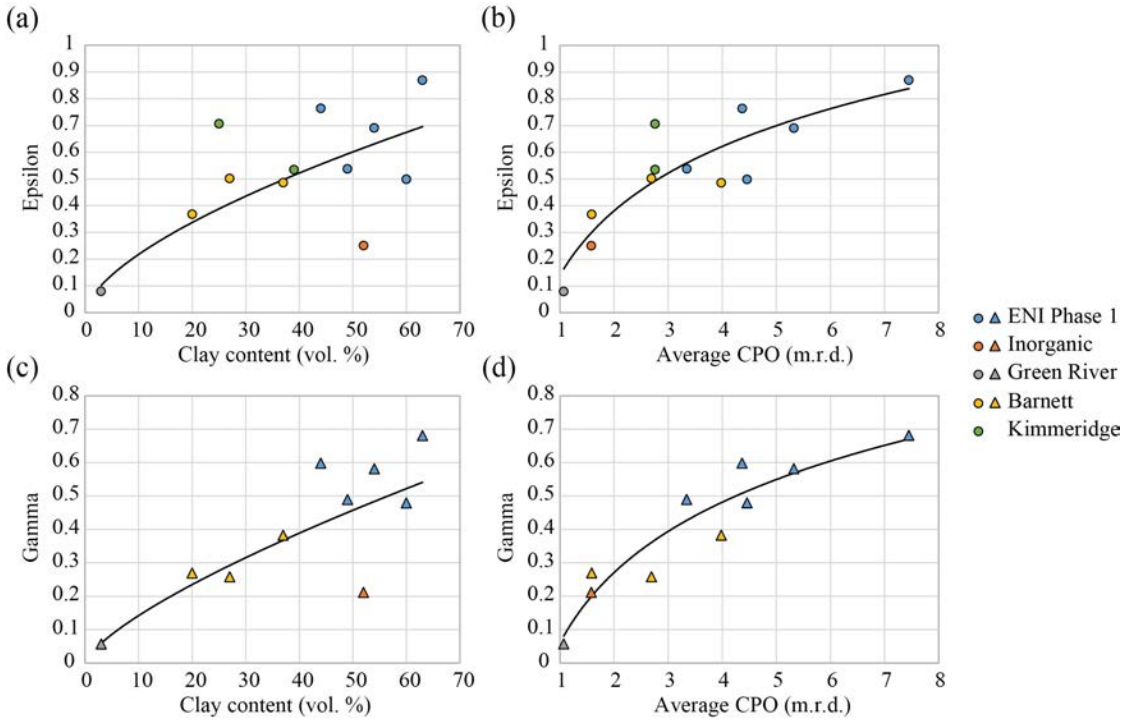

Figure 4.14: The Thomsen anisotropic parameters epsilon and gamma as a function of both volumetric clay content (a, c) and average crystallographic preferred alignment (b, d).

gamma from the known clay content and degree of CPO. The prediction error (misfit between predicted and observed values) is then quantified through the mean squared error (essentially the variance of the estimator; MSE), the root-mean-square deviation (the standard deviation of the differences between predictions and observations; RMSD), and the median absolute deviation (the median of the absolute values of the prediction errors). The measures of prediction error are defined in Equations 4.2 - 4.4 for the set of n observed and predicted anisotropy values, ψ_i and $\hat{\psi}_i$, respectively. The computed prediction error values are presented in Table 4.2. Subsequently, cross-validation further documents (via the lower error values) that mineral alignment better predicts intrinsic anisotropy than does clay content – by up to 75% for gamma prediction quantified by MSE. Note that the prediction of gamma from clay content is marginally better when characterized by MAD. The lesser error prediction of gamma results from the insensitivity of MAD to outliers (the median minimizes the L1-norm), in this case the clay-rich but weakly textured Inorganic sample.

$$MSE = \frac{1}{n}\sum_{n}\left(\hat{\psi}_i - \psi_i\right)^2 \tag{4.2}$$

$$RMSD = \sqrt{MSE} \tag{4.3}$$

$$MAD = median_i\left(|\hat{\psi}_i - \psi_i|\right) \tag{4.4}$$

Table 4.2: Quantification of the error, e.g., degree of predictability, associated with cross validation of anisotropy as a function of clay content (Clay) and average mineral alignment (CPO), respectively. The measures of fit used are mean squared error (MSE), root-mean-square deviation (RMSD), and median absolute deviation (MAD).

Measure of Fit	Epsilon		Gamma	
	Clay	CPO	Clay	CPO
MSE	0.052	0.021	0.019	0.005
RMSD	0.227	0.146	0.137	0.073
MAD	0.155	0.071	0.047	0.055

The improved predictability of elastic anisotropy from sample average CPO values over volumetric clay content is clearly documented through this study, e.g., Figure 4.14 and Table 4.2. However, in order to explicitly document the dependence of intrinsic anisotropy on crystallographic orientation, it is necessary that the numerical work of, for instance, Valcke et al. (2006) and Vasin et al. (2013) be combined with an exhaustive dataset of the scope presented here. Numerical prediction of the intrinsic anisotropy of these samples with known elastic and alignment properties would contribute additional weight to the attribution of intrinsic anisotropy to the preferred orientation of the mineral assemblage.

4.4.2.2 Intrinsic Organic Elastic Anisotropy

The organic matter can contribute to anisotropy as a mobile, crack-filling phase that may preserve soft porosity post-fluid expulsion (Tissot et al., 1974; Teerman et al., 1987; Prasad et al., 2011) and through the development of strong intrinsic elastic anisotropy through pyrographitization (Taylor et al., 1998; Peters et al., 2004). In this work, we make use of the, only recently applied to shale, CLSM technique in an attempt to nondestructively characterize the 3D structure, distribution, and alignment of the organic matter.

Due to the lack of a crystallographic structure in kerogen, it is impossible to identify an orientation of the organic matter from XRD-derived CPO measurements. However, through comparison of BSE-SEM images of shale microstructure and the 3D distribution and alignment of organic matter (Figure 4.15), it is reasonable to assume that the organic matter is aligned subparallel to the microcrystalline clay matrix in laminar shales. We are then able to model the contribution of kerogen in the CPO sample average (Equation 3.8) by assigning a kerogen CPO value equal to the average alignment of the clay content. Note that given the crystalline microstructure of the Green River sample and the kerogen distribution as a non-aligned, pore-filling phase, the Green River sample is omitted from this procedure.

The variation of epsilon and gamma as a function of mineral-based CPO and organic-inclusive CPO is documented graphically in Figure 4.16. The prediction error is computed as before and reported in Table 4.3 for clay-based, mineral CPO-based, and organic-inclusive CPO-based predictions. Graphically there is little clear improvement in the representation of intrinsic anisotropy through the inclusion of the organic content – particularly in the representation of gamma, which shows a degradation in the quality of fit. The quantification of the prediction

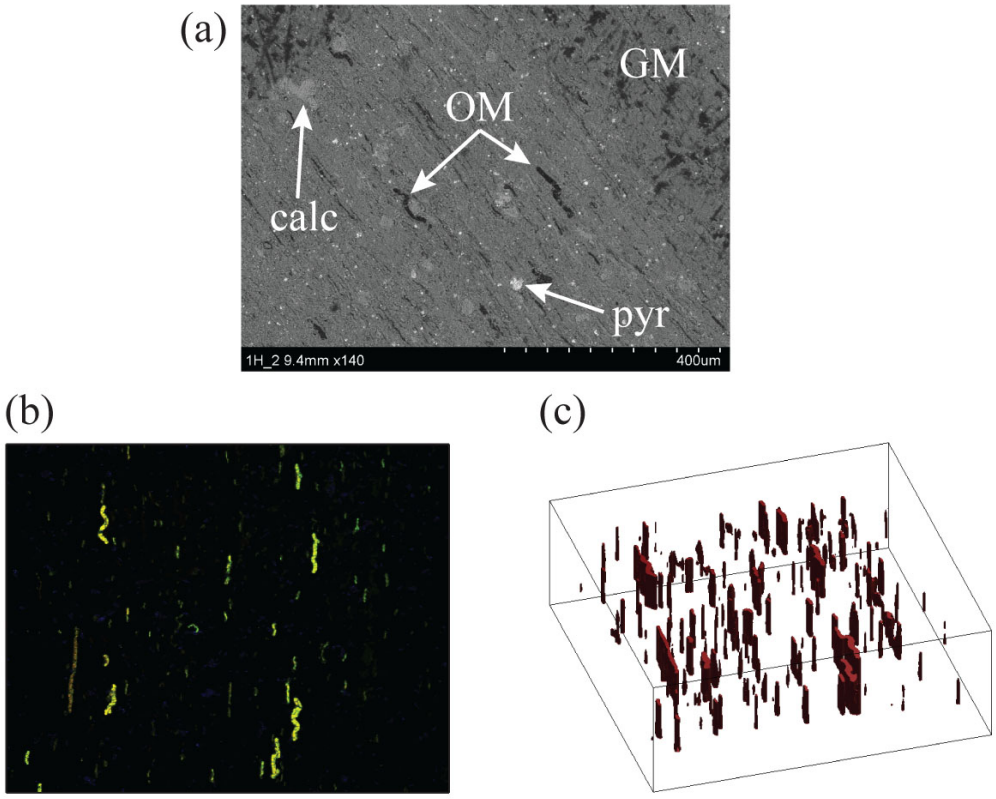

Figure 4.15: Example BSE-SEM image (a) and a 2D CLSM slice (b) and collocated 3D rendering of organic matter (c) from ENI1H. The organic matter identified in (b), by predominantly green/yellow fluorescence, corresponds with the red, segmented bodies in (c). The dimensions of the CLSM images are 900 900 µm and the 3D volume has a depth of investigation of 38 µm. Note that the BSE-SEM image is not collocated with the CLSM image, but provides a visual representation of the typical kerogen geometry and distribution in ENI1H. Identified features (in SEM) include organic matter (OM), calcite (calc), pyrite (pyr), and graphite markings used to relocate imaged areas (GM).

error (Table 4.3) corroborates the visual degradation of the representation of gamma, indicating that the predictability of gamma is up to 80% worse when the organic matter is included. The predictability of epsilon is, however, improved, although by a significantly lesser degree than between clay-based and mineral CPO-based predictions. Indeed, only the outcrop Barnett sample exhibits a change in CPO value greater than 5% post-organic inclusion – due to the high (20% by volume) organic content of the rock. Furthermore, the thermally immature outcrop sample should be expected to have developed little intrinsic organic anisotropy due to minimal devolatilization-induced aromatization. As a result of these complicating factors, to confidently identify the effect of any intrinsic organic contribution to elastic anisotropy, we require iterative elastic measurements for a single sample post-induced thermal maturation. Iterative measurements of a single sample at multiple levels of thermal maturity will enable the identification of non-mineral alignment-based changes in the intrinsic anisotropy, under the assumption of constant CPO as a function of thermal maturity.

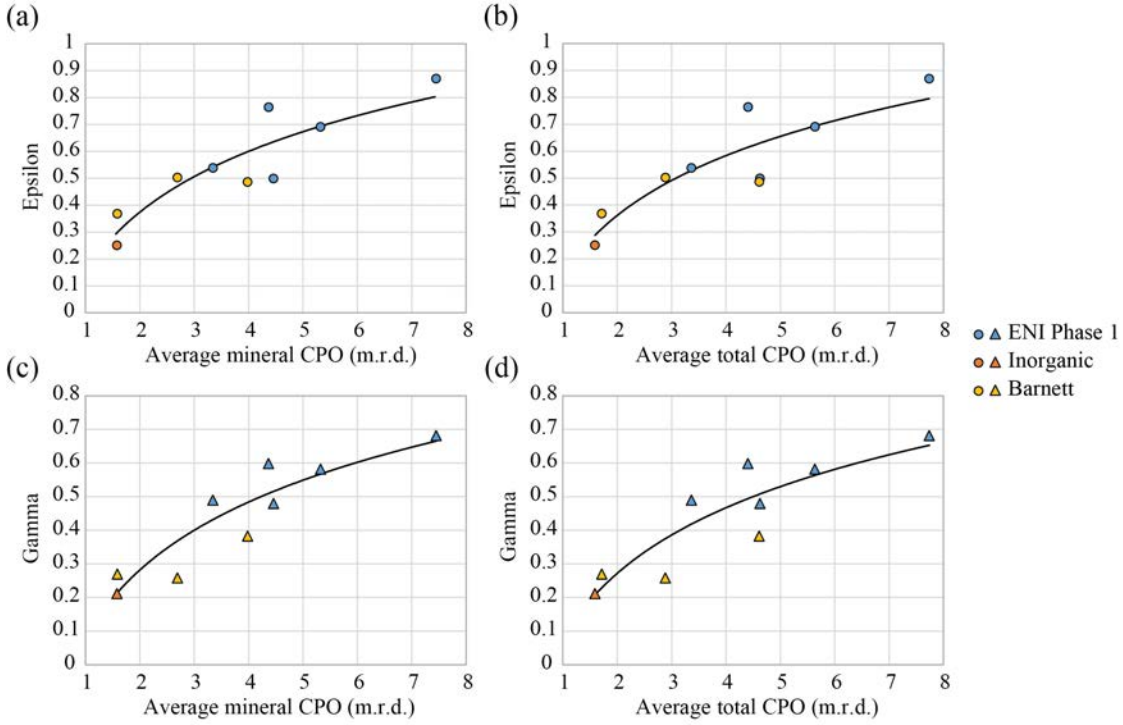

Figure 4.16: The Thomsen anisotropic parameters epsilon and gamma as a function of the average crystallographic preferred orientation of the mineral matrix (a, c) and the average crystallographic preferred orientation of both the organic and inorganic phases (b, d).

Table 4.3: Quantification of the error, e.g., degree of predictability, associated with cross validation of anisotropy as a function of clay content (Clay), average mineral alignment (CPOm), and average alignment of both the organic and inorganic phases (CPOk), respectively. The measures of fit used are mean squared error (MSE), root-mean-square deviation (RMSD), and median absolute deviation (MAD).

Measure of Fit	Epsilon			Gamma		
	Clay	CPOm	CPOk	Clay	CPOm	CPOk
MSE	0.052	0.021	0.016	0.019	0.005	0.009
RMSD	0.227	0.146	0.127	0.137	0.073	0.096
MAD	0.155	0.071	0.070	0.047	0.055	0.100

It remains to address the lack of fluorescence of the thermally immature kerogen in the outcrop Barnett sample (Figure 4.11). It is well documented that Type III and Type IV organic matter exhibit very little to no autofluorescence (Peters et al., 2004); however, given the geochemical analysis (Table 3.6), we expect the outcrop Barnett sample to be composed of Type II organic matter. Anderson et al. (2007) identify algal-derived kerogens from outcrop Eocene deposits in the Canadian Arctic, usually strongly fluorescent Type I, which exhibit no fluorescence under blue-light excitation. The authors, however, provide no inference as to the source of the lack of fluorescence. In response to the study of Anderson et al. (2007), Crosdale and Cook (2008) note that vitrinite and inertinite group macerals have been shown to experience a 70% reduction in fluorescence intensity over 3 years of exposure to air. While data is currently

unavailable for liptinite macerals (including algal-derived and other Type I/II organic matter), Crosdale and Cook hypothesize that the lack of fluorescence in liptinites is similarly affected by subaerial exposure and the subsequent weathering and oxidation. As a result, it is quite possible that prolonged exposure to outcrop conditions has reworked the organic matter in the Barnett sample such that the clearly identifiable organic bodies no longer fluoresce.

4.4.2.3 Extrinsic Elastic Anisotropy

It is often stated (Jones and Wang, 1981; Vernik, 1993; Johnston and Christensen, 1995; Wang, 2002; Allan et al., 2014) that the rapid decrease in elastic anisotropy with applied confining pressure is due to the closure of soft, i.e., crack-like porosity; however, experimental data confirming this hypothesis are scarce. Subsequently, we address the extrinsic anisotropy by correlating the change in anisotropy due to changes in the applied hydrostatic stress (Equation 4.1) with parameters quantifying the degree of microcracking.

For the ENI Phase 1 samples we can threshold microCT volumes to extract the crack volume density and standard deviation in crack orientations for each sample. The crack volume density, as used in this study, is defined in Equation 4.5, where V_{crack} is the crack volume density; a_i, L_i, w_i and are the aperture, length, and width of the i^{th} crack, respectively; and r_p and L_p are the radius and length of the plug.

$$V_{crack} = \sum_i \frac{a_i L_i w_i}{\pi r_p^2 L_p} \tag{4.5}$$

The high degree of co-alignment of the cracks documented in Table 4.4 strengthens the assumption that microcracks in well-bedded, laminar shales are oriented such that they will be closed by appropriately aligned confining stresses (in this case, perpendicular to bedding). The presence of these strongly co-aligned, subparallel to bedding cracks further indicates that intrinsic anisotropy, as characterized by high confining pressure measurements, is a mineral alignment-driven property of shale. Plotting the change in anisotropy as a function of the estimated crack volume density of the vertically cored plugs demonstrates very little correlation (Figure 4.17). The lack of correlation is not entirely surprising because the image-based volume fraction lacks any information regarding the microcrack orientation – whether deviation from co-alignment or deviation from the bedding plane. Much as plotting intrinsic anisotropy as a function of clay content lacked vital microstructural data, the volume fraction of cracks indicates nothing about the alignment or stress-sensitivity of the microcracks. Additionally, we must consider that the volume of microCT voxels is 28-48 µm cubes; subsequently, all cracks below this resolution are not included in the calculation of the volume density.

To circumvent the underestimation of cracked volumes due to the relatively poor resolution of microCT, we recast Figure 4.17 as a function of the axial strain of the vertically cored plug as computed from linear potentiometer measurements (Figure 4.18). The axial strain directly records the total degree of soft porosity, i.e., microcrack, closure, and, subsequently, is better suited for comparison with changes in anisotropy. We use the axial strain of the vertical plug as

the vertically cored plug is best oriented to monitor closure of subparallel to bedding microcracks. Note, the discussion of compliant organic body deformation under stress in Section 3.5.1 is applicable in this instance too – i.e., a fraction of the axial strain may be accommodated by kerogen deformation. However, as noted in Chapter 3, given the experimentally determined sample strain magnitudes, the deformation of kerogen is expected to be a secondary effect.

Table 4.4: The crack volume density (in volume percent) and the standard deviation of crack orientations as computed from microCT volumes.

Sample	Crack Density (vol. %)	Deviation from Alignment (deg)
ENI1V	2.49	4.56
ENI1H	1.44	2.42
ENI2V	1.78	6.13
ENI2H	1.13	2.11
ENI4V	1.02	2.95
ENI4H	1.72	2.32
ENI5V	0.64	2.58
ENI5H	0.92	2.88
ENI6V	0.52	3.59
ENI6H	0.52	5.88

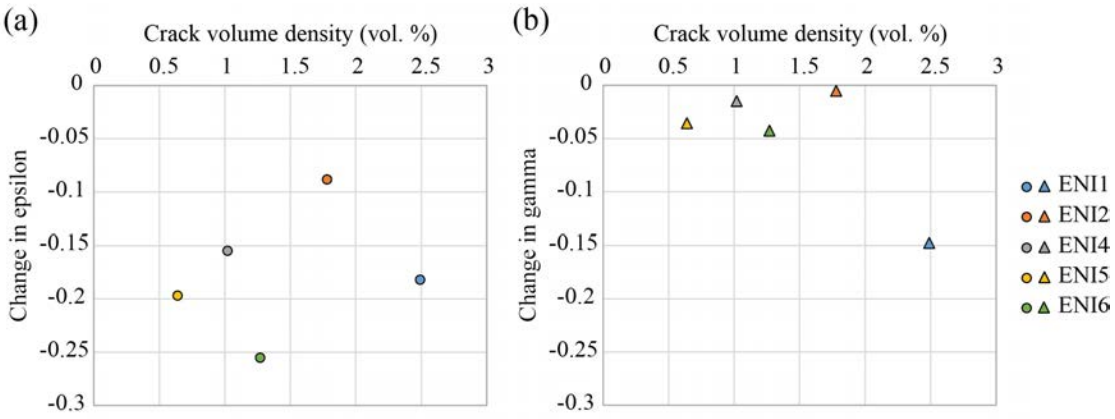

Figure 4.17: The change in the Thomsen anisotropic parameters epsilon and gamma upon unloading as a function of the computed crack volume density.

Indeed, Figure 4.18 exhibits a clear and marked increase in the degree of correlation. It is important to note that the response of the Green River and ENI1 samples are anomalous. The Green River sample exhibits little change in epsilon given the relatively high measured axial strain, indicative of isotropic deformation under stress – indeed the difference between the vertical and horizontal axial strains is 0.01% rather than 0.09%-1.2% in the laminar shale samples – further calling into question considering the interlocked micritic Green River sample as a VTI medium. The sensitivity of gamma to pressure is significantly greater for ENI1 than for the

other samples. This greater pressure-sensitivity derives, predictably, from a greater pressure-sensitivity of the elastic moduli c_{44} which is attributed to the highly fractured nature of the sample (Figure 4.9) – further highlighting the importance of sample selection, coring, and preservation practices. However, in general, there is a significant and meaningful improvement in the correlation in Figure 4.18; subsequently, we conclude that the decrease in anisotropy associated with the application of confining pressure is primarily a function of the closure of cracks as hypothesized by Jones and Wang (1981); Vernik (1993); Johnston and Christensen (1995); Wang (2002); Allan et al. (2014).

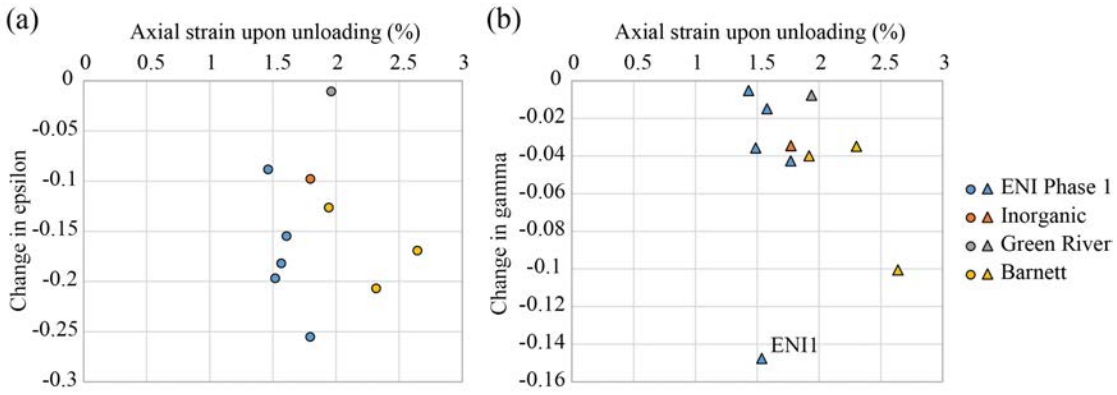

Figure 4.18: The change in the Thomsen anisotropic parameters epsilon and gamma upon unloading as a function of the measured axial strain of the vertical plug.

4.4.3 On the Relative Magnitude of Anisotropic Sources and their Variability

After the previous analyses, we are now able to combine each of the individual sources to determine their relative contribution to the elastic anisotropy of the composite shale. We assume the elastic anisotropy at high confining pressure is defined by the mineral texture and the distribution and co-alignment of the organic content. In this dataset, we see that the intrinsic anisotropy correlates strongly with the crystallographic alignment of the mineral matrix – the clay-rich ($\geq$50%), strongly aligned (CPO $>$ 4 m.r.d.) ENI Phase 1 and BO samples are highly anisotropic, while the clay-poor ($<$5%), randomly oriented (CPO = 1.07 m.r.d.) is minimally anisotropic. Efforts to extract the contribution to intrinsic anisotropy of the organic content is impeded by the lack of a crystallographic kerogenic structure and strong variability in organic properties across the dataset as a whole. A methodology for the extraction of intrinsic organic anisotropy in future work is presented in Appendix B.

The contribution of microcrack-dependent extrinsic anisotropy is governed by the applied crack-closing stresses; subsequently, the contribution of extrinsic anisotropy attains a maximum at low confining pressures. The intrinsic contribution is, thus, the anisotropy value at maximum confining pressure, while the extrinsic contributions is the magnitude of the change in anisotropy with unloading, e.g., the value at maximum confining pressure minus the final, unloaded value.

The percent contribution of intrinsic and extrinsic sources are, thus, calculated by Equations 4.6 and 4.7, where ψ_{int} and ψ_{ex} are the intrinsic and extrinsic contributions in percent, $\psi(P_{C,max})$ is anisotropy at maximum confining pressure, and $\psi(P_{C,min})$ is anisotropy upon unloading. The contributions, for both epsilon and gamma, are listed in Table 4.5. The values in Table 4.5 clearly illustrate the greater pressure-sensitivity of epsilon relative to gamma by the greater extrinsic contribution to epsilon. This greater pressure-sensitivity of epsilon results from the greater pressure-sensitivity of P-wave velocities relative to S-wave velocities (Figures 4.3, 4.4, and 4.5). The noted increased pressure-sensitivity of P-waves relative to shear modes has been previously demonstrated for a wide range of sedimentary rocks (MacBeth, 2004).

$$\psi_{int} = \frac{\psi(P_{C,max})}{\psi(P_{C,min})} \times 100 \tag{4.6}$$

$$\psi_{ex} = \frac{\Delta\psi}{\psi(P_{C,min})} = \frac{\psi(P_{C,max}) - \psi(P_{C,min})}{\psi(P_{C,min})} \times 100 \tag{4.7}$$

Table 4.5: The fraction of the total elastic anisotropy that is intrinsic and extrinsic in source for each sample, as calculated by Equations 4.6 and 4.7.

Sample	Intrinsic (%)		Extrinsic (%)	
	Epsilon	Gamma	Epsilon	Gamma
ENI1	83	82	17	18
ENI2	89	99	11	1
ENI4	76	97	24	3
ENI5	73	93	27	7
ENI6	75	93	25	7
Inorganic	72	86	28	14
Green River	88	88	12	12
BO	70	92	30	8
BW1	75	72	25	28
BW2	74	87	26	13

In Figure 4.19, the magnitude of the intrinsic contribution to anisotropy is plotted as a function of potentially pertinent parameters: clay content, average CPO, axial strain, and thermal maturity. The degree of correlation exhibited in Figure 4.19 is quite low. By omitting the anomalously textured Green River and severely cracked ENI1 and BW1 samples, there is some sensible, positive correlation between both clay content and average CPO with the contribution of intrinsic anisotropy; however, the scatter is quite severe. There exists a stronger, negative correlation between intrinsic anisotropy, particularly gamma, and axial strain. This negative correlation is, in essence, a continuation of the previously discussed point – the more cracked a sample is, the more it strains under pressure, and the greater the change in anisotropy. We observe no meaningful correlation between the relative magnitude of anisotropy sources and thermal maturity. Subsequently, we conclude that, for this sample set, it is the quantifiable crystallographic texture that determines the absolute magnitude of the intrinsic anisotropy, but that the extrinsic anisotropy is controlled by the, difficult to quantify, degree of cracking. The lack of meaningful correlation or predictability of the extrinsic anisotropy as a function of thermal maturity in this dataset may result from the obfuscation of underlying trends by the presence of

severe through-going, pressure release-induced fractures in many of the samples. Subsequently, it is pivotal that any study investigating elastic anisotropy in organic-rich shale includes the utmost care in sample selection, coring, and preservation practices.

It is also important to note between Figures 4.14, 4.18, and 4.19 that the calculated values for gamma are generally less scattered than those for epsilon. It has previously been noted that the P-wave velocities and epsilon are, for all samples, significantly more pressure-sensitive, e.g., more sensitive to cracks and compliant porosity, than the S-wave velocities and gamma. Subsequently, the effect of a fraction of the pressure release-induced cracks/fractures remaining open should have a greater effect on the measured P-waves relative to the measured S-waves. I hypothesize that the scatter present in epsilon trends (Figures 4.14, 4.18, and 4.19) are the result of open cracks/fractures at high confining pressures which have a less significant effect on the values of gamma; as a result, the gamma trends are less scattered.

Table 4.6: The contribution of the extrinsic source to the total elastic anisotropy at 25 MPa. The reported values are calculated as in Equation 4.7 with $\psi(P_{C,min})$ replaced by $\psi(P_C = 25\ MPa)$.

Sample	Extrinsic (%)	
	Epsilon	Gamma
ENI1	4	1
ENI2	4	0
ENI4	5	0
ENI5	7	0
ENI6	6	0
Inorganic	6	2
Green River	6	5
BO	9	2
BW1	0	4
BW2	3	1

The greater than 70% intrinsic contribution to both the total epsilon and gamma (Table 4.5) indicates that for these dry, drained measurements the mineral alignment-driven intrinsic anisotropy dominates over the cracking-based extrinsic contribution. Furthermore, the largely negligible extrinsic contribution (<10%) at 25 MPa (Table 4.6) indicates that the compliant porosity only opens, and becomes anisotropically important, at lower confining pressure. In situ, fluid-filled cracks will remain open at elevated confining pressures (due to the force exerted by the non-zero pore pressure), and we expect that the extrinsic anisotropic source will continue to contribute beyond the confining pressures we observe in the laboratory, e.g., ∼25 MPa. However, from the unsaturated laboratory measurements of these samples, we would expect the in situ extrinsic contribution not to exceed 30% of the total anisotropy – i.e., the unsaturated measurements serve as an upper bound for the extrinsic contribution. Furthermore, the unsaturated measurements provided in this chapter provide vital quantification of rock frame properties for future fluid substitution modeling in shales.

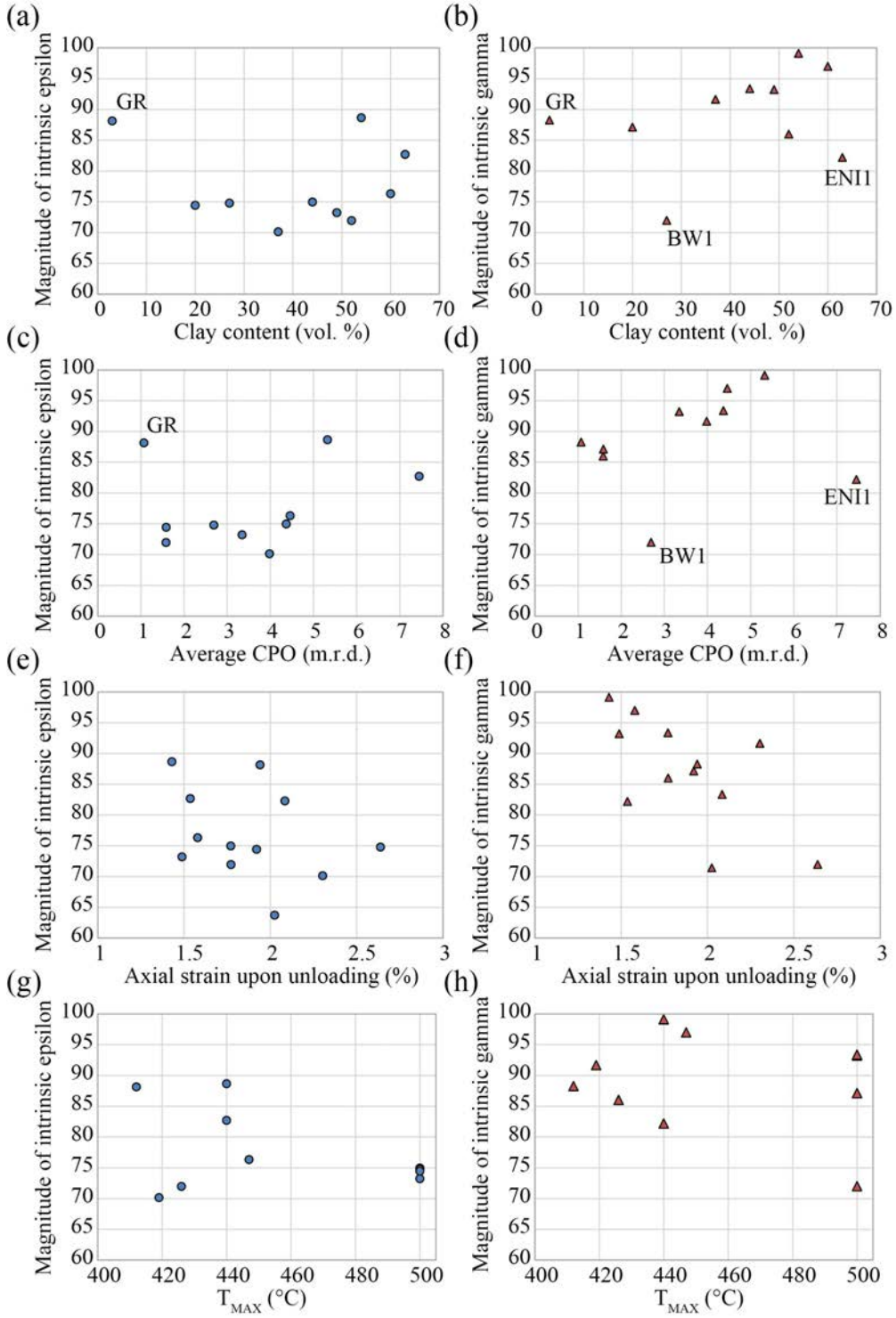

Figure 4.19: The magnitude of the intrinsic component of epsilon (left column) and gamma (right column) as a function of potentially pertinent parameters: (a, b) volumetric clay content, (c, d) average crystallographic preferred orientation, (e, f) change in axial strain upon unloading, and (g, h) thermal maturity as represented by T_{MAX}.

4.5 Conclusions

In this chapter, we have presented the application of our comprehensive experimental methodology for organic-rich shale characterization to a suite of naturally matured samples. Through the application of this methodology we are able to distinguish the contributions to elastic anisotropy of both the intrinsic, mineral alignment-based and extrinsic, compliant porosity-based sources. The strong correlation between the high confining pressure, intrinsic anisotropy value and the degree of crystallographic preferred orientation is clearly identified through cross-validation, and results in a 35-75% improvement in the predictability of intrinsic anisotropy over the, commonly used, clay content. By combining axial strain data with calculated increases in anisotropy during unloading, we demonstrate explicitly that the pressure-sensitivity of anisotropy arises primarily from the closing of soft, crack-like, porosity. Attempts to a priori predict this extrinsic source of anisotropy from X-ray microtomographic imaging, however, is hampered by issues of image resolution. For all naturally matured samples studied in this chapter, we identify that the mineral-alignment dominates the elastic anisotropy as the intrinsic component contributes greater than 70% of the total epsilon and gamma. Furthermore the extrinsic component is deemed to be negligible (<10%) at confining pressures greater than 25 MPa. In situ, with pore pressure preserving some, if not all, of the crack-like porosity, we expect the contribution of extrinsic anisotropy to remain significant at higher confining pressures than identified in this study. However, although these experiments are conducted upon unsaturated samples, they set a lower bound for the in situ contribution of the preferred orientation of minerals to shale anisotropy in fluid-filled unconventional reservoirs. Additionally, these unsaturated measurements provide a pivotal characterization of the frame needed for the application of fluid substitution models in shale.

Through the application of this methodology, we are, however, unable to definitively extract the contribution of the increasingly anisotropic residual organic matter. The difficulty in extracting the intrinsic organic contribution arises from the lack of a crystallographic structure in kerogen and pyrobitumen and the strong variability in the organic properties across the set of samples. In general, as identified from interpretation of the existing datasets in the literature (e.g., the previously discussed Vernik dataset), we find that heterogeneity between samples of different provenance, mineralogy, burial history, etc. obfuscates analysis of purely thermal maturity-dependent trends in organic-rich shale. Subsequently, iterative analysis incorporating ex situ thermal maturation (via pyrolysis) is required to address the thermal maturity dependence of the elastic properties of organic-rich shale (Chapter 5). In so doing, we expect the combination of geochemical and geophysical measurements to contribute to the improved characterization of unconventional reservoirs and the identification of sweet spots from remote sensing surveys.

4.6 Appendix

4.6.1 Appendix A: On the Correlation of the Intrinsic Values of Epsilon and Gamma

The data presented in this chapter can be compared to legacy data from the existing literature (Vernik and Nur, 1992; Vernik and Liu, 1997; Johnston and Christensen, 1995; Wang, 2002) by crossplotting epsilon and gamma (Figure 4A.1). In so doing, a strong linear relationship is apparent, where the scatter is likely attributable to small deviations from a perfectly VTI medium (as is assumed by the use of epsilon and gamma). This linear relationship is documented in Sayers (2005); however, it is not commented upon or treated in that work. In this appendix, I attempt to address the source of the strong correlation between epsilon and gamma using the existing framework of VTI theory (Thomsen, 1986).

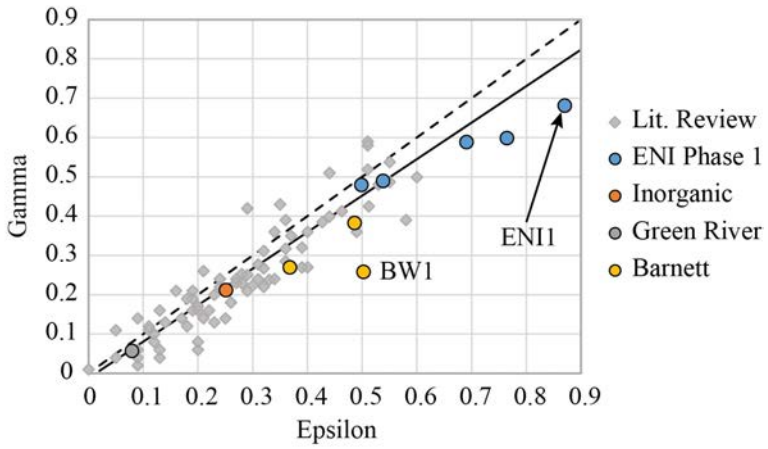

Figure 4A.1: A comparison of the high confining pressure magnitude of epsilon and gamma for the samples presented in this chapter and samples from a literature review of unsaturated measurements from Vernik and Nur (1992); Vernik and Liu (1997); Johnston and Christensen (1995); Wang (2002). The dashed black line indicates equal values of epsilon and gamma, while the solid black line is an extrapolation of the linear best fit to the literature review data.

The linear relationship observed in Figure 4A.1 can be represented as in Equation 4A.3 by application of the definitions for epsilon and gamma (Equations 4A.1 and 4A.2) in which we assume the horizontal and vertical bulk densities are equivalent.

$$\varepsilon = \frac{c_{11} - c_{33}}{2c_{33}} = \frac{\left(V_P\left(90°\right)\right)^2 - \left(V_P\left(0°\right)\right)^2}{2\left(V_P\left(0°\right)\right)^2} \tag{4A.1}$$

$$\gamma = \frac{c_{66} - c_{44}}{2c_{44}} = \frac{\left(V_{SH}\left(90°\right)\right)^2 - \left(V_S\left(0°\right)\right)^2}{2\left(V_S\left(0°\right)\right)^2} \tag{4A.2}$$

$$\frac{\left(V_{SH}\left(90°\right)\right)^2 - \left(V_S\left(0°\right)\right)^2}{2\left(V_S\left(0°\right)\right)^2} = m\left(\frac{\left(V_P\left(90°\right)\right)^2 - \left(V_P\left(0°\right)\right)^2}{2\left(V_P\left(0°\right)\right)^2}\right) + b \tag{4A.3}$$

Through simple algebra, Equation 4A.3 can be reduced to

$$\left(\frac{V_P(0°)}{V_S(0°)}\right)^2 = m\left(\frac{V_P(90°)}{V_{SH}(90°)}\right)^2 - \tau\left(\frac{V_P(0°)}{V_{SH}(90°)}\right)^2 \tag{4A.4}$$

where $\tau = m + 2b - 1$. Replacing the velocities with their respective elastic moduli and canceling out the equivalent bulk densities yields

$$\frac{c_{33}}{c_{44}} = m\frac{c_{11}}{c_{66}} - \tau\frac{c_{33}}{c_{66}}. \tag{4A.5}$$

Introducing c_{12} via Equation 4A.6 (see Mavko et al., 2009) and performing additional algebra yields Equation 4A.7 which bears underlying similarities to expressions for the Poisson Ratios of a VTI medium (Equations 4A.8-4A.10). This underlying similarity indicates that the anisotropic Poisson Ratios may be the source of the linear relationship between epsilon and gamma; however, without off-axis measurements, e.g., velocities measured on plugs cored 45 degrees to bedding, we are unable to quantify the Thomsen parameter delta and, by extension, the elastic modulus c_{13}. Future work incorporating characterization of epsilon, gamma, and delta should be able to further investigate the unexpected, consistent relationship between epsilon and gamma.

$$c_{12} = c_{11} - 2c_{66} \tag{4A.6}$$

$$\frac{c_{33}(c_{11} - c_{12})}{c_{44}} = 2(mc_{11} - \tau c_{33}) \tag{4A.7}$$

$$\nu_{31} = \nu_{32} = \frac{c_{13}}{c_{11} + c_{12}} \tag{4A.8}$$

$$\nu_{13} = \nu_{23} = \frac{c_{13}(c_{11} - c_{12})}{c_{33}c_{11} - c_{13}^2} \tag{4A.9}$$

$$\nu_{12} = \nu_{21} = \frac{c_{33}c_{12} - c_{13}^2}{c_{33}c_{11} - c_{13}^2} \tag{4A.10}$$

4.6.2 Appendix B: On Future Considerations of Intrinsic Organic Anisotropy

Given the noted difficulty in extracting the contribution to intrinsic anisotropy of the organic content due to the lack of a crystallographic kerogenic structure and strong variability in organic properties across different samples, the best candidate for identifying the contribution is iterative characterization of a sample pre- and post-pyrolysis. In order to identify any evolution in the intrinsic organic contribution to anisotropy, the sample must be characterized pre- and post-pyrolysis in terms of high confining pressure anisotropy, mineralogy, and average crystallographic preferred orientation. In Figure 4B.1, I document hypothetical examples of anisotropy evolution post-pyrolysis. An increase in the intrinsic anisotropy at constant CPO (move from the black triangle to red triangle #1 in Figure 4B.1), indicates that the degree of anisotropy of the sample

has increased with no change in the crystallographic alignment. Subsequently, this would be interpreted as the development of an alignment of the aromatized pyrobitumen – that is, the development of intrinsic organic anisotropy. On the other hand, a change in elastic anisotropy that correlates with a change in the CPO (either an increase in anisotropy and alignment or a decrease in both properties) would result in movement approximately along the underlying trend to red triangles #2 and #3. In this case, the change in intrinsic anisotropy results from a pyrolysis-induced change in the texture of the inorganic rock frame and an intrinsic organic contribution is not seen.

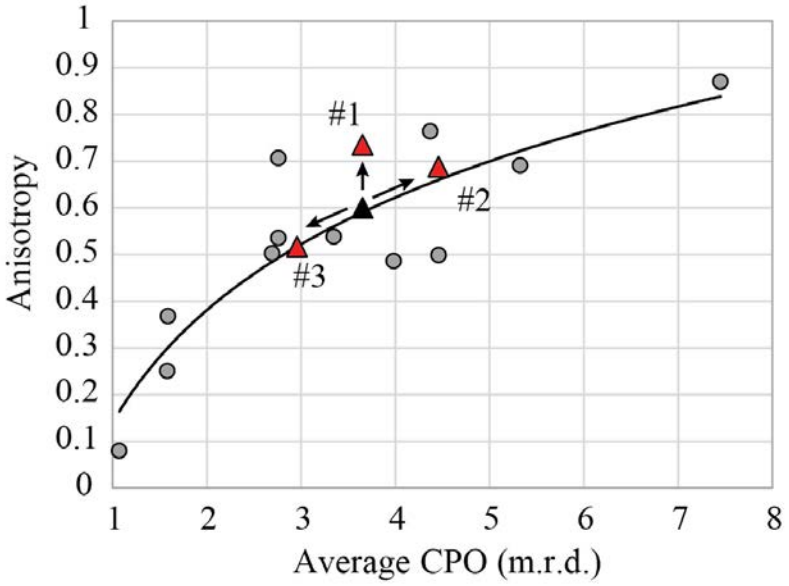

Figure 4B.1: The possible hypothetical evolutions of the intrinsic anisotropy after induced thermal maturation. The black triangle represents the thermally immature baseline value, while the red triangles represent potential post-pyrolysis anisotropy-CPO pairs. The dataset from Figure 4.14 is included to define the trendline.

The primary hindrance to the application of this technique is the fragility of the subsamples used for synchrotron X-ray diffraction experiments to quantify the mineralogy and CPO. As identified in Chapter 3, the heterogeneity between subsamples is sufficiently great that it obfuscates any changes in the mineralogy or microstructure resulting from thermal alteration (Section 3.5.2.2). Subsequently, iterative measurements must be conducted on the same 0.2 cm thick, 2.5 cm diameter subsample. The extreme thinness of the sample relative to its width makes it very fragile and likely to fracture during extraction from the pyrolysis reactor. In order to implement the iterative procedure documented here, we require the ability to use thicker subsamples during synchrotron X-ray diffraction experiments or an adaptation of the sample extraction protocol that better protects extremely thin subsamples. Further, the formation of a fully aromatized pyrographite phase requires extensive heating of the progenitor organic matter, verging upon conditions representative of greenschist metamorphism. I hypothesize that no samples in this dataset have attained, or are later pyrolyzed to attain, such a high degree of thermal alteration.

As a result of these concerns, the iterative data requisite to identifying the intrinsic organic anisotropic component was not collected. Subsequently the iterative characterization pre- and post-pyrolysis in Chapter 5 is limited to the discrimination of the bulk intrinsic and extrinsic contributions to elastic anisotropy.

4.6.3 Appendix C: Acoustic Velocity Dataset

Table 4C.1: Acoustic velocity (m/s) and computed porosity values as a function of confining pressure (P_C) for sample ENI1. Velocity phases are as illustrated in Figure 3.4, the orientation of porosity values are denoted as vertical ($\phi(0°)$) and horizontal ($\phi(90°)$), respectively.

P_C (MPa)	$V_P(0°)$	$V_S(0°)$	$V_P(90°)$	$V_{SH}(90°)$	$V_{SV}(90°)$	$\varphi(0°)$	$\varphi(90°)$
1	-	-	-	-	-	2.40	2.02
5	2723	1833	4843	2891	1804	1.59	1.21
7.5	2796	1869	4931	2905	1824	1.18	0.79
10	2840	1887	4979	2917	1834	0.82	0.43
20	2946	1911	5038	2940	1882	-0.44	-0.83
30	3012	1923	5055	2965	1927	-1.55	-1.95
40	3071	1937	5084	2983	1940	-2.67	-3.07
35	3062	1938	5076	2981	1939	-2.40	-2.80
25	3020	1932	5067	2969	1927	-1.51	-1.91
15	2965	1921	5027	2959	1894	-0.47	-0.86
7.5	2889	1906	4988	2934	1839	0.58	0.19
2	2770	1868	4882	2900	1779	1.30	0.92
0.1	-	-	-	-	-	1.89	1.51

Table 4C.2: Acoustic velocity (m/s) and computed porosity values as a function of confining pressure (P_C) for sample ENI2. Velocity phases are as illustrated in Figure 3.4, the orientation of porosity values are denoted as vertical ($\phi(0°)$) and horizontal ($\phi(90°)$), respectively.

P_C (MPa)	$V_P(0°)$	$V_S(0°)$	$V_P(90°)$	$V_{SH}(90°)$	$V_{SV}(90°)$	$\varphi(0°)$	$\varphi(90°)$
1	-	-	-	-	-	1.96	1.72
5	2997	1823	4800	2862	1952	1.21	0.96
7.5	3052	1849	4885	2877	1961	0.77	0.53
10	3077	1860	4917	2880	1965	0.39	0.15
20	3166	1885	5014	2902	1975	-0.84	-1.08
30	3221	1901	5027	2916	1981	-1.94	-2.19
40	3264	1910	5032	2924	1981	-2.94	-3.19
35	3258	1910	5034	2921	1980	-2.79	-3.04
25	3226	1905	5026	2912	1981	-1.94	-2.19
15	3179	1894	5013	2898	1975	-0.89	-1.14
7.5	3121	1877	4960	2887	1970	0.10	-0.15
2	3035	1829	4848	2874	1943	0.86	0.62
0.1	-	-	-	-	-	1.46	1.22

Table 4C.3: Acoustic velocity (m/s) and computed porosity values as a function of confining pressure (P_C) for sample ENI4. Velocity phases are as illustrated in Figure 3.4, the orientation of porosity values are denoted as vertical ($\phi(0°)$) and horizontal ($\phi(90°)$), respectively.

P_C (MPa)	$V_P(0°)$	$V_S(0°)$	$V_P(90°)$	$V_{SH}(90°)$	$V_{SV}(90°)$	$\varphi(0°)$	$\varphi(90°)$
1	-	-	-	-	-	3.74	4.92
5	2872	1815	4836	2885	2053	2.89	4.08
7.5	3061	1847	4891	2900	2070	2.52	3.72
10	3169	1863	4928	2918	2086	2.16	3.36
20	3388	1895	4990	2954	2110	1.02	2.23
30	3430	1906	5010	2963	2123	0.00	1.23
40	3484	1912	5024	2968	2123	-0.90	0.34
50	3535	1916	5047	2973	2124	-1.83	-0.58
45	3527	1916	5050	2961	2123	-1.65	-0.40
35	3505	1915	5042	2961	2123	-0.95	0.29
25	3474	1912	5027	2959	2122	-0.10	1.13
15	3415	1907	4998	2962	2109	0.90	2.11
7.5	3316	1895	4940	2939	2096	1.80	3.00
2	3159	1865	4848	2919	2070	2.50	3.70
0.1	-	-	-	-	-	3.00	4.20

Table 4C.4: Acoustic velocity (m/s) and computed porosity values as a function of confining pressure (P_C) for sample ENI5. Velocity phases are as illustrated in Figure 3.4, the orientation of porosity values are denoted as vertical ($\phi(0°)$) and horizontal ($\phi(90°)$), respectively.

P_C (MPa)	$V_P(0°)$	$V_S(0°)$	$V_P(90°)$	$V_{SH}(90°)$	$V_{SV}(90°)$	$\varphi(0°)$	$\varphi(90°)$
1	-	-	-	-	-	7.64	7.62
5	2867	1887	4763	2894	2052	6.96	6.94
7.5	2959	1909	4777	2901	2058	6.60	6.58
10	3022	1926	4780	2908	2063	6.24	6.22
20	3156	1971	4801	2915	2073	5.15	5.13
30	3234	1990	4814	2916	2075	4.14	4.12
40	3304	2010	4831	2918	2075	3.28	3.26
50	3363	2030	4847	2921	2076	2.37	2.35
45	3357	2030	4849	2919	2076	2.54	2.52
35	3323	2023	4841	2922	2079	3.25	3.23
25	3287	2010	4835	2920	2079	4.09	4.07
15	3226	1997	4811	2919	2073	5.06	5.04
7.5	3148	1979	4777	2906	2062	5.94	5.92
2	3010	1949	4731	2895	2022	6.65	6.63
0.1	-	-	-	-	-	7.14	7.12

Table 4C.5: Acoustic velocity (m/s) and computed porosity values as a function of confining pressure (P_C) for sample ENI6. Velocity phases are as illustrated in Figure 3.4, the orientation of porosity values are denoted as vertical ($\phi(0°)$) and horizontal ($\phi(90°)$), respectively.

P_C (MPa)	$V_P(0°)$	$V_S(0°)$	$V_P(90°)$	$V_{SH}(90°)$	$V_{SV}(90°)$	$\varphi(0°)$	$\varphi(90°)$
1	-	-	-	-	-	10.70	5.60
5	2626	1788	4622	2755	1836	10.08	4.95
7.5	2711	1853	4731	2827	1864	9.76	4.61
10	2780	1890	4809	2880	1885	9.48	4.63
20	2965	1930	4908	2936	1947	8.52	3.29
30	3073	1952	4953	2959	2004	7.61	2.34
40	3154	1969	4989	2994	2018	6.74	1.41
50	3227	1982	5027	3023	2040	5.91	0.53
45	3216	1980	5031	3022	2038	6.13	0.77
35	3185	1976	5011	3010	2029	6.80	1.48
25	3134	1967	4983	2985	2014	7.58	2.31
15	3049	1950	4939	2947	1963	8.49	3.26
7.5	2934	1928	4854	2903	1916	9.22	4.04
2	2741	1875	4682	2826	1871	9.82	4.67
0.1	-	-	-	-	-	10.25	5.13

Table 4C.6: Acoustic velocity (m/s) and computed porosity values as a function of confining pressure (P_C) for the Inorganic sample. Velocity phases are as illustrated in Figure 3.4, the orientation of porosity values are denoted as vertical ($\phi(0°)$) and horizontal ($\phi(90°)$), respectively.

P_C (MPa)	$V_P(0°)$	$V_S(0°)$	$V_P(90°)$	$V_{SH}(90°)$	$V_{SV}(90°)$	$\varphi(0°)$	$\varphi(90°)$
1	2612	1821	3638	2275	1842	17.47	17.55
2	2656	1840	3647	2283	1854	17.31	17.39
5	2768	1856	3673	2293	1878	16.83	16.91
7.5	2809	1867	3680	2295	1898	16.54	16.62
10	2844	1885	3697	2298	1906	16.19	16.27
20	2911	1908	3705	2305	1926	15.14	15.23
30	2968	1923	3725	2309	1929	14.09	14.17
40	3015	1935	3746	2316	1932	13.05	13.13
50	3069	1946	3767	2325	1936	12.02	12.11
45	3058	1943	3756	2323	1933	12.12	12.21
35	3049	1943	3754	2320	1932	12.80	12.88
25	3014	1934	3737	2317	1923	13.66	13.75
15	2966	1922	3716	2309	1908	14.64	14.72
7.5	2911	1902	3687	2301	1896	15.44	15.53
5	2871	1888	3676	2293	1881	15.82	15.90
2	2828	1875	3647	2287	1872	16.15	16.23
1	2789	1866	3639	2283	1861	16.35	16.43
0.1	-	-	-	-	-	16.64	16.72

Table 4C.7: Acoustic velocity (m/s) and computed porosity values as a function of confining pressure (P_C) for the Green River sample. Velocity phases are as illustrated in Figure 3.4, the orientation of porosity values are denoted as vertical ($\phi(0°)$) and horizontal ($\phi(90°)$), respectively.

P_C (MPa)	$V_P(0°)$	$V_S(0°)$	$V_P(90°)$	$V_{SH}(90°)$	$V_{SV}(90°)$	$\varphi(0°)$	$\varphi(90°)$
1	4075	2150	4401	2458	2242	0.53	1.28
2	4088	2156	4417	2463	2251	0.35	1.10
5	4106	2156	4426	2472	2260	-0.27	0.49
7.5	4126	2160	4438	2477	2269	-0.70	0.05
10	4145	2162	4460	2482	2276	-1.12	-0.37
20	4169	2168	4489	2486	2281	-2.45	-1.68
30	4196	2172	4509	2491	2286	-3.71	-2.94
40	4225	2173	4521	2496	2293	-4.90	-4.11
50	4229	2173	4535	2497	2295	-5.95	-5.16
45	4222	2171	4528	2492	2292	-5.78	-4.99
35	4207	2170	4521	2493	2288	-4.91	-4.12
25	4187	2166	4508	2488	2286	-3.74	-2.97
15	4161	2164	4489	2481	2281	-2.42	-1.65
7.5	4124	2160	4457	2469	2274	-1.37	-0.61
5	4106	2157	4445	2464	2268	-0.88	-0.13
2	4086	2155	4423	2461	2259	-0.48	0.27
1	4073	2152	4408	2458	2253	-0.23	0.52
0.1	-	-	-	-	-	0.11	0.86

Table 4C.8: Acoustic velocity (m/s) and computed porosity values as a function of confining pressure (P_C) for sample BO. Velocity phases are as illustrated in Figure 3.4, the orientation of porosity values are denoted as vertical ($\phi(0°)$) and horizontal ($\phi(90°)$), respectively.

P_C (MPa)	$V_P(0°)$	$V_S(0°)$	$V_P(90°)$	$V_{SH}(90°)$	$V_{SV}(90°)$	$\varphi(0°)$	$\varphi(90°)$
1	2222	1627	3577	2227	1638	13.23	12.72
2	2233	1632	3594	2236	1652	13.07	12.56
5	2285	1654	3608	2250	1664	12.57	12.06
7.5	2326	1665	3623	2267	1669	12.21	11.70
10	2348	1672	3632	2275	1674	11.89	11.37
20	2462	1687	3657	2284	1676	10.66	10.13
30	2548	1706	3677	2294	1680	9.38	8.84
40	2604	1726	3690	2306	1687	8.10	7.56
50	2646	1741	3717	2313	1693	6.84	6.30
45	2636	1740	3712	2312	1692	6.96	6.41
35	2605	1733	3709	2311	1629	7.82	7.28
25	2566	1725	3688	2303	1692	8.93	8.40
15	2498	1709	3674	2290	1690	10.10	9.57
7.5	2435	1692	3652	2279	1688	11.06	10.54
5	2402	1681	3637	2274	1683	11.50	10.98
2	2366	1671	3622	2262	1671	11.86	11.35
1	2338	1663	3611	2253	1661	12.09	11.58
0.1	-	-	-	-	-	12.37	11.86

Table 4C.9: Acoustic velocity (m/s) and computed porosity values as a function of confining pressure (P_C) for sample BW1. Velocity phases are as illustrated in Figure 3.4, the orientation of porosity values are denoted as vertical ($\phi(0°)$) and horizontal ($\phi(90°)$), respectively.

P_C (MPa)	$V_P(0°)$	$V_S(0°)$	$V_P(90°)$	$V_{SH}(90°)$	$V_{SV}(90°)$	$\varphi(0°)$	$\varphi(90°)$
1	2845	2087	4988	2927	2278	6.34	5.29
2	2922	2133	5037	2947	2293	6.14	5.09
5	3150	2211	5134	2959	2324	5.33	4.26
7.5	3241	2256	5183	2969	2361	4.85	3.78
10	3317	2285	5217	2974	2387	4.33	3.26
20	3554	2359	5311	2979	2404	2.78	1.69
30	3690	2398	5378	2990	2418	1.30	0.19
40	3806	2420	5433	2997	2427	-0.09	-1.21
50	3868	2440	5476	3005	2424	-1.34	-2.47
45	3850	2436	5464	3002	2419	-1.22	-2.35
35	3835	2426	5432	3001	2420	-0.30	-1.42
25	3809	2424	5362	3004	2405	1.00	-0.11
15	3710	2399	5294	2992	2391	2.38	1.28
7.5	3585	2347	5212	2980	2364	3.61	2.53
5	3475	2298	5150	2966	2327	4.20	3.13
2	3390	2274	5061	2952	2294	4.65	3.58
1	3275	2247	5013	2945	2288	4.98	3.91
0.1	-	-	-	-	-	5.40	4.34

Table 4C.10: Acoustic velocity (m/s) and computed porosity values as a function of confining pressure (P_C) for sample BW2. Velocity phases are as illustrated in Figure 3.4, the orientation of porosity values are denoted as vertical ($\phi(0°)$) and horizontal ($\phi(90°)$), respectively.

P_C (MPa)	$V_P(0°)$	$V_S(0°)$	$V_P(90°)$	$V_{SH}(90°)$	$V_{SV}(90°)$	$\varphi(0°)$	$\varphi(90°)$
1	3329	2389	4862	3087	2434	7.10	5.39
2	3481	2446	4896	3110	2479	6.94	5.23
5	3642	2529	4961	3154	2549	6.39	4.66
7.5	3735	2554	4994	3160	2562	6.03	4.30
10	3784	2573	5025	3171	2579	5.62	3.88
20	3889	2601	5081	3173	2588	4.31	2.55
30	3950	2621	5113	3175	2598	3.09	1.30
40	3997	2626	5147	3178	2623	1.91	0.11
50	4026	2631	5169	3181	2638	0.76	-1.07
45	4018	2628	5169	3176	2634	0.81	-1.01
35	3995	2628	5157	3175	2628	1.71	-0.10
25	3974	2619	5137	3172	2614	2.88	1.09
15	3930	2611	5103	3170	2600	4.08	2.31
7.5	3859	2587	5068	3166	2592	5.11	3.36
5	3808	2576	5050	3160	2585	5.57	3.83
2	3726	2561	5032	3155	2579	5.99	4.26
1	3646	2534	5010	3142	2551	6.22	4.49
0.1	-	-	-	-	-	6.53	4.81

4.6.4 Appendix D: Velocity-Derived Elastic Dataset

Table 4D.1: Computed elastic moduli and Thomsen's elastic anisotropy parameters as a function of confining pressure (P_C) for sample ENI1.

P_C (MPa)	C_{11} (GPa)	C_{33} (GPa)	C_{44} (GPa)	C_{66} (GPa)	ε (-)	γ (-)
1	-	-	-	-	-	-
5	54.91	17.37	7.62	19.56	1.081	0.784
7.5	57.16	18.39	7.83	19.84	1.055	0.768
10	58.51	19.04	7.94	20.08	1.037	0.764
20	60.64	20.74	8.46	20.65	0.962	0.720
30	61.73	21.93	8.97	21.23	0.908	0.684
40	63.13	23.04	9.20	21.73	0.870	0.681
35	62.78	22.84	9.15	21.64	0.874	0.682
25	62.00	22.04	8.97	21.29	0.907	0.687
15	60.39	21.03	8.58	20.93	0.936	0.720
7.5	58.85	19.75	8.00	20.36	0.990	0.773
2	55.96	18.03	7.43	19.75	1.052	0.829
0.1	-	-	-	-	-	-

Table 4D.2: Computed elastic moduli and Thomsen's elastic anisotropy parameters as a function of confining pressure (P_C) for sample ENI2.

P_C (MPa)	C_{11} (GPa)	C_{33} (GPa)	C_{44} (GPa)	C_{66} (GPa)	ε (-)	γ (-)
1	-	-	-	-	-	-
5	54.90	21.36	9.08	19.52	0.785	0.575
7.5	57.13	22.25	9.20	19.82	0.784	0.576
10	58.10	22.70	9.28	19.94	0.780	0.574
20	61.16	24.33	9.49	20.48	0.757	0.579
30	62.15	25.45	9.65	20.90	0.721	0.583
40	62.88	26.41	9.75	21.23	0.691	0.589
35	62.83	26.26	9.73	21.16	0.696	0.588
25	62.13	25.54	9.65	20.85	0.716	0.580
15	61.17	24.55	9.49	20.44	0.746	0.576
7.5	59.29	23.42	9.36	20.09	0.766	0.573
2	56.21	21.98	9.03	19.76	0.779	0.594
0.1	-	-	-	-	-	-

Table 4D.3: Computed elastic moduli and Thomsen's elastic anisotropy parameters as a function of confining pressure (P_C) for sample ENI4.

P_C (MPa)	C_{11} (GPa)	C_{33} (GPa)	C_{44} (GPa)	C_{66} (GPa)	ε (-)	γ (-)
1	-	-	-	-	-	-
5	56.65	20.50	10.21	20.16	0.882	0.487
7.5	58.15	23.38	10.41	20.45	0.744	0.482
10	59.27	25.13	10.62	20.78	0.679	0.479
20	61.47	29.07	10.99	21.54	0.557	0.480
30	62.61	30.09	11.24	21.90	0.540	0.475
40	63.53	31.34	11.35	22.17	0.514	0.477
50	64.69	32.57	11.46	22.44	0.493	0.479
45	64.64	32.36	11.43	22.23	0.499	0.472
35	63.99	31.73	11.35	22.07	0.508	0.473
25	63.10	30.91	11.24	21.86	0.521	0.472
15	61.73	29.58	11.00	21.69	0.544	0.486
7.5	59.78	27.62	10.76	21.16	0.582	0.483
2	57.15	24.89	10.42	20.71	0.648	0.494
0.1	-	-	-	-	-	-

Table 4D.4: Computed elastic moduli and Thomsen's elastic anisotropy parameters as a function of confining pressure (P_C) for sample ENI5.

P_C (MPa)	C_{11} (GPa)	C_{33} (GPa)	C_{44} (GPa)	C_{66} (GPa)	ε (-)	γ (-)
1	-	-	-	-	-	-
5	56.06	20.32	10.40	20.69	0.880	0.495
7.5	56.59	21.72	10.51	20.87	0.803	0.493
10	56.89	22.74	10.60	21.06	0.751	0.494
20	58.06	25.10	10.83	21.40	0.657	0.488
30	58.99	26.63	10.96	21.64	0.608	0.487
40	59.93	28.04	11.06	21.88	0.569	0.489
50	60.90	29.34	11.18	22.12	0.538	0.490
45	60.86	29.18	11.15	22.05	0.543	0.489
35	60.20	28.38	11.10	21.94	0.561	0.488
25	59.53	27.53	11.01	21.71	0.581	0.486
15	58.36	26.25	10.84	21.48	0.612	0.491
7.5	57.00	24.76	10.61	21.09	0.651	0.494
2	55.49	22.47	10.14	20.78	0.735	0.525
0.1	-	-	-	-	-	-

Table 4D.5: Computed elastic moduli and Thomsen's elastic anisotropy parameters as a function of confining pressure (P_C) for sample ENI6.

P_C (MPa)	C_{11} (GPa)	C_{33} (GPa)	C_{44} (GPa)	C_{66} (GPa)	ε (-)	γ (-)
1	-	-	-	-	-	-
5	55.02	17.04	8.68	19.55	1.115	0.627
7.5	57.84	18.24	8.98	20.66	1.086	0.651
10	59.94	19.23	9.21	21.51	1.058	0.668
20	63.11	22.11	9.93	22.59	0.927	0.637
30	64.90	23.98	10.62	23.17	0.853	0.590
40	66.48	25.51	10.88	23.94	0.803	0.601
50	68.11	26.94	11.21	24.63	0.764	0.599
45	68.05	26.69	11.16	24.55	0.775	0.600
35	67.03	25.98	10.99	24.18	0.790	0.601
25	65.73	24.95	10.74	23.58	0.817	0.598
15	63.93	23.39	10.10	22.77	0.866	0.628
7.5	61.26	21.48	9.55	21.91	0.926	0.648
2	56.61	18.63	9.04	20.63	1.019	0.641
0.1	-	-	-	-	-	-

Table 4D.6: Computed elastic moduli and Thomsen's elastic anisotropy parameters as a function of confining pressure (P_C) for the Inorganic sample.

P_C (MPa)	C_{11} (GPa)	C_{33} (GPa)	C_{44} (GPa)	C_{66} (GPa)	ε (-)	γ (-)
1	30.41	15.73	7.64	11.90	0.467	0.278
2	30.62	16.29	7.82	12.00	0.440	0.267
5	31.24	17.79	8.00	12.18	0.378	0.261
7.5	31.47	18.39	8.13	12.24	0.356	0.253
10	31.90	18.93	8.32	12.33	0.343	0.241
20	32.44	20.09	8.63	12.55	0.307	0.227
30	33.19	21.14	8.87	12.75	0.285	0.218
40	33.97	22.08	9.09	12.98	0.269	0.214
50	34.76	23.15	9.30	13.24	0.251	0.212
45	34.52	22.95	9.27	13.21	0.252	0.213
35	34.22	22.64	9.19	13.07	0.256	0.211
25	33.57	21.90	9.02	12.90	0.266	0.215
15	32.82	20.98	8.81	12.68	0.282	0.220
7.5	32.01	20.01	8.55	12.47	0.300	0.229
5	31.67	19.38	8.38	12.33	0.317	0.235
2	31.05	18.73	8.23	12.22	0.329	0.242
1	30.84	18.17	8.13	12.14	0.348	0.246
0.1	-	-	-	-	-	-

Table 4D.7: Computed elastic moduli and Thomsen's elastic anisotropy parameters as a function of confining pressure (P_C) for the Green River sample.

P_C (MPa)	C_{11} (GPa)	C_{33} (GPa)	C_{44} (GPa)	C_{66} (GPa)	ε (-)	γ (-)
1	43.80	37.27	10.38	13.67	0.088	0.070
2	44.21	37.59	10.45	13.74	0.088	0.067
5	44.66	38.14	10.52	13.93	0.085	0.069
7.5	45.09	38.68	10.61	14.05	0.083	0.067
10	45.74	39.20	10.67	14.17	0.083	0.066
20	46.94	40.18	10.87	14.40	0.084	0.063
30	47.94	41.22	11.04	14.63	0.082	0.060
40	48.75	42.26	11.18	14.86	0.077	0.060
50	49.56	42.76	11.29	15.02	0.079	0.057
45	49.32	42.55	11.25	14.94	0.080	0.057
35	48.76	41.90	11.15	14.83	0.082	0.060
25	47.95	41.04	10.99	14.60	0.084	0.060
15	46.93	40.02	10.82	14.33	0.086	0.061
7.5	45.78	38.91	10.67	14.05	0.088	0.060
5	45.32	38.38	10.59	13.93	0.090	0.060
2	44.69	37.86	10.53	13.84	0.090	0.061
1	44.28	37.52	10.47	13.77	0.090	0.065
0.1	-	-	-	-	-	-

Table 4D.8: Computed elastic moduli and Thomsen's elastic anisotropy parameters as a function of confining pressure (P_C) for sample BO.

P_C (MPa)	C_{11} (GPa)	C_{33} (GPa)	C_{44} (GPa)	C_{66} (GPa)	ε (-)	γ (-)
1	25.73	9.93	5.32	9.97	0.795	0.438
2	26.02	10.05	5.37	10.07	0.795	0.438
5	26.36	10.58	5.54	10.25	0.746	0.424
7.5	26.70	11.01	5.64	10.46	0.713	0.427
10	26.93	11.25	5.70	10.57	0.696	0.426
20	27.69	12.55	5.89	10.81	0.603	0.416
30	28.38	13.64	6.11	11.05	0.541	0.404
40	28.99	14.44	6.34	11.32	0.504	0.393
50	29.81	15.12	6.54	11.55	0.486	0.383
45	29.70	14.98	6.52	11.52	0.491	0.383
35	29.38	14.50	6.41	11.40	0.513	0.389
25	28.70	13.89	6.28	11.19	0.533	0.391
15	28.12	13.00	6.09	10.92	0.581	0.397
7.5	27.48	12.22	5.90	10.70	0.625	0.407
5	27.13	11.83	5.79	10.61	0.647	0.415
2	26.79	11.43	5.70	10.44	0.672	0.416
1	26.56	11.13	5.63	10.34	0.693	0.417
0.1	-	-	-	-	-	-

Table 4D.9: Computed elastic moduli and Thomsen's elastic anisotropy parameters as a function of confining pressure (P_C) for sample BW1.

P_C (MPa)	C_{11} (GPa)	C_{33} (GPa)	C_{44} (GPa)	C_{66} (GPa)	ε (-)	γ (-)
1	62.44	20.31	10.93	21.50	1.037	0.484
2	63.80	21.47	11.44	21.84	0.986	0.454
5	66.86	25.17	12.40	22.21	0.828	0.396
7.5	68.47	26.78	12.98	22.47	0.778	0.366
10	69.76	28.20	13.38	22.67	0.737	0.347
20	73.47	32.91	14.49	23.12	0.616	0.298
30	76.48	36.01	15.21	23.64	0.562	0.277
40	79.15	38.85	15.70	24.08	0.519	0.267
50	81.42	40.62	16.16	24.52	0.502	0.258
45	80.95	40.19	16.10	24.44	0.507	0.259
35	79.30	39.52	15.82	24.20	0.503	0.265
25	76.26	38.48	15.58	23.93	0.491	0.268
15	73.30	36.01	15.05	23.42	0.518	0.278
7.5	70.15	33.19	14.22	22.93	0.557	0.306
5	68.07	31.00	13.56	22.58	0.598	0.333
2	65.45	29.35	13.22	22.26	0.615	0.342
1	63.98	27.31	12.86	22.09	0.672	0.359
0.1	-	-	-	-	-	-

Table 4D.10: Computed elastic moduli and Thomsen's elastic anisotropy parameters as a function of confining pressure (P_C) for sample BW2.

P_C (MPa)	C_{11} (GPa)	C_{33} (GPa)	C_{44} (GPa)	C_{66} (GPa)	ε (-)	γ (-)
1	60.80	27.06	13.93	24.51	0.624	0.379
2	61.76	29.64	14.63	24.91	0.542	0.351
5	63.80	35.63	15.74	25.78	0.478	0.319
7.5	64.87	34.45	16.11	25.99	0.442	0.306
10	65.98	35.52	16.42	26.28	0.429	0.300
20	68.40	38.03	17.01	26.67	0.399	0.284
30	70.15	39.74	17.49	27.04	0.383	0.273
40	71.95	41.17	17.78	27.42	0.374	0.271
50	73.40	42.29	18.06	27.80	0.368	0.270
45	73.38	42.09	18.00	27.70	0.372	0.269
35	72.37	41.22	17.85	27.43	0.378	0.269
25	70.94	40.31	17.51	27.06	0.380	0.273
15	69.16	38.93	17.19	26.68	0.389	0.276
7.5	67.48	37.14	16.68	26.32	0.408	0.289
5	66.68	35.98	16.47	26.11	0.427	0.293
2	65.90	34.31	16.21	25.91	0.460	0.299
1	65.16	32.77	15.83	25.63	0.494	0.310
0.1	-	-	-	-	-	-

4.7 References

Allan, A. M., T. Vanorio, and J. E. P. Dahl, 2014, Pyrolysis-induced P-wave velocity anisotropy in organic-rich shales: Geophysics, 79:D41–D53.

Anderson, K. B., J. C. Crelling, F. Kenig, and W. W. Huggett, 2007, An unusual non-fluorescing algal kerogen from the Canadian Arctic: International Journal of Coal Geology, 69:144–152.

Banik, N. C., 1984, Velocity anisotropy in shales and depth estimation in the North Sea basin: Geophysics, 49:1411–1419.

Berryman, J., 1980, Long-wavelength propagation in composite elastic media: Journal of the Acoustical Society of America, 68:1809–1831.

Cholach, P. Y. and D. R. Schmitt, 2006, Intrinsic elasticity of a textured transversely isotropic muscovite aggregate: Comparisons to the seismic anisotropy of schists and shales: Journal of Geophysical Research, 111:B09410.

Crosdale, P. J. and A. C. Cook, 2008, Discussion: Anderson, K. B., Crelling, J. J., Kenig, F., Huggett, W. W., 2007. An unusual non-fluorescing algal kerogen from the Canadian Arctic: International Journal of Coal Geology, 72:388–390.

Gassmann, F., 1951, Über die Elastizität poröser Medien: Vierteljahrsschrift der Naturforschenden Gesellschaft in Zürich, 96:1–23.

Johnston, J. E. and N. I. Christensen, 1995, Seismic anisotropy of shales: Journal of Geophysical Research, 100:5991–6003.

Jones, L. E. A. and H. F. Wang, 1981, Ultrasonic velocities in Cretaceous shales from the Williston basin: Geophysics, 46(3):288–297.

Loucks, R. G., R. M. Reed, S. C. Ruppel, and D. M. Jarvie, 2009, Morphology, genesis, and distribution of nanometer-scale pores in siliceous mudstones of the Mississippian Barnett shale: Journal of Sedimentary Research, 79:848–861.

MacBeth, C., 2004, A classification for the pressure-sensitivity properties of a sandstone rock frame: Geophysics, 69(2):497–510.

Mavko, G., T. Mukerji, and J. Dvorkin, 2009, The rock physics handbook, 2nd ed.: Cambridge University Press.

Michelsen, J. K. and G. K. Khorasani, 1990, Monitoring chemical alterations of individual oil-prone macerals by means of microscopical fluorescence spectrometry combined with multivariate data analysis: Organic Geochemistry, 15:179–192.

Peters, K. E., C. C. Walters, and J. M. Moldowan, 2004, The biomarker guide: Volume 2, Biomarkers and isotopes in petroleum systems and earth history: Cambridge University Press.

Prasad, M., K. C. Mba, T. E. McEvoy, and M. L. Batzle, 2011, Maturity and impedance analysis of organic-rich shales: SPE Reservoir Evaluation and Engineering, 14:533–543.

Sayers, C. M., 1999, Stress-dependent seismic anisotropy of shales: Geophysics, 64:93–98.

Sayers, C. M., 2005, Seismic anisotropy of shales: Geophysical Prospecting, 53:667–676.

Taylor, G. H., M. Teichmüller, A. Davis, C. F. K. Diessel, R. Littke, and P. Robert, 1998, Organic petrology: Gerbrüder Borntreger.

Teerman, S. C., J. C. Crelling, and G. B. Glass, 1987, Fluorescence spectral analysis of resinite macerals from coals of the Hanna Formation, Wyoming, U.S.A.: International Journal of Coal Geology, 7:315–334.

Thomsen, L., 1986, Weak elastic anisotropy: Geophysics, 51:1954–1966.

Tissot, B., B. Durand, J. Espitalié, and A. Combaz, 1974, Influence of nature and diagenesis of organic matter in formation of petroleum: AAPG Bulletin, 58:499–506.

Valcke, S. L. A., M. Casey, G. E. Lloyd, J. M. Kendall, and Q. J. Fisher, 2006, Lattice preferred orientation and seismic anisotropy in sedimentary rocks: Geophysics Journal International, 166:652–660.

Vasin, R., H.-R. Wenk, W. Kanitpanyacharoen, S. Matthies, and R. Wirth, 2013, Anisotropy of Kimmeridge sgake: Journal of Geophysical Research, 118:1–26.

Vernik, L., 1993, Microcrack-induced versus intrinsic elastic anisotropy in mature HC-source shales: Geophysics, 58:1703–1706.

Vernik, L. and C. Landis, 1996, Elastic anisotropy of source rocks: Implications for hydrocarbon generation and primary migration: AAPG Bulletin, 80:531–544.

Vernik, L. and X. Liu, 1997, Velocity anisotropy in shales: A petrophysical study: Geophysics, 62:521–532.

Vernik, L. and A. Nur, 1992, Ultrasonic velocity and anisotropy of hydrocarbon source rocks: Geophysics, 57:727–735.

Wang, Z., 2002, Seismic anisotropy in sedimentary rocks, part 2: Laboratory data: Geophysics, 62:521–532.

Wenk, H.-R., I. Lonardelli, H. Franz, K. Nihei, and S. Nakagawa, 2007, Preferred orientation and elastic anisotropy of illite-rich shale: Geophysics, 72(2):E69–E75.

Zargari, S., M. Prasad, K. C. Mba, and E. D. Mattson, 2011, Organic maturity, hydrous pyrolysis and elastic property in shales: Presented at Canadian Unconvential Resources Conference.

Chapter 5

THE EVOLUTION OF ELASTIC ANISOTROPY OF ORGANIC-RICH SHALE UPON THERMAL MATURATION – PART 2: CONFINED PYROLYSIS

Abstract

In this chapter, I apply the novel iterative shale characterization methodology of Chapter 3 to the study of the elastic evolution of organic-rich shale upon confined pyrolysis-induced thermal maturation. Conducting these experiments on an initially thermally immature, laminar Barnett Shale sample exhibits similar results to the unconfined pyrolysis of the laminar Kimmeridge

Shale in Chapter 2. In each instance, the formation of sub-parallel to bedding cracks results in a decrease in acoustic velocities, which is coupled with a large increase in velocity sensitivity to pressure. However, the confined pyrolysis implemented in this chapter prevents both the fracturing of the sample and the development of microcrack apertures visible at the micron-scale. This technique, rather, allows the formation of nano-cracks as a result of pore pressure build-up during the generation of hydrocarbons, which is mitigated by the simulated overburden. In the absence of sample fracturing, at confining pressures greater than 20 MPa, the induced nano-cracks close at which point the sample is acoustically indistinguishable from the pre-pyrolysis sample. The presence of nano-cracks, if aligned, will, when they are propped open by fluid pressure, increase the elastic anisotropy of laminar shales in situ. Applying the same experiments to the weakly aligned micritic Green River sample does not result in the formation of aligned micro- and/or nano-cracks or any other preferentially aligned features. Rather the sample exhibits a consistent, directionally independent decrease in velocity as the load-bearing, pore-filling kerogen migrates from the system as a result of the induced maturation. Due to the poor alignment and directional-independence of the velocity evolution post-pyrolysis, there is both very little intrinsic anisotropy and very little change in anisotropy in the Green River sample as a function of thermal maturity – behavior that is very similar to that exhibited by the non-laminar Woodford Shale in Chapter 2. The results of this study indicate that, at high frequencies, regions of higher thermal maturity (and potentially greater hydrocarbon content) may be acoustically detectible in situ through lateral increases in the elastic anisotropy of laminar shales or decreases in the acoustic velocities of non-laminar shales, micritic rocks, or siltstones, respectively.

5.1 Introduction

There is a wide range of variable factors that characterize different organic-rich shales, such as mineralogy, depositional environment, burial history, and type of organic matter. Changes in any of these parameters can have a strong effect on the elastic properties of the composite organic-rich shale. As identified while describing the Vernik dataset (Vernik and Nur, 1992; Vernik and Landis, 1996; Vernik and Liu, 1997) and the analysis conducted in Chapter 4, isolating the thermal maturity-dependence of elastic anisotropy is extremely complicated by the presence of other rock properties, e.g., variable texture arising from deposition and burial. In order to isolate the effect of thermal maturity on the elastic anisotropy with respect to the other variables describing the different shales, we propose iterative characterization of organic-rich shale samples pre- and post-pyrolysis. In this manner, all identified changes in the rock properties are predominantly the result of induced thermal maturation rather than, for instance, a variable initial mineralogy.

Previously (Chapter 2), we demonstrated that iterative characterization of the acoustic velocity pre- and post-pyrolysis is experimentally practicable. Furthermore, we documented increases in the Thomsen anisotropy parameter epsilon (Thomsen, 1986) of up to 1.25 at low confining pressure. The increases in epsilon, informed by scanning electron microscopy (SEM), resulted from the formation of expulsion-induced microcracks that are subparallel to bedding. The physically anomalous magnitude of the post-pyrolysis increases in epsilon was attributed to

expulsion-induced, through-going fractures that split the sample plugs into 3-4 intact fragments. Further, fracturing on this scale during pyrolysis experiments has also been documented in other studies (Kobchenko et al., 2011; Yenugu, 2014). This fracturing of the rock, and subsequent anomalous increases in epsilon, must be minimized (or ideally removed entirely) in order to more robustly investigate the thermal maturity dependence of the elastic properties of organic-rich shale.

In this chapter, we address the need for a thorough characterization of the elastic anisotropy of organic-rich shale by closing-the-loop on the methodological approach of Allan et al. (2014, 2015). Therefore, the full methodology incorporates the iterative characterization of the microstructure, geochemistry, acoustic velocity, porosity, and axial deformation of Barnett and Green River samples pre- and post-pyrolysis. Most importantly, in this study, ex situ thermal maturation is achieved through pioneering pyrolysis measurements of intact core plugs under reservoir-magnitude confining pressures. Through the combination of a thorough shale characterization methodology and unique pyrolysis experiments, we are able to isolate and document the complete elastic evolution of the Barnett and Green River samples as a function of thermal maturity.

5.2 Experimental Methodology and Sample Characterization

5.2.1 Experimental Methodology for Pyrolyzed Samples

As this study is an investigation of the iterative effect of thermal maturation on organic-rich shale, the methodology implemented is a blend of those presented in Figures 3.13 and 4.1. The full workflow implemented for the characterization of the organic-rich shales pre- and post-pyrolysis is documented in Figure 5.1. All experimental techniques, parameters, and the subsampling process is as detailed in Chapter 3.

Pyrolysis was performed in the purpose-built, high temperature-high pressure reactor presented in Chapter 3 (see also Clark and Vanorio, 2015). For the Barnett samples, the oil window was attained by anhydrous pyrolysis at 360 °C at 22-24 MPa for 72 hours, while the oil window was reached for the Green River samples at 380 °C at 22-24 MPa for 72 hours. For both samples, the gas window was reached by pyrolysis at 425 °C at 22-24 MPa for 72 hours. The geochemical validation of the pyrolysis procedure is documented in the Results section of this chapter.

5.2.2 Barnett Shale and Green River Sample Comparison

This chapter is restricted to the analysis of the elastic evolution upon pyrolysis of the thermally immature, outcrop Barnett Shale and Green River samples. The sample characterization (detailed in Chapter 3) is briefly repeated here for convenience. Figure 5.2 documents the mineralogy while Table 5.1 reports the effective porosity, grain density, degree of crystallographic

preferred orientation (CPO), and geochemical properties of the two samples. The representative microstructures of the baseline, thermally immature samples are juxtaposed in Figure 5.3.

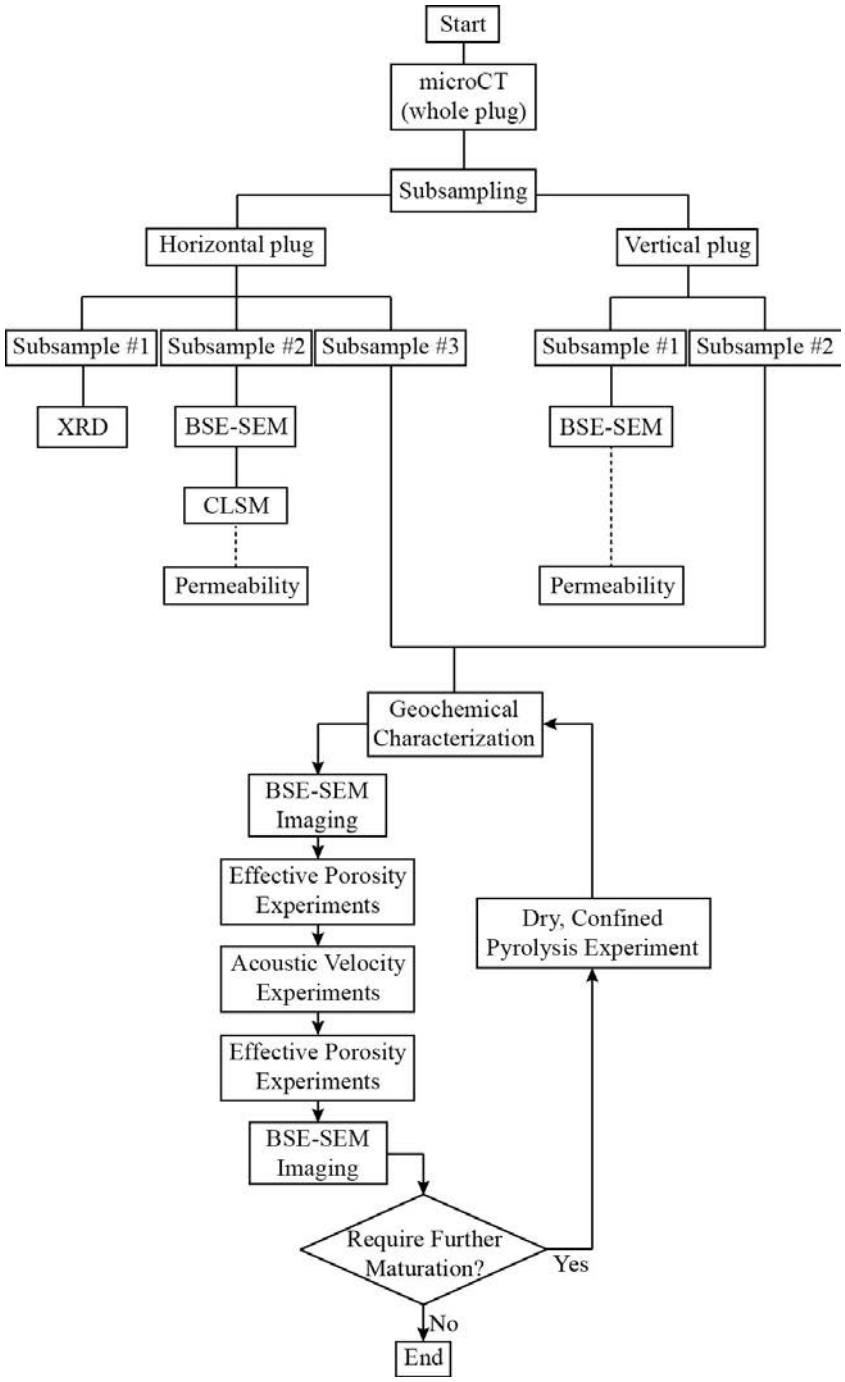

Figure 5.1: A schematic flowchart of the experimental workflow implemented for iterative shale characterization pre- and post-pyrolysis. The permeability methodology and measurements will be discussed in Chapter 6.

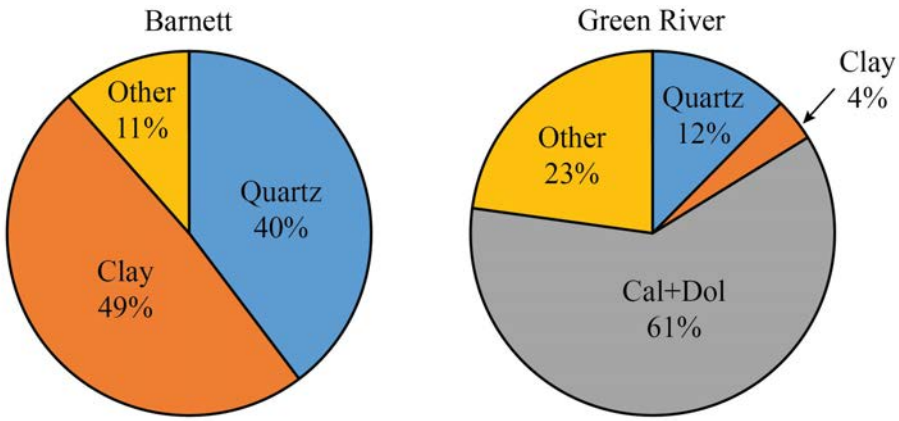

Figure 5.2: The mineralogical composition by weight of the Barnett Shale and Green River outcrop samples. Note, auxiliary mineralogies, e.g., feldspar and pyrite, are binned as 'Other.'

As is clear in Figure 5.2, the two samples are mineralogically very different. The Barnett sample is a 'classic' siliciclastic shale, with auxiliary apatite (5%), pyrite (3%), and siderite (3%). Conversely, the Green River sample is an argillaceous dolomicrite, predominantly composed of dolomite (43%) and calcite (18%) with approximately equal parts quartz (12%), analcime (12%), albite (11%) and relatively little clay (4%). While the samples have very comparable organic contents, the lacustrine Type I kerogen of the Green River contains 63% more hydrocarbons per gram of TOC than the marine Type II Barnett kerogen. The greater reactivity of the Green River kerogen results in 30% more ultimately recoverable hydrocarbons than from an equivalent mass of Barnett kerogen (Table 5.1).

Representative SEM images of the baseline, thermally immature samples are collated in Figure 5.3. The two samples exhibit vastly different textures. The clay-rich Barnett Shale exhibits a strong alignment of the microcrystalline siliciclastic matrix and dispersed lenticular kerogen (Figure 5.3.a-b). The dispersed nature of the kerogen lenses and apatite grains becomes especially apparent by comparison to images taken perpendicular to bedding (Figure 5.3.c-d). Furthermore, the apparent alignment of clay-rich matrix is confirmed through CPO measurements (Table 5.1). Meanwhile, the crystallographically randomly oriented Green River sample (Table 5.1) exhibits a significantly lesser degree of visual alignment (Figure 5.3.e-h). While bedding is present in hand sample, these beds correspond to sedimentological laminations, e.g., relatively organic-rich versus organic-lean, clay-rich layers, in a bulk dolomicrite rather than a petrophysical, mineralogical or crystallographic alignment. Additionally, the organic content of the Green River sample does not occur as discrete lenticular bodies, rather, the kerogen occurs as a largely unstructured, pore-filling phase. The pore-filling nature of the Green River kerogen results in a significantly lower effective porosity for the Green River samples relative to the Barnett samples (Table 5.1). Finally, it is important to remember that this randomly oriented Green River sample is not representative of the entire formation which can exhibit strong degrees of alignment and mineralogically based laminations (A. Carroll, personal communication, 2015).

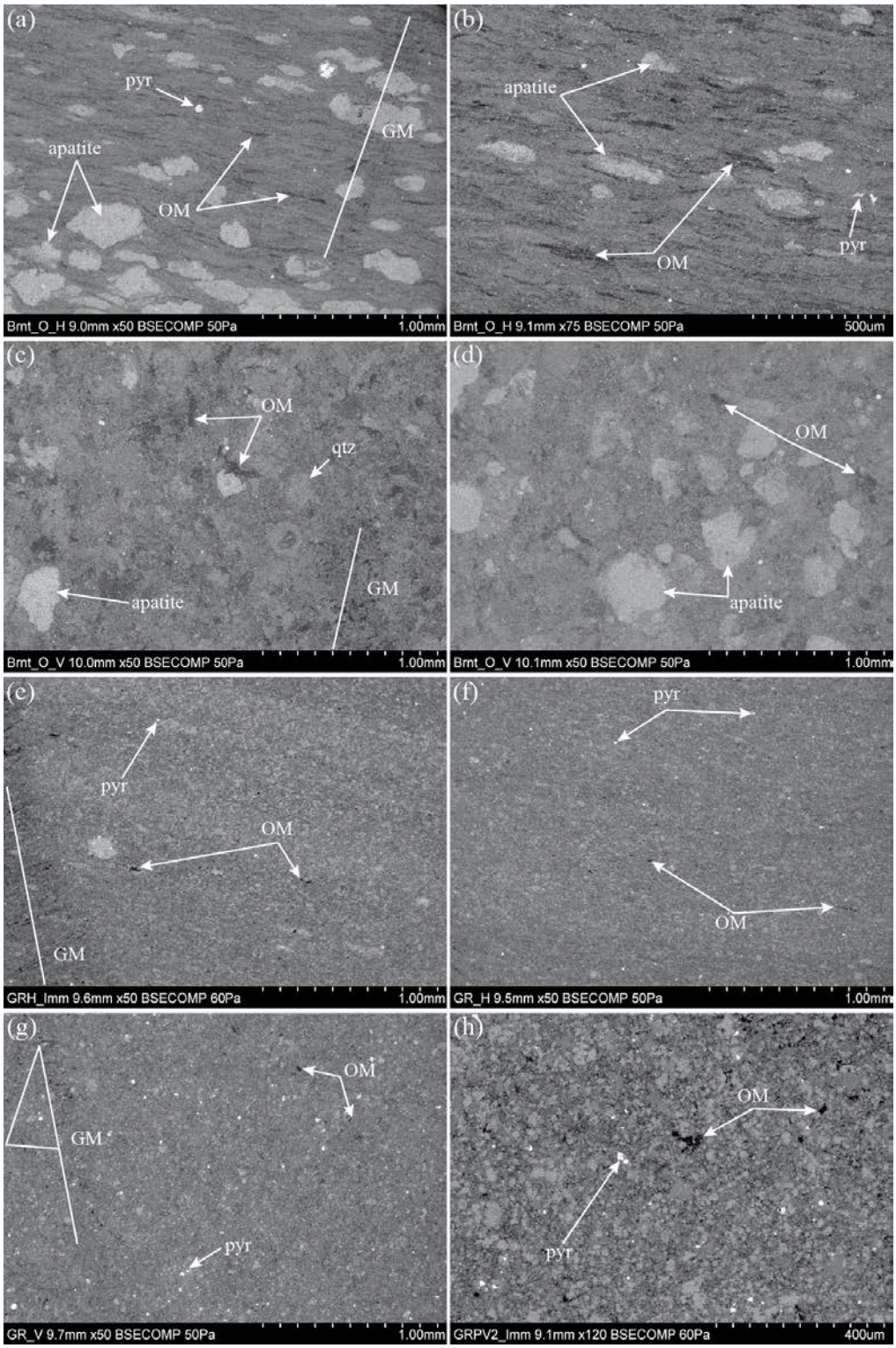

Figure 5.3: Representative SEM images of the baseline, immature window microstructures of the Barnett (a-d) and Green River (e-h) samples. For each sample there are two images collected from the horizontal (a, b, e, f) and the vertical (c, d, g, h) faces, respectively. Identified features include organic matter (OM), pyrite (pyr), apatite, quartz (qtz), and graphite markings used to recover image locations post-pyrolysis (GM).

Table 5.1: A recap of the pertinent properties (effective porosity, grain density, average crystallographic preferred orientation (CPO), and hydrocarbon potential (HP)) characterizing the samples as a function of plug orientation, as presented in Chapter 3. The CPO is reported in units of multiples of a random distribution (see Chapter 3). The hydrocarbon potential is given in milligrams of hydrocarbons per gram of dry rock and indicates the hydrocarbons ultimately recoverable from each sample.

Sample	Plug Orientation	Effective Porosity (%)	Grain Density (g/cm^3)	CPO (m.r.d.)	HP (mg/g)
Barnett	Vertical	13.23±0.36	2.32±0.01	3.98	58.30
	Horizontal	12.72±0.49	2.30±0.01		
Green River	Vertical	0.53±0.48	2.26±0.01	1.07	76.03
	Horizontal	1.28±0.32	2.29±0.01		

5.3 Experimental Results

5.3.1 Pyrolysis-Induced Physical Evolution

5.3.1.1 Mass, Density, and Porosity Evolution

Time-lapse photographs of the vertically cored Barnett and horizontally cored Green River samples are documented in Figures 5.4 and 5.5. Upon pyrolysis to the oil window, the vertically cored Barnett sample (BOV) emitted little hydrocarbon odor and showed no clear hydrocarbon staining (Figure 5.4) – the light gray discoloration on the sides of the plug is most likely the result of a high temperature reaction with the copper jacket. However, upon pyrolysis to the gas window, BOV exhibited both clear, dark brown staining (Figure 5.4) and emitted a strong odor of hydrocarbons. During pyrolysis to the oil window, the copper seal around the horizontally cored Barnett sample (BOH) sheared, resulting in rapid (∼5 minutes) equilibration of the confining and pore pressures – a pressure difference of ∼22 MPa. The rapid pressure equilibration fractured the sample subparallel to the bedding plane to a degree that the sample became unusable (Figure 5.4.d). Contrastingly, the Green River samples exhibited hydrocarbon staining and odor after both pyrolysis experiments (Figure 5.5). Furthermore, post-pyrolysis to the oil window there were clear accumulations of oil on the steel endcaps for both samples (Figure 5.5.d).

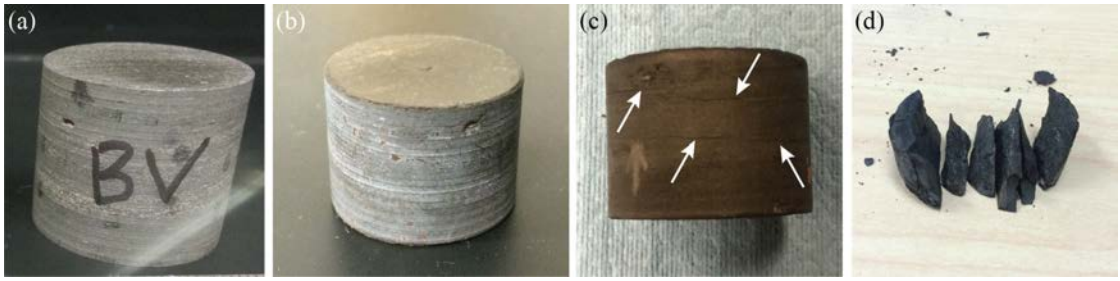

Figure 5.4: Photographs of the vertically cored Barnett sample in the immature (a), oil (b), and gas (c) windows. Subparallel to bedding cracking is identified in (c) by white arrows. Also included in (d) is the horizontally cored Barnett sample after depressurization during pyrolysis to the oil window.

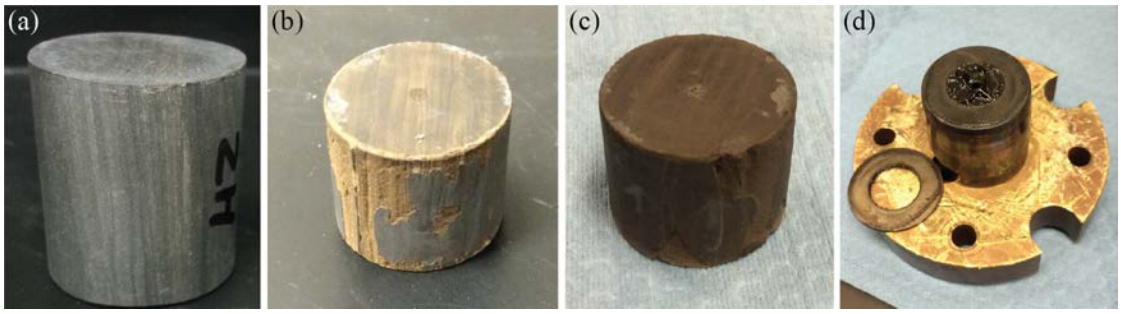

Figure 5.5: Photographs of the horizontally cored Green River sample in the immature (a), oil (b), and gas (c) windows. Also included is the steel endcap post-pyrolysis to the oil window, documenting clear oil generation (d).

The physical properties (mass, volume, effective porosity, and density) of each intact plug, pre- and post-pyrolysis, are documented in Table 5.2. Upon pyrolysis to the oil window, the Barnett sample exhibits a severe decrease in both bulk volume (-7%) and effective porosity (-7.11 p.u.). This behavior indicates that the Barnett sample has experienced significant compaction upon pyrolysis to the oil window. The Green River samples, on the other hand, show the mass loss, the decrease in grain volume (by up to 12%), and the increases in both porosity and grain density indicative of the conversion of low density kerogen to hydrocarbons and their subsequent expulsion.

Table 5.2: The physical properties (mass, volume, effective porosity, and grain density) at each stage of thermal maturity for the vertically cored Barnett Shale sample (BOV) and the vertically and horizontally cored Green River samples (GRV and GRH, respectively).

Sample	Thermal Maturity	Mass (g)	Bulk Volume (cc)	Grain Volume (cc)	Effective Porosity (%)	Grain Density (g/cc)
BOV	Immature	21.11	10.50±0.02	9.11±0.03	13.23±0.36	2.32±0.01
	Oil	20.70	9.78±0.02	9.18±0.02	6.12±0.44	2.25±0.01
	Gas	20.38	9.44±0.08	8.22±0.01	12.94±0.87	2.52±0.01
GRV	Immature	23.10	10.28±0.02	10.23±0.01	0.532±0.48	2.26±0.01
	Oil	21.90	10.07±0.03	8.97±0.02	10.96±0.36	2.44±0.01
	Gas	21.20	10.00±0.06	8.34±0.01	16.55±0.61	2.54±0.01
GRH	Immature	24.40	10.79±0.03	10.65±0.02	1.28±0.32	2.29±0.01
	Oil	23.16	10.71±0.11	9.52±0.03	11.13±1.08	2.43±0.01
	Gas	21.93	10.50±0.10	8.39±0.01	20.11±0.98	2.61±0.01

Upon pyrolysis to the gas window, all of the samples exhibit a mass loss, a decrease in grain volume, and an increase in porosity and grain density. All of these observations are indicative of the generation and expulsion of hydrocarbons. Again, both samples exhibit some compaction, most likely due to the partial closure of maturation-induced porosity during pyrolysis under elevated confining pressure. Further, the Barnett sample (composed of crack-like, low aperture pores) again compacts to a greater degree than the Green River samples (composed of rounder intergranular pores) – 3.5% versus 2%, respectively.

5.3.1.2 Microstructural Evolution

Time-lapse SEM images of microstructure from the immature and oil windows are documented for the Barnett Shale (Figure 5.6.a-d) and the Green River (Figure 5.6.e-h). The Barnett Shale exhibits little visible alteration of the organic content or porosity generation upon pyrolysis to the oil window. The time-lapse images do, however, document potential compaction in small clay-rich regions as identified by blue arrows in Figure 5.6. Contrastingly, the Green River sample exhibits clear migration of kerogen from the sample face via conversion and expulsion (yellow arrows in Figure 5.6). In addition to the migration of kerogen, we note some compaction around the newly formed pores and some largely randomly oriented microcracking (red arrows in Figure 5.6). Finally, the higher resolution Green River images (Figure 5.6.g-h) document the loss of both fines and larger grains from the sample face (bounded in green in Figure 5.6.g). Given the lack of three-dimensional imaging within the sample, we cannot exclude the potential that these grains have been dissolved by the carbon dioxide, hydrogen sulfide, or organic acids generated during thermal maturation. The dissolution of grains, if occuring throughout the sample, would then contribute to the significant noted increase in effective porosity (Table 5.2. However, given the limited, localized effect of the grain removal, the lack of rounding of grain edges/contacts, and the lack of etching or pitting on other grains, we do not believe dissolution to be the primary process at work. These grains may, however, have been removed by adhesion to the heavy oil documented in Figure 5.5.d.

Upon pyrolysis to the gas window the apparent evolution of the two shales reverses (Figure 5.7). The Barnett Shale sample exhibits both clear migration of kerogen and alteration of residual kerogen (particularly the large body in the top right of Figure 5.7.a-b). Higher resolution images document little residual organic matter; rather, kerogen is almost completely removed, revealing the underlying mineral matrix and porosity. After induced maturation to the oil window, there was very little residual kerogen on the imaged surface of the Green River sample; subsequently, there is little kerogen evolution to observe (Figure 5.7.e-h). It is important to remember that SEM images are largely restricted to a two-dimensional surface, thus, the thermal maturation and porosity generation indicated in Table 5.2 can only be inferred to occur within the three-dimensional sample. Finally, we also observe largely randomly oriented microcracking both between and within grains post-pyrolysis to the gas window (Figure 5.7.h). The microcracking may result from the expulsion of hydrocarbons from within the sample or be the result of differential thermal expansion at mineral contacts. However, given the minimal cracking in the same location after the previous pyrolysis experiment at 380 °C (Figure 5.7.g), the thermal expansion hypothesis is deemed unlikely.

5.3.1.3 Geochemical Evolution

The geochemical characterization of the Barnett and Green River samples in each window of thermal maturity is reported in Table 5.3. The thermal maturity parameter, T_{MAX}, indicates that pyrolysis at 360 °C for 72 hours results in early oil window maturity for the Barnett sample (435 °C $< T_{MAX} <$ 445 °C; Peters and Cassa, 1994). Furthermore, the fourfold increase in free hydrocarbons (S_1) and 45% reduction in remaining hydrocarbon potential confirms that thermal

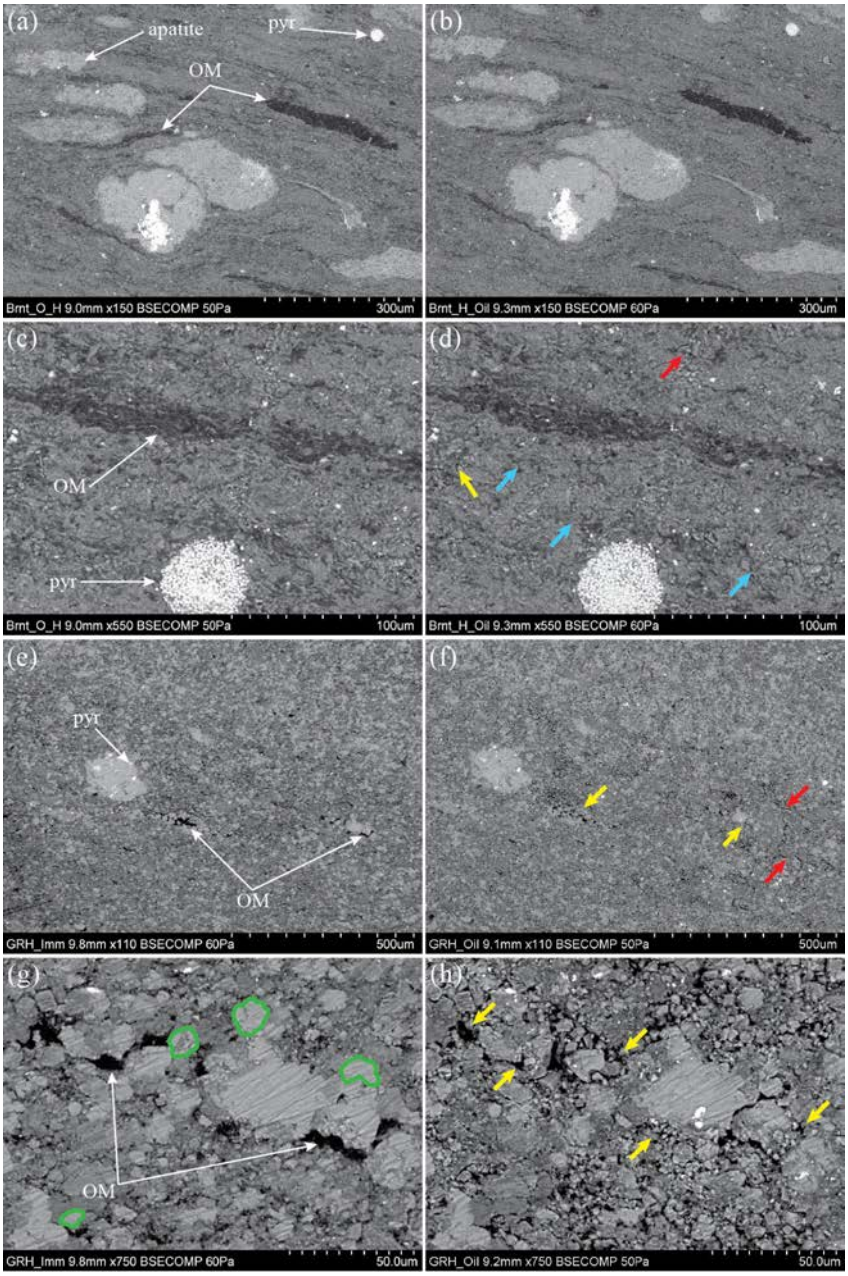

Figure 5.6: Time-lapse SEM images of the evolving microstructure of the Barnett (a-d) and Green River (e-h) samples between the immature (left column) and oil (right column) windows. Identified features include organic matter (OM), pyrite (pyr), and apatite. Evolutions noted include: blue arrows identifying potential compaction in clay-rich regions, red arrows identifying areas of cracking or developing porosity, yellow arrows identifying areas of kerogen conversion and expulsion, and green outlines around grains that cannot be accounted for in the post-pyrolysis image. The pixel size in the time-lapse images is identical.

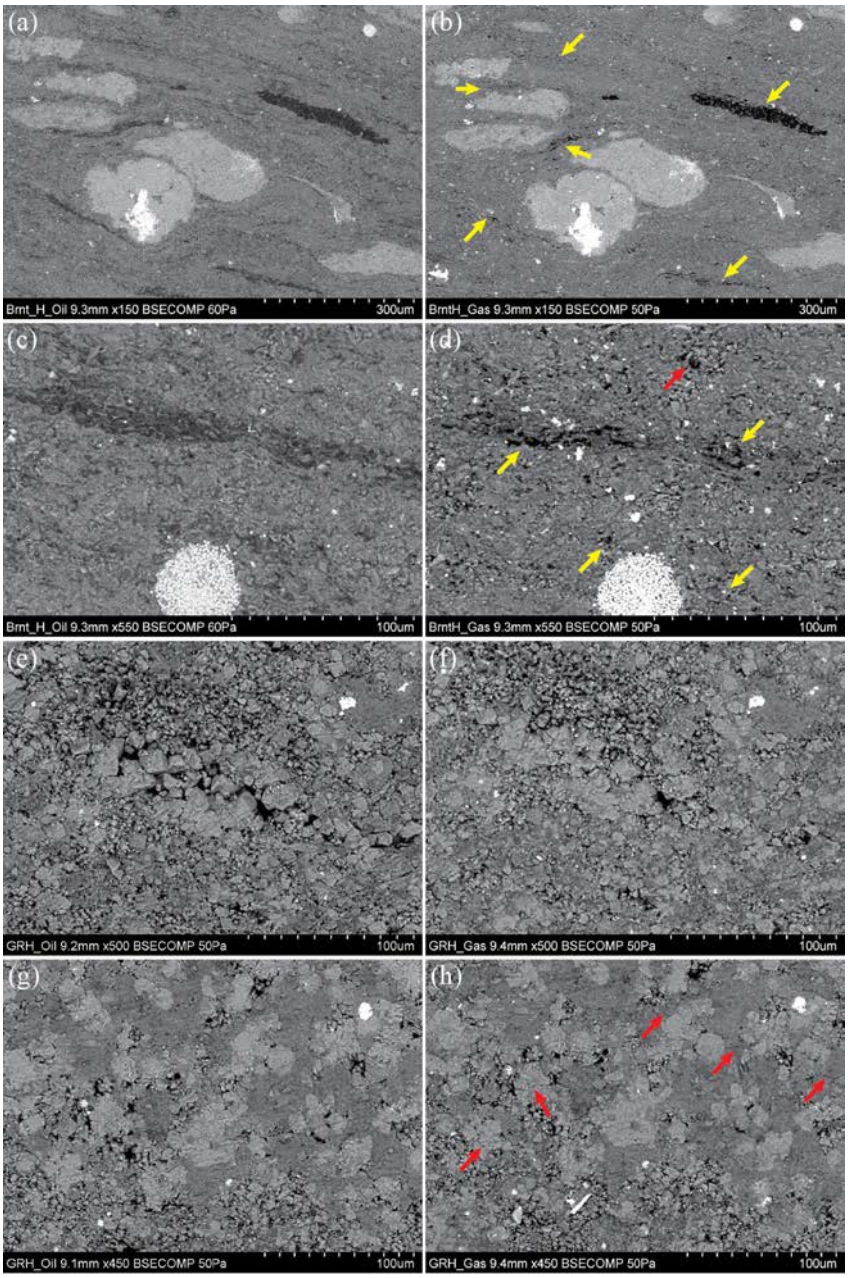

Figure 5.7: Time-lapse SEM images of the evolving microstructure of the Barnett (a-d) and Green River (e-h) samples between the oil (left column) and gas (right column) windows. The Barnett images are collocated with those in Figure 5.6.a-d, whereas the Green River images are of two new locations. Evolutions noted include: red arrows identifying areas of cracking or developing porosity and yellow arrows identifying areas of kerogen conversion The pixel size in the time-lapse images is identical.

maturation has occurred. However, it is important to note that the sample used for geochemical characterization exhibited far greater produced oil, hydrocarbon staining, and odor than the other Barnett subsamples matured at 360 °C (see Appendix A for a discussion on this issue). Subsequently, given the negligible visible alteration and lack of observed hydrocarbons (visual and olfactory) we assume that minimal thermal maturation has occurred in the 'oil window' Barnett subsamples. Rather, the clay matrix has dewatered (hence the mass loss) and the fragile, high porosity outcrop sample has been compacted by exposure to high temperature and pressure for 3 days.

Subsequently for oil window pyrolysis experiments of the Green River samples, the pyrolysis temperature was raised to 380 °C to ensure thermal maturation occurred. Table 5.3 indicates that pyrolysis at 380 °C resulted in no appreciable thermal maturation of the Green River (T_{MAX} < 435 °C; Peters and Cassa, 1994); however, the presence of hydrocarbons post-pyrolysis was clear for all subsamples (Figure 5.5.d), the free hydrocarbons increased by a factor of four, and the remaining hydrocarbon potential decreased by 25%. Subsequently, given the clear generation of oil for all Green River subsamples, we assume we have entered at least the early oil window. The source of the seemingly erroneous T_{MAX} value is also addressed in Appendix A.

Table 5.3: Geochemical characterization of the pyrolyzed Barnett and Green River samples. Each pyrolysis experiment is represented by the programmed control temperature of the experiment (T_{CTRL}). The samples are characterized by total organic carbon (TOC), free hydrocarbons (S_1), remaining thermally producible hydrocarbons (S_2), the RockEval thermal maturity indicator (T_{MAX}), the hydrogen index (HI), and the oxygen index (OI). The baseline, thermally immature values are included for convenient comparison. Asterisks indicate that the values are derived from permeability, rather than velocity, subsamples.

Sample	T_{CTRL} (°C)	TOC (wt. %)	S_1 (mg/g)	S_2 (mg/g)	T_{MAX} (°C)	HI (mg/g)	OI (mg/g)
Barnett	-	11.67	2.32	55.98	418	480	9
	360	9.47	8.91	22.65	438	239	7
	425V*	9.40	1.69	4.79	500	51	8
Green River	-	9.14	4.8	71.23	419	780	10
	380	6.43	19.25	39.72	427	617	10
	425V	4.10	12.34	6.92	439	170	17
	425H	3.14	3.25	2.08	480	66	22

As indicated in Table 5.3, pyrolysis at 425 °C results in post-mature, gas window Barnett and horizontally cored Green River samples (T_{MAX} > 470 °C; Peters and Cassa, 1994). However, the vertically cored Green River sample exhibits an anomalously low thermal maturity value (early oil window; Peters and Cassa, 1994) and 3.8 times more retained free hydrocarbons than the horizontally cored plug. At the same time, the remaining thermally producible hydrocarbons (S_2) in the vertically cored sample has decreased by 90% and 82% as compared to the baseline and oil window values, respectively. Subsequently, it appears that, again, the sample has thermally matured but there is some error associated with the reported value of T_{MAX} (see Appendix A).

Despite the different quantities of retained hydrocarbons, we can investigate the evolution of the solid matrix through simple modeling. By combining S_1, S_2, and an assumed organic density (ρ_{org} = 0.85 g/cc), we can compute the mass and volume of the residual organic material and

hydrocarbons within the sample and remove that contribution from the measured grain density and effective porosity values as detailed in Equations 5.1-5.3. In this manner, however, we must assume that all geochemically quantified residual organic material and hydrocarbons are stored within effective porosity rather than isolated, disconnected pores. The effect of accounting for the different hydrocarbon retention in the Green River samples is documented in Figure 5.8 and Table 5.4. Removal of the retained organic content results in a decrease of the porosity heterogeneity from 3.56 p.u. to 0.97 p.u. between the horizontal and vertical subsamples, while the difference in the grain density values decreases by 57% (Table 5.4). Additionally, after accounting for the organic content, all samples fall within the experimental error (Figure 5.8), indicating that the underlying physical evolution of the plugs is more homogeneous than the raw measurements imply (Table 5.2).

$$V_{oil} = \rho_{org}\left(m_{sample} \times \frac{S_1 + S_2}{1000}\right) \tag{5.1}$$

$$\rho'_G = \frac{m_{sample} - m_{oil}}{V'_G} = \frac{m_{sample} - m_{oil}}{V_G - V_{oil}} \tag{5.2}$$

$$\phi' = \frac{V_B - V'_G}{V_B} \times 100 \tag{5.3}$$

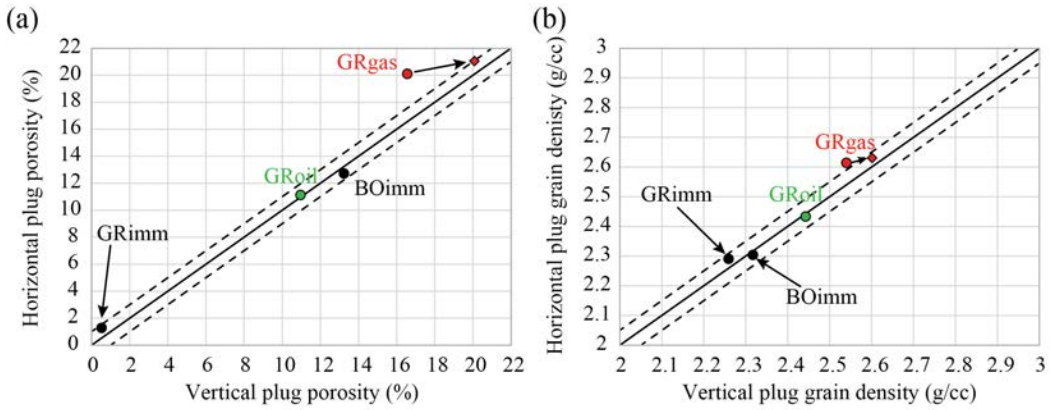

Figure 5.8: A comparison of the effective porosity (a) and grain density (b) of the horizontal plugs to those of the vertical plugs. The solid black lines indicate equal values, i.e., a pair of homogeneous plugs, while the dashed black lines indicate an error of ±1 p.u. and ±0.050 g/cc, respectively. The circular data points are the direct measurements, while the diamonds are the hydrocarbon-corrected values documented in Table 5.4.

Table 5.4: The grain volume, effective porosity, and grain density as measured in the gas window before and after correcting for the residual hydrocarbon content (see Equations 5.1-5.3) of the vertically and horizontally cored Green River samples.

Sample	Measured			Corrected		
	Grain Volume (cc)	Effective Porosity (%)	Grain Density (g/cc)	Grain Volume (cc)	Effective Porosity (%)	Grain Density (g/cc)
GRV	8.34	16.55	2.54	7.99	20.07	2.60
GRH	8.39	20.11	2.61	8.29	21.04	2.63

5.3.2 Pyrolysis-Induced Acoustic Velocity Evolution

5.3.2.1 Recap of Baseline, Immature Window

The measured P- and S-wave velocities and computed elastic anisotropy parameters epsilon and gamma in the immature window of thermal maturity, originally presented in Chapter 4, are compiled in Figure 5.9. As before, it is clear that the vertically propagating P-waves are considerably slower and more pressure-sensitive than those propagating horizontally in the Barnett Shale (Figure 5.9.a-b) due to a combination of bedding and compliant, subparallel to bedding porosity. The Barnett samples exhibit the acoustic tendencies of a VTI medium (Thomsen, 1986), in which the $V_S(0°)$ and $V_{SV}(90°)$ phases are roughly equal, with magnitude significantly less than the $V_{SH}(90°)$ phase (Figure 5.9.c). The Green River sample exhibits lesser agreement between the $V_S(0°)$ and $V_{SV}(90°)$ phases as well as exhibiting less directional dependence and pressure-sensitivity for both P- and S-waves (Figure 5.9.b,d). In Chapter 4, this unexpected acoustic behavior is attributed to the interlocking carbonate microstructure of the micritic Green River sample.

Given the differences in the acoustic behavior of the two samples, it is understandable that the samples exhibit significantly different elastic anisotropies (Figure 5.9.e-h). The strong directional dependence of P- and S-wave velocities in the laminar Barnett Shale sample gives rise to significant, pressure-sensitive elastic anisotropy. As noted for the laminar shales in Chapter 4, P-wave velocities and epsilon are considerably more pressure-sensitive than S-wave velocities and gamma, as previously noted by MacBeth (2004). The relative lack of directional dependence or pressure-sensitivity in the acoustic velocities of the Green River samples, however, results in a very low degree of elastic anisotropy which is largely insensitive to pressure.

5.3.2.2 Oil Window

Due to the depressurization and fracturing of sample BOH during the pyrolysis experiment (Figure 5.4.d), acoustic velocity experiments can only be conducted for sample BOV, which was recovered fully intact post-pyrolysis. The vertically propagating P- and S-wave velocities for the oil window Barnett Shale sample are reported in Figure 5.10. After pyrolysis to the oil window, the velocities increase significantly relative to the baseline values – P: 500 m/s (20%), S: 180 m/s (10%) at 50 MPa. The velocity increase in the Barnett velocities corresponds with the decrease in effective porosity from 13.23% to 6.12% at room temperature and pressure (Table 5.2). For the Green River samples, which were recovered intact from the HTHP, all 5 acoustic modes were recorded as a function of confining pressure and are reported in Figure 5.11. All acoustic velocities exhibit a decrease in magnitude and an increase in pressure-sensitivity post-pyrolysis, while the effective porosity of the vertical and horizontal plugs increases from 0.53% and 1.28% to 10.96% and 11.13% (Table 5.2), respectively. Pyrolysis to the oil window results in a decrease in P-wave velocities of 9% and 8% for the vertical and horizontal plugs, respectively, and a decrease in the S-wave velocities by 4.5%, 5%, and 3%, for the $V_S(0°)$, $V_{SH}(90°)$, and $V_{SV}(90°)$ phases, respectively.

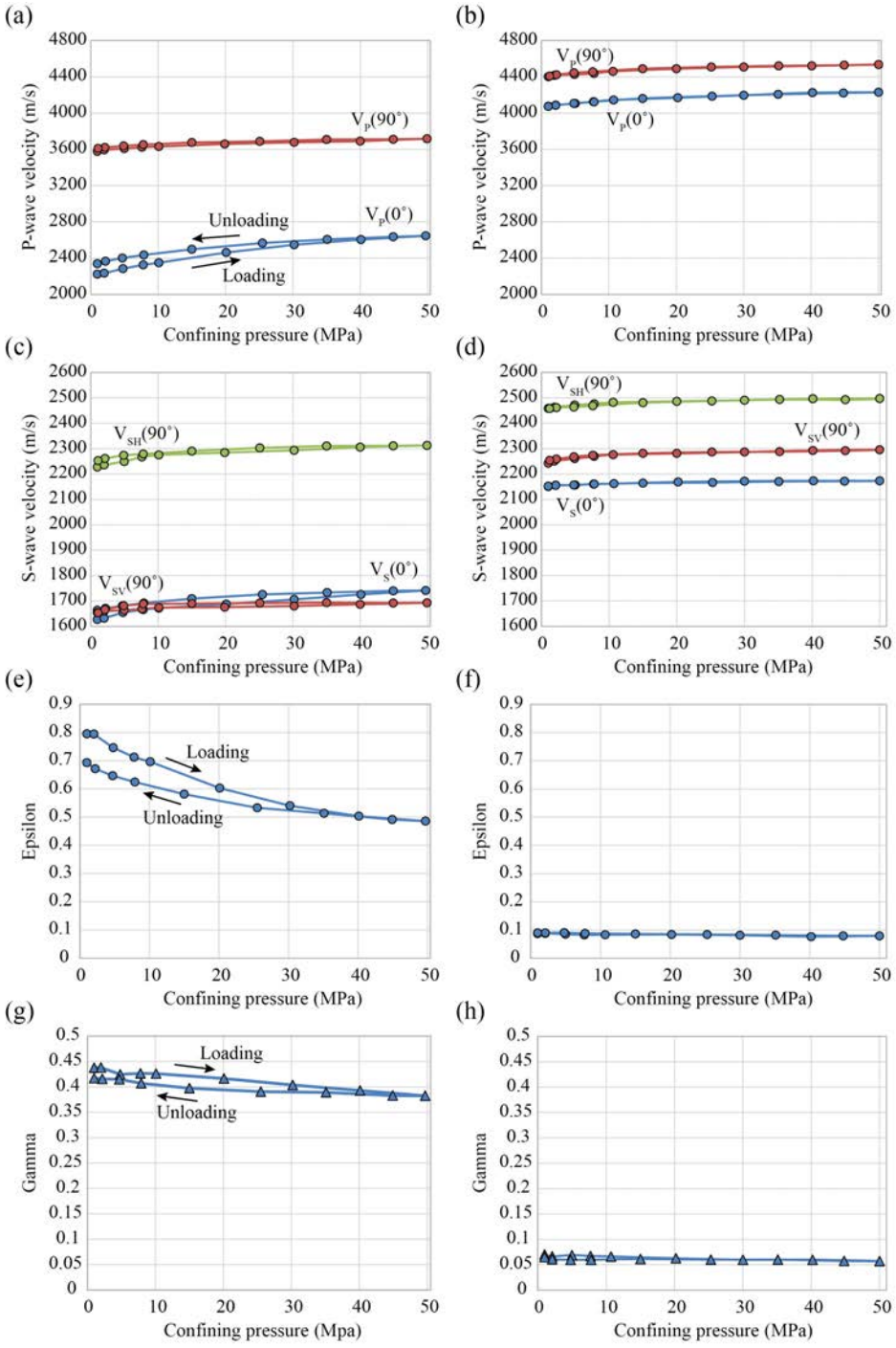

Figure 5.9: The baseline, immature acoustic velocity and elastic anisotropy of the Barnett (left column) and Green River (right column) samples, originally presented in Chapter 4. Solid lines and arrows are used to indicate hysteresis between the loading and unloading curves.

The lack of horizontally propagating velocities prevents the further quantification of the elastic anisotropy of the Barnett sample; however, a hypothetical discussion of anisotropy evolution in the Barnett Shale is documented in Appendix B. In Figure 5.12, the Green River sample is shown to exhibit very little change in epsilon post-pyrolysis to the oil window. The value of gamma, however, roughly doubles, with the increase in gamma as a function of confining pressure resulting from the greater pressure-sensitivity of the $V_{SH}(90°)$ phase relative to $V_S(0°)$.

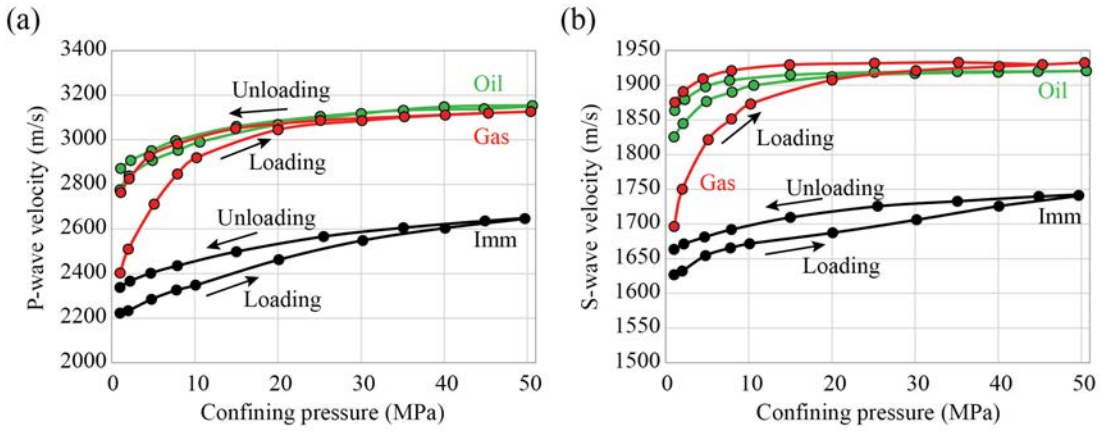

Figure 5.10: The vertically propagating P- (a) and S-wave (b) velocities as a function of confining pressure for the Barnett sample in the immature (black), oil (green), and gas (red) windows. Solid lines and arrows are used to indicate hysteresis between the loading and unloading curves.

5.3.2.3 Gas Window

After pyrolysis to the gas window, all remaining samples were recovered with no visible damage. The gas window P- and S-wave velocities perpendicular to bedding for the Barnett Shale sample are documented in Figure 5.10. Post-pyrolysis, the Barnett Shale velocities are greatly more sensitive to confining pressure. In the gas window, the P- and S-wave velocities increase by 30% and 14% upon loading to 20 MPa, respectively. Subsequently, at confining pressures greater than ∼20 MPa, the gas window velocity-pressure trend conforms well to the oil window trend: indeed, the high confining pressure velocity values do not differ by greater than ±30 m/s. The two trends remain in close agreement during unloading from 50 MPa to 5 MPa. At confining pressures less than 5 MPa, however, the gas window compressional wave becomes more sensitive to confining pressure. Conversely, as in the oil window, the Green River P- and S-velocities exhibit a significant decrease at all confining pressures and an increase in the pressure-sensitivity of velocity (Figure 5.11). Upon pyrolysis to the gas window, the P-wave velocities experience a further decrease of 9% and 7% for the vertical and horizontal plugs, respectively, and a decrease in the S-wave velocities by 5.5%, 10%, and 19%, for the $V_S(0°)$, $V_{SH}(90°)$, and $V_{SV}(90°)$ phases, respectively.

The evolution of the elastic anisotropy of the Green River sample is documented in Figure 5.12. The values of epsilon show a slight increase (∼0.02) upon pyrolysis to the gas window, with a very low degree of pressure-sensitivity – particularly upon unloading. The gas window

values of gamma return to a magnitude more comparable with those of the baseline, immature samples rather than the pre-pyrolysis, oil window values. For convenience, all experimental results, e.g., velocity, porosity, and elastic moduli measurements, are reported in Appendices C-E.

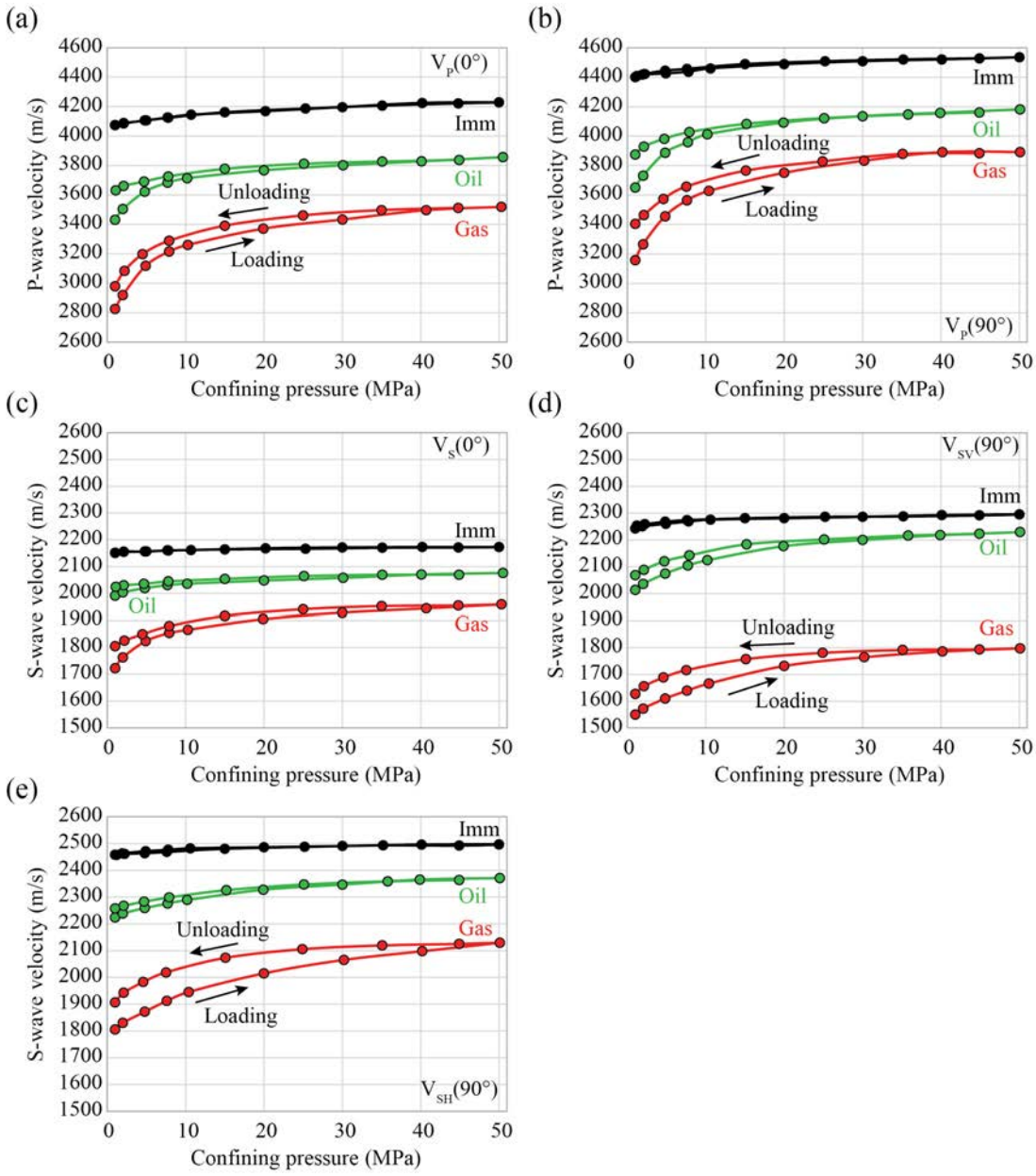

Figure 5.11: The P- and S-wave velocities as a function of confining pressure for the Green River sample in the immature (black), oil (green), and gas (red) windows. (a) $V_P(0°)$, (b) $V_P(90°)$, (c) $V_S(0°)$, (d) $V_{SV}(90°)$, and (e) $V_{SH}(90°)$. Solid lines and arrows are used to indicate hysteresis between the loading and unloading curves.

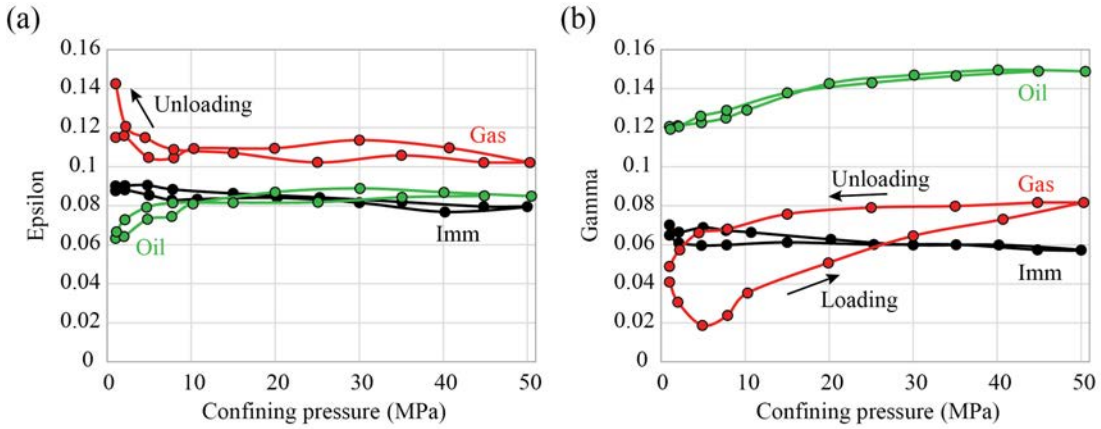

Figure 5.12: The elastic anisotropy parameters epsilon (a) and gamma (b) as a function of confining pressure for the Green River sample in the immature (black), oil (green), and gas (red) windows. Solid lines and arrows are used to indicate hysteresis between the loading and unloading curves.

5.4 Discussion

5.4.1 Evolution of Elastic Properties upon Pyrolysis

5.4.1.1 Acoustic Velocity Evolution

After pyrolysis to the oil window, the vertically propagating P- and S-waves of the Barnett Shale exhibit an increase of 510 m/s (19%) and 180 m/s (10%) at high confining pressure, respectively (Figure 5.10). This velocity increase is consistent with the 54% (7.11 p.u.) decrease in effective porosity resulting from the 7% decrease in bulk volume (Table 5.2). The velocity-porosity evolution is consistent with the well-derived samples presented in Chapter 4 (Figure 5.13), where the greater velocities exhibited by the well samples, despite the same porosity, are attributable to their greater carbonate content. The combination of the previously observed lack of hydrocarbon production, bulk volume and porosity loss, and the significant increase in acoustic velocity is all indicative of the mechanical compaction of the thermally softened, outcrop sample. Given the potential for such significant compaction in weak, clay-rich outcrop samples, it would be advantageous for future experiments that all samples be thermally pre-stressed before baseline characterization by exposing the samples to high pressure and intermediate temperatures (sufficient to soften the sample, but not so hot as to induce thermal maturation, e.g., 300 °C) for a few days. In this manner, any potential mechanical compaction will be accounted for before the baseline, thermally immature measurements are taken and, as a result, all subsequent observed evolution should be more purely a function of induced thermal maturation.

That being said due to the lack of hydrocarbon generation in the first pyrolysis experiment, we can consider the 'oil window' velocities as an updated baseline characterization. At low confining pressure, post-pyrolysis to the gas window, there is a decrease in the P- and S-wave velocities of 375 m/s (13%) and 130 m/s (7%), respectively (Figure 5.10). Again, this velocity

change is sensible when the pyrolysis-induced change in porosity is considered – in this case, a 6.82 p.u. increase (or doubling) of the effective porosity (Table 5.2). As the hydrostatic confining pressure is increased from 1 MPa to 20 MPa, the acoustic velocities increase rapidly – up to 32 m s^{-1} MPa^{-1}, twice the rate of the oil window velocities. The extreme pressure-sensitivity of both the P- and S-wave velocities is further evidence of the previously imaged subparallel to bedding microcracks (Figure 5.4). Notably, upon the closure of induced microcracks at confining pressures greater than 20 MPa, the pre- and post-pyrolysis samples become acoustically indistinguishable to both compressional and shear waves. Further, as the sample is unloaded, it remains acoustically indistinguishable from the pre-pyrolysis sample for all pressures greater than 5 MPa for compressional waves and all pressures through the end of the unloading curve for shear waves. In the following section a conceptual model is presented to interpret the complex acoustic behavior of the Barnett Shale post-pyrolysis to the gas window.

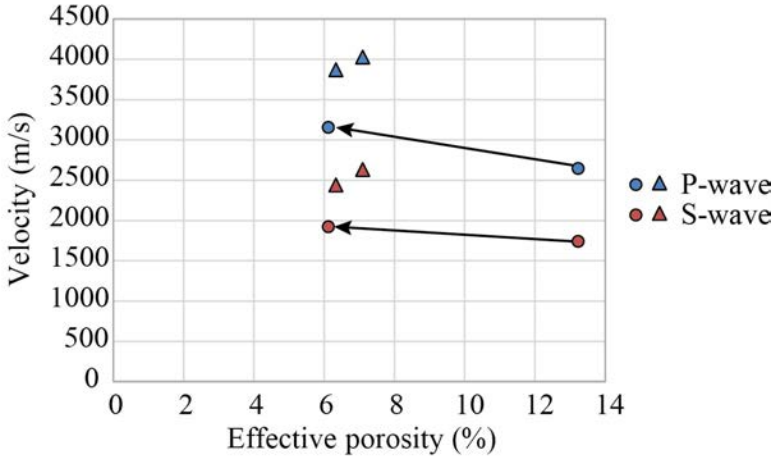

Figure 5.13: The vertically propagating P- and S-wave velocities for the outcrop (circles) and well-derived (triangles) Barnett Shale samples, at 50 MPa confining pressure, as a function of effective porosity. The arrows indicate the evolution of the outcrop sample post-pyrolysis to the oil window.

It is important to consider two potential caveats when applying these acoustic results to the in situ evolution of organic-rich shale. First, the duration of these acoustic experiments is very short relative to geological time; subsequently, while we are confident that we sufficiently account for viscoelastic deformation in this methodology (see Chapter 3), there is the potential that over longer time scales, the samples may physically relax to a greater degree upon unloading. This additional relaxation would result in lower acoustic velocities than those reported here. Second, the 'passive' opening of cracks due to relaxation reported here may be different to the 'active' opening of cracks induced by pore pressure increases, e.g., fluid injection. Any differences between 'passive' and 'active' crack opening must be quantified for the application of these results to pore pressure prediction studies.

The acoustic response of the micritic Green River sample to pyrolysis to the oil window is documented in Figure 5.11. As previously noted, the decrease in velocity is sensible given the sizable (∼10 p.u.) increase in effective porosity. The increase in velocity sensitivity to pressure

(from 3-4% of the maximum velocity to 12-15% for P-modes and from 1-2% to 5-11% for S-modes) is further indication of the conversion to fluids and expulsion of load-bearing, pore-filling organic matter during pyrolysis with subsequent formation of empty pores. Most notably, however, is that the velocity decrease in the oil window is effectively isotropic, with the maximum directional dependence being no greater than 60 m/s for any acoustic phase. This indicates that there is no appreciable development of aligned compliant porosity or other aligned features during pyrolysis to the oil window. Rather, combined with the consistent noted mass loss and increase in effective porosity and grain density between the two plugs (Table 5.2), the Green River samples appear to evolve uniformly and isotropically.

Upon thermal maturation to the gas window, the effective porosity of the vertical and horizontal plugs increases by a further 6 p.u. and 10 p.u., respectively; subsequently, there is a 7-9% and 6-19% decrease in the P- and S-wave velocities in the gas window. The generation and expulsion of additional hydrocarbons also results in an increase in the pressure-sensitivity of the acoustic velocities. The pressure-sensitivity of P-wave velocities increases from 8.5 and 10.6 m s^{-1} MPa^{-1} to 13.8 and 14.7 m s^{-1} MPa^{-1} for the vertical and horizontal samples, respectively, with an increase from 1.7-4.3 m s^{-1} MPa^{-1} to 4.9-6.5 m s^{-1} MPa^{-1} for shear phases. Again, we see that the evolution of compressional wave velocities post-pyrolysis is largely isotropic, indicative of limited induced microcracking. However, there does exist a significant directional dependence of the shear velocities post-pyrolysis.

As in Chapter 4, the acoustic heterogeneity between plugs can be established by comparing the magnitudes of the $V_S(0°)$ and $V_{SV}(90°)$ phases (Figure 5.14). Previously (Chapter 4), the thermally immature Green River sample was shown to exhibit consistent heterogeneity in shear phase velocities, potentially due to the interlocking crystalline microstructure of the randomly oriented, micritic sample. As a result of the non-aligned microstructure and the lack of observed aligned microcracks or other compliant features, the pressure-sensitivity of the S-wave velocity heterogeneity in the pyrolyzed plugs is attributed to differences in the quantity of retained hydrocarbons between the differently oriented plugs. In the gas window, $V_S(0°)$ is consistently faster than $V_{SV}(90°)$. This velocity heterogeneity is a result of the greater oil saturation of the vertically cored plug (Table 5.3), and we hypothesize that if not for the directionally dependent oil retention, the velocity heterogeneity in the Green River sample would be considerably lower. Similarly, we hypothesize that the velocity heterogeneity in the oil window – caused by the lower pressure-sensitivity of the vertical plug relative to the horizontal plug – may result from a greater quantity of retained hydrocarbons in the vertical sample. However, we do not have directional geochemistry data available for the oil window to confirm this hypothesis. At this time, the cause of the fourfold increase in retained free hydrocarbons for the vertically cored Green River sample relative to both the horizontally cored Green River and Barnett samples (Table 5.3) is unproven. However, we suspect the anomalous behavior to be a function of the vertically cored Green River microstructure inhibiting the expulsion of the generated hydrocarbons.

Clearly, the acoustic response of the micritic Green River sample is significantly different, both in magnitude and in the nature of the evolution itself, from that of the Barnett Shale. These differences are related to the respective microstructures of the samples in the following section.

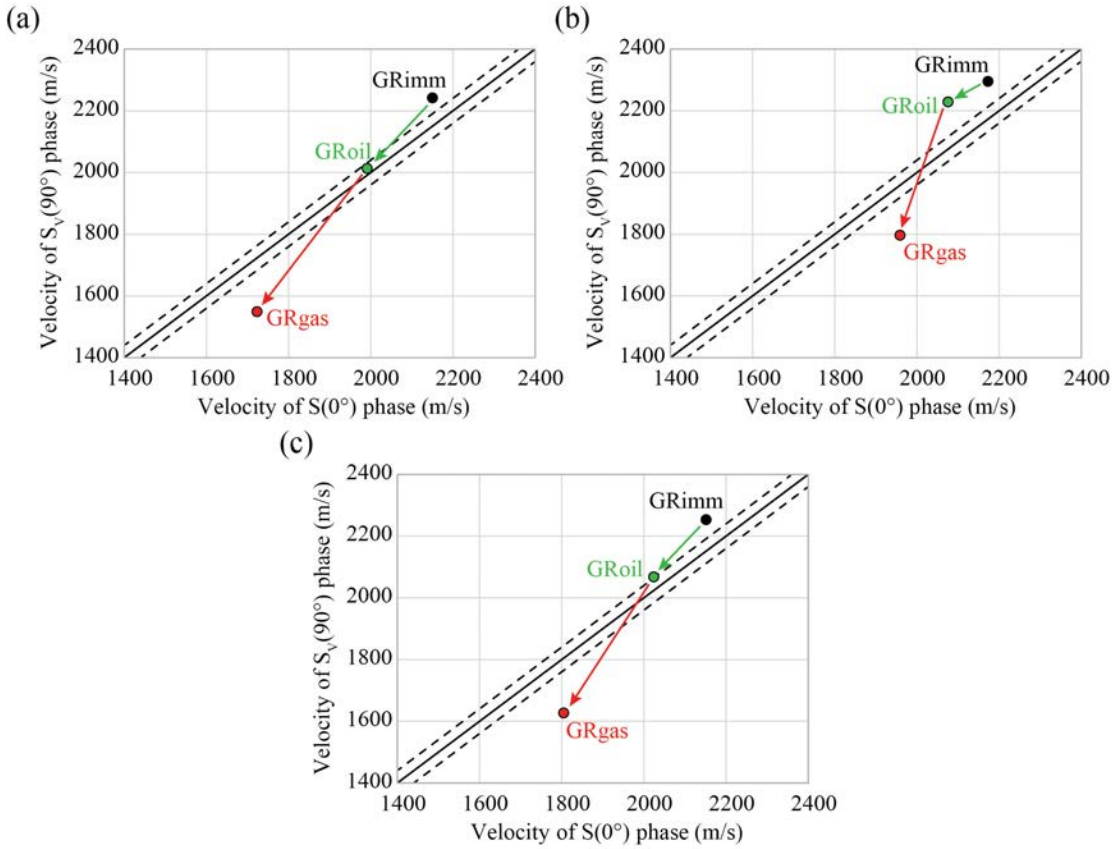

Figure 5.14: Crossplots of the $V_{SV}(90°)$ and $V_S(0°)$ phases at (a) the first pressure step (P_C = 1 MPa), (b) maximum confining pressure (P_C = 50 MPa), and (c) upon unloading (P_C = 1 MPa). For a set of homogeneous, perfectly VTI plugs, the points should fall on the solid black line. The dashed black lines mark a deviation of ±40 m/s from homogeneity, approximately the experimental error.

5.4.1.2 Elastic Anisotropy Evolution

While the loss during pyrolysis of sample BOH prevents the quantification of the elastic anisotropy of the Barnett Shale sample, we are able to make important comparisons between the laminar Barnett and Kimmeridge (Chapter 2) shale samples. After pyrolysis under confining pressure, we observe the combination of acoustically observable crack closure (Figure 5.10) and a lack of through-going or visibly abundant sample cracking in the Barnett Shale (Figure 5.15). Contrastingly, the Kimmeridge Shale sample was characterized by extensive, visible cracking at multiple length scales (e.g., Figure 5.15) and consistently lower velocities as a function of confining pressure after unconfined pyrolysis (see Chapter 2 for further discussion). Given the similarity in mineralogical composition, texture, and hydrocarbon potential of the two shales, we conclude that the significant cracking and associated extreme values of epsilon recorded for the Kimmeridge Shale samples are, as hypothesized in Chapter 2, a direct result of the lack of applied confining pressure resisting the build-up of pore pressure during the pyrolysis experiment.

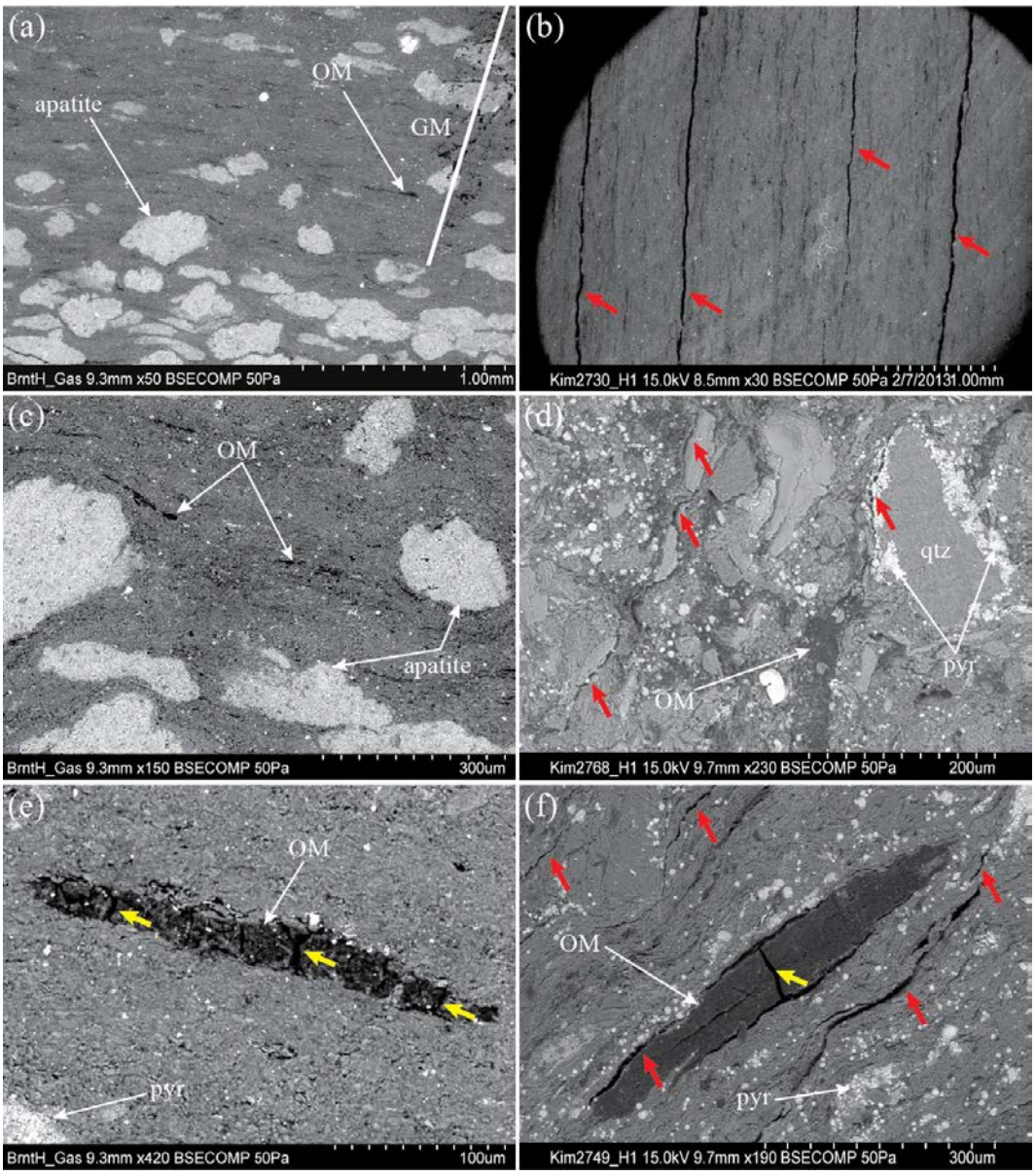

Figure 5.15: Representative SEM images of post-pyrolysis microstructures in the Barnett (left column) and Kimmeridge (right column) shales at a range of magnifications. Pyrolysis-induced noted evolutions include: red arrows identifying areas of cracking and yellow arrows identifying similar cross-kerogen cracking. The oddly textured image (d) comes from a 45 degree-cored fragment of Kimmeridge Shale that was pyrolyzed for test purposes.

The negligible evolution of epsilon (± 0.02) between the thermally immature and oil windows for the micritic Green River sample is representative of the, previously noted, largely isotropic evolution of P-wave velocities (Figures 5.11 and 5.12). At the same time, the values of gamma double due to a $\sim$3 GPa decrease in c_{44} relative to a $\sim$2 GPa decrease in c_{66} (Figure 5.12 and Appendix E). We lack the necessary data on the directional dependence of hydrocarbon retention in the oil window, but suspect that the change in gamma and underlying heterogeneous evolution of shear phases is related to differential hydrocarbon saturation and distribution between the differently oriented plugs.

After further pyrolysis to the gas window, the high confining pressure value of epsilon again shows very little change (±0.02; Figure 5.12). The small pressure-sensitivity of epsilon (±0.04) evident in the unloading curve is attributed to the greater hysteresis exhibited by the horizontal sample. The greater pressure-sensitivity of the horizontal plug may be a result of greater anelastic deformation when the pore space is relatively clear of hydrocarbons, i.e., the granular pack can re-settle more upon loading, while the relatively stiffer, pore-filling oil of the vertical sample resists this anelastic deformation. The values of gamma decrease and are largely equal to the thermally immature values (Figure 5.12). The decrease in gamma results from the relative lack of evolution in the velocities of the vertically cored sample. The previously noted suppressed thermal maturation of the vertical plug results in a greater volume of retained hydrocarbons which, in turn, results in a stiffer, acoustically faster rock. Finally, given the lack of observed aligned, compliant porosity and the relatively small degree of heterogeneity in S-wave velocity arising from such considerable hydrocarbon retention in the vertically cored sample (Figure 5.14), we hypothesize that an unsaturated Green River sample would exhibit very little evolution in elastic anisotropy post-pyrolysis to the gas window.

5.4.2 Phenomenological Conceptual Models of Shale Evolution

By combining microstructural observations and acoustic velocity measurements, we are able to develop two conceptual models for the respective phenomenological evolution of both organic-rich laminar shales and weakly aligned, micritic samples as a function of thermal maturity. If, given the visual, physical, and geochemical evidence, we consider that little thermal maturation occurred in the Barnett Shale sample during the first pyrolysis experiment, then we may consider the 'oil window' properties as the baseline for any thermal maturity-dependent discussion. Pre-pyrolysis, the laminar Barnett sample is composed of a well aligned, clay-rich matrix with dispersed stiffer grains e.g., apatite, and soft, organic inclusions (Figures 5.3 and 5.16). In this model, the vertically propagating acoustic waves exhibit pressure-sensitivity as the application of confining stress results in the partial compaction of the sizable pore space ($\phi \sim 13\%$) and compliant kerogen inclusions. Post-pyrolysis, the mineral matrix is largely unaltered (Figure 5.7); however, the organic inclusions have been expelled leaving largely porous voids (Figure 5.16). Furthermore, the expulsion of produced hydrocarbons from the thermally decomposing organic lenses, preferentially along the weak bedding planes, results in the formation of subparallel to bedding microcracks (Figure 5.16). This development of microcracks results in a significant decrease in the acoustic velocities at low confining pressures (Figure 5.10), i.e., when the microcracks are open. However, the application of increasing confining pressure closes the compliant microcracks, which stiffens the rock frame and increases the acoustic velocities (Figures 5.10 and 5.16). At high confining pressure, we observe that the acoustic velocity exhibits negligible evolution from the pre-pyrolysis values. The equivalence of velocity pre- (oil window) and post-pyrolysis (gas window) at pressures above ∼20 MPa indicates that the nature of the compliant inclusions, e.g., kerogen or pore space, is irrelevant to the load-bearing structure of the composite shale. Subsequently, in this laminar shale model, it is the thermally unaltered, load-bearing siliciclastic matrix that determines the high confining pressure acoustic velocity while the dispersed compliant inclusions (regardless of the inclusion-filling material) have no appreciable effect on the

acoustic response of the rock. In this manner, the thermal maturation of laminar shale is only acoustically observable so long as the induced, subparallel to bedding microcracks are open. Once the generated fluids migrate from the host rock, unless the fluid is replaced by other generated fluids, the cracks are expected to close and the acoustic signature of elevated thermal maturity will be lost.

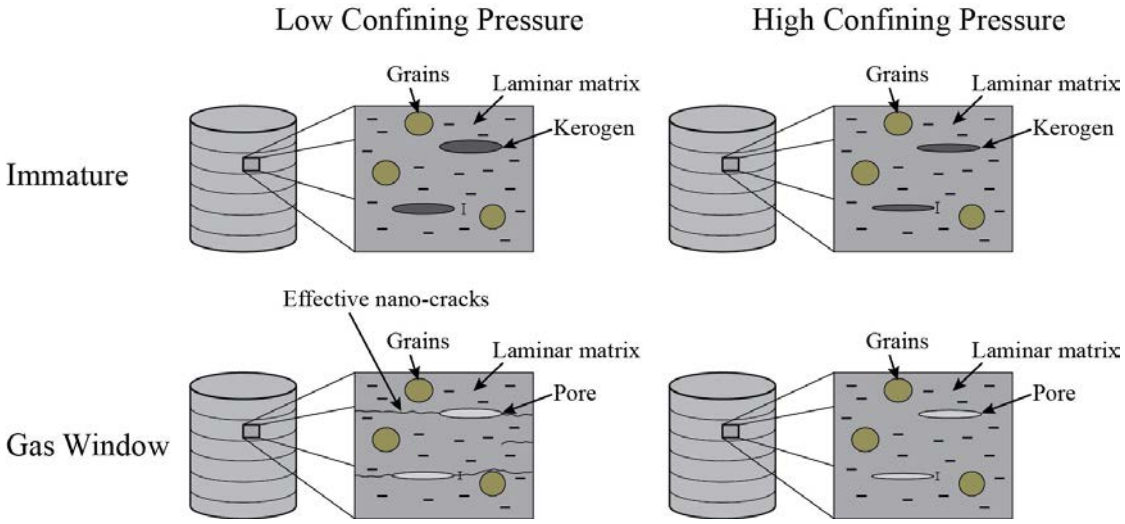

Figure 5.16: A conceptual model for the evolution of laminar shale upon thermal maturation as a function of confining pressure. Four stages of this evolution are shown: (top left) immature sample at low confining pressure, (top right) immature sample at high confining pressure, (bottom left) gas window sample at low confining pressure, and (bottom right) gas window sample at high confining pressure.

The baseline, thermally immature Green River sample is a tight (∼1% effective porosity), weakly aligned, dolomicrite rather than a 'typical' shale (Figure 5.3). The organic matter occurs in the Green River sample not as discrete, aligned lenses, but rather as an unstructured pore-filling phase. Subsequently, the sample is modeled as a sub-spherical granular pack with organic matter filling the intergranular pore space (Figure 5.17). This low porosity morphology with load-bearing, pore-filling kerogen results in fast, largely pressure-insensitive acoustic velocities (Figure 5.9). Post-pyrolysis, the visible loss of kerogen (Figures 5.6 and 5.7) and the subsequent increase in effective porosity (Table 5.2) indicates the loss of load-bearing pore-fill contributing to a significant decrease in acoustic velocities (Figures 5.11 and 5.17.c). Indeed, further pyrolysis amplifies this effect as still more pore-fill (in this case, both kerogen and heavier hydrocarbons) is expelled and the rock becomes acoustically still slower (Figure 5.11). Furthermore, the loss of still more pore-filling material enables the rock to strain to a greater degree under increasing confining pressure (Figure 5.17.d) which is acoustically visible as an increase in the pressure-sensitivity of velocities post-pyrolysis. That the acoustic evolution is largely isotropic, with no noticeable development of aligned compliant features or microcracks, indicates that in the absence of aligned features, e.g., mineral crystals, strong bedding, or organic lenses, in the microstructure of the thermally immature sample, the thermal maturation-induced evolution will occur uniformly and isotropically. Thus, in this model, the progression of thermal maturation across a micritic, non-laminar shale, or siltstone formation may be visible through lateral decreases in measured velocities, but not through anisotropic contrasts with thermally immature domains. The loss

of load-bearing, pore-filling material means that post-fluid migration, in the absence of severe re-compaction, the acoustic signature of thermal maturation will be preserved.

Importantly, these conceptual models are also applicable to the Kimmeridge Shale and Woodford Shale samples presented in Chapter 2. The laminar Kimmeridge samples exhibit a similar development of cracks as seen in the Barnett Shale. However, due to the lack of applied confining pressure during pyrolysis of the Kimmeridge samples, the effect of these cracks is compounded by the formation of sample-scale fractures. These fractures do not close at high confining pressure, as a result, the high confining pressure elastic behavior of the two laminar shales diverges; however, given the similar physical, geochemical, and low pressure elastic evolution of the two shales, we hypothesize that were the Kimmeridge Shale samples pyrolyzed under applied confining pressures the high confining pressure behavior of the two laminar shales would converge. Additionally, the directionally independent, isotropic evolution of the elastic properties of the weakly aligned, micritic Green River sample is a direct reflection of the behavior exhibited by the Woodford Shale sample. The Woodford sample was best described as a weakly aligned, clay-poor siltstone, and, subsequently, we determine that our conceptual model for the thermal evolution of the micritic Green River sample will be applicable to any weakly oriented micritic rock, non-laminar shale, or siltstone.

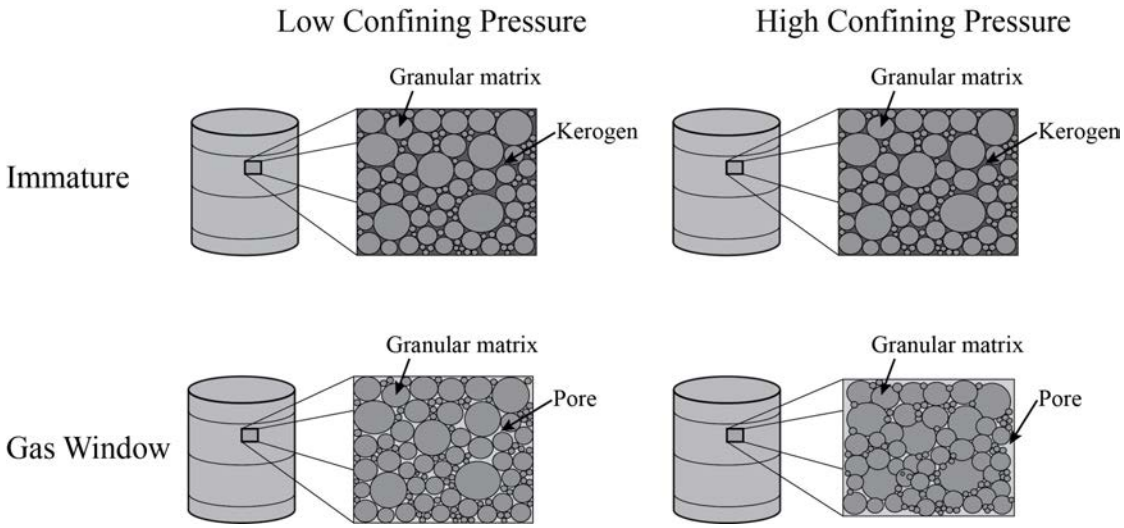

Figure 5.17: A conceptual model for the evolution of micritic rocks or siltstones upon thermal maturation as a function of confining pressure. Four stages of this evolution are shown: (top left) immature sample at low confining pressure, (top right) immature sample at high confining pressure, (bottom left) gas window sample at low confining pressure, and (bottom right) gas window sample at high confining pressure.

5.5 Conclusions

In this chapter, we have documented a set of pioneering experiments that characterize the elastic properties and microstructure of organic-rich shale after pyrolysis under representative reservoir confining pressures. By conducting these experiments on two endmember shales – one a clay-rich, laminar shale, the other an argillaceous dolomicrite – we are able to present evolutionary trends that should encompass a broad range of intermediately textured shales. Pyrolysis-induced thermal maturation of the laminar Barnett Shale leads to the formation of sub-micrometer-scale microcracks that preferentially align subparallel to bedding, most likely as a result of hydrocarbon expulsion. The development of this compliant porosity results in an up to 13% decrease in acoustic velocity perpendicular to bedding at low confining pressures. However, at confining pressures greater than 20 MPa, the microcracks close and the shale becomes acoustically indistinguishable from the pre-pyrolysis rock. Contrastingly, there is no observed alignment to the microcracks formed as a result of induced thermal maturation of the micritic Green River samples. Rather, the Green River samples exhibit a consistent, largely isotropic decrease in acoustic velocities (up to 20%) as load-bearing, pore-filling kerogen is removed from the system.

So long as the induced, aligned microcracks remain open, regions of laminar shale that have experienced thermal maturation, and subsequently may contain greater quantities of hydrocarbons, should be identifiable, at high frequencies, by an increase in elastic anisotropy. However, fluid expulsion or migration-induced closure of the microcracks will reduce, or potentially remove entirely, the anisotropic signature of elevated thermal maturity. In micritic rocks, non-laminar shales, or siltstones in which kerogen occurs as an unstructured, pore-filling phase, regions of elevated thermal maturity will be identifiable, at high frequencies, by decreases in the velocity of the formation; however, we do not expect an anisotropic signature to be developed due to the absence of aligned, compliant features.

5.6 Appendix

5.6.1 Appendix A: On the Anomalies in Tracking Thermal Maturity by RockEval Analysis and T_{MAX}

In this Appendix, I discuss issues related to establishing the thermal maturity of a pyrolyzed sample with the RockEval parameter T_{MAX}. Our geochemical analysis has identified two anomalous behaviors: firstly, the lack of observed thermal maturation of the oil window Barnett samples after the geochemical characterization subsample did exhibit hydrocarbon generation (as determined through visual, olfactory, and geochemical evidence), and secondly, the anomalously low T_{MAX} values reported for gas window, vertically cored Green River samples.

In Table 5A.1, I present the programmed control temperature (T_{CTRL}) and bulk temperature (T_{BULK}) in the reactor (computed using the ideal gas law and the confining pressure recorded during pyrolysis) to better address the thermal fidelity of the high temperature-high pressure reactor (HTHP). The samples studied and listed in Table 5A.1 include all experiments previously presented in Table 5.3 as well as the data from all other pyrolysis experiments conducted in this thesis. Consideration of Table 5A.1 reveals that, in all but one case, the bulk temperature in the reactor is less than the programmed temperature. This is sensible as the programmed temperature corresponds to the heater itself, while the bulk temperature incorporates all thermal regimes, e.g., both the hottest argon around the heater and the cooler argon away from the heater at the pressure gauges. Of greater concern is the fact that there is large variability in the misfit, or difference between T_{CTRL} and T_{BULK} across the different experiments. It is pivotal for future pyrolysis experiments that the source of the variability in the misfit be identified such that the user has greater control over the temperature at which pyrolysis is performed.

The importance of the variability of the difference between T_{CTRL} and T_{BULK} becomes evident when comparing T_{BULK} and the induced thermal maturity as characterized by T_{MAX} (Table 5A.1 and Figure 5A.1). From Table 5A.1, the lack of evolution in T_{MAX} across the different oil window experiments is apparent. At this point, it is clear that the apparent lack of thermal maturation of the Barnett oil window samples compared to the geochemical characterization subsample is a result of the anomalously low bulk temperature, i.e., colder reactor, during those experiments – 18-60 °C cooler than during the experiment for the geochemical subsample. Indeed, this conclusion is reinforced by the apparent relationship between T_{BULK} and the induced degree of thermal maturity (Figure 5A.1). Hence, the variability in the misfit between the intended pyrolysis temperature and the bulk reactor temperature must be minimized to enable reproducible thermal maturation experiments on multiple samples.

While much of the data in Figure 5A.1 indicates a first order, Arrhenius-like kinetic relationship, the vertically cored Green River samples pyrolyzed to the gas window (GRVgas) are anomalously immature for the respective calculated values of T_{BULK}. In addition to the low T_{MAX} values, the GRVgas samples retain between 3.0 and 4.8 times more free hydrocarbons

than the equivalently pyrolyzed horizontally cored samples (GRHgas). Given that GRHgas_perm and GRVgas_perm were pyrolyzed in one experiment and that GRVgas_perm retains 3.8 times more free hydrocarbons, the bulk temperature within the reactor is not the source of this T_{MAX} anomaly.

Table 5A.1: A comparison of the pertinent temperatures to each pyrolysis experiment and the resultant degree of thermal maturity for all experiments. Each pyrolysis experiment is identified by a programmed control temperature (T_{CTRL}) and a bulk temperature within the HTHP (T_{BULK}) and a subsequent misfit (T_{CTRL}-T_{BULK}). A T_{MAX} value of 'N/A' indicates it was not measured. Samples labeled 'Geochemical' were matured specifically for geochemical characterization. The targeted window of thermal maturity is noted by the suffix in the Sample Label, e.g., 'oil.' The suffix '_perm' indicates an experiment that thermally matured a permeability subsample.

Formation	Sample Label	T_{CTRL} (°C)	T_{BULK} (°C)	Misfit (°C)	T_{MAX} (°C)
Barnett	Geochemical	345	351	-6	436
	Geochemical	360	358	2	438
	BOHoil	360	322	38	431
	BOVoil	360	302	58	N/A
	BOHoil_perm	360	340	20	N/A
	BOVgas	425	350	75	N/A
	BOHgas_perm	425	373	52	486
	BOVgas_perm	425	379	46	500
Green River	Geochemical	345	338	7	430
	Geochemical	380	338	42	427
	GRHoil	380	327	53	N/A
	GRVoil	380	329	51	N/A
	GRHgas	425	406	19	480
	GRVgas	425	373	52	439
	GRHgas_perm	425	381	44	491
	GRVgas_perm	425	381	44	423

Rather there is evidence in the geochemical literature that hydrocarbon generation can be delayed in fine-grained, tight, oil-prone carbonate source rocks (Palacas, 1984). In this scenario, a moderate amount of hydrocarbon generation can create and maintain sufficient pore pressure to retard the chemical reactions necessary for further hydrocarbon generation (Jones, 1984). The Green River samples in this study are exactly fine-grained (micritic), tight, oil-prone carbonate source rocks; subsequently, if there exists a, previously un-imaged, degree of microstructural heterogeneity between the vertical and horizontal plugs that limits fluid migration within the vertical plug, thermal maturation may be retarded in the vertical plugs. Given the high gas permeability of the GRVgas sample (see Chapter 6), the retention of such sizable quantities of low viscosity gases is highly unlikely; thus, we assume the sample must be retaining more viscous, heavier hydrocarbons. This assumption would serve to support the hypothesis of pore pressure buildup preventing the progression of thermal maturation and subsequent cracking of heavier hydrocarbons to lighter molecular weight gases. In any case, targeted studies of the geochemistry of pyrolyzed intact cores of various mineralogies and textures is required to fully address this problem.

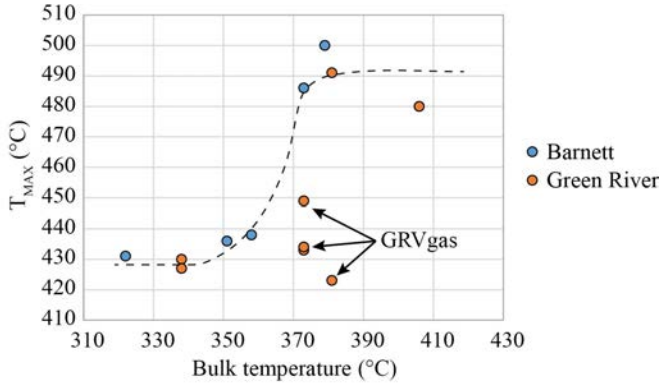

Figure 5A.1: The RockEval thermal maturity parameter, T_{MAX}, as a function of the computed bulk temperature in the HTHP for both the Barnett (blue) and Green River (orange) samples. A dashed trend line is added to display the first order, Arrhenius-like behavior of kerogen maturation as documented in Pepper and Corvi (1995).

5.6.2 Appendix B: Discussion of the Hypothetical Evolution of the Elastic Anisotropy of the Barnett Shale Sample

Due to the severe fracturing of the horizontally cored Barnett Shale sample during pyrolysis to the oil window, it is impossible to quantify the evolution of the elastic anisotropy of the Barnett Shale upon pyrolysis in this study. However, by applying a set of restrictions to the evolution of the horizontally cored sample we can establish hypothetical horizontal velocity values and qualitatively comment on the evolution of the elastic anisotropy of the Barnett Shale sample.

In order to define the evolution of the horizontal plug post-pyrolysis, we make the following observations:

1. Post-pyrolysis, the vertically cored plug exhibits subparallel to bedding cracking; subsequently, the horizontally cored plug should also preferentially crack subparallel to bedding,

2. The Kimmeridge Shale samples in Chapter 2 are of similar clay content and are similarly aligned to the Barnett Shale sample; further, the Kimmeridge samples also exhibit subparallel to bedding cracking,

3. Upon pyrolysis, the vertically propagating Kimmeridge P-wave velocity decreased by 17.8%, while the horizontally propagating P-wave velocity decreased by only 1.2%.

Subsequently, we may assume that, as with the Kimmeridge Shale, the horizontally cored Barnett plug will also evolve negligibly compared to the vertically cored Barnett plug. Thus, we can estimate the elastic anisotropy of the Barnett shale by holding the horizontally propagating velocities constant as a function of thermal maturity. It is important to note that by assuming no evolution of the horizontal velocities post-pyrolysis, we likely calculate the maximum possible anisotropic evolution with thermal maturity. If, in reality, the horizontal velocities of the more porous pyrolyzed plug decrease the true values of epsilon will be lower than those estimated here; further, it is highly unlikely that the horizontal velocities will increase given the noted 6-7 p.u. increase in effective porosity post-pyrolysis.

Given the severe compaction of the vertical sample upon pyrolysis to the oil window, it makes little sense to compute the change in elastic anisotropy from the immature to oil windows as the change is not relevant to induced thermal maturation of the organic matter. Rather, we treat the oil window sample as the baseline and study the change in elastic anisotropy from the oil to the gas window. The change in anisotropy from the oil to the gas window (for some anisotropic parameter, ψ) is then:

$$\Delta\psi = \psi_{gas} - \psi_{oil}, \tag{5B.1}$$

which, for epsilon, ε_{gas} may be written as:

$$\varepsilon_{gas} = \left(\frac{c_{11} - c_{33}}{2c_{33}}\right)_{gas} = \frac{\left(V_{P,imm}(90°)\right)^2 - \left(V_{P,gas}(0°)\right)^2}{2\left(V_{P,gas}(0°)\right)^2} \tag{5B.2}$$

The same process may then be followed for gamma using the standard definition from Thomsen (1986). The change in anisotropy upon pyrolysis to the gas window (as defined in Equation 5B.1) is presented in Figure 5B.1. For both epsilon and gamma we see that, post-pyrolysis to the gas window, the induced subparallel to bedding microcracks result in an increase in the magnitude of elastic anisotropy due to the slowing of the vertically propagating acoustic waves. However, with increasing confining pressure, as the observed microcracks close, epsilon and gamma return, within ±0.02, to their pre-pyrolysis values. Subsequently, as in the previous discussion limited to vertically propagating acoustic waves, and under the aforementioned assumptions, the thermal maturity of laminar shale is only anisotropically observable so long as the generated hydrocarbons (or some other pore fluids) are retained and propping open the induced, subparallel to bedding microcracks. The expulsion or migration of these fluids would allow the microcracks to close and the anisotropic contrast with thermally immature shale would be lost.

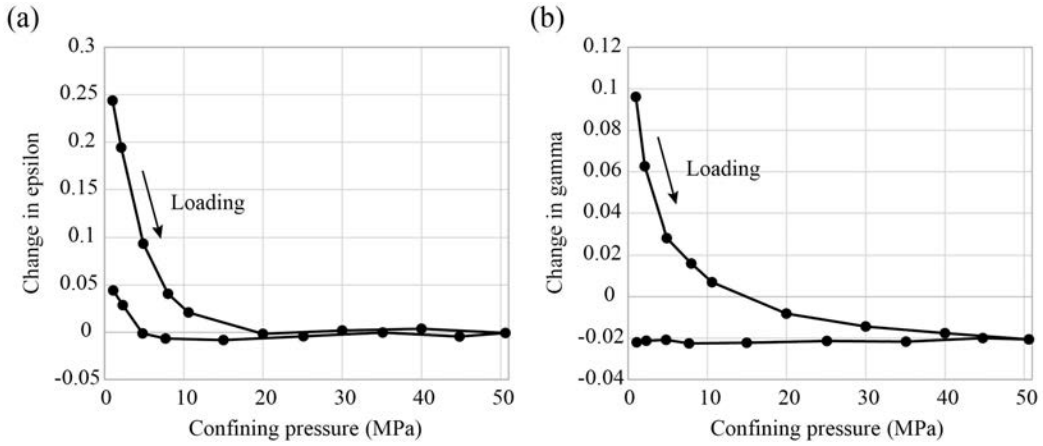

Figure 5B.1: The hypothetical change in epsilon (a) and gamma (b) of the Barnett Shale upon pyrolysis to the gas window.

5.6.3 Appendix C: Acoustic Velocity Dataset

Table 5C.1: Acoustic velocity (m/s) as a function of confining pressure (P_C) for sample BO in the immature window of thermal maturity. Velocity phases are as illustrated in Figure 3.4.

P_C (MPa)	V_P(0°)	V_S(0°)	V_P(90°)	V_{SH}(90°)	V_{SV}(90°)
1	2222	1627	3577	2227	1638
2	2233	1632	3594	2236	1652
5	2285	1654	3608	2250	1664
7.5	2326	1665	3623	2267	1669
10	2348	1672	3632	2275	1674
20	2462	1687	3657	2284	1676
30	2548	1706	3677	2294	1680
40	2604	1726	3690	2306	1687
50	2646	1741	3717	2313	1693
45	2636	1740	3712	2312	1692
35	2605	1733	3709	2311	1629
25	2566	1725	3688	2303	1692
15	2498	1709	3674	2290	1690
7.5	2435	1692	3652	2279	1688
5	2402	1681	3637	2274	1683
2	2366	1671	3622	2262	1671
1	2338	1663	3611	2253	1661

Table 5C.2: Acoustic velocity (m/s) as a function of confining pressure (P_C) for sample BO in the oil and gas windows of thermal maturity. Velocity phases are as illustrated in Figure 3.4. Note that, due to sample loss, only the vertically propagating velocities are available.

P_C	Oil		Gas	
(MPa)	V_P(0°)	V_S(0°)	V_P(0°)	V_S(0°)
1	2775	1825	2402	1696
2	2838	1844	2509	1750
5	2907	1876	2711	1821
7.5	2953	1890	2846	1851
10	2990	1900	2920	1873
20	3068	1912	3045	1907
30	3117	1917	3085	1921
40	3148	1919	3111	1927
50	3153	1921	3126	1932
45	3139	1920	3120	1930
35	3132	1919	3104	1933
25	3104	1918	3086	1932
15	3059	1915	3050	1929
7.5	2996	1907	2981	1921
5	2951	1898	2925	1909
2	2907	1879	2825	1891
1	2871	1863	2763	1875

Table 5C.3: Acoustic velocity (m/s) as a function of confining pressure (P_C) for the Green River sample in the immature window of thermal maturity. Velocity phases are as illustrated in Figure 3.4.

P_C (MPa)	$V_P(0°)$	$V_S(0°)$	$V_P(90°)$	$V_{SH}(90°)$	$V_{SV}(90°)$
1	4075	2150	4401	2458	2242
2	4088	2156	4417	2463	2251
5	4106	2156	4426	2472	2260
7.5	4126	2160	4438	2477	2269
10	4145	2162	4460	2482	2276
20	4169	2168	4489	2486	2281
30	4196	2172	4509	2491	2286
40	4225	2173	4521	2496	2293
50	4229	2173	4535	2497	2295
45	4222	2171	4528	2492	2292
35	4207	2170	4521	2493	2288
25	4187	2166	4508	2488	2286
15	4161	2164	4489	2481	2281
7.5	4124	2160	4457	2469	2274
5	4106	2157	4445	2464	2268
2	4086	2155	4423	2461	2259
1	4073	2152	4408	2458	2253

Table 5C.4: Acoustic velocity (m/s) as a function of confining pressure (P_C) for the Green River sample in the oil window of thermal maturity. Velocity phases are as illustrated in Figure 3.4.

P_C (MPa)	$V_P(0°)$	$V_S(0°)$	$V_P(90°)$	$V_{SH}(90°)$	$V_{SV}(90°)$
1	3431	1991	3650	2224	2013
2	3505	2004	3732	2239	2036
5	3622	2019	3887	2259	2074
7.5	3684	2031	3959	2276	2105
10	3713	2036	4012	2289	2124
20	3767	2048	4092	2327	2176
30	3801	2058	4136	2347	2200
40	3828	2070	4158	2365	2218
50	3856	2076	4181	2371	2229
45	3837	2070	4161	2364	2223
35	3826	2069	4147	2359	2216
25	3812	2065	4122	2347	2202
15	3777	2054	4083	2326	2184
7.5	3726	2044	4027	2299	2142
5	3690	2035	3981	2283	2120
2	3661	2030	3929	2267	2088
1	3631	2024	3875	2258	2068

Table 5C.5: Acoustic velocity (m/s) as a function of confining pressure (P_C) for the Green River sample in the gas window of thermal maturity. Velocity phases are as illustrated in Figure 3.4.

P_C (MPa)	V_P(0°)	V_S(0°)	V_P(90°)	V_{SH}(90°)	V_{SV}(90°)
1	2825	1723	3158	1806	1549
2	2920	1763	3266	1831	1572
5	3118	1823	3456	1872	1610
7.5	3216	1854	3564	1912	1639
10	3261	1866	3628	1946	1666
20	3371	1905	3751	2015	1731
30	3433	1929	3833	2065	1764
40	3497	1944	3891	2098	1785
50	3518	1959	3891	2129	1797
45	3512	1955	3884	2125	1793
35	3497	1953	3879	2119	1791
25	3461	1941	3828	2105	1781
15	3391	1917	3765	2073	1757
7.5	3288	1879	3657	2019	1716
5	3197	1849	3573	1983	1689
2	3085	1825	3464	1942	1656
1	2979	1805	3404	1906	1627

5.6.4 Appendix D: Porosity Evolution with Confining Pressure Dataset

Table 5D.1: Sample porosity (ϕ) as a function of confining pressure (P_C) for sample BO in the immature, oil, and gas windows. The plug orientations are denoted as vertical (0°) and horizontal (90°), respectively. Note that, due to sample loss, horizontal porosity values are not available above the immature window of thermal maturity.

P_C (MPa)	Immature		Oil		Gas	
	φ(0°)	φ(90°)	φ(0°)	φ(90°)	φ(0°)	φ(90°)
1	13.23	12.72	6.12	N/A	12.94	N/A
2	13.07	12.56	5.78		12.61	
5	12.57	12.06	4.79		11.67	
7.5	12.21	11.70	3.95		10.87	
10	11.89	11.37	3.38		10.32	
20	10.66	10.13	1.45		8.48	
30	9.38	8.84	-0.30		6.81	
40	8.10	7.56	-1.92		5.27	
50	6.84	6.30	-3.54		3.71	
45	6.96	6.41	-3.34		3.91	
35	7.82	7.28	-2.42		4.79	
25	8.93	8.40	-0.98		6.16	
15	10.10	9.57	0.61		7.68	
7.5	11.06	10.54	2.09		9.10	
5	11.50	10.98	2.80		9.77	
2	11.86	11.35	3.50		10.44	
1	12.09	11.58	3.90		10.82	
0.1	12.37	11.86	4.52		11.42	

Table 5D.2: Sample porosity (ϕ) as a function of confining pressure (P_C) for the Green River sample in the immature, oil, and gas windows. The plug orientations are denoted as vertical (0°) and horizontal (90°), respectively.

P_C	Immature		Oil		Gas	
(MPa)	φ(0°)	φ(90°)	φ(0°)	φ(90°)	φ(0°)	φ(90°)
1	0.53	1.28	10.96	11.13	16.55	20.11
2	0.35	1.10	10.71	10.88	16.43	19.99
5	-0.27	0.49	10.07	10.24	15.94	19.52
7.5	-0.70	0.05	9.51	9.69	15.56	19.16
10	-1.12	-0.37	9.06	9.23	15.24	18.85
20	-2.45	-1.68	7.60	7.78	14.14	17.79
30	-3.71	-2.94	6.20	6.38	13.00	16.71
40	-4.90	-4.11	4.88	5.06	11.91	15.66
50	-5.95	-5.16	3.55	3.73	10.82	14.62
45	-5.78	-4.99	3.31	3.49	10.82	14.61
35	-4.91	-4.12	4.11	4.29	11.55	15.32
25	-3.74	-2.97	5.28	5.46	12.57	16.30
15	-2.42	-1.65	6.55	6.73	13.63	17.31
7.5	-1.37	-0.61	7.59	7.77	14.52	18.16
5	-0.88	-0.13	8.13	8.31	14.92	18.54
2	-0.48	0.27	8.61	8.79	15.26	18.87
1	-0.23	0.52	8.93	9.11	15.47	19.07
0.1	0.11	0.86	9.42	9.59	15.77	19.35

5.6.5 Appendix E: Velocity-Derived Elastic Dataset

Table 5E.1: Computed elastic moduli and Thomsen's elastic anisotropy parameters as a function of confining pressure (P_C) for sample BO in the immature window of thermal maturity.

P_C	C_{11}	C_{33}	C_{44}	C_{66}	ε	γ
(MPa)	(GPa)	(GPa)	(GPa)	(GPa)	(-)	(-)
1	25.73	9.93	5.32	9.97	0.795	0.438
2	26.02	10.05	5.37	10.07	0.795	0.438
5	26.36	10.58	5.54	10.25	0.746	0.424
7.5	26.70	11.01	5.64	10.46	0.713	0.427
10	26.93	11.25	5.70	10.57	0.696	0.426
20	27.69	12.55	5.89	10.81	0.603	0.416
30	28.38	13.64	6.11	11.05	0.541	0.404
40	28.99	14.44	6.34	11.32	0.504	0.393
50	29.81	15.12	6.54	11.55	0.486	0.383
45	29.70	14.98	6.52	11.52	0.491	0.383
35	29.38	14.50	6.41	11.40	0.513	0.389
25	28.70	13.89	6.28	11.19	0.533	0.391
15	28.12	13.00	6.09	10.92	0.581	0.397
7.5	27.48	12.22	5.90	10.70	0.625	0.407
5	27.13	11.83	5.79	10.61	0.647	0.415
2	26.79	11.43	5.70	10.44	0.672	0.416
1	26.56	11.13	5.63	10.34	0.693	0.417

Table 5E.2: Computed elastic moduli as a function of confining pressure (P_C) for sample BO in the oil and gas windows of thermal maturity.

P_C (MPa)	Oil		Gas	
	C_{33} (GPa)	C_{44} (GPa)	C_{33} (GPa)	C_{44} (GPa)
1	16.30	7.05	11.95	5.96
2	17.11	7.23	13.09	6.37
5	18.14	7.56	15.44	6.97
7.5	18.89	7.74	17.18	7.27
10	19.47	7.86	18.18	7.48
20	20.91	8.13	20.19	7.92
30	21.97	8.31	21.10	8.18
40	22.77	8.46	21.82	8.37
50	23.21	8.61	22.39	8.55
45	22.95	8.59	22.25	8.51
35	22.65	8.51	21.82	8.46
25	21.94	8.38	21.27	8.33
15	20.97	8.22	20.43	8.18
7.5	19.81	8.03	19.22	7.98
5	19.08	7.89	18.37	7.82
2	18.39	7.69	17.00	7.62
1	17.86	7.52	16.20	7.46

Table 5E.3: Computed elastic moduli and Thomsen's elastic anisotropy parameters as a function of confining pressure (P_C) for the Green River sample in the immature window of thermal maturity.

P_C (MPa)	C_{11} (GPa)	C_{33} (GPa)	C_{44} (GPa)	C_{66} (GPa)	ε (-)	γ (-)
1	43.80	37.27	10.38	13.67	0.088	0.070
2	44.21	37.59	10.45	13.74	0.088	0.067
5	44.66	38.14	10.52	13.93	0.085	0.069
7.5	45.09	38.68	10.61	14.05	0.083	0.067
10	45.74	39.20	10.67	14.17	0.083	0.066
20	46.94	40.18	10.87	14.40	0.084	0.063
30	47.94	41.22	11.04	14.63	0.082	0.060
40	48.75	42.26	11.18	14.86	0.077	0.060
50	49.56	42.76	11.29	15.02	0.079	0.057
45	49.32	42.55	11.25	14.94	0.080	0.057
35	48.76	41.90	11.15	14.83	0.082	0.060
25	47.95	41.04	10.99	14.60	0.084	0.060
15	46.93	40.02	10.82	14.33	0.086	0.061
7.5	45.78	38.91	10.67	14.05	0.088	0.060
5	45.32	38.38	10.59	13.93	0.090	0.060
2	44.69	37.86	10.53	13.84	0.090	0.061
1	44.28	37.52	10.47	13.77	0.090	0.065

Table 5E.4: Computed elastic moduli and Thomsen's elastic anisotropy parameters as a function of confining pressure (P_C) for the Green River sample in the oil window of thermal maturity.

P_C (MPa)	C_{11} (GPa)	C_{33} (GPa)	C_{44} (GPa)	C_{66} (GPa)	ε (-)	γ (-)
1	28.82	25.59	8.62	10.70	0.063	0.121
2	30.21	26.77	8.75	10.87	0.064	0.121
5	33.01	28.80	8.95	11.15	0.073	0.123
7.5	34.45	29.98	9.11	11.39	0.075	0.125
10	35.57	30.61	9.20	11.58	0.081	0.129
20	37.58	32.02	9.46	12.16	0.087	0.143
30	38.97	33.09	9.70	12.55	0.089	0.147
40	39.95	34.04	9.95	12.93	0.087	0.150
50	40.96	35.02	10.15	13.17	0.085	0.149
45	40.67	34.76	10.11	13.12	0.085	0.149
35	40.06	34.28	10.02	12.96	0.084	0.147
25	39.10	33.60	9.86	12.68	0.082	0.143
15	37.85	32.55	9.63	12.28	0.082	0.138
7.5	36.41	31.32	9.43	11.86	0.081	0.129
5	35.38	30.55	9.29	11.63	0.079	0.126
2	34.27	29.91	9.20	11.41	0.073	0.121
1	33.23	29.30	9.11	11.28	0.067	0.119

Table 5E.5: Computed elastic moduli and Thomsen's elastic anisotropy parameters as a function of confining pressure (P_C) for the Green River sample in the gas window of thermal maturity.

P_C (MPa)	C_{11} (GPa)	C_{33} (GPa)	C_{44} (GPa)	C_{66} (GPa)	ε (-)	γ (-)
1	20.82	16.93	6.29	6.81	0.115	0.041
2	22.30	18.11	6.60	7.01	0.116	0.031
5	25.12	20.77	7.10	7.37	0.105	0.019
7.5	26.83	22.19	7.37	7.72	0.104	0.024
10	27.91	22.90	7.50	8.03	0.109	0.035
20	30.22	24.79	7.92	8.72	0.109	0.051
30	31.97	26.05	8.22	9.28	0.114	0.065
40	33.37	27.37	8.46	9.70	0.110	0.073
50	33.79	28.06	8.70	10.12	0.102	0.082
45	33.66	27.95	8.66	10.08	0.102	0.082
35	33.30	27.49	8.57	9.94	0.106	0.080
25	32.05	26.61	8.37	9.70	0.102	0.079
15	30.64	25.24	8.06	9.29	0.107	0.076
7.5	28.60	23.49	7.67	8.72	0.109	0.068
5	27.18	22.10	7.39	8.37	0.115	0.066
2	25.44	20.49	7.17	8.00	0.121	0.057
1	24.50	19.10	7.00	7.68	0.142	0.049

5.7 References

Allan, A. M., T. Vanorio, and J. E. P. Dahl, 2014, Pyrolysis-induced P-wave velocity anisotropy in organic-rich shales: Geophysics, 79:D41–D53.

Allan, A. M., W. Kanitpanyacharoen, and T. Vanorio, 2015, A multi-scale methodology for the analysis of velocity anisotropy in organic-rich shale: Geophysics, 80:C73–C88.

Clark, A. C. and T. Vanorio, 2015, A niche system for inducing thermo-chemo-mechanical processes in rocks and materials: SRB Volume 142.

Jones, R. W., 1984, Comparison of carbone and shale source rocks, in J. G. Palacas, ed., Petroleum geochemistry and source-rock potential of carbonate rocks: AAPG Studies in Geology 18.

Kobchenko, M., H. Panahi, F. Renard, D. K. Dysthe, A. Malthe-Sørenssen, A. Mazzini, J. Scheibert, B. Jamtveit, and P. N. Meakin, 2011, 4D imaging of fracturing in organic-rich shales during heating: Journal of Geophysical Research, 116:B12201.

MacBeth, C., 2004, A classification for the pressure-sensitivity properties of a sandstone rock frame: Geophysics, 69(2):497–510.

Palacas, J. G., 1984, South Florida basin, a prime example of carbonate source rocks of petroleum, in J. G. Palacas, ed., Petroleum geochemistry and source-rock potential of carbonate rocks: AAPG Studies in Geology 18.

Pepper, A. S. and P. J. Corvi, 1995, Simple kinetic models of petroleum formation. Part I: Oil and gas generation from kerogen: Marine and Petroleum Geology, 12(3):291–319.

Peters, K. E. and M. R. Cassa, 1994, Applied source rock geochemistry, in L. B. Magoon, and W. G. Dow, eds., The petroleum system - From source to trap: AAPG, AAPG Memoir, 60: 93–120.

Thomsen, L., 1986, Weak elastic anisotropy: Geophysics, 51:1954–1966.

Vernik, L. and C. Landis, 1996, Elastic anisotropy of source rocks: Implications for hydrocarbon generation and primary migration: AAPG Bulletin, 80:531–544.

Vernik, L. and X. Liu, 1997, Velocity anisotropy in shales: A petrophysical study: Geophysics, 62:521–532.

Vernik, L. and A. Nur, 1992, Ultrasonic velocity and anisotropy of hydrocarbon source rocks: Geophysics, 57:727–735.

Yenugu, M. R., 2014, Elastic, microstructural and geochemical characterization of kerogen maturity for shales: PhD Dissertation, University of Houston.

Chapter 6

THE EVOLUTION OF THE TRANSPORT PROPERTIES OF ORGANIC-RICH SHALE UPON THERMAL MATURATION – EXPERIMENTAL AND NUMERICAL OBSERVATIONS

Abstract

In this chapter, I apply the iterative pyrolysis-centric shale characterization methodology, previously discussed in Chapters 3 and 5, to the investigation of the effect of thermal maturation on the transport properties of organic-rich shale. Through the implementation of this methodology, I observe a significant increase in experimental permeability values between the thermally

immature and gas window samples: from 400 nD to 8 μD and <5 nD to 10 mD parallel to bedding for Barnett Shale and Green River samples, respectively. Furthermore, this induced permeability is found to be relatively insensitive to effective pressure and, thus, is not simply the result of microcracking or fracturing of the sample. Most importantly, the permeability evolution observed here fits strongly with the conceptual models for laminar and crystalline shales developed in Chapter 5. High-resolution imaging and numerical studies demonstrate a significant increase in organic porosity with increasing thermal maturity; however, this organic porosity does not correspond with a clear increase in simulated permeability values. The lack of correlation between thermal maturity and numerically simulated permeability stems from heterogeneities inherent to the pore space at the micron-scale, such as immature samples being more heavily percolated by wide intergranular pores while post-mature samples are percolated by narrow organic porosity. Additionally, I demonstrate that experimentally and numerically determined permeability values are best compared as a function of flow-controlling pore widths rather than bulk porosity as is common in many rock physics relationships.

6.1 Introduction

Advances in drilling and completion technology have driven a significant increase in the exploitation of organic-rich shales as unconventional reservoirs. Subsequently, dry gas production in the U.S. from shale is projected to grow by 113% between 2011 and 2040 (EIA, 2013). The organic-rich shale that hosts these reserves is often characterized by extremely low permeability values, on the scale of nanoDarcies ($\sim 10^{-21}$ m^2; e.g., Mullen, 2010; Kang et al., 2011; Heller et al., 2014), with the majority of the pore space composed of nanometer-scale pores in organic matter (Loucks et al., 2009; Sondergeld et al., 2010; Curtis et al., 2012). It has alternatively been argued that the gas permeability of shale is controlled by organic-rich pathways (e.g., Wang and Reed, 2009) or by interconnected networks of Darcy-scale microcracks (e.g., Vermylen, 2011). While further evidence points to natural and/or induced fractures controlling reservoir performance in the short term, and the transport properties of the matrix, composed of nanometer-scale pores, governing long term reservoir performance (Heller et al., 2014). Subsequently, a thorough understanding of the scale and nature of the microstructural components, i.e., matrix/kerogen connectivity vs. microcracks, which govern permeability in shale is pivotal. Furthermore, in this work, we address how changes in the microstructural components, e.g., relative fraction of cracks and organic porosity, during thermal maturation affect the permeability of organic-rich shale.

To this end, there has been extensive recent experimental research into the permeability of shale as a function of pressure in order to study the effect of compliant porosity and other microstructural controls (e.g., Bustin et al., 2008; Kang et al., 2011; Vermylen, 2011; Heller et al., 2014; Bhandari et al., 2015). It is clear from these studies that the presence, connectivity, and pressure-sensitivity of microcracks has a large effect on the permeability of shale samples. Previous investigations of the elastic properties and microstructure of organic-rich shale have documented the development of subparallel to bedding microcracking with increasing thermal maturity of the constituent organic matter (Vernik, 1993; Johnston and Christensen, 1995; Lash

and Engelder, 2005; Dewhurst and Siggins, 2006; Kobchenko et al., 2011; Allan et al., 2014, and Chapter 5 in this thesis). Furthermore, through high-resolution imaging, the volume of organic porosity has been shown to increase with thermal maturity (Loucks et al., 2009; Walls and Sinclair, 2011; Curtis et al., 2010, 2012; Bernard et al., 2012). As a result, with increasing thermal alteration of the organic matter, the volume of organic-rich pathways increases, as does the number of microcracks potentially enabling flow to bypass the narrower organic pathways. It is, then, important to identify the microstructural evolution upon thermal maturation, and the subsequent effect on the source of dominant flow paths and the permeability magnitude of organic-rich shales. However, the only known investigation of the effect of thermal maturity on the permeability of organic-rich shale (Ghanizadeh et al., 2013) exclusively uses naturally matured samples, which, as previously identified (see Chapter 4), are extremely susceptible to the effects of inter-sample heterogeneity.

In this chapter, I combine high-resolution imaging, experimental measurements of shale permeability, and numerically simulated permeability values to investigate the evolution of Barnett Shale and Green River samples (as introduced in Chapters 3-5) upon pyrolysis-induced thermal maturation. By combining experimental and numerical datasets I am able to compare the bulk permeability of the plug at a scale that may exhibit microcracking as well as the intact matrix permeability at the scale of a few cubic microns. To provide deeper comparison, I utilize an additional set of pyrolysis-matured Barnett Shale fragments (pyrolyzed at Kiel University, Germany) to supplement our numerical permeability dataset. Additionally, I use sets of numerically simulated permeability values for the naturally matured ENI Phase 1 and well-derived Barnett Shale samples (discussed in Chapters 3 and 4) for comparison of the effect of burial-induced and pyrolysis-induced thermal maturation on numerical estimates of permeability. In combining numerous techniques and samples, I am able to deeply investigate the effect of increasing thermal maturity on the scale and source of flow paths and the permeability magnitude of organic-rich shales.

6.2 Experimental Methodology

6.2.1 Subsampling for Permeability Quantification

As highlighted in Chapter 3, due to the sample size requirements for different experimental techniques and the destructive nature of focused ion beam scanning electron microscopy (FIB-SEM), it is necessary to subsample the core plugs for different experimental methods. The subsamples used in this chapter are schematically illustrated in Figure 6.1. Due to the destructive nature of FIB-SEM, there are three, 0.2 cm thick coins prepared so that each coin may be pyrolyzed to a desired level of thermal maturity and imaged without impacting the utility of other samples. The FIB-SEM coins are cored parallel to bedding in order to provide multiple bedding layers from which to choose the image location. Additionally, there are two, 0.7 cm thick, plugs for experimental permeability measurements – one cored parallel to bedding and the other perpendicular to bedding. The use of the remaining material from the original core has previously

been covered in Chapters 3-5, and, as in those chapters, we assume that the microstructural, mineralogical, and geochemical properties are homogenous, within some tolerance, across the subsamples.

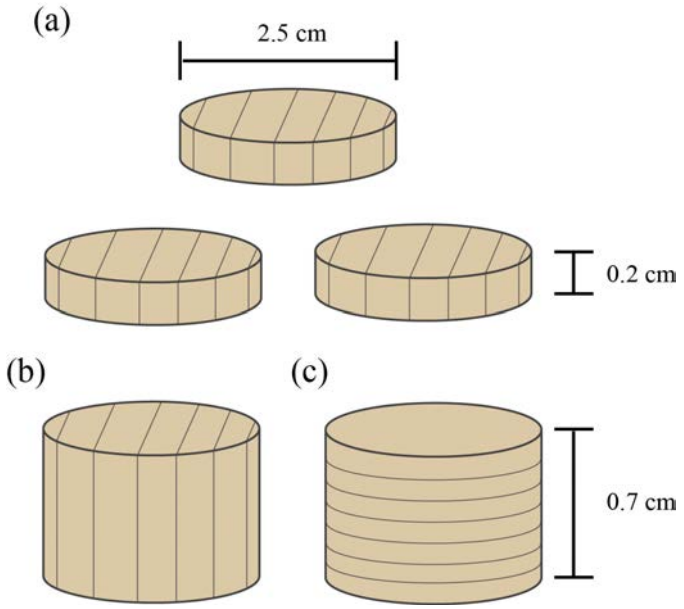

Figure 6.1: A schematic representation of the subsamples used in this chapter. (a) Three, 0.2 cm thick, horizontally cored coins for FIB-SEM imaging at each level of induced thermal maturity, (b) a horizontally cored plug (0.7 cm thick) for experimental permeability measurements, and (c) a vertically cored plug (0.7 cm thick) for experimental permeability measurements.

6.2.2 Permeability Experiments

6.2.2.1 Pulse-Decay Permeametry

Samples with a permeability less than 500 microDarcies (μD) are studied in a CoreTest Systems Inc. NDP-605 NanoDarcy Permeameter. The NDP-605 uses the pulse-decay method of Jones (1997) to avoid the extreme equilibration times required for steady-state methods. A schematic of the NDP-605 is presented in Figure 6.2. The coreholder consists of a rubber sleeve to prevent the intrusion of the confining fluid (water), sealed over two O-rings on the steel pistons that hold the sample in place. The permeameter consists of two reservoirs (termed upstream and downstream), which are saturated along with the sample at a user-defined pore pressure. A pressure pulse is then built up in the downstream reservoir, establishing a pressure gradient across the sample. The decay across the sample over time of this pressure pulse is then related to the permeability of the sample as detailed in Jones (1997).

Before conducting permeability experiments, the samples are pre-stressed at 34.5 MPa (5,000 psi; 125% of the maximum experimental effective pressure) for 24 hours to remove any inelastic deformation. All experiments are temperature controlled at 27 °C with helium as the probe gas to remove thermal effects and the effect of adsorption and/or sample swelling from measured

permeability values (Cui et al., 2009). Each experiment is conducted with the recommended pressure pulse of 0.05 MPa (∼6.5 psi) and the experimental error is less than 5 nanoDarcies (nD).

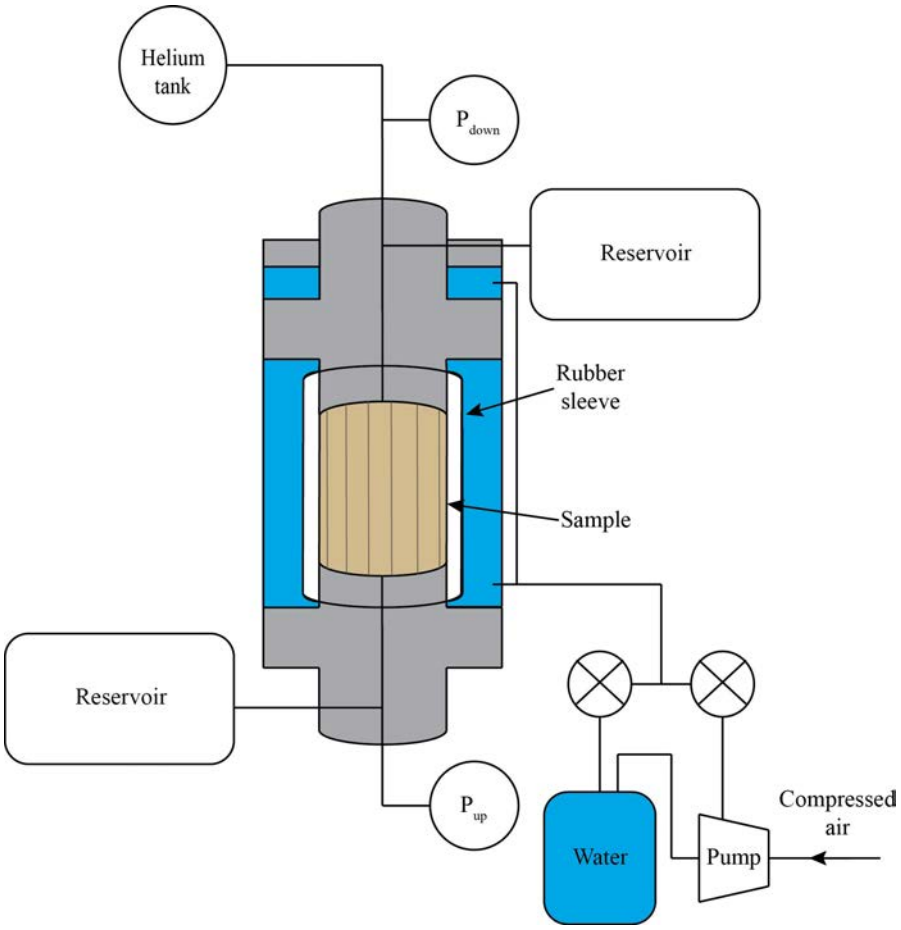

Figure 6.2: A schematic representation of the pulse-decay permeameter.

After previous studies (Kwon et al., 2001; Vermylen, 2011; Heller et al., 2014), permeability experiments are performed at a range of pore and confining pressures to better identify the relative effects of effective pressure, confining pressure, and pore pressure on permeability. The pressure cycle experienced by each sample is illustrated in Figure 6.3. At each pore pressure, permeability is measured as confining pressure is incrementally increased. The pore pressure is then increased and confining pressure iteratively increased such that the effective pressures are consistent with previous measurements. Note that the samples are left to settle for four hours after each change in pressure before the permeability is measured. After permeability measurements are completed, the effective porosity is re-measured in order to quantify the pore volume lost due to stressing the sample.

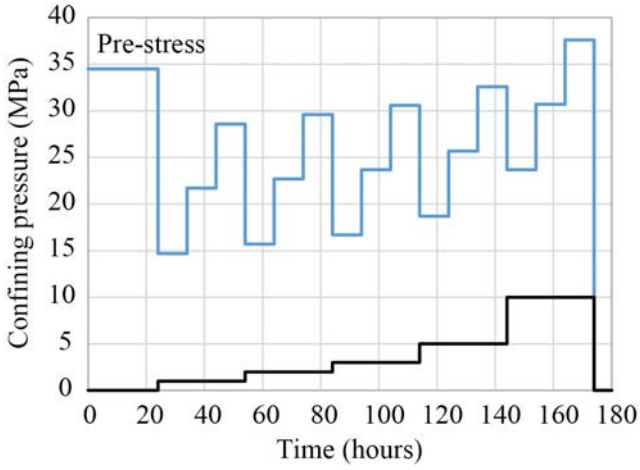

Figure 6.3: A schematic representation of confining (blue) and pore pressure (black) steps applied during pulse-decay permeability experiments.

6.2.2.2 Pressure Drawdown Permeametry

Samples that were too permeable to be measured in the NDP-605, e.g., permeability greater than 500 μD, are studied in a CoreTest Systems Inc. AP-608 Automated Permeameter. The AP-608 uses the pressure drawdown method of Jones (1972) to account for the large equilibration times required for steady-state methods in these samples. A schematic of the AP-608 is documented in Figure 6.4. The AP-608 is schematically very similar to the NDP-605; for instance, the coreholder and pressure vessel are identical. The principal difference between the pulse-decay and pressure drawdown systems is that, rather than equilibrating a pressure pulse between two reservoirs, a single reservoir is pressured, and the pressure in that reservoir decays across the sample to an open atmosphere at the downstream end. The decay across the sample, as measured at the upstream reservoir, is then related to the permeability of the sample as detailed in Jones (1972).

As a result of technical issues with pre-stressing samples in the AP-608, in order to account for any inelastic deformation, each sample is pre-stressed at 125% of the maximum experimental effective pressure for 6-12 hours rather than a full day. The permeability is then measured multiple times to ensure consistent values are obtained. Again helium is used as the probe gas to remove the effect of adsorption and/or sample swelling on measured permeability values. For each experiment the upstream reservoir is pressured to 1.4 MPa (200 psi).

Unlike the NDP-605, there is no user control of pore pressure in the AP-608, rather the pore pressure is constant at 1.4 MPa. Subsequently, the permeability is measured for each sample at a pore pressure of 1.4 MPa as the confining pressure is ramped from 5.2 MPa (750 psi) to 41.6 MPa (6,000 psi) in steps of 5.2 MPa (Figure 6.5). Again, upon changing the confining pressure, the sample is left to settle for four hours before the permeability is measured. Additionally, after the permeability experiment is completed, the effective porosity is re-measured in order to quantify the pore volume lost during pressure cycling.

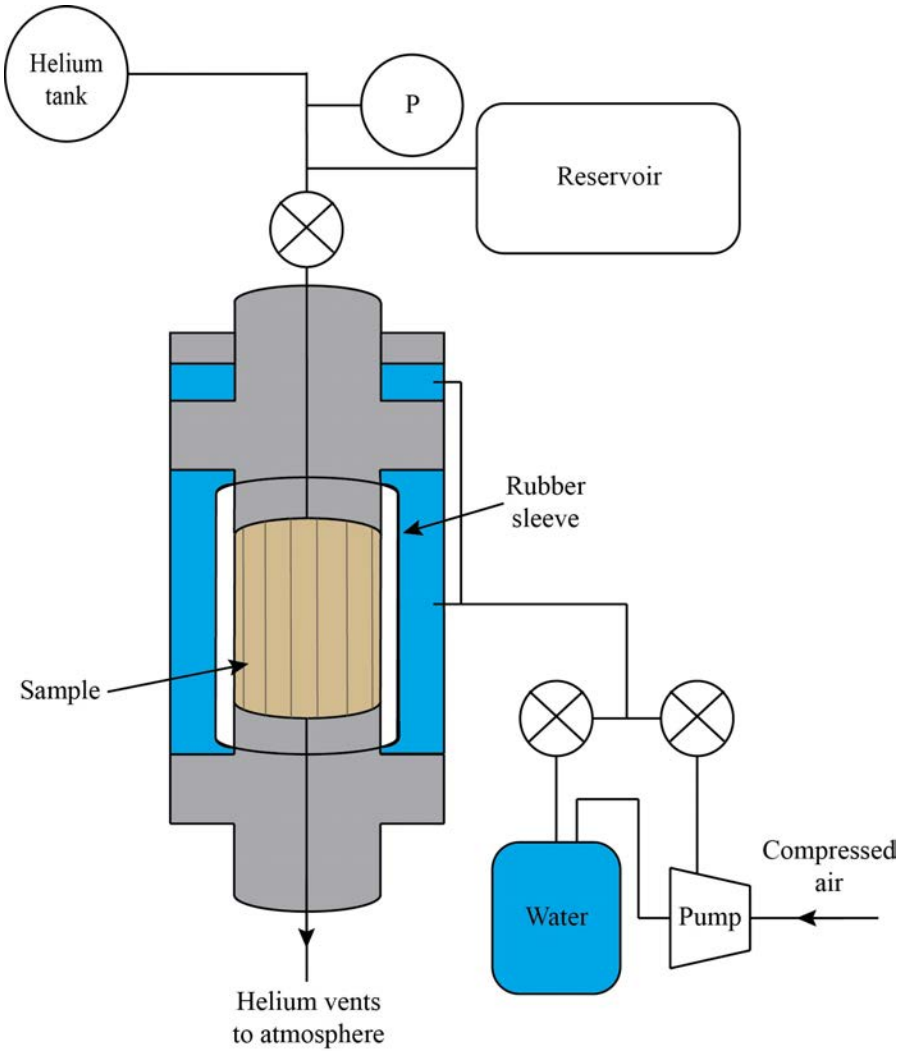

Figure 6.4: A schematic representation of the pressure drawdown permeameter.

6.2.3 Digital Permeability Quantification from High-Resolution Images

The digital pore geometries used for permeability simulations are derived from FIB-SEM volumes collected from small volumes of intact sample matrix. All FIB-SEM volumes are imaged at Ingrain and provided as raw image files. The raw image files are in backscattered electron mode, with gray-scale values proportional to the atomic number of the material at each location. The volumes are then segmented, based on this gray-scale value, to separate the pore space from the solid matter (both minerals and organic content). The digital geometries are composed of cubic voxels 15 nm in length. An example FIB-SEM volume pre- and post-segmentation is shown in Figure 6.6.

Continuum, Darcy flow is simulated, and the numerical continuum permeability is quantified, using an in-house $D3Q19$ Lattice Boltzmann (LBM) simulator (Keehm, 2003). The Lattice

Boltzmann method simulates viscous fluid flow by the streaming and collision of a finite number of pseudo-particles in the pore space of the digital pore geometry. The solution of the discrete Boltzmann equation, coupled with a collision model (e.g., Bhatnagar et al., 1954), in this manner, approximates the full Navier-Stokes equations (Succi, 2001). Using the LBM simulator, the segmented volumes are tested for percolation. The geometries which do not support flow across the whole volume are then processed following one of three methodologies: either (a) two-dimensional slices are removed from the inlet face, (b) two-dimensional slices are removed from the outlet face, or (c) two-dimensional slices are removed iteratively from the inlet and outlet faces. Post-processing, the continuum permeability of all samples is quantified using the LBM simulator.

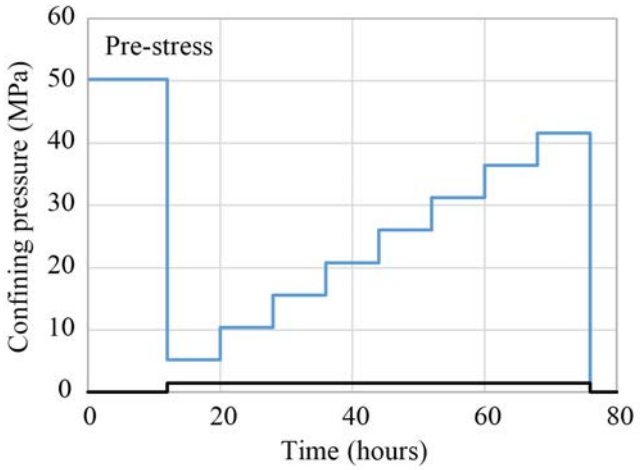

Figure 6.5: A schematic representation of confining (blue) and pore pressure (black) steps applied during pressure drawdown permeability experiments.

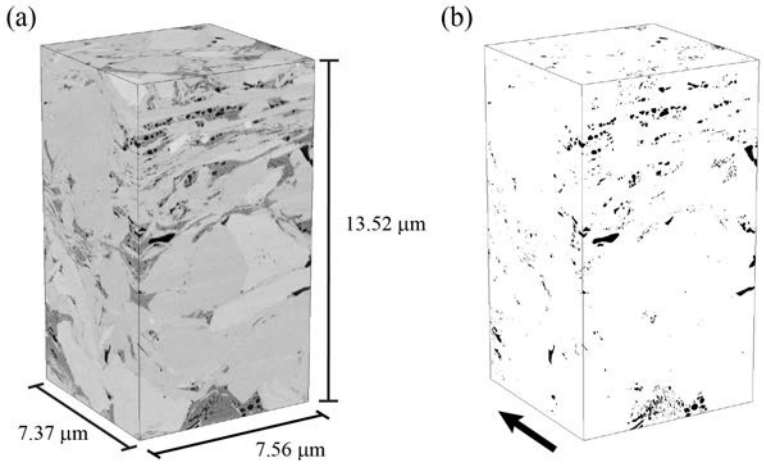

Figure 6.6: An example FIB-SEM volume pre- (a) and post-segmentation (b) of the pore space. In (a) the dark grey regions are organic matter, the black regions (that coincide with black regions in the segmented image) are pores, while lighter regions are mineral matrix. The imaged volume is 7.56 $\times$ 7.37 $\times$ 13.52 μm. The large black arrow in (b) indicates the direction of the pressure gradient in flow simulations.

6.2.4 Experimental Workflow for Permeability Subsamples

The experimental protocol for studying the pyrolyzed experimental samples in this chapter is effectively identical to the protocol used in Chapter 5. The permeability characterization workflow for the experimental samples is documented in Figure 6.7. The effective porosity methodology and BSE-SEM imaging parameters are as reported in Chapter 3.

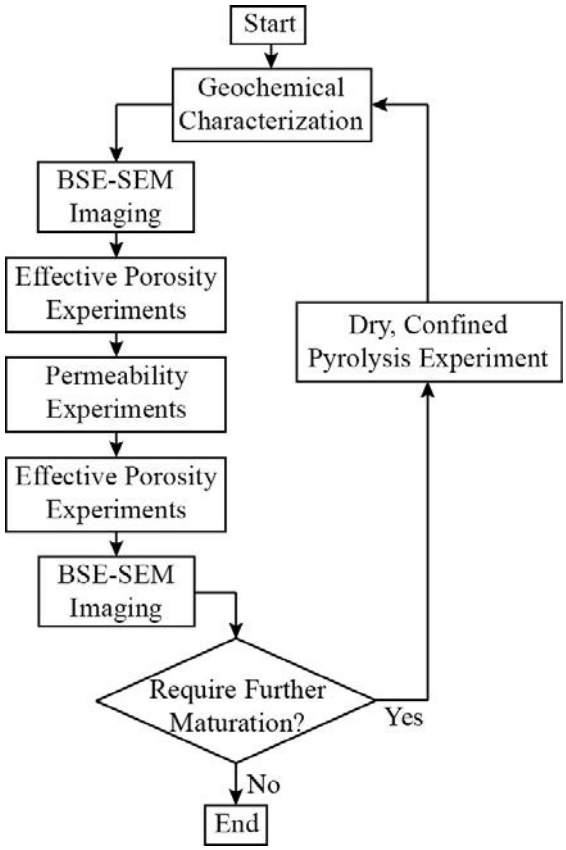

Figure 6.7: A schematic flowchart of the ordering of experimental methods and pyrolysis for the permeability subsamples. This figure is adapted from Figure 3.13.

The FIB-SEM coins are treated as in Figure 6.8, where each coin is pyrolyzed to the desired level of thermal maturity (with the exception of the baseline, thermally immature subsample, Coin #1) in the same steps as the experimental permeability subsamples before being sent to Ingrain for imaging. The samples received from the University of Kiel were previously pyrolyzed at their facility (as discussed in the next section), and, subsequently, are sent to Ingrain for FIB-SEM imaging without further alteration – as are the naturally matured ENI Phase 1 subsamples.

As in Chapter 5, thermal maturation at Stanford University, is induced in the laboratory in the purpose-built, high pressure-high temperature reactor (Clark and Vanorio, 2015). In order to facilitate the comparison of results from the elastic and transport studies, the subsamples are pyrolyzed in an identical manner between Chapters 5 and 6. Thus, the oil window for the Barnett Shale samples was reached by pyrolysis at 360 °C at 22-24 MPa for 72 hours, while the

oil window for the Green River samples was reached at 380 °C at 22-24 MPa for 72 hours. For both samples, the gas window was reached by pyrolysis at 425 °C at 22-24 MPa for 72 hours. The geochemical validation of the pyrolysis procedure is documented in the Discussion section of this chapter.

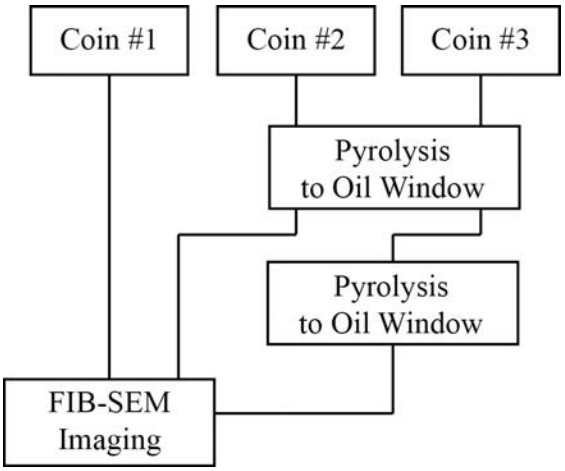

Figure 6.8: A schematic flowchart of the ordering of pyrolysis and FIB-SEM imaging for each subsampled coin.

6.3 Permeability Subsample Characterization

The detailed sample characterization of Chapter 3 is abridged here for convenience. To this effect, the mineralogical, physical, and geochemical properties of the samples are reported in Tables 6.1 and 6.2.

As detailed in Chapter 5, the outcrop Green River and Barnett samples that are studied experimentally pre- and post-pyrolysis constitute a pair of end member samples samples. The Green River sample is a low effective porosity, randomly oriented, argillaceous dolomicrite (Tables 6.1 and 6.2). The pre-pyrolysis Green River sample is thermally immature and extremely TOC (total organic carbon) and hydrocarbon-rich – ∼9 wt. % TOC and 76 mg of hydrocarbons per gram of dry rock, respectively (Table 6.1). The outcrop Barnett Shale sample is a high effective porosity, more classic siliciclastic laminar shale (Tables 6.1 and 6.2). Pre-pyrolysis the sample is thermally immature and TOC-rich (∼12 wt. %) but contains 23% fewer hydrocarbons per gram of dry rock than the Green River sample (Table 6.1).

Due to the previously noted (Chapter 3) extreme through-going fracturing of many of the naturally matured samples, the experimental permeability values of the Barnett well and ENI Phase 1 samples are not discussed here. Simply, the extensive fracturing prevents any meaningful quantification of the maturity-dependent matrix permeability. However, intact subvolumes of organic-rich matrix can be studied numerically despite the extensive fracturing. The Barnett well samples are thermally post-mature and contain very little residual or producible hydrocarbons (∼1 mg per gram of dry rock; Table 6.1). Subsequently, digital rock volumes acquired from

the gas window Barnett well samples provide an important direct point of comparison between natural and pyrolysis-induced maturation for initially organic-rich, micron-scale subvolumes from the same formation. Additionally, the ENI Phase 1 samples span a full range of in situ thermal maturities from immature to the gas window (Table 6.1). As such, the ENI Phase 1 samples are a perfect complement to the numerical permeability-thermal maturity trends established for the pyrolyzed Barnett and Green River samples. Note that sample ENI3 (heretofore unreported due to extreme mineralogical heterogeneity between the vertically and horizontally cored plugs) is included for numerical permeability analysis as the issue of heterogeneity between plugs is irrelevant for permeability simulations of only the horizontal plug.

Table 6.1: A summary of the mineralogy, sample average crystallographic preferred orientation (CPO), thermal maturity, TOC, and hydrocarbon potential (HP) for each sample in this study. The minerals calcite and dolomite are abbreviated as Cal and Dol, respectively. The CPO and hydrocarbon potential are measured in multiples of a random distribution (see Chapter 3 for discussion) and mg of hydrocarbons per gram of dry rock, respectively.

Sample	Mineralogy (wt. %)			CPO (m.r.d.)	Thermal Maturity	TOC (wt. %)	HP (mg/g)
	Clay	Quartz	Cal+ Dol				
BO	40	49	0	3.98	Immature	11.67	58.30
BW1	28	38	22	2.69	Gas	2.72	1.10
Green River	4	12	61	1.07	Immature	9.14	76.03
ENI1	71	19	4	7.45	Immature	7.49	44.76
ENI2	60	17	17	5.33	Early Oil	7.14	47.56
ENI3	6	2	90	1.00	Early Oil	5.72	23.71
ENI4	65	21	4	4.46	Early Oil	4.34	17.54
ENI5	55	19	21	3.35	Gas	4.13	1.49
ENI6	48	22	22	4.37	Gas	4.78	0.77

Table 6.2: The effective porosity and grain density of each subsample used in permeability experiments. All measurements are for the pre-pyrolysis, thermally immature samples.

Sample	Orientation	Effective Porosity (%)	Grain Density (g/cc)
BO	Vertical	12.58±1.03	2.22±0.02
	Horizontal	13.74±0.99	2.31±0.03
Green River	Vertical	1.60±0.67	2.30±0.01
	Horizontal	2.12±0.48	2.28±0.01

In addition to the samples prepared at Stanford, we have acquired digital rock volumes of formerly thermally immature, outcrop Barnett Shale fragments that were pyrolyzed in the lab of Professor L. Schwark at the University of Kiel, Germany. The pyrolysis technique employed at the University of Kiel is more comparable to that employed in Chapter 2 than to the current technique in our lab – that is, pyrolysis proceeds under uniaxial confining pressure with no containment of produced fluids during pyrolysis. All of the geochemical data for these samples is reported in

Table 6.3, while no additional experiments, e.g., porosimetry or experimental permeability, can be conducted on these irregularly shaped fragments. Note the considerably lower temperatures required to induce thermal maturation for these samples (Table 6.3). This difference in pyrolysis temperature, coupled with the temperatures employed in Chapter 2, indicates that thermal maturation requires higher temperatures for a confined, compacted pore space. Subsequently, this secondary pyrolyzed Barnett Shale dataset provides both a complement to the breadth of numerical data available, as well as a direct comparison of the effect of the nature of applied confining pressure during pyrolysis on organic microstructures.

Table 6.3: A geochemical summary of the post-pyrolysis Barnett Shale fragments received from the University of Kiel. Reported are: the window of thermal maturity, the temperature of the pyrolysis experiment, TOC, the RockEval thermal maturity indicator (T_{MAX}), the remaining thermally producible hydrocarbons (S_2), and the hydrogen index (HI). The window of thermal maturity is identified by T_{MAX} as in Peters and Cassa (1994).

Sample	Thermal Maturity	Pyrolysis Temperature (°C)	TOC (wt. %)	T_{MAX} (°C)	S_2 (mg/g)	HI (mg/g)
Exp 32	Immature	300	10.46	428	63.50	607
Exp 33	Early Oil	330	6.11	438	12.87	211
Exp 34	Peak Oil	345	6.00	445	8.52	142
Exp 35	Late Oil	360	5.29	461	3.17	60

6.4 Experimental Results

6.4.1 Pyrolysis-Induced Physical Evolution

6.4.1.1 Mass, Density, and Porosity Evolution

Time-lapse photographs of the horizontally cored Barnett and Green River samples are documented in Figures 6.9 and 6.10. While retrieving the horizontally cored Barnett sample, the sample was split into two intact fragments – this mechanically induced fracture is clearly visible as is a distinct lack of hydrocarbon staining in the oil window (Figure 6.9.b). Contrastingly, the gas window sample shows clear staining and the precipitation of a cupric compound (light gray material) on the surface of the sample (Figure 6.9.c); note, the quantity of the cupric compound is insufficient to affect the grain density measurements. The Green River sample which was pyrolyzed directly to the gas window exhibits clear hydrocarbon staining and some minor damage to the radial surface of the plug (Figure 6.10). However, the rubber jacket in the permeameter will conform to such low amplitude surface roughness and prevent the roughness from affecting matrix permeability measurements.

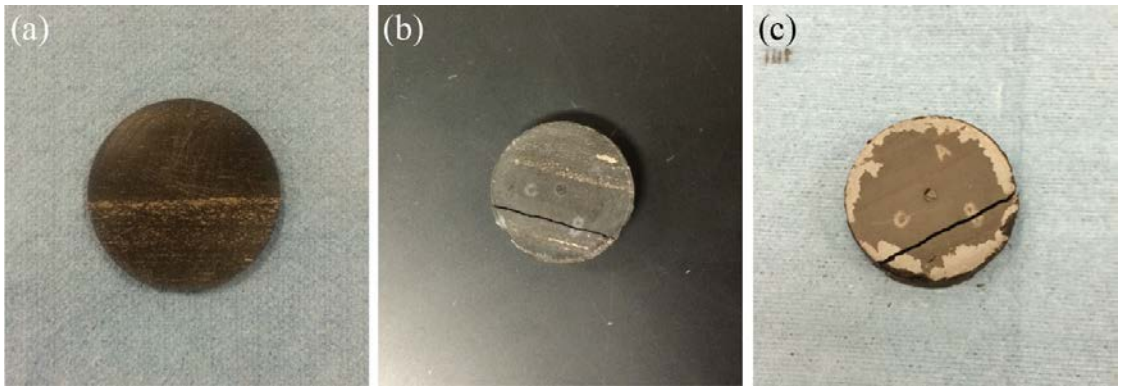

Figure 6.9: Photographs of the horizontally cored Barnett sample in the immature (a), oil (b), and gas (c) windows.

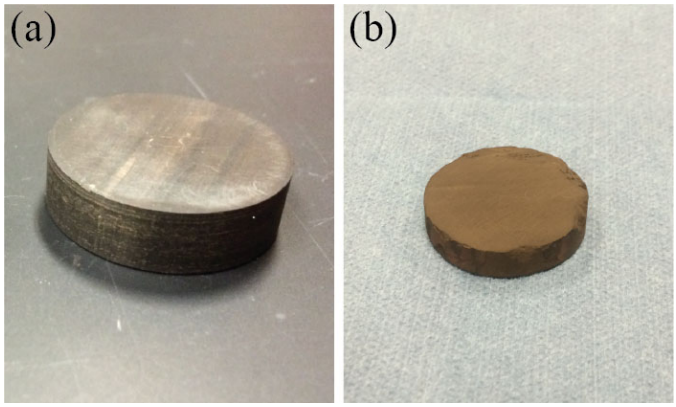

Figure 6.10: Photographs of the horizontally cored Green River sample in the immature (a) and gas (b) windows.

Table 6.4: The physical properties (mass, volume, effective porosity, and grain density) at each stage of thermal maturity for the vertically and horizontally cored Barnett Shale (BOV and BOH, respectively) and micritic Green River samples (GRV and GRH, respectively).

Sample	Thermal Maturity	Mass (g)	Bulk Volume (cc)	Grain Volume (cc)	Effective Porosity (%)	Grain Density (g/cc)
BOV	Immature	7.45	3.84±0.02	3.36±0.03	12.58±1.03	2.22±0.02
	Gas	6.16	3.22±0.17	2.44±0.02	24.33±5.49	2.53±0.02
BOH	Immature	7.18	3.61±0.01	3.11±0.03	13.74±0.99	2.31±0.03
	Oil	6.95	3.42±0.10	3.05±0.02	10.87±3.02	2.28±0.02
	Gas	6.83	3.33±0.18	2.72±0.03	18.28±5.56	2.51±0.03
GRV	Immature	16.79	7.42±0.02	7.30±0.04	1.60±0.67	2.30±0.01
	Gas	15.31	7.10±0.03	6.02±0.02	15.19±0.49	2.54±0.01
GRH	Immature	8.77	3.93±0.01	3.84±0.01	2.12±0.48	2.28±0.01
	Gas	6.19	3.09±0.11	2.40±0.03	22.27±3.76	2.58±0.03

As in Chapter 5, the physical properties (mass, volume, effective porosity, and density) of each plug, pre- and post-pyrolysis, are documented in Table 6.4. And, as in Chapter 5, the evolution of the Barnett sample after being pyrolyzed at 360 °C for 72 hours is consistent with clay dewatering and mechanical compaction rather than hydrocarbon conversion and expulsion – that the magnitude of this compaction is lower than in Chapter 5 is attributable to the different sample orientation and their respective sensitivity within the copper jacket. The vertically cored sample is largely free to deform axially (the most compliant principal direction) within the HTHP coreholder; however, the radial compaction (one component of which is the most compliant principal direction) of the horizontal sample is limited by the deformation of the copper jacket around the less compliant alumina spacers (Figure 6.11).

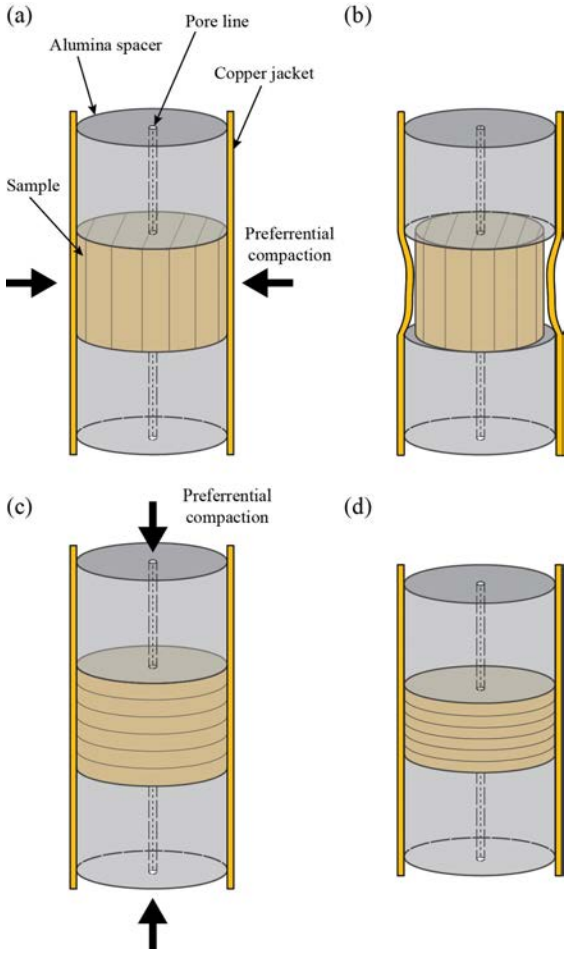

Figure 6.11: A schematic representation of compaction within the HTHP coreholder for horizontally (a, b) and vertically (c, d) cored samples. (Left column) No applied confining pressure. (Right column) Under applied confining pressure.

Upon pyrolysis to the gas window, both the Barnett and Green River samples exhibit the mass loss, decrease in grain volume, and increase in effective porosity and grain density indicative of the generation and expulsion of hydrocarbons. In each instance, the samples exhibit some additional degree of compaction during pyrolysis to the gas window, ranging from a 2.5% bulk volume loss for BOH to a 21% bulk volume decrease for GRH. For the Barnett samples

this compaction is attributed to the partial compaction of compliant pores and voids created by kerogen conversion, while for the Green River samples the compaction is attributed to the re-stabilization of the granular pack upon the conversion and expulsion of the load-bearing, pore-filling kerogen. Note that in neither case does the decrease in bulk volume correspond with a decrease in effective porosity. It is important to note that the post-pyrolysis values of both porosity (Table 6.4) and permeability (Figure 6.17) are significantly greater than typical values reported for in situ, naturally matured shale samples. This issue of transport property magnitude is addressed in Appendix A.

6.4.1.2 Microstructural Alteration

In Figure 6.12 the coarser-scale SEM documentation of the pyrolysis-induced microstructural alteration from the thermally immature to gas windows, as documented in Figures 5.6 and 5.7, is summarized for completeness. In both the Barnett and Green River samples the loss of kerogen between the immature and gas windows is clear. The loss of kerogen from the samples leaves some residual organic matter, but, predominantly, results in the revealing of the underlying mineral matrix and porosity. For the micritic Green River samples (particularly Figure 6.12.e-f), the compaction of the mineral matrix around the previously existing organic bodies is evident – this is evidence of the previously hypothesized stabilization of the granular pack accounting for the measured decrease in bulk volume. Finally, it is important to note that compared to the time-lapse imaging of the Kimmeridge Shale post-pyrolysis (e.g., Figure 2.11) there is very little evidence of microcracking in and/or around the organic bodies in either the Barnett or Green River samples. This is consistent with the hypothesis that the application of confining pressure during pyrolysis minimizes the development and preservation of microcracks and has important implications for the later interpretation of the permeability evolution.

High-resolution SEM images of the Barnett Shale, which have been brightness and contrast adjusted to emphasize porosity, are used to document both the organic-rich matrix and the nature of matrix porosity as a function of thermal maturity (Figure 6.13). It is important to note that these images are not time-lapse as in Figure 6.12, but are collected from the individual FIB-SEM subsamples post-pyrolysis (Figure 6.1). For the thermally immature Barnett Shale (Figure 6.13.a-b), the organic matter is generally imporous, as depicted by the mid-gray regions. Rather, the porosity is concentrated in crack-like features in and around mineral grains (light gray to white regions) and as intergranular porosity in mineral-rich domains. After pyrolysis to the oil window both with and without applied confining pressure (Figure 6.13.c and Figure 6.13.d, respectively), there is a marked increase in the porosity of the organic matter. Primarily, this porosity occurs topologically as a few large, sub-rounded pores within, or nearly completely replacing, organic bodies – commonly referred to as pendular porosity (Walls and Sinclair, 2011). Considerable organic porosity is also visible in the gas window samples (Figure 6.13.e-f). In contrast to the oil window images, the gas window subsamples exhibit a slight increase in the number of pores per organic body, particularly visible in Figure 6.13.e. In other words, individual organic bodies tend to host a greater number of narrower pores. This texture is more representative of the spongy porosity of Walls and Sinclair (2011). The topology of these organic pores, as compared to naturally occurring organic pores, is further discussed in Appendix A.

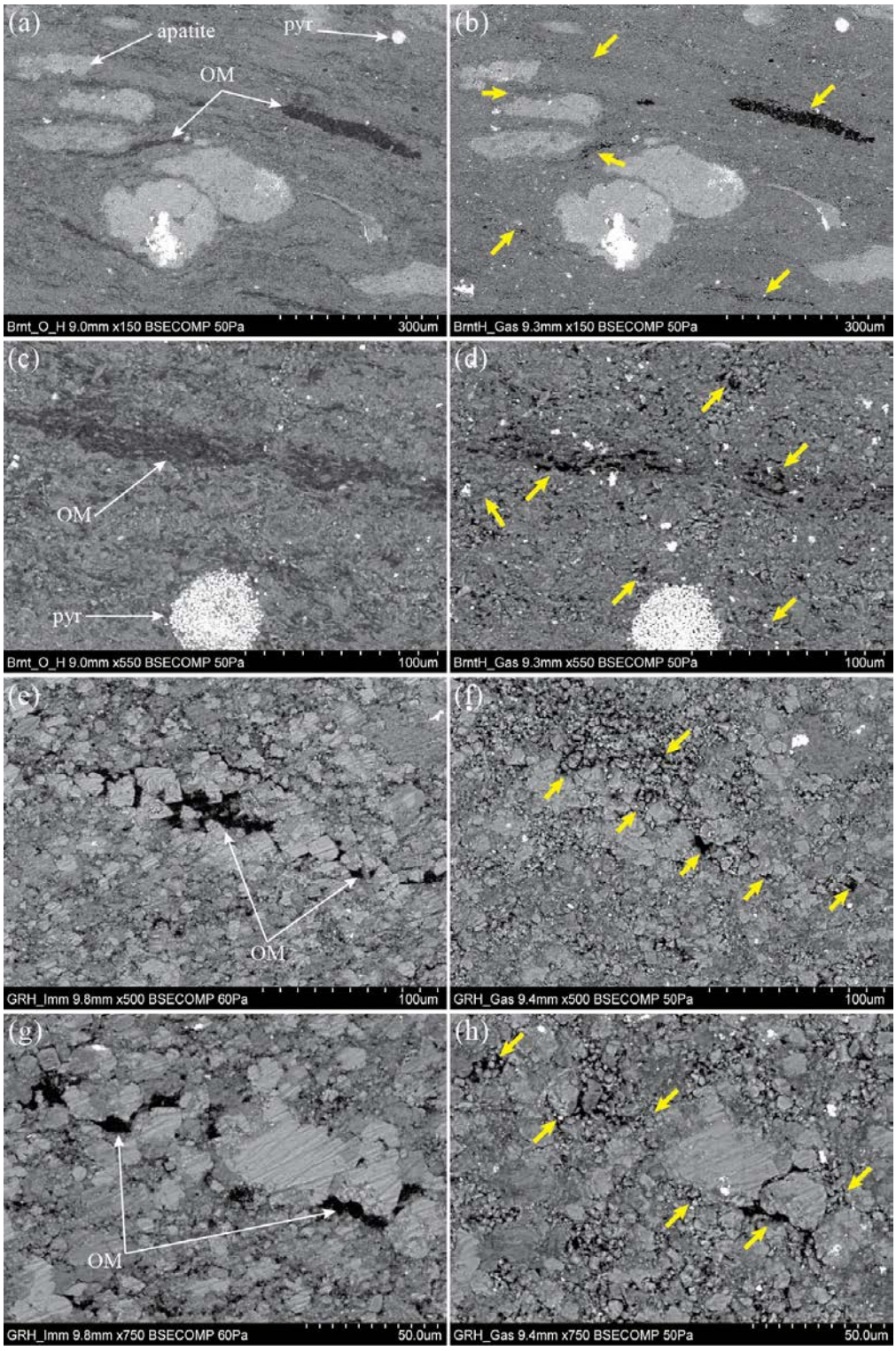

Figure 6.12: Time-lapse SEM images of the evolving microstructure of the Barnett (a-d) and Green River (e-h) samples between the immature (left column) and gas (right column) windows – as documented in Figures 5.6 and 5.7. Identified features include organic matter (OM), pyrite (pyr), and apatite. Yellow arrows identify areas of kerogen conversion and expulsion in the gas window images. The pixel size in the time-lapse images are identical.

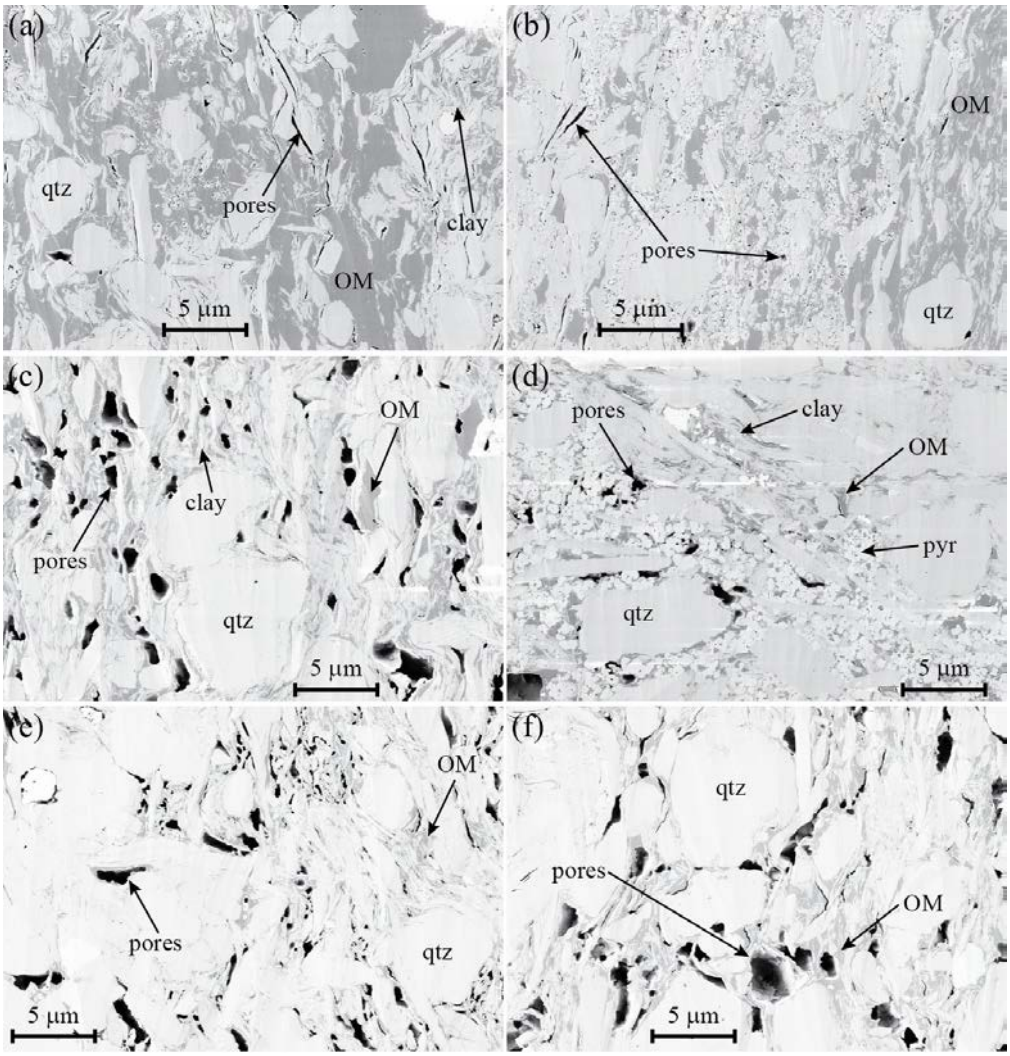

Figure 6.13: High-resolution SEM images of the Barnett Shale sample in the baseline, thermally immature state (a-b), oil window (c-d), and gas window (e-f). Note that these images are not time-lapse. All images except (d) are taken from Stanford subsamples, while image (d) is from the Exp 34 fragment pyrolyzed at Kiel University. Identified features include organic matter (OM), porosity, quartz grains (qtz), pyrite (pyr), and clay platelets.

6.4.1.3 Geochemical Evolution

The geochemical properties of the Barnett and Green River samples pre- and post-pyrolysis are detailed in Table 6.5. Note that the Barnett oil window (360 °C) characterization is from the same subsample as in Chapter 5; thus, it is maintained that minimal thermal maturation has occurred in the 'oil window' Barnett sample. Instead, the exposure to elevated temperature and pressure results in the dewatering of the clay matrix and the compaction of the fragile, high porosity outcrop sample. A complete discussion of the issues encountered during the pyrolysis experiments can be found in Appendix A of Chapter 5.

Pyrolysis at 425 °C for 72 hours results in, as identified by T_{MAX} values, post-mature ($T_{MAX} > 470$ °C; Peters and Cassa, 1994) Barnett and horizontally cored Green River samples (Table 6.5). However, the vertically cored Green River sample is incorrectly identified by T_{MAX} as thermally immature ($T_{MAX} < 435$ °C; Peters and Cassa, 1994), while the remaining thermally producible hydrocarbons has decreased by 91% (Table 6.5). As in Chapter 5, the issue of erroneous T_{MAX} values is attributed to a combination of technical issues reaching the programmed pyrolysis control temperature in the HTHP reactor and a microstructure that promotes fluid retention that, in turn, retards the decomposition of heavier hydrocarbons to gas (Price et al., 1981; Palacas, 1984; Jones, 1984).

Table 6.5: Geochemical characterization of the pyrolyzed Barnett and Green River samples. Each pyrolysis experiment is represented by the programmed control temperature of the experiment (T_{CTRL}). The samples are characterized by total organic carbon (TOC), free hydrocarbons (S_1), remaining thermally producible hydrocarbons (S_2), the RockEval thermal maturity indicator (T_{MAX}), the hydrogen index (HI), and the oxygen index (OI). The baseline, thermally immature values are included for convenient comparison. The gas window samples are characterized by two different subsamples (425V & 425H) – one cored vertically and the other horizontally.

Sample	T_{CTRL} (°C)	TOC (wt. %)	S_1 (mg/g)	S_2 (mg/g)	T_{MAX} (°C)	HI (mg/g)	OI (mg/g)
Barnett	-	11.67	2.32	55.98	418	480	9
	360	9.47	8.91	22.65	438	239	7
	425V	9.40	1.69	4.79	500	51	8
	425H	8.08	3.25	6.14	486	76	10
Green River	-	9.14	4.8	71.23	419	780	10
	425V	3.44	15.57	6.44	423	187	29
	425H	3.98	4.06	2.92	491	73	27

Important to the interpretation of the evolution of the transport properties of the Green River post-pyrolysis is the observation that, again, the vertically cored subsample retains 3.8 times more free hydrocarbons than the horizontally cored subsample (Table 6.5). Note that the issue of differential retention does not affect the Barnett samples, reinforcing the hypothesis that the cause of the differential retention is a function of microstructure rather than being a systematic issue of sample orientation.

As documented for acoustic velocities in Chapter 5, the preferential retention of hydrocarbons can result in significant heterogeneity in the physical properties of a pair of plugs. In Figure 6.14, the effective porosity and grain density of the Green River plugs are crossplotted pre- and post-pyrolysis. The horizontal plug is clearly more porous and denser than the vertical plug in the gas window, indicative of the lower retained hydrocarbon content. As in Chapter 5, the effect of hydrocarbon retention on porosity and grain density can be modeled using Equations 6.1-6.3. In this methodology, the mass and volume of organic material (quantified by geochemistry and an assumed hydrocarbon density) are removed from the bulk measurement leaving behind the estimated mineral response. The results of this process are documented in Table 6.6 and Figure 6.14 for an assumed hydrocarbon density of 0.85 g/cc.

$$V_{oil} = \rho_{org}\left(m_{sample} \times \frac{S_1 + S_2}{1000}\right) \tag{6.1}$$

$$\rho'_G = \frac{m_{sample} - m_{oil}}{V'_G} = \frac{m_{sample} - m_{oil}}{V_G - V_{oil}} \tag{6.2}$$

$$\phi' = \frac{V_B - V'_G}{V_B} \times 100 \tag{6.3}$$

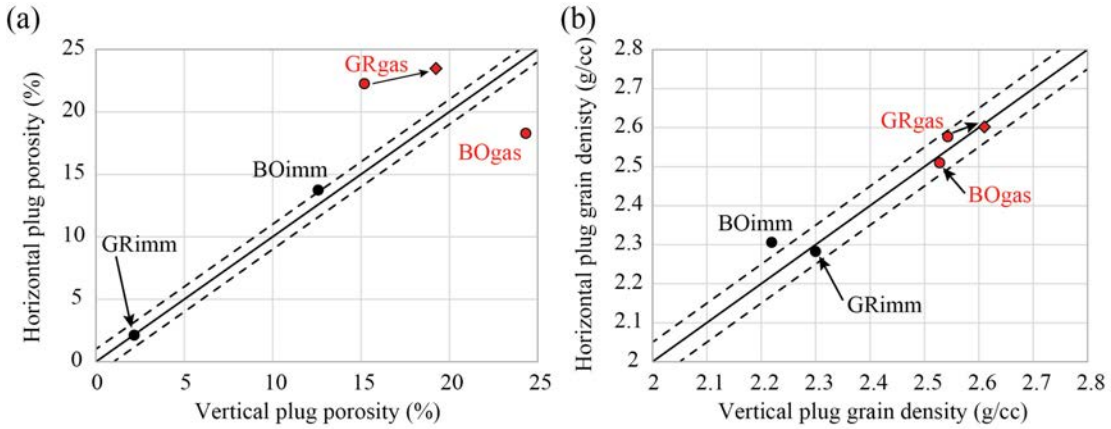

Figure 6.14: A comparison of the effective porosity (a) and grain density (b) of the horizontal plugs to those of the vertical plugs. The solid black lines indicate equal values, e.g., a pair of homogeneous plugs, while the dashed black lines indicate an error of ±1 p.u. and ±0.050 g/cc, respectively. The circular data points are the direct measurements, while the diamonds are the hydrocarbon-corrected values documented in Table 6.6.

Upon numerically removing the retained organics from the Green River samples, the difference between effective porosity values halves, while the grain densities conform to within the experimental error (0.01 g/cc). While heterogeneity still exists between the samples, accounting for retained hydrocarbons significantly improves the comparison between the samples and shows that the underlying evolution of the plugs may be more uniform than the raw measurements imply.

Table 6.6: The grain volume, effective porosity, and grain density as measured in the gas window before and after being corrected for residual hydrocarbon content (see Equations 6.1-6.3) for vertically and horizontally cored Green River samples.

Sample	Measured			Corrected		
	Grain Volume (cc)	Effective Porosity (%)	Grain Density (g/cc)	Grain Volume (cc)	Effective Porosity (%)	Grain Density (g/cc)
GRV	6.02	15.19	2.54	5.73	19.25	2.61
GRH	2.40	22.27	2.58	2.36	23.52	2.60

6.4.2 Experimental Permeability Results

6.4.2.1 Baseline, Immature Window

The gas permeability as a function of confining and pore pressure is shown for the thermally immature Barnett Shale in Figure 6.15. For the Barnett Shale samples, the decrease of permeability as a function of increasing confining pressure is small both perpendicular and parallel to bedding (Figure 6.15). The confining pressure-sensitivity is less than 1 nD/MPa parallel to bedding and less than 0.2 nD/MPa perpendicular to bedding at a pore pressure of 1 MPa. However, the decrease of permeability as a function of pore pressure at constant effective pressure is much greater: 35 nD/MPa parallel to bedding and 2 nD/MPa perpendicular to bedding at an effective pressure of 13.7 MPa. The permeability decrease with increasing pore pressure results from a decrease in the magnitude of slip flow and other diffusive flow mechanisms as the number of gas molecules per pore increases and the gas behaves increasingly as a continuum fluid.

In addition to being more sensitive to pressure, the permeability magnitude parallel to bedding is significantly greater (on the order of 100s of nanoDarcies) than perpendicular to bedding (<10 nD). The permeability anisotropy, defined as the ratio of the permeability parallel to bedding to the permeability perpendicular to bedding, varies between 35.5 and 42 over the range of experimental pressures. This range of values is consistent with the value of ∼40 reported by Bhandari et al. (2015) for a well-derived Barnett Shale sample.

Note that pulse decay permeability measurements could not be completed perpendicular to bedding at an effective pressure of 27.6 MPa or at pore pressures greater than 3 MPa due to the relative impermeability of the sample. Additionally, the thermally immature Green River samples were impermeable within the sensitivity of the pulse-decay system, i.e., permeability is less than approximately 5 nD.

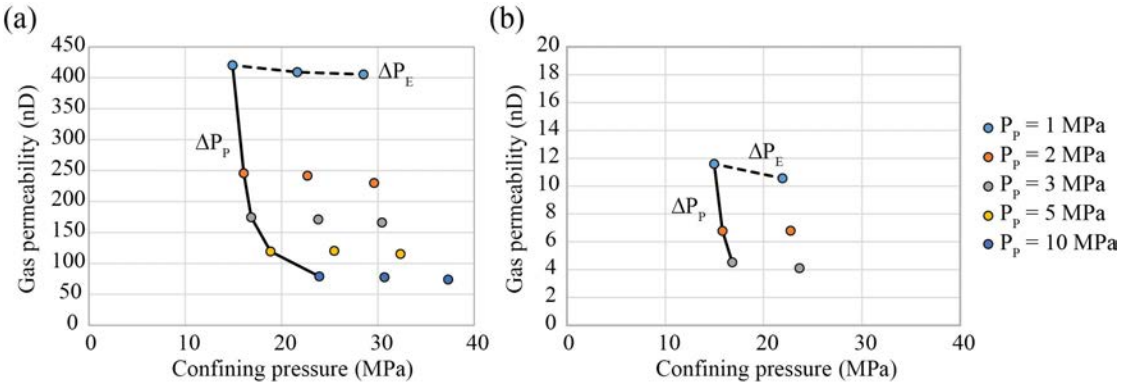

Figure 6.15: The experimental gas permeability, for the immature Barnett Shale samples, parallel (a) and perpendicular to bedding (b) as a function of confining pressure, colored by pore pressure. To aid the interpretation of the plots, an example line of constant pore pressure (dashed line) at 1 MPa and constant effective pressure (solid line) at 13.7 MPa have been added. Note the difference in scale of the y-axis between (a) and (b).

6.4.2.2 Oil Window

Due to the extreme quantities of oil retained by the velocity subsamples of the Green River after pyrolysis to the oil window in Chapter 5 (19.25 mg per gram of dry rock; Table 5.3), the permeability of the Green River samples is not measured in the oil window to prevent oil migration into, and damage to, the pulse-decay permeameter. Furthermore, due to the initial scope of this project, the permeability of the Barnett Shale is only measured parallel to bedding in the oil window.

The effect of the visible fracture parallel to bedding (Figure 6.9.b) on permeability is documented in Figure 6.16. In the oil window, the gas permeability of the sample is an order of magnitude greater than the baseline value. Similarly, the decrease of permeability as a function of confining and pore pressure increases. The sensitivity to confining pressure is 46 nD/MPa at a pore pressure of 1 MPa, up from 1 nD/MPa in the immature window: while the sensitivity to pore pressure at an effective pressure of 13.7 MPa increases to 103 nD/MPa from 35 nD/MPa in the immature window.

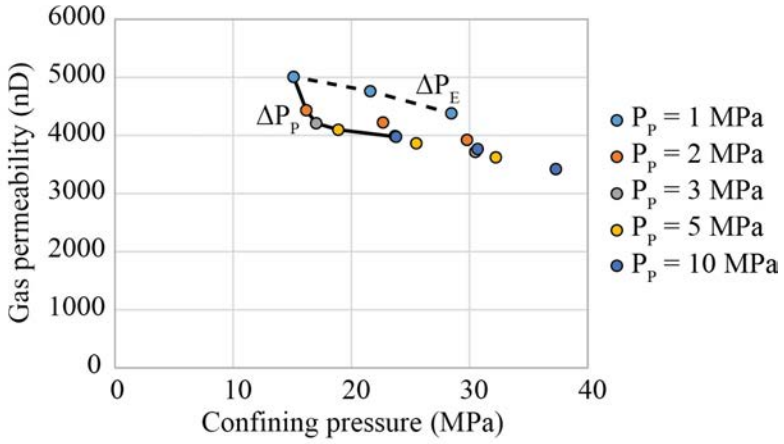

Figure 6.16: The experimental gas permeability, for the oil window Barnett Shale sample, parallel to bedding as a function of confining pressure, colored by pore pressure. To aid the interpretation of the plots, an example line of constant pore pressure (dashed line) at 1 MPa and constant effective pressure (solid line) at 13.7 MPa have been added.

6.4.2.3 Gas Window

After further pyrolysis-induced maturation to the gas window, the horizontally cored Barnett Shale sample exhibited no additional subparallel to bedding fracturing. The permeability parallel to bedding in the gas window is approximately double the oil window value, while the permeability perpendicular to bedding increases by two orders of magnitude over the baseline value (Figure 6.17.a-b). Similarly, the sensitivity to confining pressure at constant pore pressure (1 MPa) increases – from 46 nD/MPa to 73 nD/MPa parallel to bedding and from <0.2 nD/MPa to 12 nD/MPa perpendicular to bedding. Furthermore, the sensitivity to pore pressure at 13.7 MPa effective pressure increases to 1.43 μD/MPa from 103 nD/MPa parallel to

bedding and from 2 nD/MPa to 129 nD/MPa perpendicular to bedding, respectively. Note that due to the high permeability of the horizontally cored gas window sample, a 0.09 MPa pressure pulse could not be sustained at pore pressures greater than 3 MPa – hence, no data was collected at those pressures.

The initially impermeable Green River samples experienced a many order of magnitude increase in permeability upon pyrolysis to the gas window (Figure 6.17.c-d). The gas window permeability values at 41.4 MPa confining pressure are 9.74 milliDarcies (mD) and 23 μD parallel and perpendicular to bedding, respectively. However, this many order of magnitude increase in permeability is not the result of any visible cracking or fracturing of the sample. In addition to the very large permeability magnitude, the gas window Green River samples exhibit large sensitivity to confining pressure – 790 μD/MPa and 490 nD/MPa parallel and perpendicular to bedding, respectively. Due to the inability to change the pore pressure magnitude in the AP-608, there is no quantification of pore pressure-sensitivity for the Green River samples.

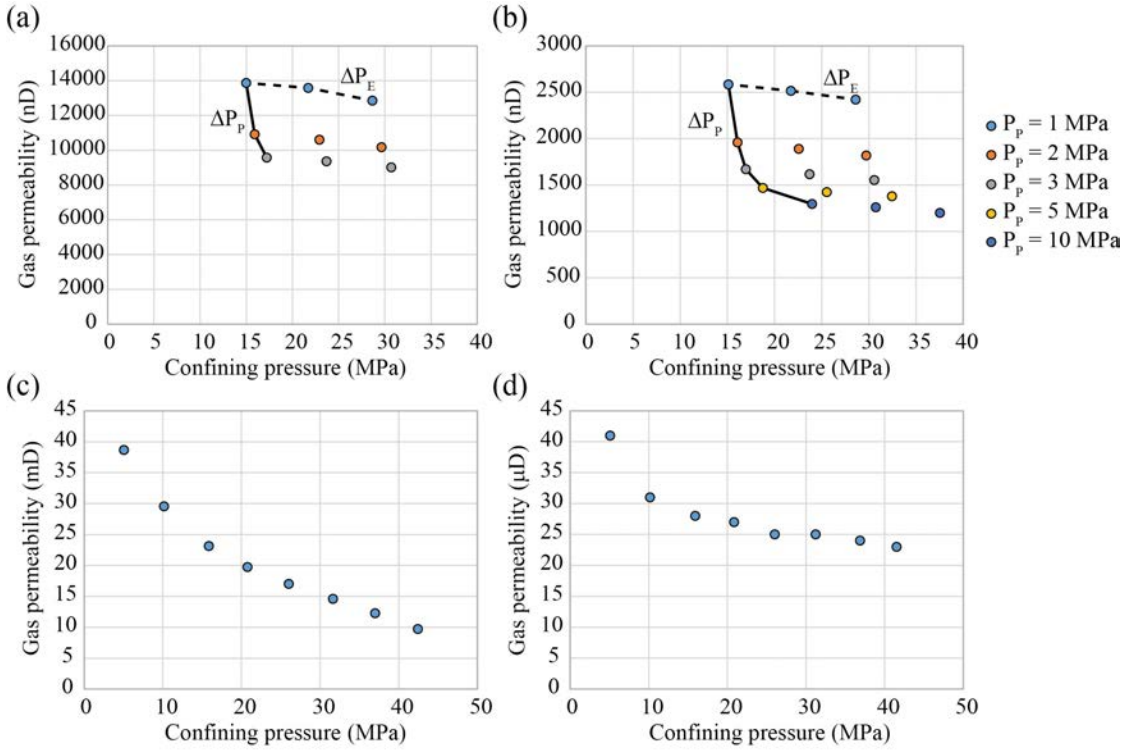

Figure 6.17: The experimental gas permeability for both the Barnett Shale (a-b) and micritic Green River (c-d) samples post-pyrolysis to the gas window. The Barnett Shale is reported parallel (a) and perpendicular to bedding (b) as a function of confining pressure, colored by pore pressure. The Green River is reported parallel (c) and perpendicular to bedding (d) at a constant pore pressure of 1.4 MPa. Note the difference in scale of the y-axis between each panel.

6.4.3 Numerical Permeability Results

The numerically simulated permeability values of all FIB-SEM volumes, i.e., both Barnett and ENI Phase 1 samples, are documented in Figure 6.18 as a function of the effective porosity of

the digital pore geometry. The primary observations from the numerically obtained permeability-porosity trend are: (a) there is a wide range of permeability values obtained at a given porosity value, particularly at low effective porosities (e.g., $\phi < 2\%$), and (b) there is little to no thermal maturity-dependence to the numerically calculated permeability values. The strong agreement in the porosity-permeability relationship for the Barnett and ENI Phase 1 samples indicates that, at the scale of a few microns, the matrix pore geometries are quite similar between the otherwise very different samples. These numerical values will be compared to the experimental measurements in the following section.

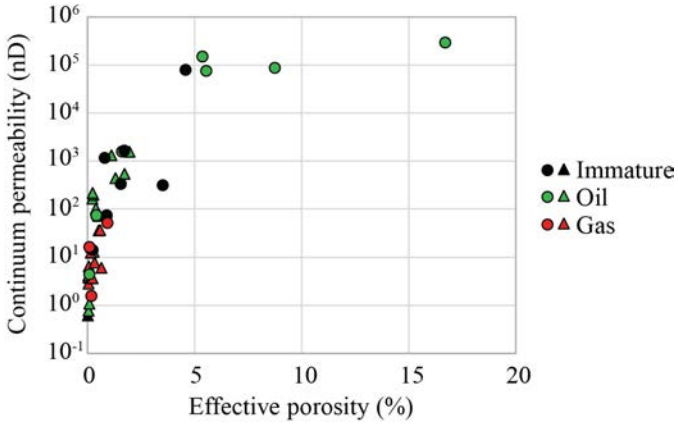

Figure 6.18: The numerically simulated continuum permeability as a function of the effective porosity of the digital rock geometry for the Barnett (circles) and ENI Phase 1 (triangles) datasets. Data point color indicates thermal maturity: immature (black), oil window (green), and gas window (red).

6.5 Discussion

6.5.1 Evolution of the Permeability of Organic-Rich Shale upon Pyrolysis

6.5.1.1 Barnett Shale

As a result of the mechanically induced, through-going fracture created during pyrolysis to the oil window, the order of magnitude increase in the permeability parallel to bedding of the Barnett sample is not unexpected. Indeed, if we assume that all flow through the oil window sample is supported by a planar, through-going fracture, we can estimate the fracture aperture, h, from:

$$h = \sqrt{\frac{12k}{\phi}} \tag{6.4}$$

where k is the continuum permeability and ϕ is the sample porosity (Mavko et al., 2009). The low effective pressure (13.7 MPa), continuum permeability value (the y-intercept of a classical Klinkenberg plot; Klinkenberg, 1941) is 3.8 μD and results in a computed fracture aperture of

215 nm. The fracture aperture is observed to be approximately 10 μm through SEM imaging under high vacuum conditions (Figure 6.19). Under 13.7 MPa of effective pressure, it is possible that the visually observed crack will compact to a value closer to the computed 215 nm. Furthermore, the average pore width of the sample, computed from experimental permeability values (method discussed in Section 6.5.2), is 209 nm – considerably closer to the permeability-derived aperture. Subsequently we attribute the increase in permeability post-pyrolysis to the oil window *primarily* to the induced fracture rather than to thermal maturation-dependent processes occurring in the matrix of the sample.

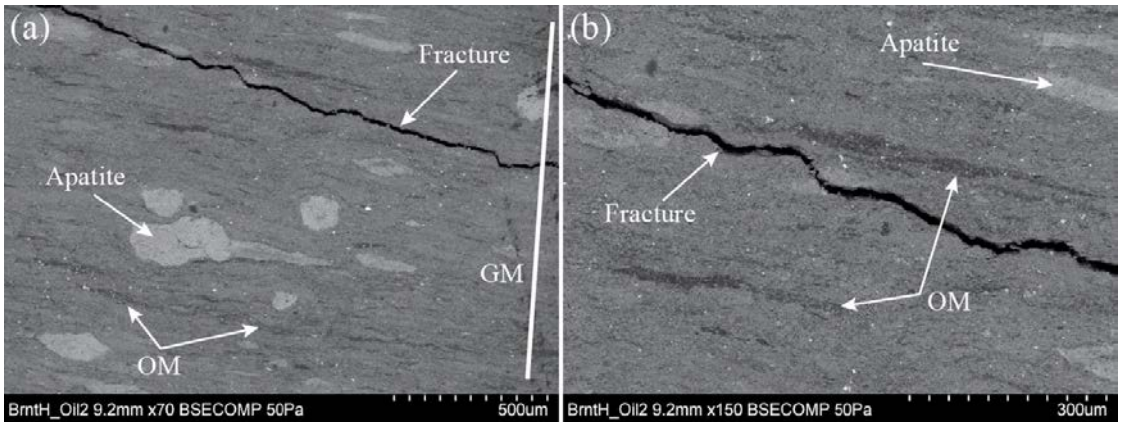

Figure 6.19: SEM images, at two magnifications, documenting the mechanically induced fracture during oil window pyrolysis of the Barnett Shale sample. Identified features include organic matter (OM), apatite, and graphite markings used to recover image locations post-pyrolysis (GM).

Given that the increase in permeability upon pyrolysis to the gas window will also largely be a function of the induced fracture, we address the post-pyrolysis matrix permeability by re-characterizing the permeability after gluing and stressing the fracture closed. In an attempt to more completely isolate the fracture, we filling the fracture with glue and seal the axial faces of the sample in the vicinity of the fracture. The change in permeability due to fracture closure is documented in Figure 6.20. Post-gluing, the permeability decreases 40-45% relative to the unglued values, but remains significantly greater than the baseline and oil window values (by a factor of 20 and 2, respectively). By comparing the glued, gas window permeability values to the acoustic results of Chapter 5 (Figure 6.21), we observe that at effective pressures greater than 20 MPa, above which acoustic measurements indicate induced nano-cracks have closed: (a) the gas window permeability value is significantly greater than the baseline value and (b) there is little confining pressure dependence of the gas window permeability values. Combined, these observations demonstrate that the thermal decomposition of organic matter and hydrocarbon expulsion induce a connected, low compliance pore network, in addition to the compliant nano-cracks. Comparison to the conceptual model for laminar shale maturation indicates that with the compliant nano-cracks closed, there exists a significantly less compliant, three-dimensional pore network connecting the dispersed porous inclusions throughout the siliciclastic network (Figure 6.22).

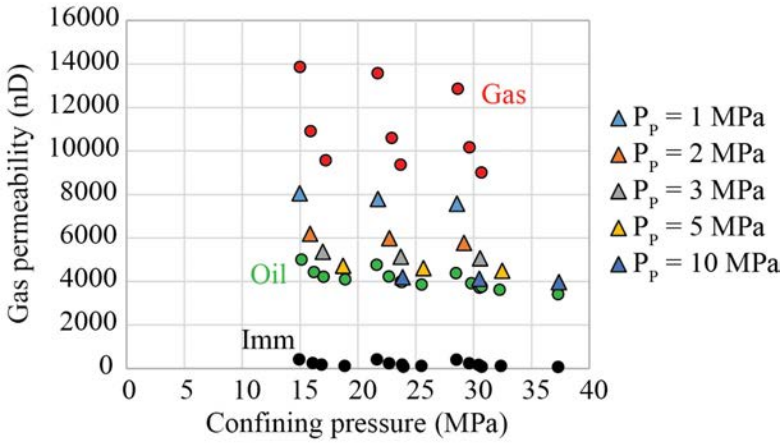

Figure 6.20: The experimental gas permeability perpendicular to bedding for the glued gas window Barnett Shale sample (triangles) as a function of confining pressure, colored by pore pressure. For comparison, the thermally immature, oil window, and un-glued gas window values have been added in black, green, and red circles, respectively.

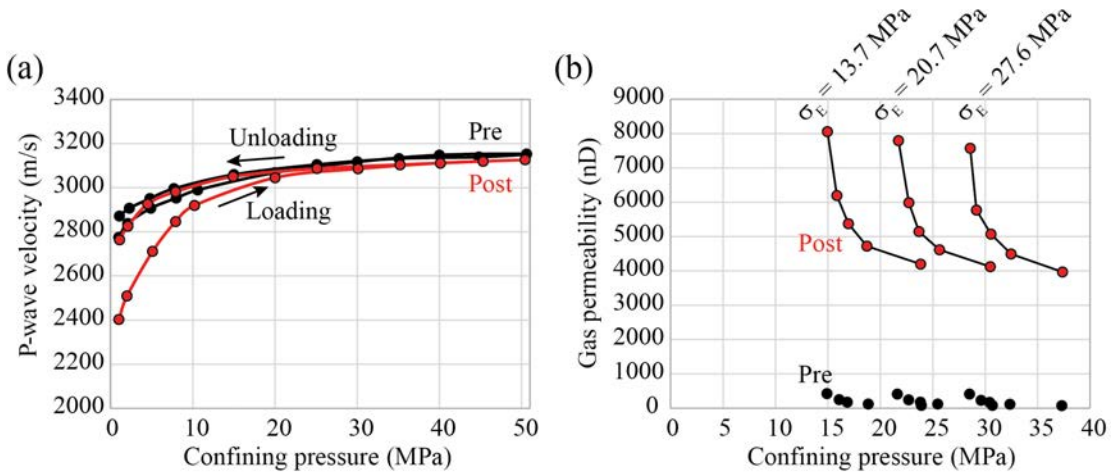

Figure 6.21: A comparison of the acoustic velocity (a) and glued gas permeability (b) as a function of confining pressure, pre- (black) and post-thermal maturation (red).

SEM imaging indicates that the considerable (two order of magnitude) increase in permeability perpendicular to bedding post-pyrolysis to the gas window is attributable to damage of the pore plug (Figure 6.23). In order to address this hypothesis, the permeability magnitude perpendicular to bedding is re-investigated by characterizing the permeability values of the three times longer velocity subsample. In doing so, we assume that any induced damage will have a smaller effect on the bulk properties measured for a considerably longer sample. In comparing the magnitude of the permeability of the two vertically cored, gas window plugs (Figure 6.24), we observe that the damage induced to the permeability subsample results in an increase in measured gas permeability between a factor of 11 (low effective pressure) and 15 (high effective pressure) relative to the undamaged velocity subsample. While this indicates that much of the previously noted permeability increase is due to pyrolysis-induced damage, we also observe that the velocity subsample is between 20 and 25 times more permeable than the immature, baseline

permeability subsample. Clearly, comparing the values of these two subsamples is not valid in a true time-lapse sense; however, such a sizable increase (a factor of 20-25) strongly suggests that the permeability of the undamaged matrix does increase perpendicular to bedding post-pyrolysis.

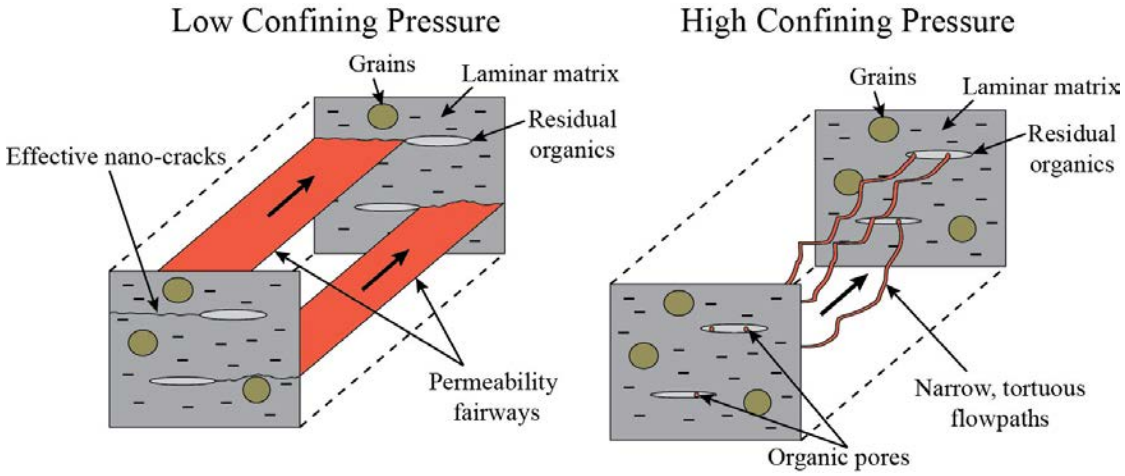

Figure 6.22: The extension of the conceptual model of the acoustic evolution of laminar organic-rich shale to three-dimensions for permeability interpretation. The two post-pyrolysis flow regimes are documented as: (left) open nano-cracks at low confining pressure enabling high flux through the sample (thus, high permeability), and (right) closed nano-cracks leaving only tortuous, narrow, less permeable organic pores at high confining pressure.

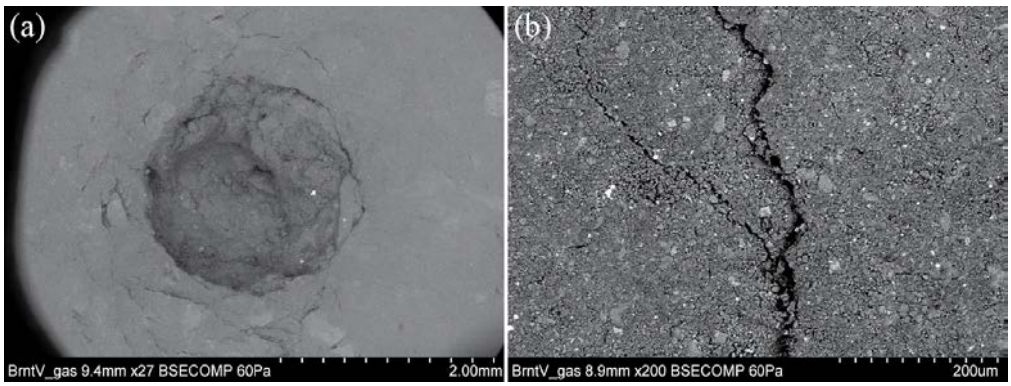

Figure 6.23: SEM images documenting damage to the vertically cored, gas window Barnett Shale subsample. Identified features include (a) a large void caused by material adhesion to the HTHP endcap and (b) an induced perpendicular to bedding microcrack.

6.5.1.2 Green River

In the conceptual model of the micritic Green River presented in Chapter 5, the Green River was represented by an approximately spherical, granular pack representative of a micritic rock or siltstone (Figure 6.25). Applying this schematic model, we can quality control the many order of magnitude increase in permeability parallel to bedding through computing an average spherical grain diameter from the Kozeny-Carman model as formulated in Equation 6.5 (Mavko et al., 2009), where k is the continuum permeability, ϕ is the porosity, τ is the tortuosity and, d is the

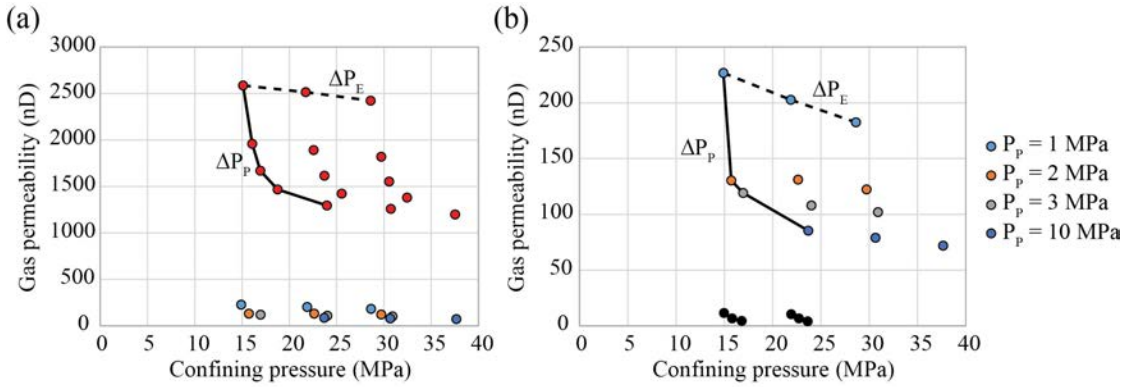

Figure 6.24: The experimental gas permeability perpendicular to bedding, for the gas window Barnett Shale velocity subsample, as a function of confining pressure, colored by pore pressure. To aid the interpretation of the plots, an example line of constant pore pressure (dashed line) at 1 MPa and constant effective pressure (solid line) at 13.7 MPa have been added. For comparison, in (a) the gas window permeability subsample values are plotted in red, while in (b) the baseline, thermally immature permeability subsample values are plotted in black.

average spherical grain diameter. Allowing tortuosity, which we cannot quantify experimentally, to range over representative values of 1.2 to 5 in combination with experimental porosity and permeability values yields an average spherical grain diameter of between 7 and 30 microns. Visual inspection of SEM images of the Green River samples (Figure 6.26.a-b) indicates grain diameters ranging from 1 to 20 microns. This is an important result for two reasons: first, the many order of magnitude increase in permeability is deemed to be physical rather than indicative of intense, undocumented damage or cracking, and, second, the strong agreement in grain sizes serves as further reinforcement of our conceptual model for micritic rocks or siltstones.

$$k = \frac{1}{72}\frac{\phi^3}{(1-\phi)^2\tau^2}d^2 \tag{6.5}$$

As with the Barnett Shale, the parallel to bedding permeability in the Green River is re-characterized for the velocity subsample as a means of confirming the many order of magnitude increase in permeability. The two permeability-confining pressure trends are presented in Figure 6.27 and exhibit quite similar values, particularly relative to the scale of heterogeneity visible in the Barnett Shale subsamples (Figure 6.24). This relative agreement between the two subsamples further indicates that the many order of magnitude increase in permeability after pyrolysis is physical rather than the result of undocumented damage or cracking.

Additionally, given our roughly isotropic, spherical pack model, we would expect that the permeability anisotropy should be quite low for the Green River samples; however, we observe permeability anisotropy values on the order of 400-800 (horizontal permeability/vertical permeability). We can further interpret the permeability value perpendicular to bedding by applying the same Kozeny-Carman formulation as was applied previously to the horizontal sample (Equation 6.5). For the same range of tortuosity values (τ: 1.2-5), the average spherical grain diameter perpendicular to bedding is calculated to be between 500 nm and 2.3 microns. Again, SEM imaging documents a range of grain diameters on the order of 2 to 20 microns, i.e., the assumption of a

sub-spherical granular morphology is not unphysical (Figure 6.26.c-d). Clearly, for the vertically cored samples, the two order of magnitude lower permeability value results in the underestimation of the average grain size. The primary physical difference between the two orientations of plug post-pyrolysis is the directionally dependent retention of hydrocarbons. The vertically oriented plug retains 3.8 times more free hydrocarbons than the horizontally oriented plug (S_1 values of 15.57 mg/g and 4.06 mg/g, respectively; Table 6.5). The presence of hydrocarbons in the pore space will block pores and pore throats and suppress the experimental permeability perpendicular to bedding as the relative permeability (more accurately what is measured here), assuming the respective irreducible saturations are exceeded, will always be less than the single phase gas permeability value.

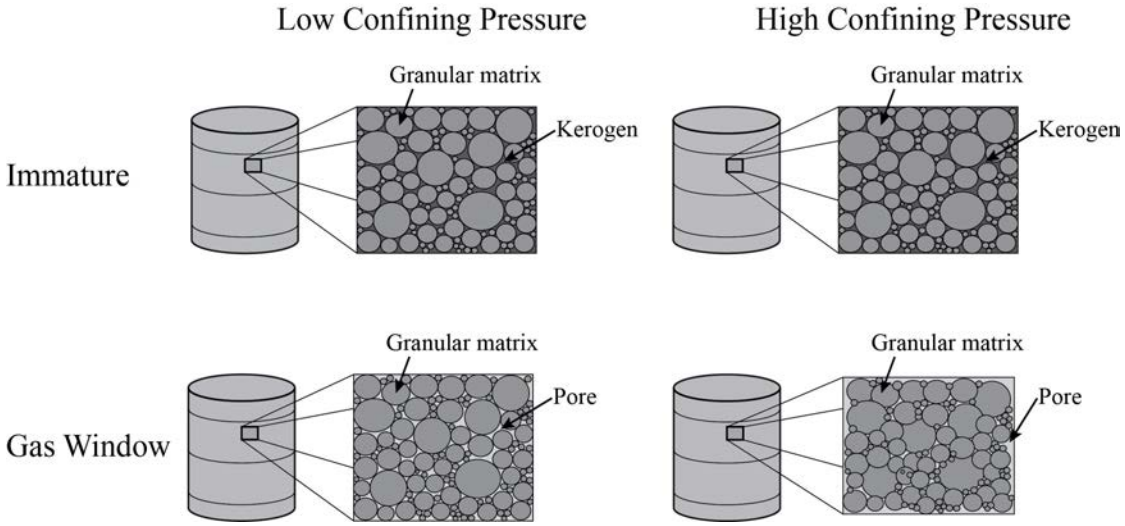

Figure 6.25: A conceptual model for micritic rock and siltstone evolution as a function of thermal maturity, as presented in Figure 5.17.

Subsequently, the many order of magnitude increase in the permeability of the micritic Green River samples is determined to be both physically realistic for an intact sample and to be representative of the previously proposed, elasticity-based conceptual model of the Green River samples. Further, given the greater hydrocarbon retention (Table 6.5), reproducibility of vertical permeabilities between subsamples of different scale (Figure 6.27), and the visually similar microstructure and average grain sizes in the horizontal and vertical subsamples (Figure 6.26), the permeability anisotropy observed in the Green River is attributed to pore-filling and the partial blockage of pores/pore throats by hydrocarbons preferentially retained in the vertically cored subsample.

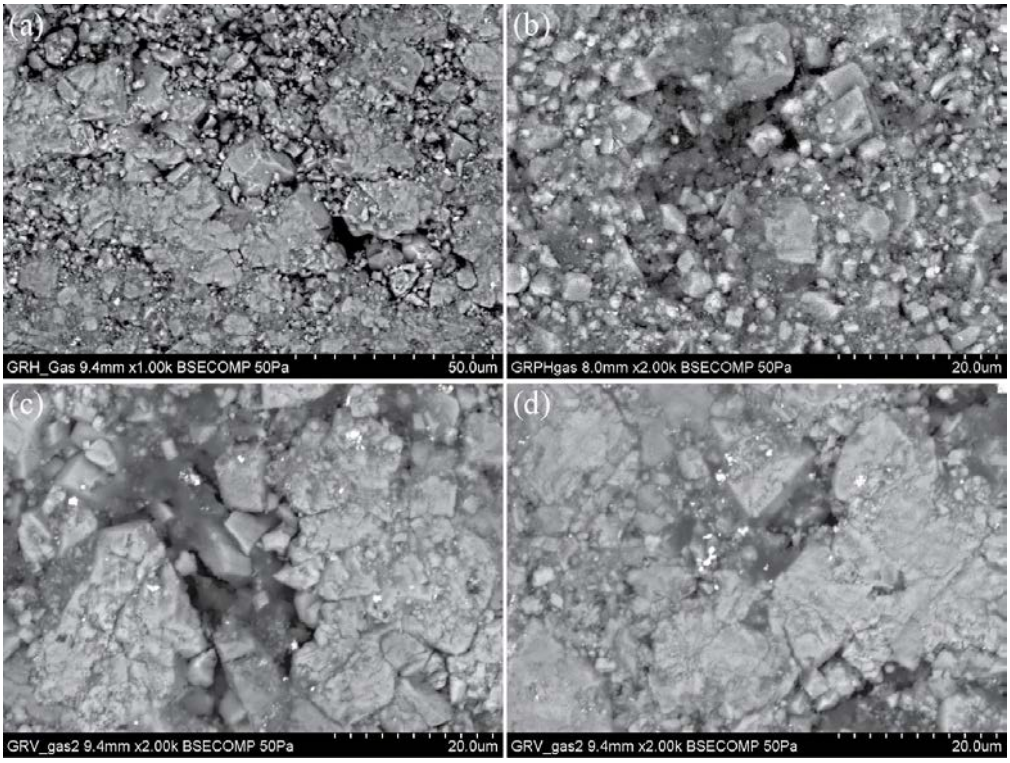

Figure 6.26: SEM images documenting the range of grain sizes in the Green River samples both from horizontally (a-b) and vertically cored (c-d) samples.

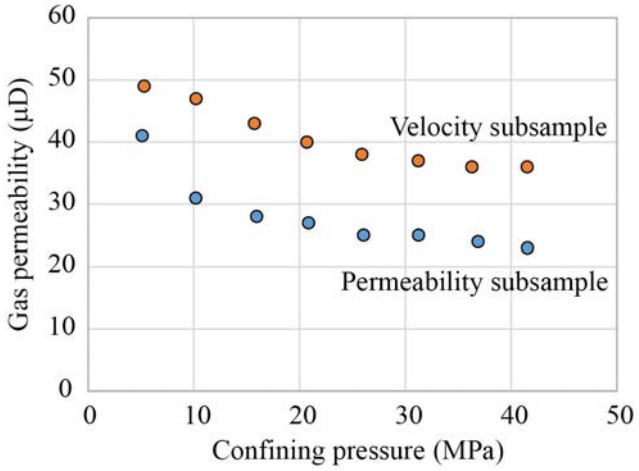

Figure 6.27: The experimental gas permeability as a function of confining pressure for the vertically cored Green River permeability (blue) and velocity (orange) subsamples.

6.5.1.3 Thermal Evolution of Numerically Determined Permeability

As previously noted, the full suite of numerical permeability values exhibits no appreciable trend as a function of thermal maturity (Figure 6.18). Indeed, the most permeable samples are a set of one thermally immature and four oil window Barnett Shale samples, while the gas window ENI Phase 1 and Barnett Shale samples are among the least permeable geometries simulated. These results appear in direct conflict with the hypothesis that thermal maturation should increase the number and size of flow paths through the volume, thus increasing the permeability. However, if we consider the nature of the percolating flow paths in each sample, the source of this discrepancy becomes apparent.

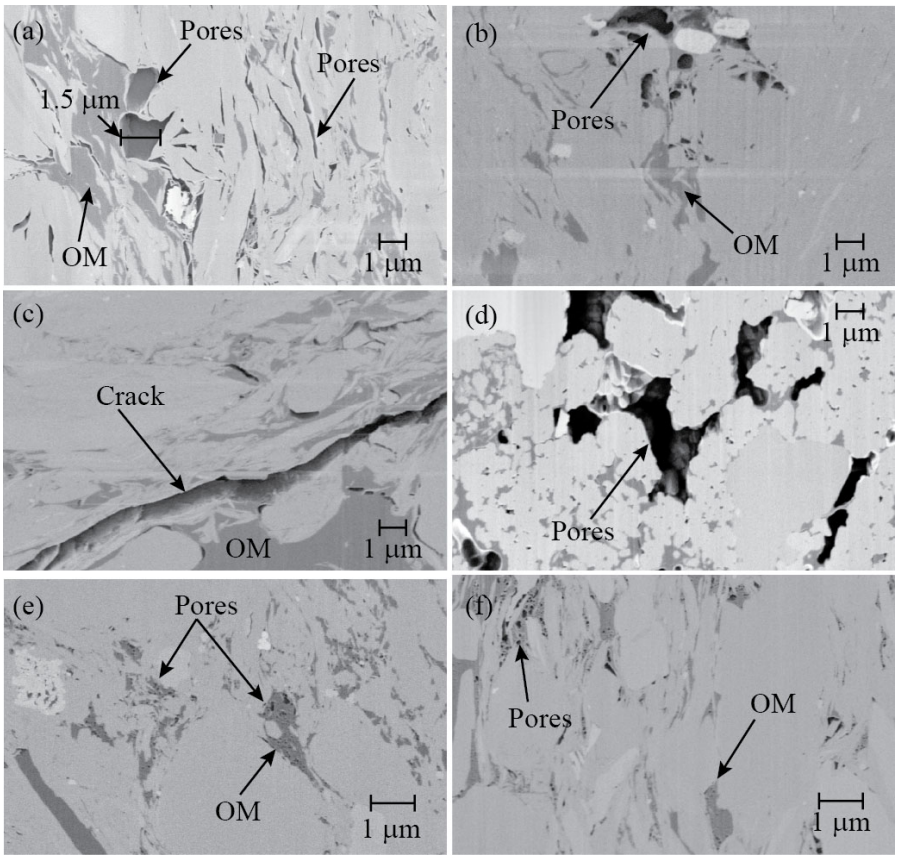

Figure 6.28: Representative two-dimensional slices extracted from FIB-SEM volumes used to generate digital pore geometries. (a) Thermally immature Barnett Shale, (b) thermally immature ENI1, (c-d) pyrolyzed oil window Barnett Shale, (e) gas window Barnett well sample, and (f) gas window ENI5. Identified features include the major porous features and organic matter (OM).

Representative porous structures within more permeable low maturity samples are compared with typical gas window pore morphologies in Figure 6.28. The thermally immature Barnett and ENI1 and pyrolyzed oil window volumes exhibit intergranular porosity on the scale of a few microns wide (Figures 6.28.a-b and 6.28.d), while a second pyrolyzed oil window Barnett sample is split by a through-going fracture with an aperture of nearly one micron (Figure 6.28.c). Contrastingly, typical gas window pore morphologies from the Barnett well and ENI5 samples are collections of spongy organic porosity (after Walls and Sinclair, 2011) consisting of pores 15

to 200 nm wide. The pore morphologies of the less thermally mature samples are inherently more permeable (up to 300 μD) relative to the spongy gas window porosity (up to 50 nD). It is subsequently clear that the lack of a thermal maturity-dependent trend in the simulated permeability values arises from inherent heterogeneities in the porous structures contributing to flow across each micron-scale volume. The effect of pyrolysis on pore morphology is further discussed in Appendix A.

6.5.2 On the Direct Comparison of Experimental and Numerical Permeability Values

In order to compare the magnitude of the experimental gas permeability and numerical continuum permeability values, the experimental gas permeability values must be corrected for slip flow and other diffusive mechanisms. This correction is applied through Klinkenberg plots (Figure 6.29; Klinkenberg, 1941), where the y-intercept of the linear fit is the experimental continuum permeability. The computed continuum permeability of all samples is documented in Appendix B.

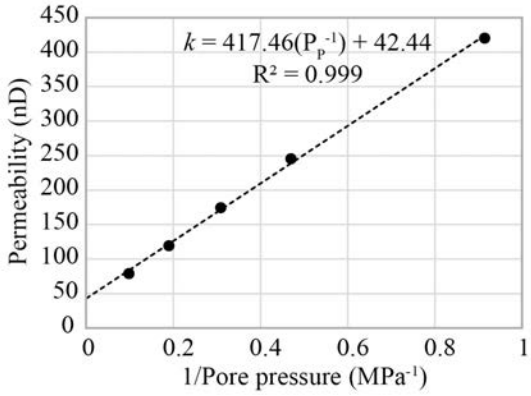

Figure 6.29: Example Klinkenberg plot for the thermally immature, horizontally cored Barnett outcrop sample.

In Figure 6.30, all numerical and experimental continuum permeability values are compared as a function of effective porosity – included in this plot are all experimental samples that were excluded from a more complete analysis due to extensive through-going fracturing, e.g., the ENI Phase 1 samples. Note that all comparisons use the lowest effective pressure experimental values as FIB-SEM volumes are imaged under vacuum. While a strong trend exists between porosity and permeability for the numerically simulated values, the experimentally determined permeability values exhibit no such trend (Figure 6.30).

In order to better compare the scale of flow paths in experimental and numerical samples, we compute the effective pore width of the experimental samples from the gas permeability values, while extracting the pore width directly from the digital rock geometry (see Allan and Mavko, 2013 for the numerical implementation). The effective pore width of the experimental samples is estimated through application of the Unified Flow Model (UFM) of (Karniadakis et al., 2005). In

the UFM, the continuum and gas permeability values are related by the dimensionless Knudsen number (Kn) as in Equations 6.6 and 6.7 where k_0 is the continuum permeability and k_{gas} is the gas permeability.

$$k_{gas} = k_0 \left[1 + \alpha(Kn)Kn\right]\left[1 + \frac{4Kn}{1+Kn}\right] \tag{6.6}$$

$$\alpha(Kn) = \frac{128}{12\pi^2}\tan^{-1}(4Kn^{0.4}) \tag{6.7}$$

$$Kn = \frac{\lambda}{H} = \frac{k_B T}{\sqrt{2}\pi P_P d^2 H} \tag{6.8}$$

The dimensionless Knudsen number, as defined in Equation 6.8, is the ratio of the mean free path (λ) to the effective pore width (H), where the mean free path is a function of temperature (T), pore pressure (P_P), and probe gas collision diameter (d = 256 pm for helium). Subsequently, given the experimental conditions (which define P_P and T), gas permeability, and Klinkenberg-corrected continuum permeability, we can solve numerically for the effective pore width.

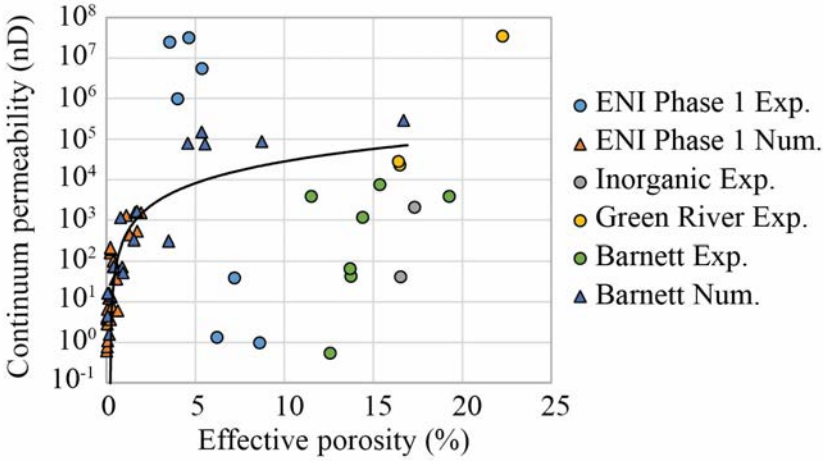

Figure 6.30: Continuum permeability as a function of effective porosity for all experimental measurements (circles) and numerical simulations (triangles). A power function is fit to the numerical dataset for clarity.

In Figure 6.31.a, we recast Figure 6.30 as a function of the calculated pore width, while in Figure 6.31.b the anomalous heavily fractured samples and extremely permeable horizontal Green River sample are removed to better illustrate the bulk of the relationship. There remains significant scatter in the relationship – likely due to the assumptions of UFM and the difficulty in correctly estimating the true average pore width from the complex digital pore geometries – however, in general, there is an enormous increase in the agreement between the experimental and numerical values. We attribute the improvement in agreement between experimental and numerical datasets to be a result of the scale of measurement – a cylinder approximately 0.7 cm by 2.54 cm versus a cube on the order of 10's of microns. At the fine scale of the FIB-SEM volumes (15 nm resolution), the bulk of the porosity percolates the sample and, thus, contributes to fluid flow. However, at the plug-scale, we expect considerably more non-percolating porosity,

resulting in the apparent underestimation of permeability for a given porosity value. Additionally, the heavily fractured ENI Phase 1 samples overestimate permeability, as at relatively low porosity values, highly conductive fractures result in anomalously large permeability values (Figure 6.30).

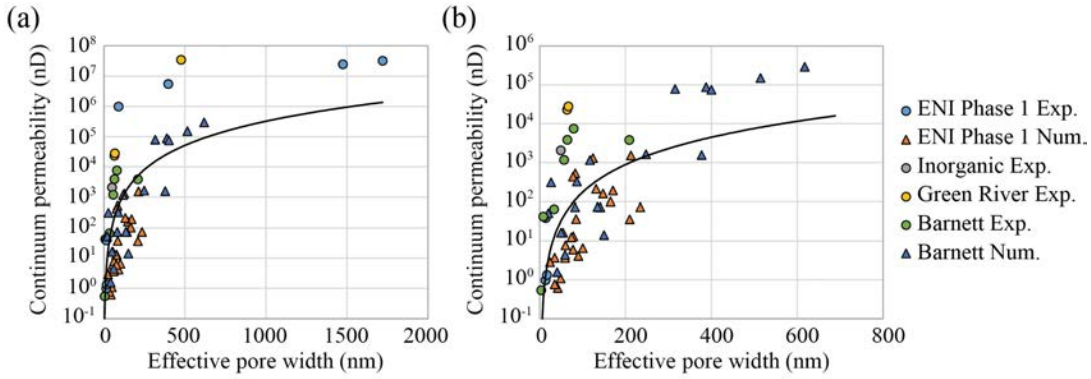

Figure 6.31: Continuum permeability as a function of the calculated effective pore width for all experimental samples (circles) and digital geometries (triangles). The plot in panel (b) is an inset of panel (a). Best fit power functions are fit to the full dataset for clarity.

Considering permeability as a function of pore width removes the effect of non-percolating, effective porosity. The computed effective pore width is the pore width that best describes the pressure-dependent fluid dynamics of each experiment and, as such, correlates better with permeability than a tangentially informative bulk property such as effective porosity. Under the assumption that, regardless of the scale of the sample, the governing fluid dynamics are the same, the effective pore width must, by definition, better predict the permeability of the sample. Subsequently, when possible, it is recommended that when comparing experimental and numerical permeability trends that porosity-dependent trends be replaced by the effective pore width of the sample.

6.6 Conclusions

In this chapter, we have presented a first-of-its-kind, combined numerical and experimental dataset of the transport properties of organic-rich shale as a function of induced thermal maturity. Through the implementation of these experiments we are able to make detailed observations on the change in porosity and permeability resulting from hydrocarbon generation and expulsion and relate those changes to the underlying microstructural evolution that governs them. The expulsion of generated hydrocarbons from the laminar Barnett Shale results in the formation of subparallel to bedding nano-cracks, as previously documented in Chapter 5. However, as confining pressure is increased and these nano-cracks close, there remains an induced, less compliant, connected pore network that increases permeability by as much as two orders of magnitude parallel to bedding. Similarly, the loss of pore-filling kerogen from the weakly aligned, micritic Green River samples results in a permeability increase from previously impermeable to $\sim$10 mD. Furthermore, this immense increase in permeability correlates well with Kozeny-Carman-based predictions for a spherical back geometry reminiscent of the Green River samples in this study.

The iterative high-resolution imaging component of this study clearly documents the increase in organic porosity as the organic matter thermally matures. However, this clear increase in organic porosity does not coincide with any observed thermal dependence in permeability values simulated from image-based digital rock geometries. The lack of a thermal maturity-dependent trend is attributed to nanoscale heterogeneities in the location of porosity in the high-resolution volumes, e.g., volume-splitting cracks, large intergranular pores, and narrow organic pores. Finally, given the breadth of this dataset, we are able to document the previously observed difficulty in directly comparing experimental and numerical permeability values as a function of porosity. The lack of agreement between experimental and numerical values is attributed to complications arising from the four order of magnitude difference in the scale of measurements. However, we demonstrate that significantly stronger agreement can be developed by comparing experimental and numerical permeability values as a function of the width of the pore throats that control the permeability of each sample rather than the bulk porosity of the samples.

6.7 Appendix

6.7.1 Appendix A: On the Issue of Direct Comparison between Naturally and Pyrolysis-Matured Shale Samples

6.7.1.1 Organic Porosity Topology

Through the comparison of the topology and scale of organic pores in naturally matured and pyrolyzed samples, we have noted a consistent set of dissimilarities that need to be addressed in future work. As documented in Figure 6A.1, naturally matured Barnett Shale samples are typically composed of a large number of 15 nm to 250 nm diameter, sub-spherical pores located within the organic matter in what is referred to as a spongey texture (Walls and Sinclair, 2011). Contrastingly, pyrolyzed Barnett Shale samples are composed of a small number of irregularly shaped pores up to 5 microns in diameter that in many cases have almost completely replaced the original organic body. If this topological discrepancy should prove to be a systematic idiosyncrasy of pyrolysis-induced thermal maturation, there are large implications for iterative imaging-based studies of organic porosity and studies of numerical fluid flow through digital organic-rich rock geometries.

It is important to consider that when samples are thermally matured in situ, there is little migration of fluids from the site of generation on short time scales due to the presence of pre-existing pore fluids and the relative impermeability of shale. However, in our pyrolysis methodology, in order to thermally isolate the sample while preventing the pore pressure from exceeding the confining pressure, the sample is held between alumina spacers with a small cylindrical void in the core of the spacer (Figure 6A.2.a). As a result, hydrocarbons produced at the surface of the sample are free to migrate into the pore line as they are generated. It is our hypothesis that the migration of generated fluids from the surface and subsequent decrease in pore pressure at the generation site enables a more rapid and complete conversion of organic matter to hydrocarbons at that site. This accelerated conversion of solid organic matter to hydrocarbons then results in the preferential development of pendular rather than spongey porous textures. Furthermore, it is the surface of the plug (where this process is hypothesized to occur) that is sampled during FIB-SEM imaging.

While produced hydrocarbons are relatively free to migrate from the axial faces of the plug, hydrocarbons generated within the core of the plug will encounter similar pressure conditions to those that are prevalent in situ. Thus, we hypothesize that pore topologies within the core of the plug, where fluid and pressure build-up slow down the rate of thermal maturation, will better resemble in situ pore topologies. In order to test this hypothesis, we propose that future imaging studies subsample the pyrolyzed core and image both the outer surface and the newly exposed interior surface as illustrated in Figure 6A.2.b-c. If the disparity in pore topologies proves to be systematic to pyrolysis-induced thermal maturation regardless of where FIB-SEM volumes are collected, an important caveat must be added to imaging and numerical studies of microstructure and transport properties in pyrolyzed organic-rich shale.

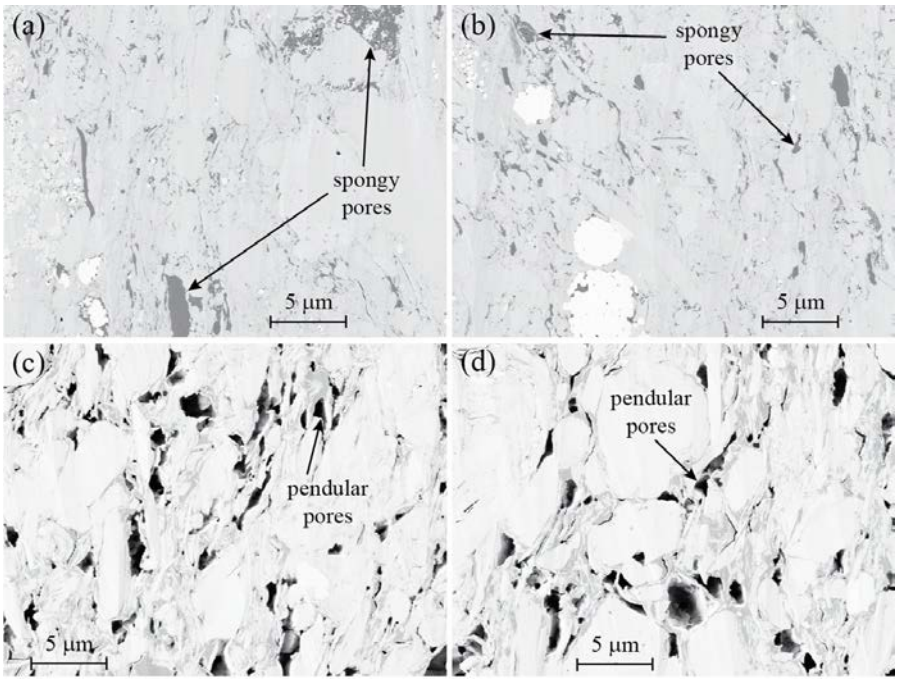

Figure 6A.1: High-resolution SEM images of characteristic organic pore topologies as seen in the naturally matured Barnett well samples (a-b) and in the gas window pyrolyzed outcrop Barnett sample (c-d).

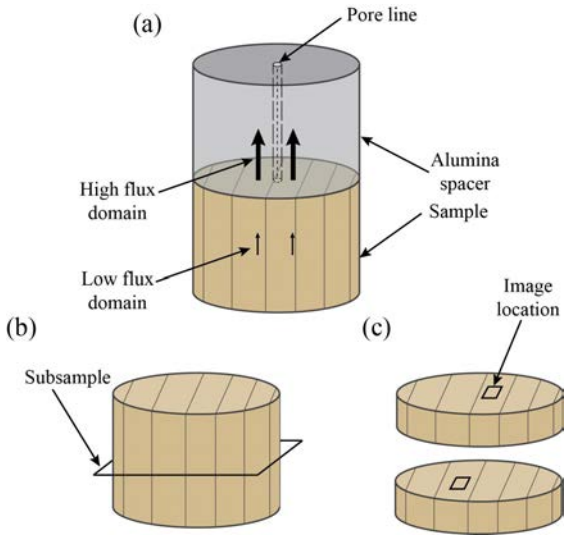

Figure 6A.2: Schematic representation of potential issues associated with, and a proposed amendment to, our iterative FIB-SEM imaging procedure. (a) The location of the currently imaged surface relative to the low pressure pore line, (b) proposed, post-pyrolysis subsampling technique, and (c) updated imaging locations.

6.7.1.2 Physical Property Magnitude

As noted in the main text, the experimental porosity and permeability values are anomalously large. For instance, in this study, we observe porosity values up to 18% and 22% (Table 6.4) and permeability values up to 8 μD and 35 mD (Figures 6.20 and 6.17) for the Barnett

Shale and Green River samples, respectively, post-pyrolysis. However, experimental values reported in the literature for clay-rich, naturally matured Barnett Shale samples range only from 20-160 nD at porosities ranging from 3-4% (Ghanizadeh et al., 2013; Heller et al., 2014; Bhandari et al., 2015). Subsequently, we question why the pyrolyzed samples are so much more porous and permeable.

The primary differences between ex situ pyrolysis and in situ thermal maturation are the temperature magnitude and time scale. Time-lapse SEM imaging (Figure 6.12) indicates that there is little to no thermally induced evolution of the composition or alignment of the mineral matrix; subsequently, we suspect the issue lies in the time scale of the process. In situ, during and after the generation and expulsion of produced hydrocarbons, the rock remains under significant lithostatic pressures for millions of years; however, in our methodology, the applied confining pressure is released over a few days. In this manner, the rock frame has little chance to compact and viscoelastically deform post-pyrolysis, and, as a result, we preserve significant porosity and permeable pathways that may close over time in situ.

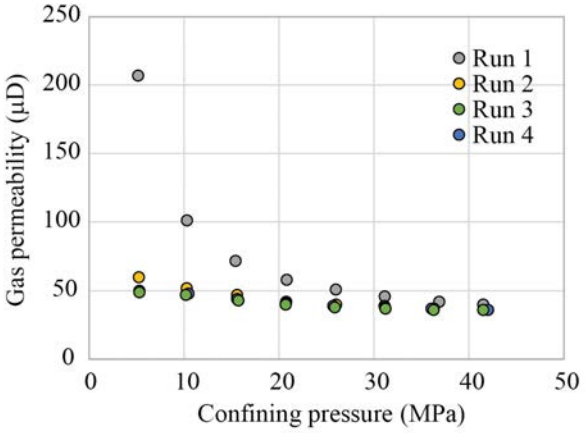

Figure 6A.3: The experimental gas permeability as a function of confining pressure for the vertically cored Green River velocity subsample. Each curve corresponds to a different pressure cycle, with the cycles conducted on consecutive days.

In order to test and overcome this issue, the transport properties of the sample would have to be studied after leaving the sample under reservoir-scale confining pressures for an extended period of time. In Figure 6A.3, we document changes in the permeability of the vertically cored Green River velocity subsample over a period of four days, where the sample was left at ∼40 MPa overnight between runs. The permeability at low confining pressure decreases by as much as 75% between the first and second runs; however, thereafter the change in permeability is quite low between runs 2 and 4. Subsequently, in order to address the ability of post-pyrolysis characterization to capture representative in situ transport properties, investigative experiments must be conducted in which the samples are left under reservoir-scale confining pressure for periods of time on the order of months. If the experimentally determined transport properties continue to so greatly exceed in situ values, iterative characterization pre- and post-pyrolysis may have no predictive applications for reservoir characterization, but would be restricted to the investigation of phenomenological evolutions.

6.7.2 Appendix B: Experimental Permeability Dataset

Table 6B.1: Pulse-decay gas permeability measurements and derived continuum permeability and effective pore width values at 13.7 MPa effective pressure for the Barnett Shale samples, pre- and post-pyrolysis. Sample labels are: horizontally cored (BOH), vertically cored permeability subsample (BOV), and vertically cored velocity subsample (BOV2).

Sample	Thermal Maturity	Pressure (MPa)		Permeability (nD)		Effective Pore Width (nm)
		Pore	Confining	Gas	Continuum	
BOH	Immature	1.09	14.92	420	42	8
		2.13	16.07	246		
		3.24	16.85	175		
		5.27	18.85	120		
		10.16	23.92	79		
	Oil	1.10	15.12	5,007	3,846	201
		2.16	16.20	4,436		
		3.23	17.04	4,212		
		5.30	18.89	4,100		
		10.22	23.79	3,975		
	Gas	1.06	14.98	13,863	7,560	78
		2.09	15.90	10,918		
		3.19	17.20	9,577		
	Gas (Glued)	1.02	14.96	8,056	3,883	64
		2.04	15.85	6,193		
		3.14	16.97	5,369		
		5.00	18.72	4,719		
		10.06	23.85	4,191		
BOV	Immature	1.17	14.97	12	0.5	4
		2.13	15.81	7		
		3.17	16.80	5		
	Gas	1.06	15.11	2,585	1,177	55
		2.08	16.07	1,958		
		3.14	16.95	1,670		
		5.18	18.76	1,468		
		10.10	23.98	1,295		
BOV2	Gas	0.98	14.91	226	66	34
		2.06	15.72	130		
		3.13	16.95	119		
		5.11	18.63	95		
		9.87	23.70	85		

Table 6B.2: Pulse-decay gas permeability measurements and derived continuum permeability and effective pore width values at 20.7 MPa effective pressure for the Barnett Shale samples, pre- and post-pyrolysis. Sample labels are: horizontally cored (BOH), vertically cored permeability subsample (BOV), and vertically cored velocity subsample (BOV2).

Sample	Thermal Maturity	Pressure (MPa)		Permeability (nD)		Effective Pore Width (nm)
		Pore	Confining	Gas	Continuum	
BOH	Immature	1.10	21.63	409	44	8
		2.12	22.70	242		
		3.14	23.81	171		
		5.27	25.47	120		
		10.16	30.69	78		
	Oil	1.10	21.61	4,763	3,630	193
		2.17	22.68	4,225		
		3.23	23.70	3,990		
		5.30	25.50	3,863		
		10.21	30.69	3,764		
	Gas	1.07	21.70	13,579	7,319	75
		2.09	22.91	10,605		
		3.19	23.68	9,366		
	Gas (Glued)	1.03	21.72	7,794	3,788	64
		2.04	22.72	5,984		
		3.14	23.69	5,142		
		5.00	25.66	4,608		
		10.05	30.49	4,122		
BOV	Immature	1.17	21.92	11	0.8	6
		2.14	22.73	7		
		3.17	23.64	4		
	Gas	1.06	21.73	2,515	1,165	61
		2.08	22.58	1,891		
		3.14	23.70	1,616		
		5.18	25.54	1,423		
		10.10	30.73	1,260		
BOV2	Gas	0.98	21.88	203	65	34
		2.06	22.64	131		
		3.14	24.02	108		
		9.87	30.66	79		

Table 6B.3: Pulse-decay gas permeability measurements and derived continuum permeability and effective pore width values at 27.6 MPa effective pressure for the Barnett Shale samples, pre- and post-pyrolysis. Sample labels are: horizontally cored (BOH), vertically cored permeability subsample (BOV), and vertically cored velocity subsample (BOV2).

Sample	Thermal Maturity	Pressure (MPa)		Permeability (nD)		Effective Pore Width (nm)
		Pore	Confining	Gas	Continuum	
BOH	Immature	1.10	28.50	406	38	7
		2.13	29.62	230		
		3.24	30.42	166		
		5.27	32.36	115		
		10.16	37.31	74		
	Oil	1.10	28.46	4,380	3,364	189
		2.17	29.80	3,924		
		3.23	30.50	3,715		
		5.30	32.24	3,623		
		10.21	37.31	3,419		
	Gas	1.07	28.63	12,856	7,169	81
		2.09	29.63	10,168		
		3.19	30.68	9,017		
	Gas (Glued)	1.03	28.57	7,572	3,682	67
		2.04	29.17	5,768		
		3.14	30.56	5,070		
		5.00	32.47	4,491		
		10.05	37.37	3,965		
BOV	Gas	1.06	28.60	2,422	1,090	54
		2.09	29.73	1,818		
		3.14	30.56	1,552		
		5.18	32.46	1,379		
		10.10	37.53	1,198		
BOV2	Gas	0.99	28.64	183	62	38
		2.06	29.72	122		
		3.14	30.92	102		
		9.88	37.66	72		

Table 6B.4: Pressure drawdown permeability measurements and effective pore width values at 1.4 MPa pore pressure, in the gas window, for the horizontally cored Green River sample.

Confining Pressure (MPa)	Permeability (mD)		Effective Pore Width (nm)
	Gas	Continuum	
5.06	38.686	34.835	475
10.15	29.565	27.728	581
15.84	23.137	21.996	654
20.75	19.764	18.717	581
26.00	17.018	16.062	550
31.63	14.591	13.718	498
36.99	12.270	11.482	436
42.42	9.738	9.05	373

Table 6B.5: Pressure drawdown permeability measurements and effective pore width values at 1.4 MPa pore pressure, in the gas window, for the vertically cored Green River permeability subsample.

Confining Pressure (MPa)	Permeability (μD)		Effective Pore Width (nm)
	Gas	Continuum	
5.09	41	23	64
10.17	31	16	54
15.92	28	14	50
20.84	27	14	54
26.04	25	13	54
31.24	25	12	46
36.87	24	12	50
41.53	23	11	46

Table 6B.6: Pressure drawdown permeability measurements and effective pore width values at 1.4 MPa pore pressure, in the gas window, for the vertically cored Green River velocity subsample.

Confining Pressure (MPa)	Permeability (μD)		Effective Pore Width (nm)
	Gas	Continuum	
5.29	49	28	67
10.20	47	27	68
15.71	43	24	63
20.69	40	22	62
25.88	38	21	62
31.22	37	20	59
36.28	36	20	63
41.51	36	19	56

6.7.3 Appendix C: Numerical Permeability Dataset

Table 6C.1: The numerically simulated continuum permeability and effective pore width as a function of the porosity of the Barnett Shale digital rock geometries.

Sample	Thermal Maturity	Porosity (%)		Continuum Permeability (nD)	Effective Pore Width (nm)
		Total	Effective		
Barnett (Stanford)	Immature	1.62	0.79	1,160	117
		3.10	1.54	328	87
		5.95	3.50	311	26
		3.96	1.71	1,643	248
Barnett (Kiel)	Immature	3.40	0.88	72	141
		3.40	0.23	14	150
		5.34	4.57	78,974	316
	Early Oil	3.06	1.60	1,563	377
		14.44	8.74	87,357	388
		17.57	16.70	292,551	618
	Peak Oil	0.85	0.08	4	59
		1.01	0.40	73	82
	Late Oil	1.87	0.41	74	135
		6.11	5.36	149,932	515
		6.16	5.53	75,285	400
Barnett (Well)	Gas	2.45	0.93	52	20
		0.80	0.17	1	41
		0.80	0.07	16	50

Table 6C.2: The numerically simulated continuum permeability values and effective pore width as a function of the porosity of the ENI Phase 1 digital rock geometries.

Sample	Thermal Maturity	Porosity (%)		Continuum Permeability (nD)	Effective Pore Width (nm)
		Total	Effective		
ENI1	Immature	1.17	0.51	36	210
		0.87	0.49	73	234
		0.25	0.01	0.6	42
ENI3	Early Oil	2.79	1.95	1,540	213
		0.32	0.17	16	54
		0.61	0.21	162	147
		0.47	0.26	194	171
		0.83	0.22	214	131
		0.51	0.28	13	78
ENI4	Early Oil	1.38	1.11	1,305	125
		2.32	1.72	532	83
		1.76	1.30	436	78
		0.83	0.38	102	165
		0.32	0.04	0.8	35
		0.11	0.04	4	35
		0.37	0.07	1	49
ENI5	Gas	1.49	0.14	12	74
		0.76	0.06	7	101
		1.80	0.03	4	90
		3.36	0.33	8	60
ENI6	Gas	4.12	0.64	6	78
		3.71	0.59	37	85
		3.53	0.04	3	24
		3.45	0.23	4	59

6.8 References

Allan, A. M. and G. Mavko, 2013, The effect of adsorption and Knudsen diffusion on the steady-state permeability of microporous rocks: Geophysics, 78:D75–D83.

Allan, A. M., T. Vanorio, and J. E. P. Dahl, 2014, Pyrolysis-induced P-wave velocity anisotropy in organic-rich shales: Geophysics, 79:D41–D53.

Bernard, S., R. Wirth, A. Schreiber, H. M. Schulz, and B. Horsfield, 2012, Formation of nanoporous pyrobitumen residues during maturation of the Barnett Shale (Fort Worth Basin): International Journal of Coal Geology, 103:3–11.

Bhandari, A. R., P. B. Flemings, P. J. Polito, M. B. Cronin, and S. L. Bryant, 2015, Anisotropy and stress dependence of permeability in the Barnett Shale: Transport in Porous Media.

Bhatnagar, P. L., E. P. Gross, and M. Krook, 1954, A model for collision processes in gases. I. Small amplitude processes in charged and neutral one-component systems: Physical Review, 94:511–525.

Bustin, R. M., A. M. M. Bustin, X. Cui, J. K. Ross, and V. S. Murthy Pathi, 2008, Impact of shale properties on pore structure and storage characteristics: SPE Shale Gas Production Conference, SPE 119892.

Clark, A. C. and T. Vanorio, 2015, A niche system for inducing thermo-chemo-mechanical processes in rocks and materials: SRB Volume 142.

Cui, X., A. M. M. Bustin, and R. M. Bustin, 2009, Measurements of gas permeability and diffusivity of tight reservoir rocks: different approaches and their applications: Geofluids, 9: 208–223.

Curtis, M. E., C. H. Sondergeld, R. J. Ambrose, and C. S. Rai, 2010, Structural characterization of gas shales on micro- and nano-scales: Proceedings of the Canadian Unconventional Resrources and International Petroleum Conference.

Curtis, M. E., B. J. Cardott, C. H. Sondergeld, and C. S. Rai, 2012, Development of organic porosity in the Woodford Shale with increasing thermal maturity: International Journal of Coal Geology, 103:26–31.

Dewhurst, D. N. and A. F. Siggins, 2006, Impact of fabric, microcracks and stress field on shale anisotropy: Geophysics Journal International, 165:135–148.

EIA, 2013: Annual energy outlook.

Ghanizadeh, A., M. Gasparik, A. Amann-Hildenbrand, Y. Gensterblum, and B. M. Krooss, 2013, Lithological controls on matric permeability of organic-rich shales: An experimental study: Energy Procedia, 40:127–136.

Heller, R., J. Vermylen, and M. Zoback, 2014, Experimental investigation of matrix permeability in gas shales: AAPG Bulletin, 98:975–995.

Johnston, J. E. and N. I. Christensen, 1995, Seismic anisotropy of shales: Journal of Geophysical Research, 100:5991–6003.

Jones, R. W., 1984, Comparison of carbone and shale source rocks, in J. G. Palacas, ed., Petroleum geochemistry and source-rock potential of carbonate rocks: AAPG Studies in Geology 18.

Jones, S. C., 1972, A rapid accurate unsteady-state Klinkenberg permeameter: SPE Journal, 12: 383–397.

Jones, S. C., 1997, A technique for faster pulse-decay permeability measurements in tight rocks: SPE Formation Evaluation, 12:19–25.

Kang, S. M., E. Fathi, R. J. Ambrose, I. Y. Akkutlu, and R. F. Sigal, 2011, Carbon dioxide storage capacity of organic-rich shales: SPE Journal, pages 842–855.

Karniadakis, G., A. Beskok, and N. Aluru, 2005, Microflos and nanoflows: Fundamentals and simulation: Springer.

Keehm, Y., 2003, Computation rock physics: Transport properties in porous media and applications: PhD Dissertation, Stanford University.

Klinkenberg, L. J., 1941, The permeability of porous media to liquids and gases in drilling and production practice: American Petroluem Institute, pages 200–213.

Kobchenko, M., H. Panahi, F. Renard, D. K. Dysthe, A. Malthe-Sørenssen, A. Mazzini, J. Scheibert, B. Jamtveit, and P. N. Meakin, 2011, 4D imaging of fracturing in organic-rich shales during heating: Journal of Geophysical Research, 116:B12201.

Kwon, O., A. K. Kronenberg, A. F. Gangi, and B. Johnson, 2001, Permeability of Wilcox shale and its effective pressure law: Journal of Geophysical Research, 106:19339–19353.

Lash, G. G. and T. Engelder, 2005, An analysis of horizontal microcracking during catagenesis: Example from the Catskill delta complex: AAPG Bulletin, 89:1433–1449.

Loucks, R. G., R. M. Reed, S. C. Ruppel, and D. M. Jarvie, 2009, Morphology, genesis, and distribution of nanometer-scale pores in siliceous mudstones of the Mississippian Barnett shale: Journal of Sedimentary Research, 79:848–861.

Mavko, G., T. Mukerji, and J. Dvorkin, 2009, The rock physics handbook, 2nd ed.: Cambridge University Press.

Mullen, J., 2010, Petrophysical characterization of the Eagle Ford Shale in south Texas: Presented at Canadian Unconvential Resources and International Petroleum Conference.

Palacas, J. G., 1984, South Florida basin, a prime example of carbonate source rocks of petroleum, in J. G. Palacas, ed., Petroleum geochemistry and source-rock potential of carbonate rocks: AAPG Studies in Geology 18.

Peters, K. E. and M. R. Cassa, 1994, Applied source rock geochemistry, in L. B. Magoon, and W. G. Dow, eds., The petroleum system - From source to trap: AAPG, AAPG Memoir, 60: 93–120.

Price, L. C., J. L. Clayton, and L. L. Rumen, 1981, Organic geochemistry of the 9.6 km Bertha Rogers No. 1 well, Oklahoma: Organic Geochemistry, 3:59–77.

Sondergeld, C. H., R. J. Ambrose, C. S. Rai, and J. Moncrieff, 2010, Micro-structural studies of gas shales: presented at SPE Unconventional Gas Conference.

Succi, S., 2001, The latice Boltzmann equation for fluid dynamic and beyond: Oxford University Press.

Vermylen, J. P., 2011, Geomechanical studies of the Barnett Shale, Texas, USA: PhD Dissertation, Stanford University.

Vernik, L., 1993, Microcrack-induced versus intrinsic elastic anisotropy in mature HC-source shales: Geophysics, 58:1703–1706.

Walls, J. D. and S. W. Sinclair, 2011, Eagle Ford Shale reservoir properties from digital rock physics: First Break, 29:97–101.

Wang, F. P. and R. M. Reed, 2009, Pore networks and fluid flow in gas shales: SPE Annual Technical Conference and Exhibition: SPE 124253.

Chapter 7

FINAL REMARKS

In this thesis, I have addressed the need for a more thorough understanding of the evolution of organic-rich shale as the organic content thermally matures. Shales, which account for much of the volume of rocks in sedimentary basins, are being increasingly targeted as unconventional reservoirs and, as such, detailed rock physics-based relationships are required to improve unconventional exploration workflows and procedures. In particular, the effect of thermal maturation, i.e., hydrocarbon generation and expulsion, on the elastic properties, e.g., anisotropy, must be understood in order to enable the identification from remote sensing studies of regions of elevated thermal maturity across an organic-rich shale formation. The effect of thermal maturation on the elastic properties may then be complemented by an understanding of the simultaneously occurring evolution of transport properties such as porosity and permeability. Together, the development of a deeper understanding of the elastic and transport evolution as organic-rich shale thermally matures may be expanded to the in situ identification of sweet spots and more targeted exploitation of unconventional reservoirs.

Towards this goal, the primary accomplishment of this thesis is the implementation of a pioneering set of rock physics experiments on individual intact core plugs pre- and post-pyrolysis. This study consists of the first documented iterative characterization of the elastic and transport properties of organic-rich shale plugs as a function of thermal maturation. Furthermore, the results of these experiments provide important insights into the in situ thermal evolution of organic-rich shale.

In Chapter 2, I identify that the application of confining pressure during pyrolysis is requisite to the successful characterization of pyrolyzed core plugs. The omission of confining pressure results in runaway hydrocarbon generation with subsequent fast expulsion that fractures the rock and corrupts further characterization of both the elastic and transport properties. Additionally, building on previous research (Vernik and Nur, 1992; Vernik and Landis, 1996; Vernik and Liu, 1997), in Chapter 4 I document that the direct comparison of shale samples from different locations, as a function of thermal maturity, is severely compromised by inherent differences in mineralogy, texture, and burial history; thus reinforcing the importance of iterative characterization of individual samples pre- and post-pyrolysis. However, I *am* able to use this broad dataset to demonstrate that, even for shales of vastly different mineralogies, textures, etc., intrinsic anisotropy can indeed be predicted from the average degree of crystallographic preferred orientation (CPO) in the mineral frame of the shale. Finally, the lessons of Chapter 2 are combined with the implementation of a novel iterative shale characterization methodology (described in detail in Chapter 3) in Chapters 5 and 6. Through the numerous experiments conducted in Chapters 5 and 6, I demonstrate that the microstructure of the thermally immature organic-rich shale has immense control on the thermal evolution of the composite shale. This finding implies that the initial microstructure of the organic-rich shale determines the ability to elastically detect regions of elevated thermal maturity, which is pivotally important to attempts to identify regions of elevated thermal maturity, and potential hydrocarbon accumulation, through remote sensing studies and well logging. Further, I identify that induced thermal maturation increases the permeability of organic-rich shale: importantly, this increase in permeability is demonstrated not to be entirely a function of cracking, whether induced by mechanical damage or hydrocarbon expulsion. Rather, the increase in permeability is relatively insensitive to effective pressure and is indicative of the development of a less compliant, matrix-based pore network.

While through this work, I provide experimental evidence and phenomenological implications for the modeling of thermal maturation in organic-rich shales, it is important to consider potential biases. In particular, when interpreting any experimental shale for application to rock physics models, it is important to bear in mind the nature of shale core. Samples are successfully cored and recovered at the surface from only the most 'well-behaved' of horizons, any horizons that are prone to fracturing during coring will be undersampled or nonexistent in the experimental dataset. Thus a full sampling of thermal maturities may be difficult due to differences in mechanical properties. Through the methodology presented in this work, one may be able to induce thermal maturity in a well behaved horizon and thus sample a more complete range of the formation than is possible through coring alone. Both the limited nature of natural datasets and the potential to better populate those datasets through laboratory experiments must be

considered when designing shale-based experiments.

Through the development and implementation of the experiments presented in this thesis, avenues for future research have been opened. The primary avenues of future research raised by this work are twofold: firstly, this thesis presents the first attempts at ex situ pyrolysis on several intact core plugs for iterative rock physics analysis; however, in order to cover all possible conditions and permutations of pyrolysis experiments, a large dataset of these experiments on a vast array of different shales must be compiled. In so doing, the effect of different effective pressure magnitudes, of different time and temperature combinations, and of open vs. closed pyrolysis on shales of different mineralogies, porosities, and textures may be more thoroughly discerned. The identification of these effects from a dense dataset of samples and experiments will enable more targeted pyrolysis experiments based on the specific research question at hand in future studies.

Secondly, the question remains: what effect does the presence of a non-zero pore water saturation have on the thermal evolution of the elastic and transport properties of organic-rich shale? Saturating and pyrolyzing intact core plugs is a very challenging problem to implement experimentally; however, such experiments have to be the ultimate goal in the quest to fully characterize the in situ evolution of organic-rich shale. And, again, such knowledge would enable the more specific implementation of pyrolysis experiment parameters to address the research question at hand. Subsequently, this thesis provides both the first round of results with regard to the implementation of ex situ pyrolysis experiments and both lays the framework *and* documents the practicability for the expansion of this field of experimental investigation.

7.1 References

Vernik, L. and C. Landis, 1996, Elastic anisotropy of source rocks: Implications for hydrocarbon generation and primary migration: AAPG Bulletin, 80:531–544.

Vernik, L. and X. Liu, 1997, Velocity anisotropy in shales: A petrophysical study: Geophysics, 62:521–532.

Vernik, L. and A. Nur, 1992, Ultrasonic velocity and anisotropy of hydrocarbon source rocks: Geophysics, 57:727–735.